The Effects of Alloying Additions and Heat Treatment on Creep Properties and Microstructure of High-Pressure Die-Cast Magnesium-Rare-Earth Alloys

A Thesis Submitted for the Degree of
Doctor of Philosophy
by

Serge Gavras

Department of Materials Engineering
Monash University
Victoria, Australia
March 2014

To my parents

John and Christine Gavras

Statement of Originality

This thesis does not contain material that has been submitted or accepted for the award of another degree, diploma or qualification at this or any other university or institution. To the best of my knowledge and belief, it does not contain any materials that have been previously published or written by any other person, expect where due reference is made in the text of the thesis.

Serge Gavras

March 2014

Acknowledgements

Firstly, I would like to thank my supervisors Prof. Mark Easton, Dr. Mark Gibson and my primary supervisor Prof. Jian-Feng Nie for their guidance and patience in me. I am truly grateful for all the time they spent assisting me.

A special thanks goes to Dr. Suming Zhu for his assistance with creep training, electron microscopy and for always being available to help answer my questions. I would also like to thank Assoc. Prof. Carlos Cáceres, Dr. Colleen Bettles and Dr. Trevor Abbot for providing useful feedback during my candidature.

I would like to thank Prof. Nick Birbilis for this support both in his role as the Head of the Department of Materials Engineering and also as a convenor for my candidature progress seminars.

I am also grateful to CAST Cooperative Research Centre (CAST CRC) for funding this research. CAST CRC was established under, and was supported in part by the Australian Government's Cooperative Research Centres Scheme.

I acknowledge the Monash Centre for Electron Microscopy (MCEM) for providing access to experimental facilities. I would like to thank my electron microscope trainers Ms. Ellen Lavoie, Dr. Tim Williams and Dr. Xiya Fang. Furthermore, thank you to Mr. Renji Pan and the rest of the staff at MCEM for all their assistance with training.

I would like to thank and acknowledge Dr. Hajo Dieringa and the Helmholtz-Zentrum Geesthacht, Germany for the compression creep tests performed on my material.

Thank you to Mr. Graham Prior, Mrs. Yeannette Lizama, Mr. Daniel Curtis and Mr. Irek Kozicki for their assistance in training me on numerous pieces of equipment used to conduct my experiments.

Greatest thanks go to my dear friends and colleagues Dr. Katharina Strobel and Dr. Jessica TerBush for the countless productive discussions we had related to my research as well all the time we spent having fun. Additionally, I would like to thank Dr. Marie Clancy for her words of wisdom in relation to completing a thesis, Dr. Kun Yang for our fruitful discussions and to Mr. Paul Firbas for the welcomed respites from work.

I would also like to pay my respects to the late Dr. Marie-Faith Fiawoo. She was an absolutely brilliant electron microscopist who's passing was an utter tragedy. Memory Eternal.

Finally, my deepest thanks go to my family for their never-ending support, love and prayers without which none of this would be possible.

Abstract

Poor elevated temperature creep properties have limited the use of traditional Mg alloys, such as Mg-Al alloys, in the automotive industry primarily to ambient temperature applications in automobiles. Grain boundary reinforcement was commonly used to improve elevated creep properties of Mg alloys by preventing grain boundary sliding. However, the main creep mechanism is still under debate. More recently, precipitation hardening, solid solution strengthening and/or the diffusion rate of solute in the matrix have been proposed as the key factors that influence creep. High-pressure die-cast (HPDC) Mg-rare earth (Mg-RE) alloys are an ideal choice for elevated temperature automotive parts, such as powertrains, due to their excellent elevated temperature creep resistance and high production rate.

In this investigation the differences in elevated temperature creep properties of three high-pressure die-cast Mg-rare earth alloy series, Mg-La-Nd, Mg-La-Y and Mg-La-Gd have been determined. A consistent concentration of La (0.45at.%) was used to maintain similar grain boundary strengthening for all the alloys and also to assist with castability. The ternary RE concentration was varied and the RE elements were chosen to have differing solubility in Mg. This was done to investigate the influence of solid solution strengthening and precipitation hardening on creep.

The creep stress exponent in combination with electron microscopy was used to determine that the main creep mechanism was diffusion-controlled dislocation climb. Dislocations were shown to be decorated by precipitates in all three alloy series. It was shown that the Mg-La-Nd alloy series had significantly worse creep resistance at 177°C and 90 MPa when compared with the Mg-La-Y or Mg-La-Gd alloys series. For alloys with approximately 0.2 at.% ternary RE or greater, the Mg-La-Y and Mg-La-Gd alloys had minimum creep rates of approximately 5×10^{-10} s^{-1} in comparison with Mg-La-Nd alloys which had 1×10^{-8} s^{-1}. Alloys with high concentrations of ternary RE such as Mg-0.45La-

1.18Y (at.%) and Mg-0.45La-0.87Gd (at.%) reached 0.1% creep strain following 600 h of creep testing at 90 MPa and 177°C. The relatively high Nd-concentrated alloy Mg-0.45La-0.63Nd had significantly worse creep properties reaching 1 % creep strain in less than 350 h.

The morphology of the microstructure of three HPDC Mg-La-RE alloy series with varying ternary alloying concentrations was compared. It was found that all alloys had relatively similar morphologies with respect to average grain size, volume fraction of eutectic present at grain boundaries and the intermetallic phase present in the eutectic. The age hardening response of the alloys revealed that the Mg-La-Nd alloys reached peak-aged conditions sooner than Mg-La-Y or Mg-La-Gd but also overaged more rapidly. This was used to indicate that Mg-La-Nd alloys had the poorest thermal stability/fastest diffusion rate of solute out of the three alloys series investigated. The precipitates formed dynamically during creep testing and were finer in Mg-La-Y and Mg-La-Gd alloys than in Mg-La-Nd alloys.

It was shown that it is possible to solution treat for a relatively short duration, or solution treat and then age HPDC Mg-La-RE alloys without causing any surface blistering to the casting. However, creep properties as well as yield strength were negatively affected unless relatively high concentrations of solute in solid solution or a relatively high number density of precipitates were present. This was the result of a reduction in grain boundary reinforcement that was caused by the intermetallic becoming less continuous and also by the removal of the supersaturated region of solute in the matrix near the grain boundaries.

It was concluded that improvements to elevated temperature creep resistance of HPDC Mg-La-RE alloys could be achieved by building on a base Mg-RE alloy (Mg-La) that had sufficiently good castability and grain boundary reinforcement with low diffusive/thermally stable soluble ternary RE additions in solid solution.

Publications and Presentations

Publications:

S. Gavras, S. Zhu, M.A. Easton, M.A Gibson, J-F. Nie; Effects of Heat Treatment on a High-Pressure Die-Cast Mg-La-Y Alloy. 5th International Light Metals Technology Conference Proceedings, Lüneburg, Germany, 2011

S. Gavras, S. Zhu**,** M.A. Gibson, M.A. Easton, J-F Nie; Influence of Rare Earth Elements on Creep Resistance of High-Pressure Die-Cast Magnesium-Rare Earth Alloys. 9th International Conference on Magnesium Alloys and their Applications Proceedings, Vancouver, Canada, 2012.

S. Gavras, M.A. Easton, M.A. Gibson, S. Zhu, J-F. Nie; Microstructure and Property Evaluation of High-Pressure Die-Cast Mg-La-Rare Earth (Nd, Y or Gd) Alloys. J. Alloys and Compounds, 2014 (597), pp. 21.

B. Zhang, **S. Gavras**, A.V. Nagasekhar, C.H. Cáceres M.A. Easton; The Strength of the Spatially Interconnected Eutectic Network in HPDC Mg-La, Mg-Nd and Mg-La-Nd Alloys. Met. Trans, 2014, in press.

Presentations:

5th International Light Metals Technology Conference

Lüneburg, Germany, 19-22 July 2011.

9th International Conference on Magnesium Alloys and their Applications

Vancouver, Canada, 8-12 July 2012.

Contents

Statement of Originality ii

Publications and Presentations vii

List of Figures xii

List of Tables xxiii

1 Introduction 1

2 Literature Review 6

2.1 Introduction 7

2.2 Microstructure and High-Pressure Die-Castability of Mg-Alloys 7
2.2.1 Microstructure of HPDC Mg Alloys 7
2.2.2 Castability 11
2.2.3 Influence of Heat Treatment on HPDC Alloys 15

2.3 Creep in Pure Metals 17
2.3.1 Primary Creep 18
2.3.2 Secondary Creep 19
2.3.3 Determination of Creep Mechanisms 22
2.3.4 Tertiary Creep 26

2.4 Creep Properties of Mg Alloys 28
2.4.1 Creep of Mg-Al alloys 28
2.4.2 Creep of Mg-RE Alloys 38
2.4.3 Influence of Different RE on Creep 39

2.5 Effects of Microstructural Features on Creep 46
2.5.1 Grain Boundary Reinforcement 46
2.5.2 Solute in Solid Solution and Its Effect on Creep 49
2.5.3 Precipitation and Its Effect on Mechanical Properties and Creep 50

2.6 Summary 57

3 Experimental Procedures 60

3.1 Introduction 61

3.2 HPDC of Experimental Materials 62

3.3 Hot Tearing 64

3.4 Mechanical Testing 65
3.4.1 Hardness Testing 65
3.4.2 Heat Treatment 66
3.4.3 Tensile Testing 67
3.4.4 Creep Testing 68

3.5 Microstructural Analysis 73
3.5.1 Scanning Electron Microscopy 74
3.5.2 Transmission Electron Microscopy 76

4 As-Cast Microstructure and Castability of Mg-La-RE Alloys 79

4.1 Introduction 80

4.2 Experimental Results on Microstructure 80
4.2.1 Microstructure of As-Cast Mg-La-RE Alloys 80
4.2.2 Eutectic and Intermetallic Characterisation 82

4.3 Castability 88

4.4 Discussion 90
4.4.1 Effects of alloying elements on microstructure 90
4.4.2 Modelling the castability of alloys with different alloying elements 92

4.5 Conclusions 99

5 Effects of Alloying Elements on As-Cast Mechanical Properties and Microstructure 101

5.1 Introduction 102

5.2 Tensile Properties of As-die-cast Mg-La-RE Alloys 103

5.3 Age Hardening of Mg-La-RE Alloys 108

5.4 Creep Properties of HPDC Mg-La-RE Alloys 112
5.4.1 Tensile Creep 112
5.4.2 Compression Creep 113

5.5 Microstructure of HPDC Mg-La-RE Alloys Following Creep Testing 118

5.6 Discussion 127
5.6.1 Effect of Alloying Elements on Tensile Properties 127
5.6.2 Effect of Alloying Elements on Hardening Response of As-Cast Alloys 130
5.6.3 Effect of Alloying Elements on Creep Properties and Microstructure 131

5.7 Conclusions 133

6 Effects of Heat Treatment on Mechanical Properties and Creep on Mg-La-RE Alloys 134

6.1 Introduction 135

6.2 Ageing Response of Solution Treated HPDC Mg-La-RE Alloys 136

6.3 Tensile Properties of Heat Treated HPDC Mg-La-RE Alloys 138

6.4 Creep Properties of Heat Treated HPDC Mg-La-RE Alloys 144

6.5 Microstructures of Heat Treated HPDC Mg-La-RE Alloys 150
6.5.1 Surface After Solution Treatment 150
6.5.2 Microstructure After Heat Treatment 151
6.5.3 Microstructure After Heat Treatment and Creep Testing 153

6.6 Discussion 166
6.6.1 Heat Treatment of HPDC Mg-La-RE Alloys 166
6.6.2 Age Hardening Response 167
6.6.3 Influence of Heat-Treatment on Tensile Properties of HPDC Mg-La-RE Alloys 168
6.6.4 Precipitates in Mg-La-RE Alloys following Heat Treatment and Creep 170
6.6.5 Influence of Heat Treatment on Creep Properties and Microstructure 171

6.7 Conclusions 174

7 Discussion 176

7.1 Introduction 177

7.2 Simulating Microstructure 178

7.3 Mechanical Properties 184

7.4 Effect of Microstructure on Creep 187

7.5 Improving Creep Performance by Microstructure Engineering 195

7.6 Summary 197

8 Conclusions and Recommendations for Future Work 199

8.1 Conclusion 199

8.2 Future Work 202

References 205

Appendix A 212

Appendix B 213

List of Figures

Figure 1.1: Stress for 0.1 % creep strain in 100 h for cast Mg alloys and Al alloy A380 [9, 10]. 2

Figure 1.2: Methods used in the current work to vary the microstructure and properties of the HPDC Mg-La-RE alloys under investigation in order to determine the influence of different ternary RE alloys on properties. 5

Figure 2.1: Schematic of a cold chamber high-pressure die-casting machine showing the molten metal being poured from a ladle into the shot chamber before being injected into the die [17]. 7

Figure 2.2: As-cast microstructure (SEM) of Mg–3.44 wt.%La (a and d), Mg–2.87 wt.%Ce (b and e) and Mg–2.60 wt.%Nd (c and f) alloys. The amount of intermetallic phase is highest in the La containing alloy and lowest in the Nd containing alloy [14]. 8

Figure 2.3: The micrograph and corresponding schematic diagram of the cross-section of a tensile bar normal to the flow direction (FD) showing 'skin' and 'core' regions and externally solidified grains (ESG) [24]. 10

Figure 2.4: (a) Micro-hardness profile with a colour scale and (b) indentation pattern for the cross-section of the alloy studied [25]. 10

Figure 2.5: Scanning electron microscope backscatter electron micrographs of (a) corner, (b) surface, (c) macrograph of the entire cross section, and (d) 'core' region [25]. 11

Figure 2.6: Picture of a series of flat tensile test pieces each of which is representative of one of the categories in the hot tearing scale defined below (the reference number corresponding to the scale is indicated at the bottom of each). The white arrows indicate the surface dimples that are associated with internal cracking (see also Figure 2.7) [39]. 13

Figure 2.7: Low magnification photomicrographs of polished longitudinal cross-sections through flat rectangular tensile test pieces that display differing degrees of hot tearing as determined by the hot tearing index. a) HTI 0, b) HTI 2 (the white arrow indicates the dimple that is visible on the specimen surface) and c) HTI 3 (the white arrow indicates that the crack is clearly visible in the specimen surface) [39]. 13

Figure 2.8: a) Hot tear index (HTI) of the binary Mg-RE alloys plotted against the alloy content b) predictions of S_{ht2} for $f_{s,0}$=0.7, $f_{s,c0}$=0.98 for the three magnesium-rare earth alloy systems [39]. 14

Figure 2.9: (a) As-cast HPDC aluminium alloy, (b) HPDC aluminium alloy following a solution treatment of 545°C for 16 hours [6]. 16

Figure 2.10: Surface appearance of Al alloy A380 in as-cast condition (a) and a number of different solution treatment (ST) temperatures. Note the dramatic difference in surface appearance of sample (b) aged for 16h in comparison to the 15-minute ST samples (c)-(i) [6]. 16

Figure 2.11: Average values for 0.2% proof stress and elongation for five batches of A380 in as-cast, as-solution treated, T4 and T6 conditions. Note in [6] T4 includes both a solution treatment stage and a natural ageing stage (in this case naturally aged for 14 days) [6]. 17

Figure 2.12: Idealized creep curve identifying the three stages of creep as well as the initial instantaneous strain that can be experienced by the material. 18

Figure 2.13: a) Dislocation glide, the arrows indicate the applied shear stress and the numbers indicate the movement of atoms, b) dislocation climb, in (2) the dislocation is centred in row A and is shown to climb in a positive sense in (1) and negative in (3) via diffusion of atoms and vacancies. [54]. 21

Figure 2.14: Depiction of a) Nabarro-Herring and b) Coble creep on crystals by an applied stress [65]. 21

Figure 2.15: Grain boundary sliding revealed through the use of a transverse marker line across grain boundaries for a Mg-0.78Al (wt.%) alloy creep tested at 17.2 MPa and 200°C [67]. 22

Figure 2.16: Deformation mechanism map for pure Mg with average grain size of 0.1mm [61]. 23

Figure 2.17: A number of strain rate versus stress plots showing the n values for a) Mg-0.8wt.%Al at various temperatures [79] and b) Two creep-resistant Mg alloys MEZ and AE42 at 175°C [80]. 24

Figure 2.18: Plot of strain rate vs. 1/T at various stress levels for a Mg-Nd alloy. The value shown next to each line is the activation energy of creep for that particular stress level [81]. 25

Figure 2.19: Mg-Al binary phase diagram [100]. 29

Figure 2.20: Creep curves for as-cast AZ91D (die-cast) under constant loads at 150°C [102]. 29

Figure 2.21: Typical microstructure of HPDC AZ91 [103]. 30

Figure 2.22: TEM bright-field image, microbeam electron diffractions, and EDS spectra showing typical microstructure and identification of intermetallic phases in as-cast AE44. The lamellar-like intermetallic phase was identified to be Al11RE3 (body-centred orthorhombic structure) whereas the particulate-shaped intermetallic phase is Al2RE (diamond cubic structure) [110]. 32

Figure 2.23: Minimum creep rate plotted against applied stress at 175°C for AE44 compared with AE42 [87]. 33

Figure 2.24: Creep curves for HPDC AE44-based alloys at 150°C under the applied stresses of a) 45 MPa and b) 60 MPa. 34

Figure 2.25: Tensile creep behaviour of AXJ530, MRI153M and MRI230D crept at 110 MPa at 180°C. Failed specimens are indicated by an 'x'. [22] 35

Figure 2.26: SEM (BSE) images of die-cast a) AXJ530, B) MRI230D and c) MR1153M. The darker grey regions are cells of primary α-Mg, while the brighter contrast features are intermetallic phases in the eutectic. [22] 36

Figure 2.27: Least-mean-squares fit of concentration profiles for (a) Mg, (b) Al, and (c) Ca in MRI153M, MRI230D, AXJ530, and AX44, as measured by the electron microprobe. (d) Same as (b), except showing the scatter in the experimental data, which is caused by errors in the Mg concentrations used to sort the rest of the elements [118]. 37

Figure 2.28: Cost of Nd per tonne also showing cost of Al for comparison [122]. 38

Figure 2.29: Calculated isothermal Mg-La-Nd phase diagram section at 500°C. Three-phase triangles are shaded in grey [132]. 40

Figure 2.30: a) Full binary phase diagram for Mg-La in at.%, b) Mg-rich section of the phase diagram (wt.%) [131, 133]. 41

Figure 2.31: a) Full binary phase diagram for Mg-Nd, b) Mg-rich section of the phase diagram (wt.%) [131, 134]. 41

Figure 2.32: a) Full binary phase diagram for Mg-Y, b) Mg-rich section of the phase diagram (wt.%) [131]. . 41

Figure 2.33: a) Full binary phase diagram for Mg-Gd, b) Mg-rich section of the phase diagram (wt.%) [131, 135]. 42

Figure 2.34: Dynamic precipitation during creep of Mg-2.4Y (wt.%) at 277°C and 100 MPa: a) Just after applying load and b) After creep for 20 h [13]. 44

Figure 2.35: TEM micrographs showing microstructures of Mg-3.44La (wt.%) (a and d), Mg-2.87Ce (wt.%) (b and e) and Mg-2.60Nd (c and f) before and after creep testing at 177°C and 50 MPa for 300 h. Note the increased presence of precipitates in the Mg-2.87Ce and particularly Mg-2.60Nd alloys after creep [14]. 44

Figure 2.36: Creep curves for Mg-3.44La, Mg-2.87Ce and Mg-2.60Nd (wt.%) at 177°C and 90 MPa [14]..... 45

Figure 2.37: Detail of creep cavities on dendrite boundaries nucleated during exposure of Mg-3Y-2Nd-1Zn-1Mn at 300°C and 50 MPa: (a) Single creep cavity in earlier stage of creep exposure (relative time of test *t*/*t*f=0.47); (b) Coalescence of cavities in later stages (relative time of test *t*/*t*f=0.67); (c) Continuous crack in crept specimen [146]. 46

Figure 2.38: (a-g) Sets of creep rates at indicated stress levels at a testing temperature of 200°C. Open circles shown in (c) illustrate the evaluation of minimum creep rates. All graphs share the same axes. The corresponding SEM micrographs of the alloys are shown in h) - n). Note the step measurements indicate the depth of the stepped plate used during casting [148]. 47

Figure 2.39: a) Cubic volume of the HPDC Mg-La alloy examined using FIB. The lighter phase is the pro-eutectic α-Mg whereas the darker one is the percolating 3D (α-Mg)-$Mg_{12}La$ eutectic. The latter is shown on its own in (b) [149]..... 48

Figure 2.40: Comparison of the steady-state creep rates of Mg-1.0at.%Al and Mg-1.1at.%Y solid solution alloys subjected to different stresses at 277°C [12]..... 49

Figure 2.41: a) Arrangement of $\{10\bar{1}0\}_\alpha$ or $\{2\bar{1}\bar{1}0\}_\alpha$ precipitate plates in a triangular prismatic volume of α-Mg matrix, and b) projection of intersected prismatic plates in $(0001)_\alpha$ slip plane of α-Mg [157]. L_p is the mean planar centre-to-centre inter-precipitate spacing, d_p is the mean diameter of the plate, t_p is the mean planar thickness and λ is the effective planar inter-particle spacing. 51

Figure 2.42: Variation of ratio $\Delta\tau$(plate/rod)/$\Delta\tau$(sphere) with plate/rod aspect ratio for strengthening attributing to a) $(0001)_\alpha$, b) $\{10\bar{1}0\}_\alpha$ or $\{2\bar{1}\bar{1}0\}_\alpha$ prismatic plates, and c) $[0001]_\alpha$ rods, at precipitate volume fractions of 0.02 and 0.04 [157]. 52

Figure 2.43: Variation of effective inter-particle spacing with number density of particles per unit volume of the magnesium matrix at a precipitate volume fraction of 0.04. Plate/rod aspect ratio is 40:1 [157]. 53

Figure 2.44: a) Isothermal ageing curves of magnesium alloy AZ91 at 373 K and 473 K (100°C and 200°C), b) Transmission electron micrograph showing the distribution and morphology of β precipitates in AZ91 aged for 8 h at 473 K (200 °C) with the electron beam parallel to $[0001]_{\alpha}$. Age-hardening response of WE54 alloy, c) at 523 K (250°C), d) Transmission electron micrograph showing distribution of precipitates in a WE54 sample peak-aged at 523 K (250°C) [139]. 54

Figure 2.45: Schematic diagram showing the microstructural evolution from G-P zones to β' then a combination of β' and β_1 to the eventual formation of equilibrium β precipitates in Mg-15Gd-0.5Zr and Mg-10Gd-3Y-0.4Zr (wt.%) alloys at 250°C [162]. 55

Figure 2.46: a) Age hardening response at 225°C for Mg-10Y-5Gd (wt.%) b) creep curves of Mg-10Y-5Gd alloys in as-cast and peak aged conditions tested at different temperatures and stress [163]. . 55

Figure 2.47: Creep curves for Alloy A and Alloy B for (a) as-cast and (b) T6 conditions tested at 177°C and 90MPa [167]. 57

Figure 3.1 A HPDC casting showing two round and one flat tensile sample. [45]. 63

Figure 3.2: Schematic diagram of a) round and b) flat "dog-bone" shaped tensile bars used in this work. Note: Dimensions are in mm. 64

Figure 3.3: a) Side view of the creep rig, b) samples locked into the holders, c) oil bath in raised position, completely immersing the creep samples in silicon oil which is at the testing temperature of 177°C. 70

Figure 3.4: Photo of Mg-0.45La-1.18Y in as-cast condition cut and drilled for creep testing with an Instron extensometer attached to it. 71

Figure 3.5: Photo of an ATS compression creep machine showing the components of the rig inside the oven [172]. 72

Figure 3.6: Kikuchi map overlaid with identification lines from EBSD phase identification for Mg-0.49La-0.24Y for a map with an MAD of a) less than 0.5° and b) of approximately 1°. 75

Figure 3.7: Scanning electron microscopes used in the current studies a) JEOL JSM 7001F field emission scanning electron microscope and b) FEI Quanta 3D FEG FIB. 76

Figure 3.8 Transmission electron microscopes used in this work a) FEI Tecnai G2 T20 TWIN LaB6 TEM, and b) Philips CM20. 77

Figure 4.1: SEM BSE micrographs of the dendritic morphology of the "core" region of Mg-0.43La-0.18Nd, Mg-0.49La-0.24Y and Mg-0.46La-0.21Gd (at.%) are shown in images a), b) and c) respectively. The brighter feature in the microstructure is the eutectic and the darker grey feature is the α-Mg matrix. Gas pores (dark/black features) are circled. 81

Figure 4.2: EBSD maps showing grains in (a) Mg-0.45La-1.18Y and (b) Mg-0.45La-0.63Nd alloys in the as-cast condition [130]. 81

Figure 4.3: SEM BSE micrographs of a) "skin" region and b) "core" region of Mg-0.49La-0.24Y. 82

Figure 4.4: An example SEM BSE micrograph used to determine the amount of eutectic present in an alloy of as-cast Mg-0.45La-0.63Nd a) original image from SEM and b) inverted high contrast image to isolate eutectic. 83

Figure 4.5: SEM BSE micrographs showing eutectic morphologies in a) Mg-0.46La, b) Mg-0.43La-0.18Nd, c) Mg-0.45La-0.63Nd, d) Mg-0.49La-0.24Y, e) Mg-0.45La-1.18Y, f) Mg-0.46La-0.21Gd and g) Mg-0.45La-0.87Gd alloys. 84

Figure 4.6: Atomic ratio of total ternary alloying addition to La present in the eutectic for alloys with relatively low, medium and high concentrations of Nd, Y or Gd determined from EDS and predicted from the Scheil-Gulliver equation. The dashed lines indicate upper and lower bounds of the predicted Nd to La ratio predicted by the Scheil-Gulliver equation. 86

Figure 4.7: Kikuchi maps obtained from the intermetallic present in the eutectic are overlaid with identification lines from EBSD phase identification for $Mg_{12}RE$ a) Mg-0.45La-0.63Nd b) Mg-0.45La-1.18Y and c) Mg-0.45La-0.87Gd alloys. 87

Figure 4.8: a) STEM micrograph of Mg-0.45La-1.18Y grain in as-cast condition showing where the EDS line scan recorded and b) the corresponding EDS line scan measurements for Mg, La and Y across the grain. 87

Figure 4.9: Hot tearing index as a function of total ternary alloying addition for Mg-La-Nd, Mg-La-Y and Mg-La-Gd alloy series. Note: lower hot tearing indices indicate better castability. 89

Figure 4.10: Comparison between experimentally determined eutectic volume fraction (Exp) and Scheil-Gulliver (S-G) equation calculations for the volume fraction of eutectic as a function of total ternary alloying concentration for each alloy series and a binary Mg-0.46La alloy. The Scheil-Gulliver (S-G) equation predicted volume fraction of intermetallic in Mg-La-Nd alloys is also included for comparison. 91

Figure 4.11: Temperature – fraction solid curve for Mg-0.49La-0.18Nd. The blue highlighted area indicates the region of the curve between the points of coherency and coalescence, which were chosen to be 0.7 and 0.98 respectively. 93

Figure 4.12: Temperature-fraction solid curves determined using Scheil-Gulliver equation for Mg-La-Nd alloys with varying concentrations of Nd alloying addition. 95

Figure 4.13: Comparison between experimentally determined HTS and predicted HTS for the Mg-La-Nd alloy system (compositions given in Table 4.3). Note: lower hot tearing indices indicate better castability. 96

Figure 4.14: a) HTS predictions for Mg-Y and Mg-Gd. The predicted HTS for Mg-La-Nd and the binary equivalent alloys Mg-Nd is included for comparison and b) comparison between experimentally (Exp) determined HTS and predicted HTS using binary Mg-Y and Mg-Gd equivalent alloys for the Mg-La-Y and Mg-La-Gd alloy systems when the point of coherency is $0.7f_s$ and the point of coalescence is $0.98f_s$. 97

Figure 4.15: Comparison between experimentally (Exp) determined HTS and predicted HTS using binary Mg-Y and Mg-Gd equivalent alloys for the Mg-La-Y and Mg-La-Gd alloy systems when the point of coherency is $0.9f_s$ and the point of coalescence is $0.99f_s$. 98

Figure 5.1: Stress-strain curves at room temperature for as-cast alloys with ternary RE additions of a) Nd, b) Y and c) Gd. 104

Figure 5.2: a) 0.2% proof stress and b) elongation for Mg-La-Nd, Mg-La-Y and Mg-La-Gd alloys, tested at room temperature. 105

Figure 5.3: Stress-Strain curves for at 177°C of as-cast alloys with ternary RE additions of a) Nd, b) Y and c) Gd. 106

Figure 5.4: a) 0.2% proof stress and b) elongation for Mg-La-Nd, Mg-La-Y and Mg-La-Gd alloy series, tested at 177°C in as-cast condition. 107

Figure 5.5: Solvus line projections for a) Mg-Nd, b) Mg-Y and c) Mg-Gd constructed from binary phase diagram data from [131] for Mg-Nd and Mg-Y and [135] for Mg-Gd. 109

Figure 5.6: Age hardening response of Mg-0.45La-0.63Nd, Mg-0.45La-1.18Y and Mg-0.45La-0.87Gd at a) 160°C, b) 177°C and c) 200°C. 110

Figure 5.7: Age hardening response of Mg-0.43La-0.18Nd, Mg-0.49La-0.24Y and Mg-0.46La-0.21Gd during isothermal ageing at a) 160°C and b) 200°C. 111

Figure 5.8: Creep strain curves for three as-cast a) Mg-La-Nd b) Mg-La-Y and c) Mg-La-Gd alloys tested at 177°C and 90MPa. 112

Figure 5.9: Minimum creep rate as a function of total ternary alloying addition concentration for Mg-La-Nd, Mg-La-Y and Mg-La-Gd alloy series tested at 177°C and 90MPa. 113

Figure 5.10: Comparison between compression and tensile creep for a) Mg-0.45La-0.63Nd and b) Mg-0.45La-1.18Y creep tested at 177°C and 90 MPa. 114

Figure 5.11: Compression creep curves for a) Mg-0.45La-0.63Nd and b) Mg-0.45La-1.18Y alloys tested over a range of temperatures and stresses. 115

Figure 5.12: Creep rate versus stress for Mg-0.45La-0.63Nd at 177°C and 275°C. Note the open symbol indicates tensile creep data. 116

Figure 5.13: Creep strain rate vs. 1/T with activation energies (Q) for Mg-0.45La-0.63Nd at 30 and 90MPa. 116

Figure 5.14: Creep rate versus stress for Mg-0.45La-1.18Y at 177°C and 275°C to determine the n-values. Note the open symbol indicates tensile creep data. 117

Figure 5.15: Creep strain rate vs. 1/T with activation energies (Q) for Mg-0.45La-1.18Y at 90 and 130MPa. 118

Figure 5.16: $[0001]_{\alpha}$ Bright field (BF) TEM micrographs following creep testing at 177°C and 90 MPa in the as-cast condition of a) Mg-0.47La-0.10Nd, b) Mg-0.43La-0.18Nd, c) Mg-0.45La-0.63Nd following tensile creep, d) Mg-0.45La-0.63Nd following compression creep. Higher resolution micrographs more clearly showing precipitates are also included for tensile crept e) Mg-0.43La-0.18Nd and f) Mg-0.45La-0.63Nd and precipitate morphology g) Mg-0.43La-0.18Nd and h) Mg-0.45La-0.63Nd. 119

Figure 5.17: $[0001]_{\alpha}$ BF TEM micrographs following tensile creep testing at 177°C and 90 MPa a) Mg-0.48La-0.12Y, b) Mg-0.49La-0.24Y and c) Mg-0.45La-1.18Y following tensile creep and d) Mg-0.45La-1.18Y following compression creep. 120

Figure 5.18: Precipitate in Mg-0.49La-0.24Y alloy following creep testing at 177°C and 90 MPa for 600 h in the as-cast condition. 121

Figure 5.19: a) and b) Region of a Mg-0.45La-1.18Y specimen densely populated with β' precipitates tensile crept at 177°C and 90 MPa, c and d) comparable region of precipitates in a compression crept sample at 177°C and 90 MPa, e) higher resolution micrograph of the β' precipitates from tensile crept sample and f) diffraction pattern from the region which identifies the precipitates as β'. 122

Figure 5.20: BF TEM micrographs of as-cast a) Mg-0.45La-0.10Gd, b) Mg-0.46La-0.21Gd c) Mg-0.45La-0.87Gd following creep testing at 177°C and 90 MPa. 123

Figure 5.21: Dynamic precipitates of Mg-0.46La-0.21Gd a) nucleating near grain boundary and b) higher resolution micrograph of precipitates. Micrographs recorded along the $[0001]_{\alpha}$ direction. 124

Figure 5.22: Dynamic precipitates observed in alloy Mg-0.45La-0.87Gd a) Dynamic precipitates nucleating throughout grain b) diffraction pattern from densely populated region of precipitates aligned along [0001] showing β' precipitates, c) dense concentration of β' precipitates near grain boundary d) outer region of densely concentrated precipitate region showing a combination of β' and β'+ β_1 precipitates and e) elongated β' precipitates near grain centre. 125

Figure 5.23: Dislocations in a) Mg-0.45La-0.63Nd and b) Mg-0.45La-1.18Y and c) Mg-0.45La-0.87Gd with higher resolution localised micrographs. 126

Figure 5.24: a) 0.2% proof stress and b) elongation at room temperature as a function of predicted volume fractions of eutectic or intermetallic phase in pure Mg, Mg-La from Chia *et al.* [18] and Mg-La-Nd alloys from the current work. 128

Figure 6.1: Repeated age hardening response of Mg-0.45La-1.18Y solution treated at 520°C for 1 h and aged at a) 160°C or b) 177°C. Note: AC = as-cast and AQ = as-quenched..... 137

Figure 6.2: Age hardening response for Mg-0.45La-0.63Nd, Mg-0.45La-1.18Y and Mg-0.45La-0.87Gd following solution treatment at 520°C for 1 h and then aged at a) 160°C or b) 177°C. Note c) is a combination of the 177°C ageing curves of the Mg-La-Nd and Mg-La-Gd alloys with the 160°C ageing curve of the Mg-La-Y alloy. Note: AC = as-cast and AQ = as-quenched. 138

Figure 6.3: Stress-strain curves at 177°C for a) Mg-0.47La-0.10Nd, b) Mg-0.43La-0.18Nd and c) Mg-0.45La-0.63Nd in T4 (520°C/1h) and T6 (520°C/1h and 177°C/16h) conditions. As-cast stress-strain curves are also included for comparison. Note: There is a change in scale size for c) for clarity. 140

Figure 6.4: Stress-strain curves at 177°C for a) Mg-0.48La-0.12Y, b) Mg-0.49La-0.24Y and c) Mg-0.45La-1.18Y in T4 (520°C/1h) and T6 (520°C/1h and 160°C/1700h) conditions. As-cast stress-strain curves are also included for comparison. Note: There is a change in scale size for c) for clarity. 142

Figure 6.5: Stress-strain curves at 177°C for a) Mg-0.45La-0.10Gd, b) Mg-0.46La-0.21Gd c) Mg-0.45La-0.87Gd in T4 (520°C/1h) and T6 (520°C/1h and 177°C/400h) conditions. As-cast stress-strain curves are also included for comparison. Note: There is a change in scale size for c) for clarity. 144

Figure 6.6: Creep strain comparisons of as-cast, T4 (520°C/1h) and T6 (520°C/1h and 177°C/16h a) for Mg-0.47La-0.10Nd, b) Mg-0.43La-0.18Nd and c) Mg-0.45La-0.63Nd alloys creep tested at 177°C and 90MPa. 145

Figure 6.7: Comparison of minimum creep rates as a function of ternary addition concentration in the as-cast, T4 (520°C/1h) and T6 (520°C/1h and 177°C/16h) for the Mg-La-Nd alloy series and creep tested at 177°C and 90MPa..... 146

Figure 6.8: Creep strain comparisons of as-cast, T4 (520°C/1h) and T6 (520°C/1h and 160°C/1700h) for a) Mg-0.48La-0.12Y, b) Mg-0.49La-0.24Y and c) Mg-0.45La-1.18Y alloys creep tested at 177°C and 90MPa. Note: There is a change in scale for c) for clarity..... 147

Figure 6.9: Comparison of minimum creep rates as a function of ternary addition concentration in the as-cast, T4 (520°C/1h) and T6 (520°C/1h and 160°C/1700h) for the Mg-La-Y alloy series and creep tested at 177°C and 90MPa..... 148

Figure 6.10: Creep strain comparisons of as-cast, T4 (520°C/1h) and T6 (520°C/1h and 177°C/400h) for a) Mg-0.45La-0.10Gd, b) Mg-0.46La-0.21Gd c) Mg-0.45La-0.87Gd alloys creep tested at 177°C and 90MPa. Note: There is a change in scale for c) for clarity..... 149

Figure 6.11: Comparison of minimum creep rates as a function of ternary addition concentration in the as-cast, T4 (520°C/1h) and T6 (520°C/1h and 177°C/400h) for the Mg-La-Gd alloy series and creep tested at 177°C and 90MPa..... 150

Figure 6.12: Mg-0.49La-0.42Y specimens a) as-cast, b) solution treated at 520°C for 1h, c) solution treated at 520°C for 1h and aged at 160° for 24h, and d) SEM topographical image of 'skin' region in the T6 specimen showing no blistering of pores..... 151

Figure 6.13: SEM BSE micrographs of the "core" region of solution treated (520°C for 1 h) a) Mg-0.47La-0.10Nd, b) Mg-0.48La-0.12Y, c) Mg-0.45La-0.10Gd, d) Mg-0.43La-0.18Nd e) Mg-0.49La-0.24Y, f) Mg-0.46La-0.21Gd, g) Mg-0.45La-0.63Nd, h) Mg-0.45La-1.18Y and i) Mg-0.45La-0.87Gd alloys. 152

Figure 6.14: a) Measured volume fraction of eutectic in as-cast or intermetallic in T4 (520°C/1h) and T6 (520°C/1h and peak ageing) Mg-La-RE alloys with varying concentrations of ternary alloying additions, and b) Atomic ratio of total ternary alloying addition to La present in the eutectic for alloys in as-cast and in the intermetallic for alloys in the T4 condition determined from EDS..... 153

Figure 6.15: Low magnification bright field TEM micrographs along $[0001]_{\alpha}$ of a) Mg-0.47La-0.10Nd, b) Mg-0.43La-0.18Nd and c) Mg-0.45La-0.63Nd following creep testing at 177°C and 90 MPa T4 (520°C-1h) condition. 154

Figure 6.16: Higher magnification bright field TEM micrographs along $[0001]_{\alpha}$ of dynamic precipitates formed during creep testing at 177°C and 90 MPa in T4 a) and b) Mg-0.47La-0.10Nd, c and d) Mg-0.43La-0.18Nd and e) and f) and Mg-0.45La-0.63Nd. Note: precipitates are circled in a) for clarity. 155

Figure 6.17: Low magnification bright field TEM micrographs along $[0001]_{\alpha}$ of a) Mg-0.47La-0.10Nd, b) Mg-0.43La-0.18Nd and c) Mg-0.45La-0.63Nd following creep testing at 177°C and 90 MPa in T6 (520°C-1h and then peak aged) condition..... 156

Figure 6.18: Higher magnification bright field TEM micrographs along $[0001]_{\alpha}$ of precipitates following creep testing at 177°C and 90 MPa in T6 (520°C for 1h and peak aged) a) and b) Mg-0.47La-0.10Nd, c) Mg-0.43La-0.18Nd and d) Mg-0.45La-0.63Nd alloys. 157

Figure 6.19: Low magnification bright field TEM micrographs along $[0001]_\alpha$ of a) Mg-0.48La-0.12Y, b) Mg-0.49La-0.24Y and c) Mg-0.45La-1.18Y following creep testing at 177°C and 90 MPa T4 (520°C-1h) condition. 158

Figure 6.20: Low magnification bright field TEM micrographs along $[0001]_\alpha$ of cast a) Mg-0.48La-0.12Y, b) Mg-0.49La-0.24Y and c) Mg-0.45La-1.18Y following creep testing at 177°C and 90 MPa in T6 (520°C-1h and then peak aged) condition. 159

Figure 6.21: Bright field TEM micrographs along $[0001]_\alpha$ of precipitates following creep testing at 177°C and 90 MPa in T6 (520°C for 1h and peak aged) a) and b) Mg-0.49La-0.24Y..... 159

Figure 6.22: TEM micrographs along $[0001]_\alpha$ of precipitates following creep testing at 177°C and 90 MPa in T6 (520°C for 1h and peak aged) a) – c) Mg-0.45La-1.18Y and d) diffraction pattern from the region shown in (a) indicating that the globular phase is β'. Note: image c) was obtained by Ms Wen-Fan Xu on my behalf use a FEI F20 in dark field mode..... 160

Figure 6.23: Low magnification bright field TEM micrographs along $[0001]_\alpha$ of a) Mg-0.45La-0.10Gd, b) Mg-0.46La-0.21Gd c) Mg-0.45La-0.87Gd following creep testing at 177°C and 90 MPa T4 (520°C-1h) condition. 161

Figure 6.24: Higher magnification bright field TEM micrographs along $[0001]_\alpha$ of a) Mg-0.45La-0.10Gd, b) and c) Mg-0.46La-0.21Gd following creep testing at 177°C and 90 MPa T4 (520°C-1h) condition. Note: c) shows a higher resolution micrographs of one of the dislocations decorated with precipitates from b). 162

Figure 6.25: a) – c) Bright field TEM micrographs along $[0001]_\alpha$ of dynamic precipitates formed during creep testing at 177°C and 90 MPa in Mg-0.45La-0.87Gd in T4 condition and d) diffraction pattern from the region which identifies the precipitates as β'. 163

Figure 6.26: Low magnification bright field TEM micrographs along $[0001]_\alpha$ of a) Mg-0.45La-0.10Gd, b) Mg-0.46La-0.21Gd c) Mg-0.45La-0.87Gd following creep testing at 177°C and 90 MPa in T6 (520°C-1h and then peak aged) condition. 164

Figure 6.27: Higher magnification bright field TEM micrographs along $[0001]_\alpha$ of precipitates following creep testing at 177°C and 90 MPa in T6 condition (520°C for 1h and peak aged) a) Mg-0.45La-0.10Gd and b) - c) Mg-0.46La-0.21Gd. 165

Figure 6.28: Bright field TEM micrographs along $[0001]_\alpha$ of precipitates following creep testing at 177°C and 90 MPa in T6 (520°C for 1h and peak aged) a) – b) Mg-0.45La-0.87Gd and c) diffraction pattern from the region which identifies the precipitates as β'. Note: A dislocation decorated by precipitates is circled in a)..... 166

Figure 6.29: Influence of the volume fraction of intermetallic at grain boundaries on 0.2 % PS at 177°C for Mg-La-Nd, Mg-La-Y and Mg-La-Gd in as-cast (AC) T4 and b) T6 conditions. The alloys with the highest concentration of ternary RE and those with approximately 0.25 at.% ternary RE or less that were tested in the present work are indicated. 169

Figure 7.1: Summary diagram of the influence of microstructure including grain boundary reinforcement and varying ternary RE concentrations on the creep properties. Note: GBR is grain boundary reinforcement, SSS is solid solution strengthening and PP^{tn} is precipitation hardening..... 177

Figure 7.2: Composition profiles of a) Mg-0.47La-0.10Nd, b) Mg-0.10Nd, c) Mg-0.43La-0.18Nd, d) Mg-0.18Nd, e) Mg-0.45La-0.63Nd and f) Mg-0.63Nd in as-cast, equilibrium T4 (520°C) and T6 (177°C) conditions. The solubility of Nd at ageing/testing temperature of 177°C is also included. Note in a) the region of supersaturation is shown, in e) the distinct regions of the composition profile curve are labelled and f) the distinct regions of the curve following solution treatment and then ageing at 177°C are labelled. 181

Figure 7.3: Composition profiles of a) Mg-0.12Y and b) Mg-0.10Gd in as-cast condition and at equilibrium following T4 solution treatment (520°C) and T6 ageing (160°C or 177°C) temperatures. The solubility of Y or Gd at their respective ageing temperatures is also included. 183

Figure 7.4: Composition profiles of a) Mg-0.24Y and b) Mg-0.21Gd in as-cast condition and at equilibrium following T4 solution treatment (520°C) and T6 ageing (160°C or 177°C) temperatures. The solubility of Y or Gd at their respective ageing temperatures is also included. 184

Figure 7.5: Composition profiles of a) Mg-1.18Y and c) Mg-0.87Gd in as-cast condition and at equilibrium following T4 solution treatment (520°C) and T6 ageing (160°C or 177°C) temperatures. The solubility of Y or Gd at their respective ageing temperatures is also included. 184

Figure 7.6: 0.2 % PS at a) room temperature and b) 177°C for Mg-La-Nd, Mg-La-Y and Mg-La-Gd alloys as a function of the volume fraction of eutectic in as-cast (AC) alloys or intermetallic in T4 and T6 heat-treated alloys experimentally measured. The volume fraction of intermetallic for Mg-La-Nd alloys determined from temperature-fraction of phase curves (Sim) is included for comparison. 186

Figure 7.7: Example of a typical creep strain curve of the alloys investigated in the current work. The primary creep strain at 5 h and the region where the minimum creep rate is calculated are indicated. 188

Figure 7.8: Minimum creep rate of as-cast Mg-La-Nd, Mg-La-Y and Mg-La-Gd alloys with change in ternary RE in comparison with a) eutectic volume fraction and b) 0.2 % PS. 189

Figure 7.9 Primary creep strain after 5 h of creep strain ($\varepsilon_{p,\ t=5h}$) as a function of 0.2% PS and eutectic or intermetallic fraction for Mg-La-Nd, Mg-La-Y and Mg-La-Gd creep tested at 177°C and 90 MPa and tensile tested at 177°C in a) as-cast, b) T4 and c) T6 conditions. Note: Mg-0.47La-0.10Nd, Mg-0.48La-0.12Y and Mg-0.45La-0.10Gd are circled. 191

Figure 7.10: Minimum creep rate of Mg-La-Nd, Mg-La-Y and Mg-La-Gd alloys in the as-cast condition in relation to concentration of supersaturation measured from Mg-Nd, Mg-Y and Mg-Gd binary alternative simulations. Note: the supersaturation was calculated from binary Cs – fraction of phase profiles of Mg-Nd, Mg-Y and Mg-Gd. 192

Figure 7.11: Comparison of minimum creep rates in Mg-La-Nd alloys in the as-cast condition and T4 condition as a function of supersaturation of solute and volume fraction of intermetallic. Note the intermetallic volume fraction for the as-cast alloys was determined from the Mg-La-Nd temperature-fraction of phase curves and for T4 from BSE SEM micrograph image analysis. 193

Figure 7.12: Minimum creep rate of Mg-La-Nd, Mg-La-Y and Mg-La-Gd alloys in the as-cast condition in relation to concentration of total solute is solid solution measured from Mg-Nd, Mg-Y and Mg-Gd binary alternative simulations. 194

Figure 7.13: Minimum creep rate at 177°C and 90 MPa for Mg-0.45La-0.63Nd, Mg-0.45La-1.18Y and Mg-0.45La-0.87Gd in relation to peak ageing duration at 160°C. 194

Figure 7.14: Overview of a HPDC Mg-La-RE sample (Mg-0.45La-0.87Gd) that shows the influence of the alloy features on the properties of the sample. 197

Figure 7.15: Influence of solute in Mg solid solution on creep. Examples of commonly used alloying additions in Mg alloys are included along with RE elements for comparison. 198

List of Tables

Table 2.1: Summary of some of the creep studies on Mg alloys with assessment of dominant creep mechanism (n). Note: * indicates compression creep testing. 27

Table 2.2: Typical steady-state creep rates (minimum creep rates) and tensile 0.2 % proof strength of selected die-cast Mg alloys. The Al alloy A380 is also included for comparative purposes. [7, 12, 125, 127]..... 39

Table 2.3: Radii of rare-earth elements and Mg and maximum solid solubility of Y, La, Ce, Nd and Gd in Mg [131]. 40

Table 2.4: Precipitation sequences in individual magnesium alloy systems [139]. Note: * d is the separation distance of columns of RE atoms. 43

Table 2.5: Solid diffusivity of Mg, Ce and Al in magnesium D_o = diffusion coefficient and Q = activation energy [12]. * Values of D_0 and Q for Zn were obtain from [152] for comparison. 50

Table 2.6: Minimum creep rates (compression tests) of AZ91 and WE54 alloys. Note: * indicates creep rate measured at a plastic strain of 4% [159]..... 53

Table 3.1: Casting parameters for HPDC of alloys in this project. 62

Table 3.2: Actual alloy compositions determined by inductively coupled plasma atomic emission spectroscopy (ICP-AES)..... 63

Table 3.3: T5 peak ageing heat treatment for the three alloy series investigated. 66

Table 3.4: T6 heat treatment for the three alloy series investigated 67

Table 3.5: Test conditions for each alloy that are tensile creep tested. Note * indicates tests performed by Dr. Mark Gibson at CSIRO. 68

Table 3.6: Test conditions for each alloy that was compression creep tested. 73

Table 3.7: Summary of the techniques used and their application in the results chapters (Chapters 4 – 6).. 78

Table 4.1: Average grain sizes in “core” and “skin” regions for Mg-La-RE alloys. 82

Table 4.2: Average volume fraction of eutectic for Mg-La-Nd, Mg-La-Y and Mg-La-Gd with similar concentrations of La but with varying concentrations of ternary RE. The average volume fraction of binary Mg-0.46La is also included for comparison. 83

Table 4.3: List of alloys used to determine hot tearing susceptibility. The number of samples per alloy that received a particular hot tearing rating and the hot tearing index (HTI) and standard error (SE) are included..... 89

Table 4.4: Eutectic concentration [131] and concentration of $Mg_{12}RE$ in binary Mg-RE alloys with the ratio of the two concentrations where greater than 1 means the eutectic composition is less than the $Mg_{12}RE$ phase. Mg-La is shown for comparative purposes..... 92

Table 4.5: Eutectic temperatures of RE elements in Mg at the Mg-rich side of the phase diagram [131]..... 94

Table 5.1: Average tensile properties at room temperature for Mg-La-Nd, Mg-La-Y and Mg-La-Gd alloys in the as-cast condition. 103

Table 5.2: Average tensile properties at 177°C for Mg-La-Nd, Mg-La-Y and Mg-La-Gd alloys in the as-cast condition. 105

Table 5.3: Compression properties of Mg-0.45La-0.63Nd and Mg-0.45La-1.18Y in as-cast condition. 107

Table 5.4: Solubilities of Y, Nd and Gd in Mg at 160°C, 177°C and 200°C. Note: Nd solubility values were taken from the Mg-La-Nd ternary phase diagram and Y and Gd solubility in Mg were determined from solvus line projections of binary phase diagrams, [135] and [131] respectively. 108

Table 5.5: Comparison of the solubility of Nd in Mg determined from solvus line projections of the Mg-Nd phase diagram [131] and ternary Mg-La-Nd phase diagram [132]..... 109

Table 5.6: Approximate peak ageing duration for Mg-0.45La-0.63Nd, Mg-0.45La-1.18Y and Mg-0.45La-0.87Gd at 160, 177 and 200°C. 111

Table 5.7: Average minimum (±SD) creep rate of Mg-0.45La-0.63Nd and Mg-0.45La-1.18Y specimens compression creep tested over a number of temperatures and stresses. Tests were performed at HZG, Germany. 114

Table 6.1: Tensile properties at 177°C of Mg-La-Nd alloys in as-cast, T4 and T6 conditions. 139

Table 6.2: Tensile properties at 177°C of Mg-La-Y alloys in as-cast, T4 and T6 conditions. 141

Table 6.3: Tensile properties at 177°C of Mg-La-Gd alloys in as-cast, T4 and T6 conditions. 143

Table 6.4: Average grain size for Mg-0.45La-0.63Nd, Mg-0.45La-1.18Y and Mg-0.45La-0.87Gd in T4 and T6 conditions. As-Cast average grain sizes are included for comparison. 151

Table 7.1: Values of the gradient of the liquidus line and partition coefficients for Mg-Nd, Mg-Y and Mg-Gd alloy systems [131]. 180

Table 7.2: Supersaturation approximations for Mg-La-Nd, Mg-Nd, Mg-Y and Mg-Gd alloys obtained from ternary and binary temperature-fraction of phase curves respectively. 182

1 Introduction

Automobile usage accounts for 10% of greenhouse gas emissions worldwide [1]. As a result of this, weight-saving has become increasingly important for the automotive sector as regulatory pressure is imposed by Governments worldwide to compel the industry to improve the fuel efficiency of automobiles. It has been shown that fuel consumption reduces by 0.3–0.4 l/100 km of travel for every 100 kg of weight reduction for a similar vehicle size and acceleration performance [2, 3]. Significant weight-saving can be achieved by replacing the heavier components in automobiles, such as those in the powertrain, with parts manufactured from light-weight magnesium alloys. There are a number of advantages related to the use of magnesium alloys over existing light-weight materials such as aluminium alloys. Magnesium is approximately 1/3 the weight of steel and 2/3 the weight of aluminium. However, conventional Mg alloys have relatively poor creep resistance at elevated temperatures such as those present in powertrain applications.

Powertrain components are traditionally produced by high-pressure die-casting (HPDC) in order to maximise efficiency and reduce the cost per casting [4, 5]. These castings are rarely heat treated at high temperatures as the porosity or entrained gas trapped within may cause blistering on the surface of the cast products. In recent years, it has been demonstrated that some HPDC Al alloys can be heat treated at high temperatures without causing any surface blistering if the heat treatment temperature and time are properly controlled [6]. However, little research has been performed for HPDC Mg alloys in relation to high temperature heat treatments. In addition, for HPDC alloys that can be precipitation hardened, the use of heat treatment may offer an opportunity for improvements in strength and creep resistance.

The Mg-rare-earth (Mg-RE) based alloys are age hardenable and in some cases high-pressure die-castable [7, 8]. Moreover, the elevated temperature creep resistance of RE containing Mg alloys such as AE42 (Mg-4Al-2RE wt.%), AM-SC1 (Mg-1.7Nd-0.5Zn-1.0Zr and 1.0 other RE wt.%), WE43 (Mg-4.0wt.%Y-3.3wt.%RE-0.5wt.%Zr) and WE54 (Mg-5.1wt.%Y-4wt.%RE-0.5wt.%Zr) is excellent in comparison to other Mg alloys [9, 10] (Figure 1.1).

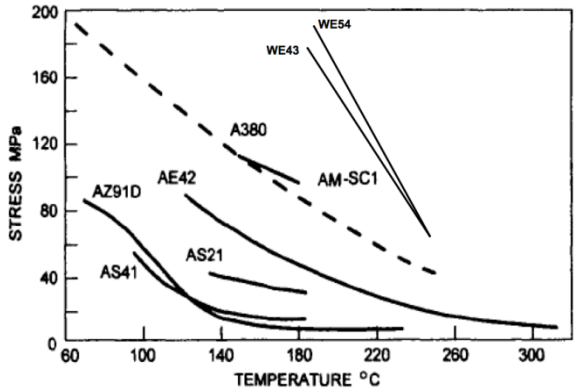

Figure 1.1: Stress for 0.1 % creep strain in 100 h for cast Mg alloys and Al alloy A380 [9, 10].

There is still debate in the literature relating to the main mechanism that influences creep in Mg alloys. Grain boundary sliding has long been thought to be the critical mechanism influencing creep [11]. However more recently, improved creep properties have been attributed to pinning or otherwise retarding the motion of dislocations by solute in solid solution with a low diffusivity and/or by thermally stable precipitates in the α-Mg matrix [12].

The aims of this project are to:

- Determine what influence different RE elements (with different solid solubilities in Mg) have on creep resistance through solid solution strengthening, precipitation hardening, grain boundary reinforcement and solute diffusion.
- Determine the effects of heat treatment on HPDC Mg-La-RE alloys, specifically if heat treatment has any positive influence on the creep resistance of the alloys.
- Determine the key microstructural influences on creep performance in Mg alloys.

In **Chapter 2** of this thesis a review of the current literature will be presented. Firstly, high-pressure die-casting will be introduced. The importance of castability and the

influence of heat treatment on precipitation hardenable Mg alloys will be discussed. Attention will be brought to the issue of heat-treating HPDC alloys and the limited research on heat-treated HPDC Mg and also Al alloys will be included. The stages of creep in pure metals will then be described. Creep mechanisms will also be described in detail. Following this, the effects of alloying additions on the creep properties of Mg will be investigated. Particular attention will be given to various RE alloying additions in Mg alloys and the role of solid solubility, precipitation hardening and diffusion of solute and grain boundary reinforcement.

In **Chapter 3** the casting procedure of the alloys, experimental procedures and techniques applied to those alloys used in this thesis are explained in detail. A hot tearing measurement scale of HPDC alloys will be described in this chapter. Heat treatment and age hardness measurement procedures will be detailed. Mechanical testing including tensile testing (both at room temperature and elevated temperatures) and compression testing will be described. The creep testing procedure will also be described in detail. To investigate the microstructure of the alloys used in this thesis, electron microscopy (SEM and TEM), energy-dispersion X-ray spectroscopy (EDS) and electron backscatter diffraction (EBSD) are employed.

A preliminary investigation of the as-cast microstructure of Mg-La-Nd, Mg-La-Y and Mg-La-Gd alloy series and their castability is presented in **Chapter 4**. It is shown that for a given concentration of ternary rare earth addition the alloys in each series have similar average grain sizes and volume fractions of eutectic present at the grain boundaries. Furthermore it is confirmed that the intermetallic present in the eutectic is $Mg_{12}RE$. It is shown that as the concentration of ternary RE is increased the eutectic morphology changed from lamellar to fibrous to increasingly divorced. A hot tearing index is also used to describe the castability of the three alloy series investigated. It is shown that the temperature-fraction solid curves for Mg-La-RE alloys can be used as an indication of hot tearing susceptibility. Furthermore, the solidification temperature of the eutectic can be used as an approximate indication for hot tearing susceptibility.

Chapter 5 presents the effects of alloying additions on mechanical and creep properties as well as the microstructure of alloys in the as-cast condition and following creep testing. The age hardening response of Mg-La-Nd containing alloys is more rapid than either Mg-La-Y or Mg-La-Gd alloys. The thermal stability of the Nd precipitates within the α-Mg matrix of Mg-La-Nd is significantly worse than either the precipitates present in Mg-La-Y or Mg-La-Gd alloys. The peak ageing condition in the Mg-La-Nd alloys is reached earlier than the Mg-La-Y or Mg-La-Gd alloys but also begins to overage relatively quickly following peak hardening. The creep properties of the Mg-La-Nd alloys are also shown to be significantly worse than those of either the Mg-La-Y or Mg-La-Gd alloys, with comparable ternary RE concentrations. Microstructural observations of the alloys following creep testing reveal that all alloys with approximately 0.2 at.% (or greater) ternary RE can form dynamic precipitates. This helps to show that it is not only the mere presence of dynamic precipitates that is important for creep resistance but rather the thermal stability of the precipitates and ultimately of the solute in solid solution are also important.

Building on from the previous chapter, **Chapter 6** isolates the influences from other microstructural features/components/properties of the alloys such as grain boundary reinforcement, solid solution strengthening and precipitation hardening. This was achieved by varying the microstructure of the alloys with heat treatment. However, firstly, it was necessary to identify if HPDC Mg-RE alloys could be successfully heat-treated without causing any surface blistering. This was shown to be possible using solution treatments of a relatively short duration. However, at best, heat treatment had a minimal improvement in the alloys under investigation and in general the creep resistance deteriorated significantly. The average grain size did not change following solution treatment or solution treatment and then peak ageing. The intermetallic phase present at the grain boundaries did, however, become discontinuous following heat treatment. This indicated that a combination of the strength obtained from a continuous intermetallic network at the grain boundaries, coupled with thermally stable solute in solid solution

and thermally stable precipitates are critical for good elevated temperature creep properties.

In **Chapter 7** the results of the previous chapters are rationalised and a general explanation of creep resistance in HPDC Mg-La-RE alloys is given. A quantification of the key microstructural features of Mg-La-RE alloys are made to assist with the discussion of the influence of different RE elements and concentrations in Mg-La alloys. The Scheil-Gulliver equation is used to model the concentration of solute in the fraction of phase. Predicted values of supersaturation, solute in solid solution, eutectic and intermetallic phase volume fractions are used to help discuss the results presented in the previous chapters.

Key conclusions reached in this present work and recommendations for future work are then given in **Chapter 8**. A summary of the ways in which the microstructure of the alloys under investigation will be modified is presented in Figure 1.2.

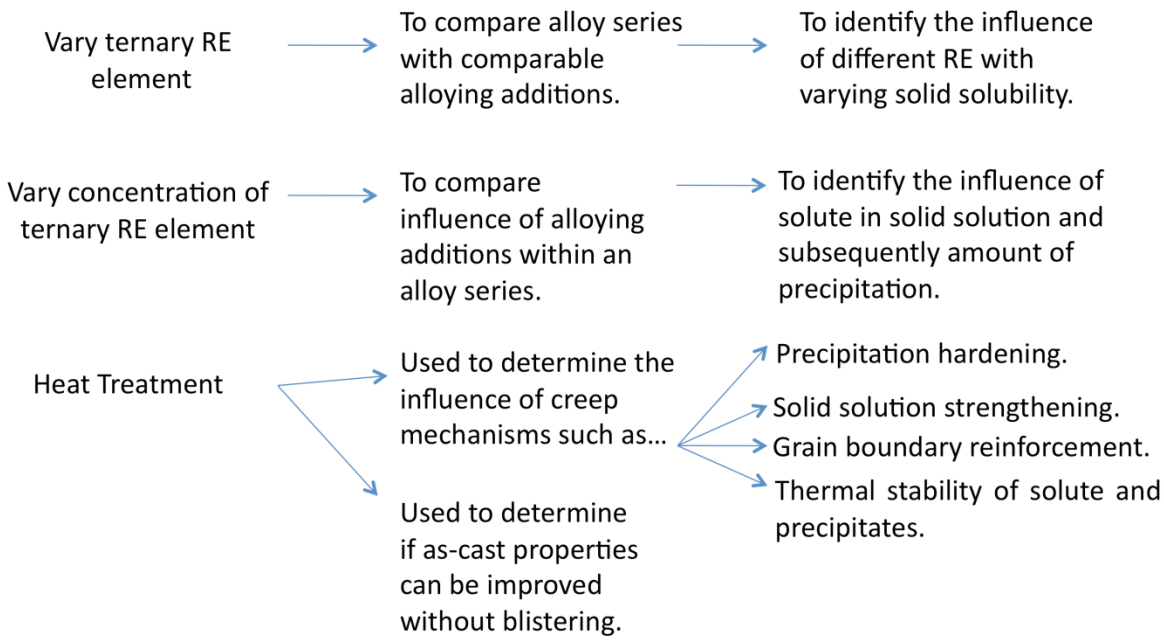

Figure 1.2: Methods used in the current work to vary the microstructure and properties of the HPDC Mg-La-RE alloys under investigation in order to determine the influence of different ternary RE alloys on properties.

2 Literature Review

2.1 Introduction 7

2.2 Microstructure and High-Pressure Die-Castability of Mg-Alloys 7
2.2.1 Microstructure of HPDC Mg Alloys 7
2.2.2 Castability 11
2.2.3 Influence of Heat Treatment on HPDC Alloys. 15

2.3 Creep in Pure Metals 17
2.3.1 Primary Creep 18
2.3.2 Secondary Creep 19
2.3.2.1 Dislocation Creep 20
2.3.2.2 Diffusional Creep 21
2.3.2.3 Grain Boundary Sliding 22
2.3.3 Determination of Creep Mechanisms 22
2.3.4 Tertiary Creep 26

2.4 Creep Properties of Mg Alloys 28
2.4.1 Creep of Mg-Al alloys 28
2.4.1.1 Mg-Al-Zn Alloys 29
2.4.1.2 Mg-Al-Si Alloys 30
2.4.1.3 Mg-Al-RE Alloys 31
2.4.1.4 Mg-Zn-Al-RE Alloys 33
2.4.1.5 Mg-Al-Sr Alloys 34
2.4.1.6 Mg-Al-Ca Alloys 34
2.4.2 Creep of Mg-RE Alloys 38
2.4.3 Influence of Different RE on Creep 39

2.5 Effects of Microstructural Features on Creep 46
2.5.1 Grain Boundary Reinforcement 46
2.5.2 Solute in Solid Solution and Its Effect on Creep 49
2.5.3 Precipitation and Its Effect on Mechanical Properties and Creep 50

2.6 Summary 57

2.1 Introduction

This chapter provides an introduction into high-pressure die-casting (HPDC) and the castability of HPDC Mg-RE alloys. The current literature on heat treatment of HPDC alloys and its effect on the microstructure, mechanical and creep properties will be reviewed. An introduction into creep and creep properties of Mg alloys is also included. As there is still debate in relation to the primary creep mechanism in Mg alloys [8, 13-16], a description of the various creep mechanisms will be given. After that the current knowledge about creep in relation to Mg alloys will be presented and it will be shown that Mg-RE alloys have particularly good creep properties at elevated temperatures.

2.2 Microstructure and High-Pressure Die-Castability of Mg-Alloys

2.2.1 Microstructure of HPDC Mg Alloys

High-pressure die-casting (HPDC) can produce castings rapidly (20 castings per minute) and in near net shape. This makes HPDC an ideal casting method for industries requiring rapid production of large quantities of cast parts such as in the automotive industry. There are a number of different types of die-casting methods [5], however, since all the alloys in this thesis were cast using a cold-chamber high-pressure die-casting machine a schematic of such a device is provided in Figure 2.1.

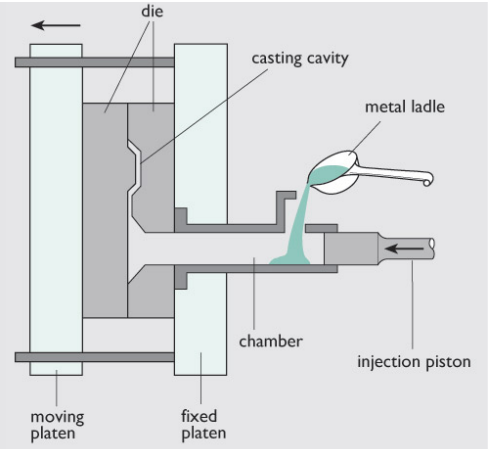

Figure 2.1: Schematic of a cold chamber high-pressure die-casting machine showing the molten metal being poured from a ladle into the shot chamber before being injected into the die [17].

The casting process involves melting the metal/alloy, then pouring it into the shot sleeve. An injection piston then forces the melt into a die at which point the melt rapidly solidifies (order of seconds). The casting is then ejected from the die and the process is repeated.

The as-cast microstructure of the Mg–RE alloys contains a mixture of primary α-Mg dendrites and eutectic (intermetallic phase and eutectic α-Mg) in the interdendritic regions (Figure 2.2).

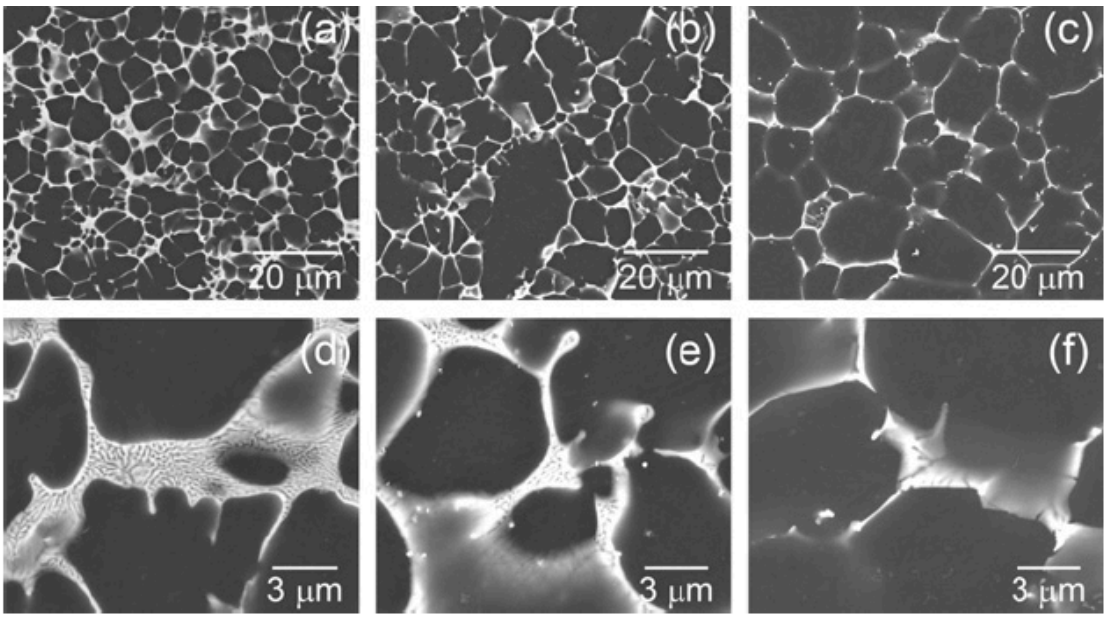

Figure 2.2: As-cast microstructure (SEM) of Mg–3.44 wt.%La (a and d), Mg–2.87 wt.%Ce (b and e) and Mg–2.60 wt.%Nd (c and f) alloys. The amount of intermetallic phase is highest in the La containing alloy and lowest in the Nd containing alloy [14].

Solidification of a HPDC alloy occurs under highly non-equilibrium conditions due to the high cooling rates (100 – 1000°C/s) in the casting process [18]. As a result there is a compositional variation across the dendrite cell where the central area of a grain/cell is leaner in solute than at the edges, this is referred to as coring [19, 20]. Under non-equilibrium solidification conditions the solid composition differs from the equilibrium composition and is typically lower in solute in comparison to the equilibrium composition. This is a result of diffusion in the solid state being slow and not having sufficient time to reach equilibrium under normal cooling rates. Thus the remaining liquid becomes increasingly concentrated/enriched in solute. In the final stages of solidification of a

grain/cell, the enriched liquid transforms via a eutectic reaction at an appropriate temperature to form the intermetallic phase as part of this reaction [20, 21]. Chia *et al.* [18] have shown that the segregation of solute during solidification that is expected to form under such non-equilibrium solidification conditions can be approximated to a good degree by the non-equilibrium lever rule or Scheil-Gulliver equation:

$$C_s = kC_o(1 - f_s)^{k-1} \quad \textbf{(2.1)}$$

where, C_s is the concentration of solute in solid solution, k is the partition coefficient, C_o is the composition of the alloy, and f_s is the fraction solid.

Eq. (2.1) approximates non-equilibrium solidification by assuming a local equilibrium at the liquid-solid interface and no diffusion in the solid and instantaneous diffusion in the liquid. This allows the use of equilibrium phase diagram information in solidification analysis [20]. More recently, TerBush *et al.* [22] have shown that while the Scheil-Gulliver equation can approximate the solute profile of HPDC alloys at lower fraction solid percentages, the equation generally underestimates the concentration of solute at high fraction solid (> 80% fraction).

It is possible for an alloy that was cast by HPDC to have a region of supersaturated solid solution near the grain boundaries even if the alloying addition is below the maximum solid solubility. Thus it is possible to form precipitates in such alloys either by some form of ageing (static precipitates) or during the time when the alloy is exposed to elevated temperatures during its use (dynamic precipitates) [14].

The casting microstructure of cold chamber HPDC alloys is generally described in terms of a hard 'skin' layer; comprised of fine grains (approximately 5μm [18]), a higher volume fraction of intermetallic phases and more solute in the α-phase, and a relatively softer 'core' region; comprised of large grains (approximately 20μm [18]) together with an agglomeration of still larger grains (approximately 100μm [18]), formed externally from the die in the shot sleeve (referred to as externally solidified grains, ESG) [23], as shown in Figure 2.3.

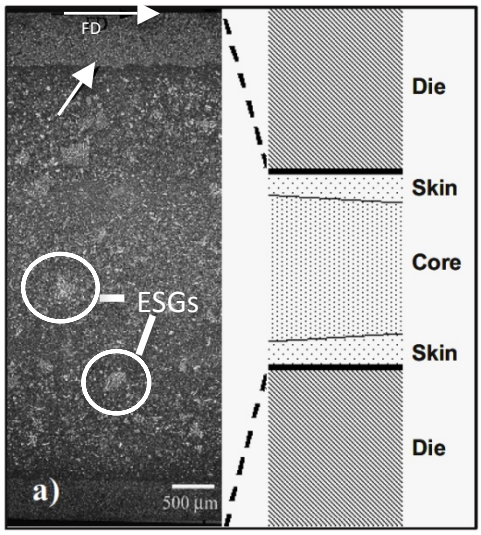

Figure 2.3: The micrograph and corresponding schematic diagram of the cross-section of a tensile bar normal to the flow direction (FD) showing 'skin' and 'core' regions and externally solidified grains (ESG) [24].

It has been reported that HPDC alloys obtain a significant proportion of their strength from the fine-grained 'skin' region of the casting [25, 26]. Through extensive micro-hardness testing over the entire cross section of a HPDC Mg-3.44 wt.% La alloy, Figure 2.4 [25], it was shown that the 'skin' region had significantly higher hardness values (ranging from 75 - 100 HV) than the 'core' region (ranging from 30 - 45 HV).

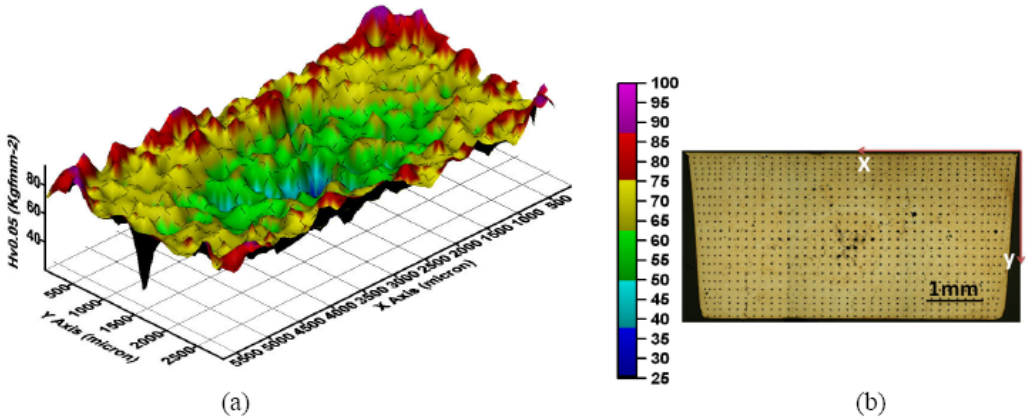

Figure 2.4: (a) Micro-hardness profile with a colour scale and (b) indentation pattern for the cross-section of the alloy studied [25].

While there has been no research published directly comparing the effects of creep resistance on the 'core' and 'skin' regions of a HPDC alloy, there have been some publications that compare creep resistance in relation to grain size. Dargusch *et al*. [26] compared the creep response of HPDC Mg-Al-Zn alloy (AZ91) samples that were 1 mm or

6 mm thick. The elevated temperature mechanical properties were improved in the thinner castings due to an increased proportion of the fine-grained 'skin' region.

Another microstructural feature of HPDC alloys are segregation bands formed parallel to the casting surface. Scanning electron microscope (SEM) micrographs depicting the 'skin', 'core' and banded microstructures for an as-cast HPDC binary Mg-La alloy is shown in Figure 2.5.

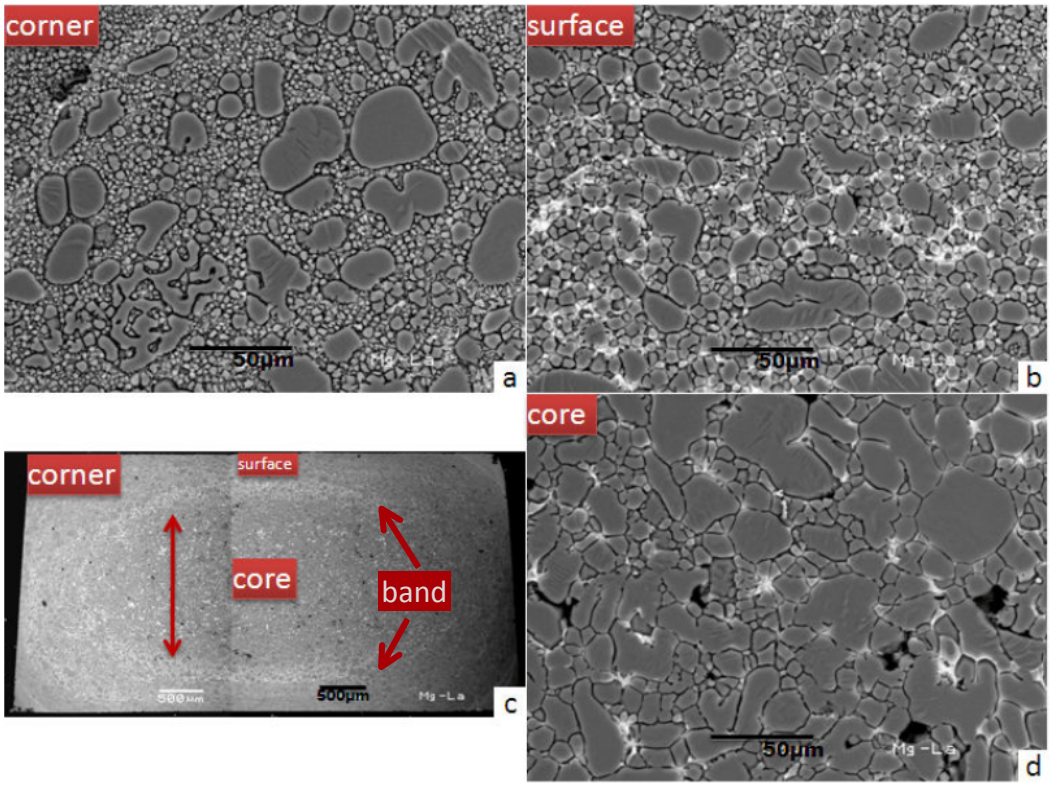

Figure 2.5: Scanning electron microscope backscatter electron micrographs of a) corner, b) surface, c) macrograph of the entire cross section, and d) 'core' region [25].

The composition of these bands may vary considerably and may consist of cracks, porosity (shrinkage and/or gas porosity) and/or segregated bands of intermetallic phases [27].

2.2.2 Castability

Castability is a critical property that is required for the successful adoption of Mg alloys in powertrain components by the automotive industry [4, 28, 29]. HPDC can produce near-net shape castings rapidly and relatively cheaply. The castability is strongly related to the

alloy composition [28, 30]. Hot tearing is a major defect that can form during casting when the cast piece is still in a semi-solid state and is often a key defect related to the rejection of castings and imposes a limitation to the use of some alloys [31]. Campbell [32] has proposed that hot tearing is predominately controlled by the presence of double oxide films (bifilms) forming during casting. Bifilms are created when a dry film on the surface of the melt is folded and becomes entrained within the melt. The folded faces do not bond and thus form a defect within the casting that can promote crack formation [33]. However, casting shrinkage may manifest as other defects such as surface slumping [34]. Hot tearing has also been linked to the lack of liquid flow to provide sufficient compensation for solidification shrinkage in the presence of the imposed thermal stresses due to solidification shrinkage [31, 35], thus indicating that the final stages of solidification are most important. In comparison to Al alloys [31] and steels [36], relatively little work has been published on the hot tearing susceptibility (HTS) of Mg alloys. Some previous work has been published on the castability of binary Mg-RE alloys [37-39]. Wang *et al.*[40] have recently shown in binary Mg-Y mould cast alloys that HTS is influenced by grain size, solidification range and amount of eutectic. It was also found that increasing the mould temperature decreased hot tearing since it reduced the cooling rate of the casting and thus produced a lower thermal gradient and lower strain rate imposed on the casting as it solidified [40].

A number of methods involving complex integrals have been used to help predict the HTS [32, 41-43]. Due to the complexity of these methods less complex, but also less accurate, models such as the Clyne and Davies model [41] are often used to predict hot tearing properties [37, 44]. Hot tearing is often measured using restrained bar castings, including “dog-bone” sections [7, 45]. In the current work, a more discerning scale, originally created by Easton *et al.* [39] is used to assess hot tearing differences in alloys. Easton *et al.* [39] used flat tensile specimens to provide an in-situ test for evaluating hot tearing, which were also used previously [30, 45]. In order to create a relatively easy and also accurate method to rank castability, a five-scale rating was developed to evaluate the hot tearing (Figure 2.6).

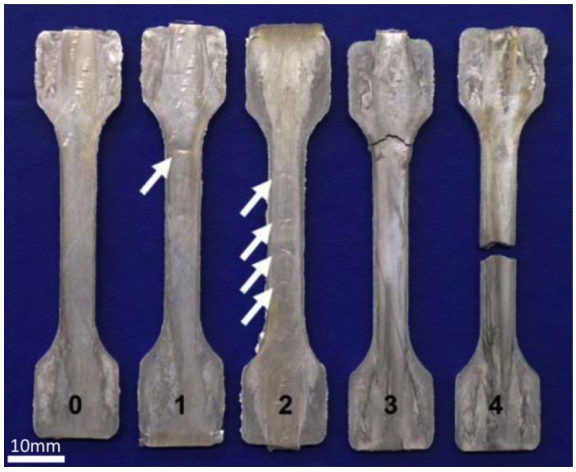

Figure 2.6: Picture of a series of flat tensile test pieces each of which is representative of one of the categories in the hot tearing scale defined below (the reference number corresponding to the scale is indicated at the bottom of each). The white arrows indicate the surface dimples that are associated with internal cracking (see also Figure 2.7) [39].

The rating scale for the hot tearing index (HTI) was as follows:

0 = No cracks/dimples in the sample observed by the naked eye.

1 = Small observable dimple/s that require close examination to see.

2 = Dimple/s easily seen by the naked eye.

3 = Crack/s observed on the surface of the sample, but the sample remains intact.

4 = Sample is fractured.

Easton *et al.* [39] also gave examples of the outside as-cast surface of flat tensile specimens using low magnification optical microscopy (Figure 2.7). Very minor tears can be present in samples with ratings of 0, however, Easton *et al.* [39] stated that this is rare.

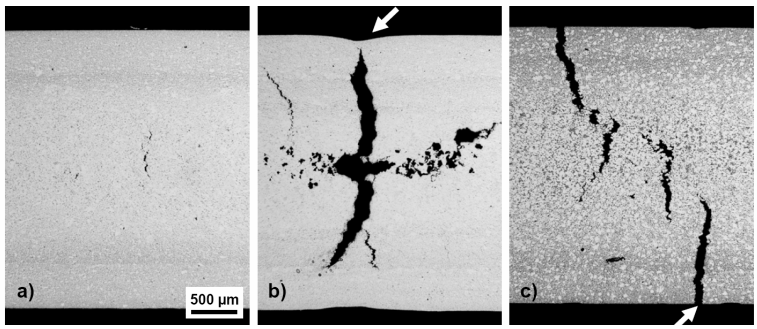

Figure 2.7: Low magnification photomicrographs of polished longitudinal cross-sections through flat rectangular tensile test pieces that display differing degrees of hot tearing as determined by the hot tearing index. a) HTI 0, b) HTI 2 (the white arrow indicates the dimple that is visible on the specimen surface) and c) HTI 3 (the white arrow indicates that the crack is clearly visible in the specimen surface) [39].

Recently, it has been shown that a simple hot tearing indicator (S_{ht2}) determined from the temperature-fraction solid curve of binary HPDC Mg-RE alloys can be used to indicate alloys that are likely to have high HTS (Figure 2.8) [39]. The hot tearing index results (Figure 2.8a) showed that the HPDC Mg-La alloys were significantly less susceptible to hot tearing than either Mg-Ce or Mg-Nd alloys and the simulated hot tearing susceptibility (Figure 2.8b) also showed similar results.

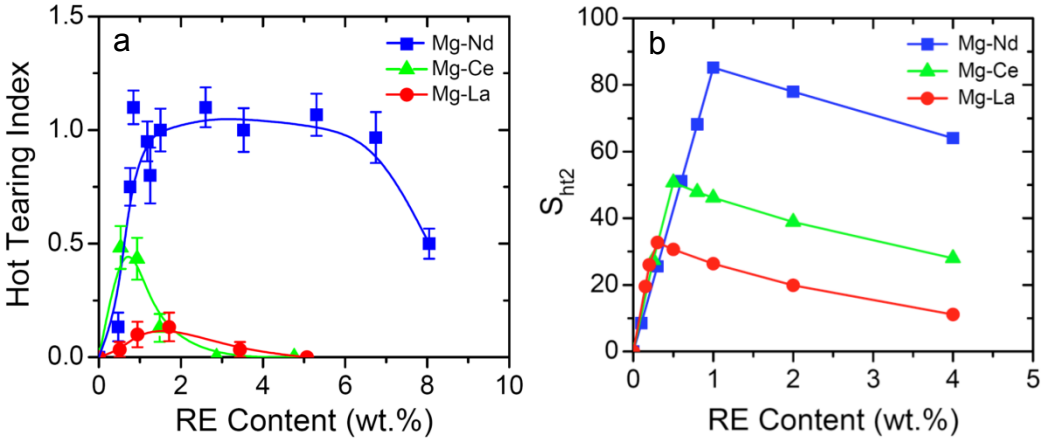

Figure 2.8: a) Hot tear index (HTI) of the binary Mg-RE alloys plotted against the alloy content b) predictions of S_{ht2} for $f_{s,0}$=0.7, $f_{s,c0}$=0.98 for the three magnesium-rare earth alloy systems [39].

The indicator (S_{ht2}) predicts hot tearing susceptibility from the integral of the temperature-fraction solid curve from the coherency temperature (the temperature when feeding becomes interdendritic) to the coalescence temperature (the temperature at which the metal has solidified sufficiently to act as a solid) Eq. (2.2),

$$S_{ht2} = \int_{T_0}^{T_{co}} f_s(T)\, dT \qquad \textbf{(2.2)}$$

where $f_s(T)$ is the fraction solid at temperature T, T_0 is the temperature at which coherency occurs, T_{co} is the temperature at which coalescence has been achieved. The HTS indicator (S_{ht2}) (Figure 2.6b) accurately ranked the binary Mg-RE alloys in order of castability and also showed the approximate concentration of RE that has the worst HTS in each alloy series.

Computational thermodynamics was used for microstructure prediction and Eq. (2.2) [39] was used to estimate the HTS. To estimate the HTS using S_{ht2}, f_s values that correspond to the temperature of coherency (T_0) and the temperature of coalescence (T_{co}) were

required. As there is still uncertainty in the literature as to what fraction solid corresponds to the appropriate T_0 [46, 47], Easton *et al.* [39] performed a sensitivity analysis to determine how changes in the selection of the coherency and coalescence points influenced the predicted values of HTS (S_{ht2}). The coherency point is defined as the point where the liquid metal flows through (or feeds through) the interdendritic regions of a not completely solidified casting. For binary HPDC Mg-RE alloys, increasing the coherency point from f_s = 0 to 0.9 (the fraction solid at which a barrier to interdendritic feeding may become significant) did not change the concentration at which peak hot tearing occurs significantly. As a result of this, a f_s value of 0.7 (the fraction solid at which spherical grains touch) was chosen for the coherency point, as it showed a moderate decrease in hot tearing susceptibility after the peak was reached, which was similar to the results reported in Ref. [39]. There was, however, a more significant effect on the concentration at which peak hot tearing was noted when the coalescence point was selected in the range between f_s = 0.97 and 0.99. Thus 0.98 f_s was selected as the coalescence point since it is mid range and it has also been used in other research [41, 42, 48].

2.2.3 Influence of Heat Treatment on HPDC Alloys.

Entrained gas (such as hydrogen) porosity and shrinkage porosity can be distributed throughout the microstructure of HPDC material [23]. Porosity in HPDC alloys can interfere with subsequent heat treatments performed on the alloy following casting. Lumley *et al.* [6] have demonstrated that traditional high temperature, long-term solid solution heat treatments can cause the surface of the alloy (HPDC Al-based alloy A380) to blister due to the expansion of gas pores within or near to the ‘skin’ region of the casting (Figure 2.9).

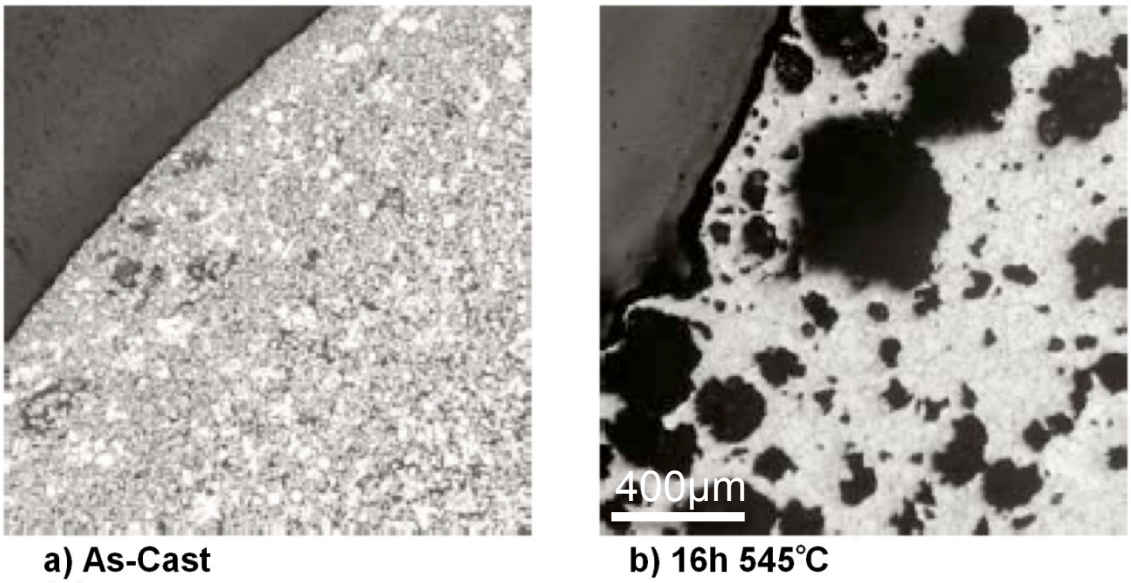

Figure 2.9: a) As-cast HPDC aluminium alloy, b) HPDC aluminium alloy following a solution treatment of 545°C for 16 hours [6].

However, modified heat treatments could be used to improve the strength of the HPDC Al alloys without causing blistering or deformation. Figure 2.10 [6] shows that relatively short-term solution treatments (15 minutes) at relatively low temperatures (≈ 490°C) did not cause any obvious surface blistering of the samples.

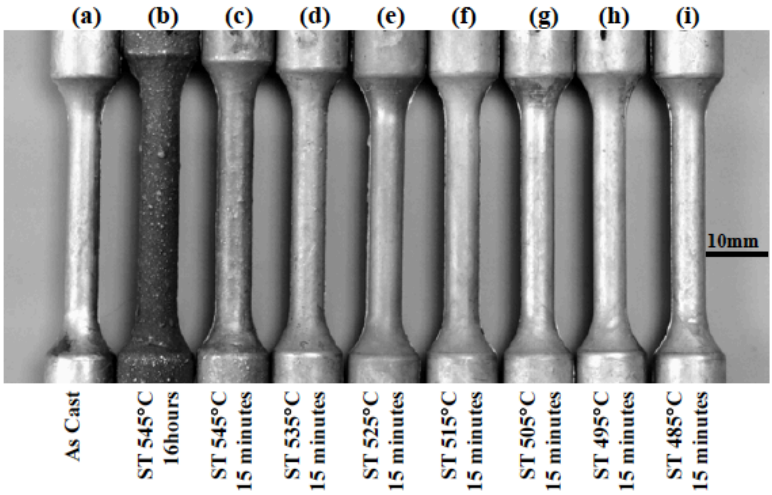

Figure 2.10: Surface appearance of Al alloy A380 in as-cast condition (a) and a number of different solution treatment (ST) temperatures. Note the dramatic difference in surface appearance of sample (b) aged for 16h in comparison to the 15-minute ST samples (c)-(i) [6].

The 0.2% proof stress was also improved significantly, without significant loss of elongation, after a T6 (solution treated, quenched in cold water then aged) heat

treatment (Figure 2.11). However, no information was given with respect to the improvement of creep resistance.

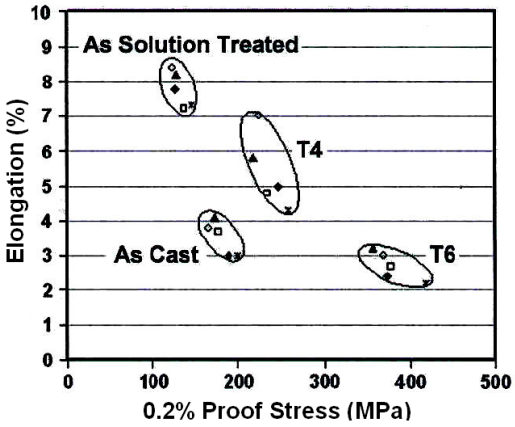

Figure 2.11: Average values for 0.2% proof stress and elongation for five batches of A380 in as-cast, as-solution treated, T4 and T6 conditions. Note in [6] T4 includes both a solution treatment stage and a natural ageing stage (in this case naturally aged for 14 days) [6].

Alternatively, porosity in high-pressure die-castings can be reduced through the use of specifically designed vacuum dies [24, 35]. It has been shown in a HPDC aluminium alloy A356 that the amount of porosity in a casting can be reduced from approximately 3 % (for a piece cast under conventional HPDC methods) to 0.8 % with the use of a vacuum die [49]. Subsequent heat treatments of vacuum die-castings are thus prone to less damage due to thermal expansion of pores. However, this process adds extra costs both in terms of maintenance and equipment.

2.3 Creep in Pure Metals

Creep is time and temperature dependant > 0.4 T_m (T_m = absolute melting temperature) evolution of strain experienced by a material where an applied stress, below the associated yield strength, acts on the material. There are three stages of creep deformation namely, primary, secondary (or steady-state) and tertiary creep (Figure 2.12). Instantaneous strain is also included in Figure 2.12 even though it is not attributed to creep strain. It is comprised of a combination of elastic and plastic strain experienced

by the material upon the application of a stress. This thesis is focused on creep properties and thus instantaneous strain will not be discussed in any great detail.

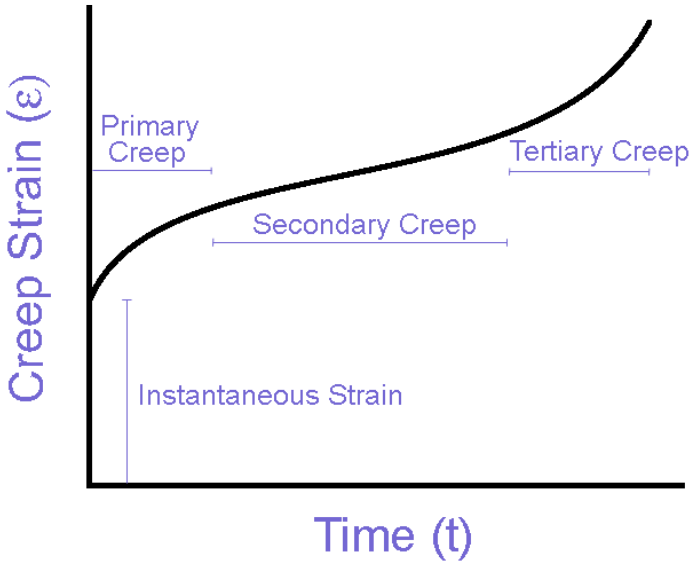

Figure 2.12: Idealized creep curve identifying the three stages of creep as well as the initial instantaneous strain that can be experienced by the material.

The primary stage of creep deformation is a period of decreasing creep rate where strain hardening occurs more rapidly than thermal softening. The second stage of creep deformation, also referred to as steady-state creep, is a period of near constant creep rate, which is a result of a balance between strain hardening and thermal softening. Tertiary creep is a result of microstructure instability caused by prolonged exposure to high temperatures and a gradual increase in stress level and stress concentration associated with cavity growth at grain boundaries and interphase boundaries [50]. Rupture of the material then follows.

2.3.1 Primary Creep

In pure metals, primary (or transient) creep occurs immediately following any instantaneous strain that the metal may experience upon the application of a load. This stage of creep is characterised by a rapid decrease in creep rate as a result of thermal softening being less effective than work (or strain) hardening, which occurs simultaneously. This stage of creep can be defined as the creep strain experienced by the sample up to the point of where the minimum creep rate is reached [51].

A number of processes may take place during transient creep such as recrystallisation, which increases the creep rate. Dislocation pile-ups as well as subgrain formation act to work or strain harden the metal and thus help to decrease the creep rate [52, 53]. Dislocation pile-ups occur as a result of an obstacle such as another dislocation, inclusion, precipitate, grain boundary etc. acting as barriers to the motion of dislocations in the matrix [54]. Subsequent dislocations can thus group together (or pile-up) if the barrier is strong enough. The creep rate can be described as the product of density, ρ, and average glide velocity, v_g, of mobile dislocations [55] as given in Eq.(2.3):

$$\dot{\varepsilon}_s = M^{-1} b \rho v_g \qquad \textbf{(2.3)}$$

where b = magnitude of the Burgers vector and M = geometric factor (for polycrystals: Taylor factor). As the material hardens with increasing strain (during creep) a decrease in dislocation spacing occurs. It can thus be stated that the factor v_g in Eq.(2.3) is dominant in the transient behaviour of primary creep.

2.3.2 Secondary Creep

The minimum creep rate is generally found within the secondary or steady-state period of creep. Under steady-state conditions, the creep rate, $\dot{\varepsilon}_s$, can be expressed by the Mukherjee-Bird-Dorn equation [56],

$$\dot{\varepsilon}_s = \frac{ADGb}{kT}\left(\frac{b}{d}\right)^p\left(\frac{\sigma}{G}\right)^n \qquad \textbf{(2.4)}$$

where A = dimensionless constant

G = shear modulus of elasticity

b = magnitude of the Burgers vector

k = Boltzmann's constant

T = absolute temperature

d = grain size

σ = applied stress

p = exponent of inverse grain size

n = exponent of stress

D = diffusivity.

The diffusivity is given by the following Arrhenius type equation,

$$D = D_o \exp\left(-\frac{Q_c}{RT}\right) \quad \textbf{(2.5)}$$

where D_o = diffusion coefficient

Q_c = activation energy of diffusion

Thus $\dot{\varepsilon}_s$ can be expressed as,

$$\dot{\varepsilon}_s = \frac{AGb}{kT} D_o \exp\left(-\frac{Q_c}{RT}\right)\left(\frac{b}{d}\right)^p \left(\frac{\sigma}{G}\right)^n \quad \textbf{(2.6)}$$

However, generally a more simplified version of Eq.(2.6) is use,

$$\dot{\varepsilon}_s = A\sigma^n \exp\left(\frac{-Q_c}{RT}\right) \quad \textbf{(2.7)}$$

During secondary creep, three major mechanisms relevant to creep deformation, occur:

- dislocation creep,
- diffusional creep,
- grain boundary sliding.

In the following sections the major mechanisms will be reviewed in detail.

2.3.2.1 Dislocation Creep

Dislocation creep is the result of dislocations moving through the material causing plastic deformation. Dislocation motion may be obstructed by precipitates, grain boundaries, other dislocations and solute in solid solution [57]. Solute in solid solution may also slow the kinetics of dislocation motion through solute drag [58, 59]. The seminal paper by Cottrell and Jaswon [60] described that the speed of the dislocation motion is limited by the migration rate of the solute atoms. There are two basic types of dislocation motion, glide and climb as is depicted in Figure 2.13. Glide or conservative motion occurs in the slip plane and slip direction of the dislocation. It is possible, at relatively high temperatures, for dislocations to avoid those obstacles through the thermally activated process of dislocation climb [61]. Climb or non-conservative motion occurs perpendicularly to the direction and plane of gliding.

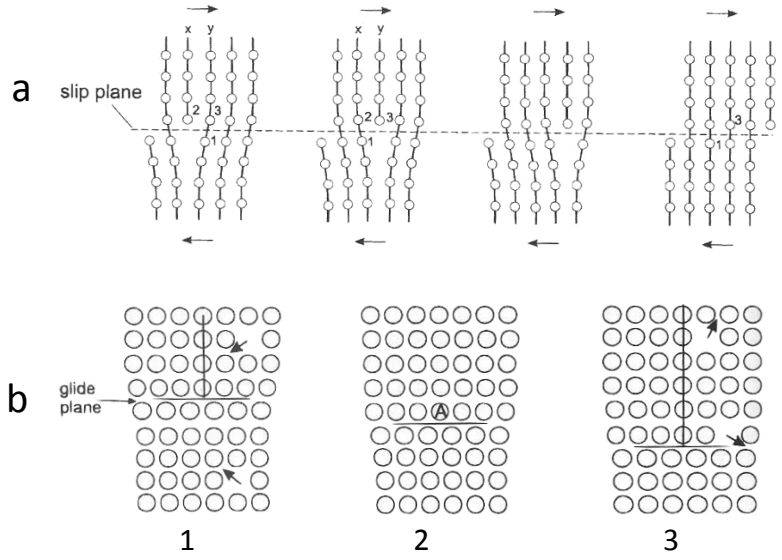

Figure 2.13: a) Dislocation glide, the arrows indicate the applied shear stress and the numbers indicate the movement of atoms, b) dislocation climb, in (2) the dislocation is centred in row A and is shown to climb in a positive sense in (1) and negative in (3) via diffusion of atoms and vacancies. [54].

2.3.2.2 Diffusional Creep

In a material undergoing diffusional creep, there is a transport of material via the flow of atoms and vacancies due to an applied stress [62]. Simultaneously, there is a corresponding flow or diffusion of atoms in the opposite direction of motion of the vacancies. Diffusion can occur through the grain, this is referred to as Nabarro-Herring creep [63] or along grain boundaries, known as Coble creep [64] (Figure 2.14).

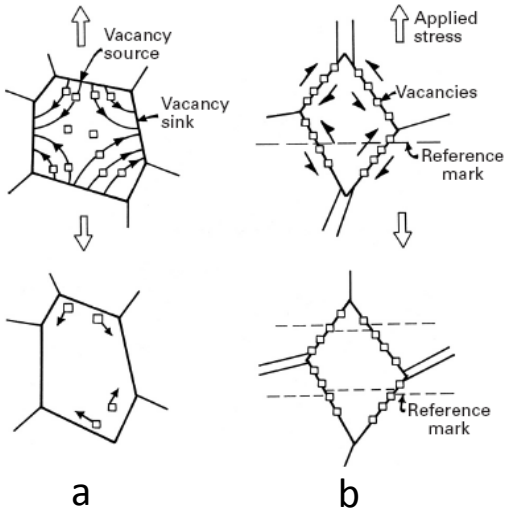

Figure 2.14: Depiction of a) Nabarro-Herring and b) Coble creep on crystals by an applied stress [65].

2.3.2.3 Grain Boundary Sliding

Grain boundary sliding (GBS) is a shear process caused by an applied external stress, which causes grains in polycrystalline materials to move or "slide" past each other [66]. There are distinct types of GBS: Rachinger sliding and Lifshitz sliding [67]. Rachinger sliding is strain accommodated by intragranular dislocation slip. The grains thus experience little elongation and are shifted relative to one another. During Lifshitz sliding there is a diffusive mass and/or vacancy flow either through grains or around grain boundaries as described by the Nabarro-Herring or Coble creep mechanism, respectively. Unlike Rachinger sliding, elongation, or otherwise deformation, of the grains does occur due to the shearing stresses applied normal to the grain boundaries inducing mass transfer.

The degree of GBS can be measured by scribing lines or using a focused ion beam (FIB) to mark lines across grain boundaries before creep testing and measuring the offset following creep testing (Figure 2.15). Another experimental method is to measure the offset perpendicular to the sample surface using interferometry [67].

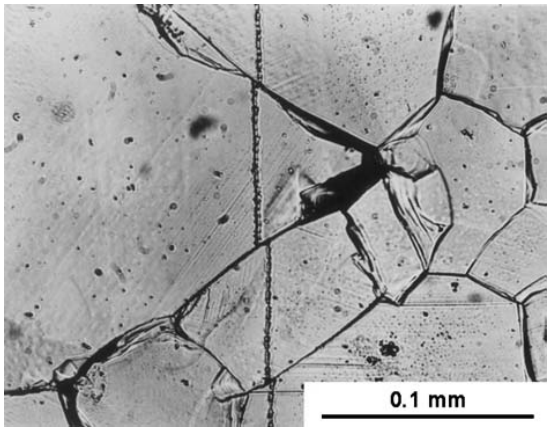

Figure 2.15: Grain boundary sliding revealed through the use of a transverse marker line across grain boundaries for a Mg-0.78Al (wt.%) alloy creep tested at 17.2 MPa and 200°C [67].

2.3.3 Determination of Creep Mechanisms

Ashby [61] introduced the concept of deformation mechanism maps: maps that display the fields of stress and temperature in which a particular mechanism of plastic flow is dominant (Figure 2.16). A point on the map identifies the dominant mechanism at a

particular stress and temperature (for some given grain size) and indicates the resulting strain-rate.

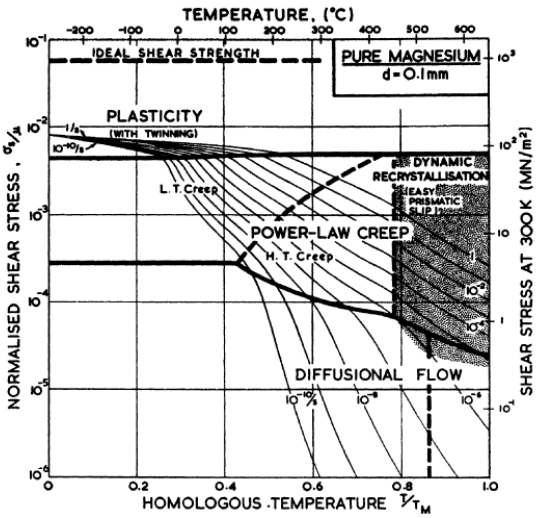

Figure 2.16: Deformation mechanism map for pure Mg with average grain size of 0.1mm [61].

Deformation maps can be used to provide useful information as to the creep mechanism at different temperatures and stresses. However, few deformation mechanism maps exist for Mg alloys [68]. Also, much like phase diagrams, deformation maps are only as accurate as the theory and experimental data used to construct them.

Alternatively, a method which uses the stress exponent (n), exponent of inverse grain size (p) and the activation energy of diffusion (Q_C) from Eq. (2.6) is commonly used [69-73] to infer the dominant creep mechanism at a particular temperature and applied stress. It should be noted that Eq. (2.6) is purely empirical and although the values for p, n and Q_c are dependent on microstructure they do not provide any information on specific microstructural features [70]. Also, Eq. (2.6) does not accurately identify the dominant creep mechanism at higher stress levels. An alternative equation (hyperbolic sine equation [74, 75]), related to Eq. (2.6), is sometimes used to indicate higher stress creep mechanisms. There are also alternative techniques in determining creep mechanisms such as the θ projection concept, the hyperbolic tangent method and the Wilshire equations, which are reviewed in the paper by Williams *et al.* [76]. "However, from an alloy development perspective, these constants (p, n and Q_c), in indicating a rate controlling mechanism, can highlight the weakest aspect of the microstructure from the

perspective of creep resistance and thus indicate the best place to start when looking at microstructural manipulations to further improve creep resistance." [70]

The stress exponent, n, can be obtained from the gradient of the logarithm of strain rate versus the logarithm of stress plot at a specific temperature (Figure 2.17). It is usually regarded that a stress exponent value of 1 is due to diffusion creep, a value of 2 due to grain boundary sliding [77]. Stress exponents near 3 are due to glide controlled dislocation creep [78] and stress exponents between 4 to 7 are attributed to the motion of dislocations [51]. Higher stress exponent values indicate the "power-law" method for determining creep mechanisms has stopped being accurate i.e. power-law breakdown has occurred.

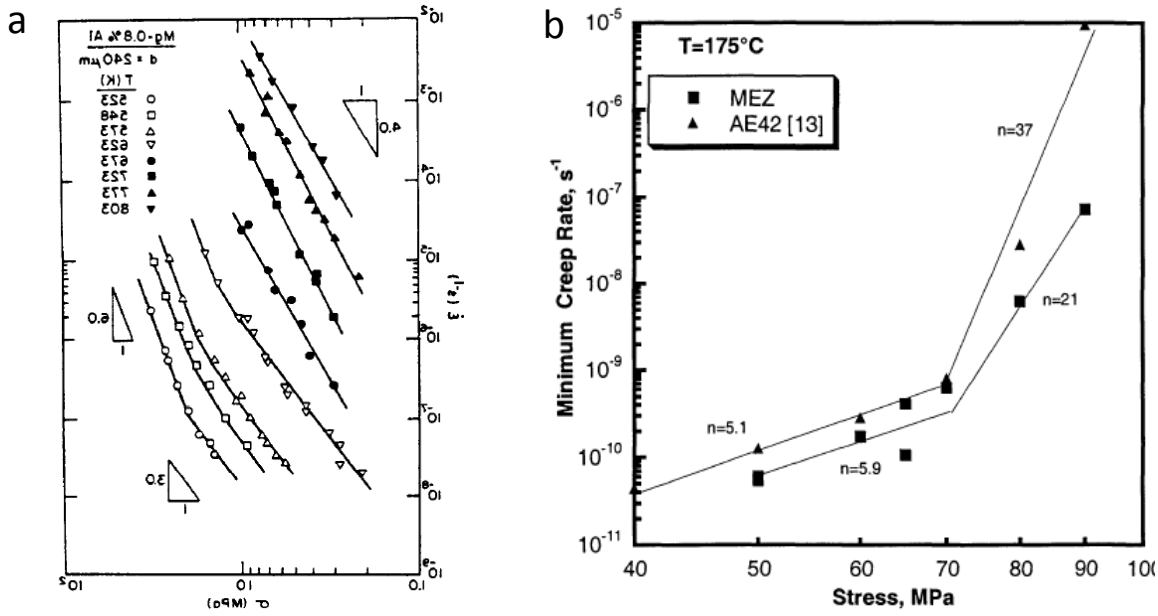

Figure 2.17: A number of strain rate versus stress plots showing the n values for a) Mg-0.8wt.%Al at various temperatures [79] and b) Two creep-resistant Mg alloys MEZ and AE42 at 175°C [80].

An Arrhenius plot (strain rate vs.1/T) at a specific stress level will determine the apparent activation energy of creep Q_c (Figure 2.18).

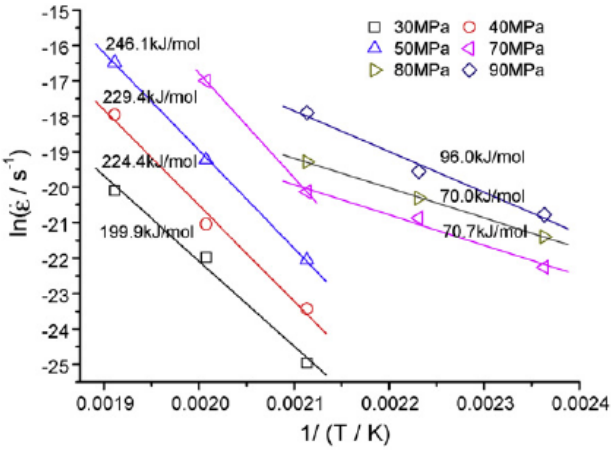

Figure 2.18: Plot of strain rate vs. 1/T at various stress levels for a Mg-Nd alloy. The value shown next to each line is the activation energy of creep for that particular stress level [81].

Numerous research papers have been published where the stress exponents and activation energies have been calculated for a wide range of Mg alloys [58, 82-84]. A summary of some of this work performed on Mg alloys is shown in Table 2.1 (at the end of this section). From Table 2.1, it is clear that numerous different creep mechanisms are claimed to be dominant at different temperatures and/or stresses. The large variation in creep mechanisms not only occurs over a range of temperatures but also between alloys when temperatures and stresses remain comparable. It is thus difficult to deduce a trend in creep mechanisms with regard to temperature and/or stress. Table 2.1 also shows that certain alloys can have very large stress exponents (n > 10) [58, 85]. The high n values are typically rationalised by introducing a threshold stress, σ_0, below which creep cannot be accurately measured [72, 86, 87]. The power law equation given in Eq. (2.7) is thus modified to take into account the threshold stress:

$$\dot{\varepsilon}_s = A(\sigma - \sigma_0)^n \exp\left(\frac{-Q_c}{RT}\right) \qquad \textbf{(2.8)}$$

It has been shown, however, that this method cannot always be used to correct the theorem and furthermore that using the stress exponent alone is not a reliable method for identifying creep mechanisms [85, 88, 89]. Rather, it is suggested that microstructural investigations should be used in combination with modelling approaches in order to accurately identify the creep mechanisms in high-stress exponent materials.

The exponent for the inverse grain size p can be obtained from the slope of the strain rate vs. grain size plot from a series of creep tests performed at the same stress and temperature using samples with different grain diameters [90]. Thus, if the creep mechanism is not dependent on grain size then p = 0. When creep occurs by diffusion-controlled generation and movement of dislocations it has been suggested that the steady-state creep rate is independent of grain size, and therefore p = 0 [56, 91]. When the primary creep mechanism is either Nabarro-Herring or Coble creep the inverse grain size exponent is taken to be 2 or 3, respectively [56, 91]. For grain boundary sliding p has been reported to equal 1 [56].

2.3.4 Tertiary Creep

The research presented in this thesis is focused on the properties of Mg alloys during steady-state creep. Tertiary creep will, thus, be discussed relatively briefly. For this final stage of creep, strain hardening and thermal softening are no longer balanced. The creep rate begins to accelerate until rupture of the material occurs due to microstructural and/or metallurgical changes such as voids or cavities forming, cracking of the grains and grain boundary separation. On the macroscopic scale, necking (reduction of the effective cross sectional area of the material) can be observed. This typically occurs at the point of the material, which will soon fail due to the growth and linking up of cavities [92].

Table 2.1: Summary of some of the creep studies on Mg alloys with assessment of dominant creep mechanism (n). Note: * indicates compression creep testing.

Alloy (wt.%)	T (°C)	σ (MPa)	n	Q (kJ mol^{-1})	Ref
Pure Mg	200	20-40	6.5	135 ± 10	[93]
Pure Mg	250	10-25	5.2	135 ± 10	[93]
Mg-16Al	327	5-30	4-7	-	[13]
AZ31	150-225	35-140	3-6	93.8-126.6	[71]
AZ91	150	40-100	6.3	-	[94]
AZ91*	152	200-650	6.0	112.6	[82]
AZ91-1RE*	152	200-650	6.8	118.2	[82]
AZ91-2RE*	152	200-650	6.7	110.2	[82]
AZ91-3RE*	152	200-650	7.0	125.8	[82]
AS31	125	80-110	14.4	165	[85]
MRI153	150	60-110	6-15	-	[95]
Mg-1Ca-1Zn-0.6Zr	150	75-110	6.2	-	[94]
Mg-1Ca-1Zn-1Nd-0.6Zr	150	90-110	7.2	-	[94]
AE42	175	70-90	34	-	[96]
AE44	175	90-110	41	-	[96]
AE44	125	110-160	27	140	[97]
Mg-1.5Mn-0.3Ce	400	33	3.4	-	[84]
Mg-3.44La	177	50-90	9	-	[14]
Mg-2.87Ce	177	50-90	8	-	[14]
Mg-2.6Nd	177	50-90	6.9	-	[14]
Mg-0.7 Y	277	> 70	12	-	[58]
Mg-3.9 Y	277	50-100	5	-	[58]
Mg-5.6 Y	277	50-120	5	-	[58]
Mg-8.3 Y	277	> 150	12	-	[58]
Mg-6Y-4 Nd	290-360	30-80	6-7	-	[58]
Mg-5.8Y-2.8Nd-0.9Zr	< 200	20	-	150	[58]
Mg-5.8Y-2.8Nd-0.9Zr	< 200	40	-	135	[58]
Mg-5.8Y-2.8Nd-0.9Zr	< 200	60	-	122	[58]
Mg-5.8Y-2.8Nd-0.9Zr	< 300	-	3.1	-	[58]
Mg-5.8Y-2.8Nd-0.9Zr	> 200	20	-	257	[58]
Mg-5.8Y-2.8Nd-0.9Zr	> 200	40	-	202	[58]
Mg-5.8Y-2.8Nd-0.9Zr	> 200	60	-	179	[58]
Mg-5.8Y-2.8Nd-0.9Zr	> 300	-	3.7	-	[58]
Mg-6.2Y-3Nd-0.4Zr	200-300	40	-	606-68	[58]
Mg-6.2Y-3Nd-0.4Zr	300-350	40	-	100-226	[58]
Mg-6Y-3Nd-0.5Zr	200-280	20	-	50-90	[58]
Mg-6Y-3Nd-0.5Zr	280-350	20	-	200-300	[58]
Mg-1Y-Zn-Nd-Zr	250-350	40	-	212	[58]
Mg-3Y-Zn-Nd-Zr	250-350	40	-	187	[58]
Mg-5Y-Zn-Nd-Zr	250-350	40	-	165	[58]
Mg-10Gd-3Y-Zr (T6)	250	50-120	5.2	-	[98]
Mg-10Gd-3Y-Zr (T6)	300	35-65	5.9	-	[98]

Table 2.1 cont.

Alloy (wt.%)	T (°C)	σ (MPa)	n	Q (kJ mol^{-1})	Ref
WE43	130-170	180-225	14	140	[58]
WE43	230-270	180-225	2-3	170	[58]
WE54	< 200	100	-	150	[58]
WE54	< 200	150	-	160	[58]
WE54	> 200	100	-	14	[58]
WE54	> 200	150	-	40	[58]
WE54	150	50-150	1.5	-	[58]
WE54	200	50-150	3.4	-	[58]
WE54	230-270	32-82	4-5	175-221	[58]
WE54	250	50-150	3.3	-	[58]

2.4 Creep Properties of Mg Alloys

A large number of alloying additions have been used to improve the creep and mechanical properties of Mg Alloys. Alloying elements in Mg such as Al, Zn, Mn, Ag, Si, Sn, Ca and the rare earth elements (including Y which will be referred to as a rare earth element in this current work) have been used to improve the strength, creep resistance, mechanical properties or castability of Mg. More recently a debate has begun relating to the importance of precipitation hardening and/or solid solution strengthening with regards to creep. Some Mg alloys have been found to be age hardenable and/or have thermally stable solute in solid solution and less emphasis has been placed on grain boundary reinforcement to Mg alloys [8, 13-16]. In the following sections, creep properties of various Mg alloy systems will be briefly investigated. Following that, the creep properties of Mg-rare earth alloys will be described in detail.

2.4.1 Creep of Mg-Al alloys

Mg-Al based alloys are some of the more common commercially used Mg alloy systems [99]. Aluminium has a relatively high solid solubility in Mg, 11.7 at.% (12.9 wt.%) at the eutectic temperature of 437°C (Figure 2.19).

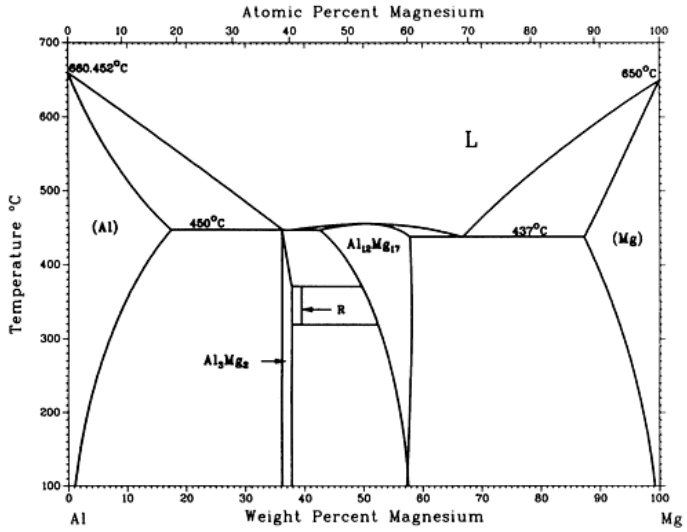

Figure 2.19: Mg-Al binary phase diagram [100].

2.4.1.1 Mg-Al-Zn Alloys

One of the earliest mass-produced Mg alloys was AZ91 (Mg-9wt.%Al-1wt.%Zn). Due to the poor elevated temperature (> 130°C) creep properties of AZ91 subsequent Mg-Al based alloys were developed [101, 102] (Figure 2.20).

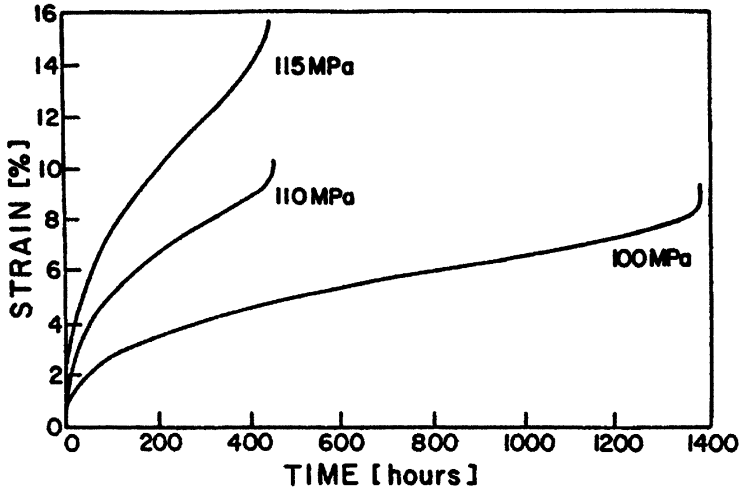

Figure 2.20: Creep curves for as-cast AZ91D (die-cast) under constant loads at 150°C [102].

The typical microstructure of a HPDC AZ91 alloy is shown in Figure 2.21. The matrix is composed of α-primary phase and an intermetallic β phase ($Mg_{17}Al_{12}$) along with a supersaturated solid solution Mg-Al rich phase α-eutectic (referred to as α-secondary in [103]) is present at grain/cell boundaries.

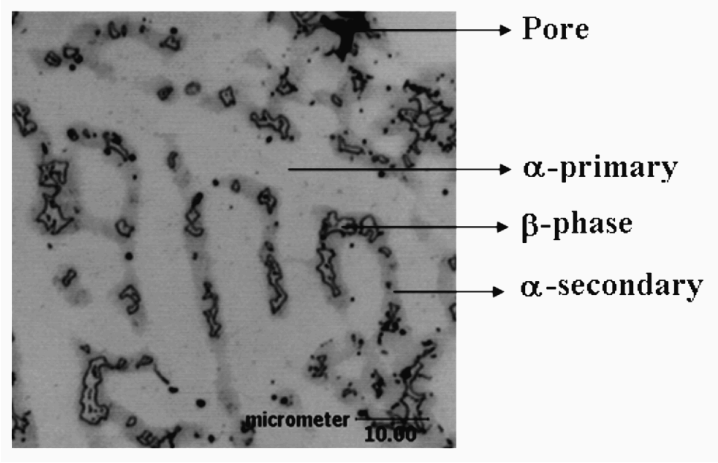

Figure 2.21: Typical microstructure of HPDC AZ91 [103].

There is still debate as to the exact reason for the poor creep properties of AZ91. It is often stated that the poor creep properties of Mg-Al alloys are related to the softening of the intermetallic β phase, $Mg_{17}Al_{12}$, present in the intergranular region of the microstructure that forms through a eutectic reaction at 437°C [82, 104-106]. Another commonly stated cause of poor creep resistance in Mg-Al alloys is the discontinuous precipitation of $Mg_{17}Al_{12}$ which can lead to grain boundary sliding [4, 12, 107]. The relatively poor creep properties of Mg-Al alloys have also been attributed to high diffusivity of Al in Mg solid solution [12].

2.4.1.2 Mg-Al-Si Alloys

In an attempt to address the poor creep properties of Mg-Al-Zn alloys up to 150°C, alternative alloying additions to Mg were required. The die-cast Mg-Al-Si alloy system was developed [108] and Volkswagen adopted Mg-Al-Si alloys such as AS41 in the 1970s for automotive applications [106]. Mg_2Si precipitates formed in the AS alloys have high hardness, low thermal expansion coefficient and, as opposed to $Mg_{17}Al_{12}$, have a high melting temperature (1085°C). The improved elevated temperature strength was attributed to the increased dispersion strengthening obtained from the Mg_2Si phase that forms at the grain boundaries [106]. However, the addition of Si does not significantly

hinder the formation of β-phase and thus does not substantially increase creep resistance in Mg alloys and is also difficult to die-cast [88, 109].

2.4.1.3 Mg-Al-RE Alloys

Mg-Al-RE alloys showed promising improvements to elevated temperature creep properties [72, 110-112]. The RE component in this alloy series is often added as La or Ce-rich mischmetal (a mixture of a number of RE elements). Two of the more common Mg-Al-RE alloys are AE42 and AE44. The improved creep resistance of AE alloys in comparison to Mg-Al alloys such AZ91 and AS21 is commonly attributed to the suppression of $Mg_{17}Al_{12}$ due to the preferential formation of $Al_{11}RE_3$ phase (body-centred orthorhombic, a = 0.45 nm, b = 1.32 nm and c = 0.99 nm) [72, 110]. AE44 has a typical dendritic microstructure characterised by primary α-Mg dendrites and intermetallic phases present at grain boundaries (lamellar-like morphology) or in the interdendritic regions (particulate shape) (Figure 2.22). Zhu *et al.* [110] showed that the lamellar-like intermetallic phase present in AE44 at the grain boundaries is $Al_{11}RE_3$ while the particulate shaped intermetallic was Al_2RE, which has also been reported [111].

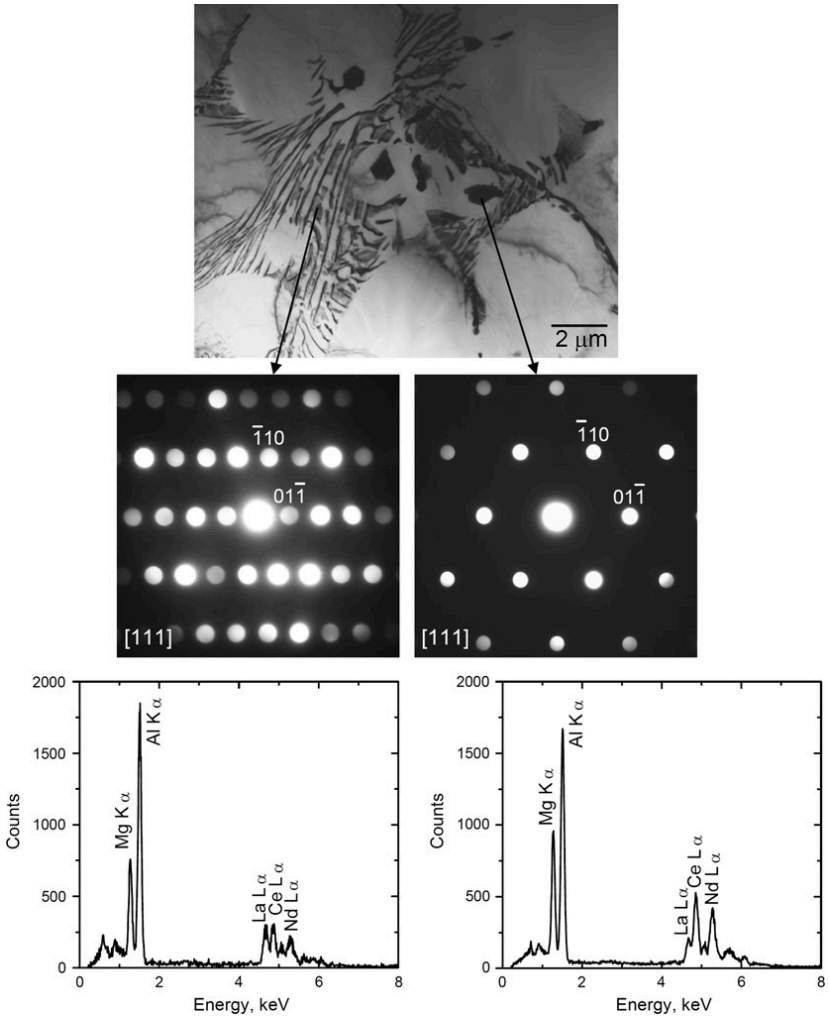

Figure 2.22: TEM bright-field image, microbeam electron diffractions, and EDS spectra showing typical microstructure and identification of intermetallic phases in as-cast AE44. The lamellar-like intermetallic phase was identified to be $Al_{11}RE_3$ (body-centred orthorhombic structure) whereas the particulate-shaped intermetallic phase is Al_2RE (diamond cubic structure) [110].

AE44 has better creep resistance than AE42 (Figure 2.23). Powell *et al.* [111] proposed that at temperatures above 150°C, the $Al_{11}RE_3$ phase is unstable and decomposes to the Al_2RE phase leading to the availability of more Al atoms to react with Mg and form $Mg_{17}Al_{12}$. Since $Al_{11}RE_3$ was found to be the predominant intermetallic in both AE42 and AE44 the superior creep resistance of the latter cannot be explained by this mechanism.

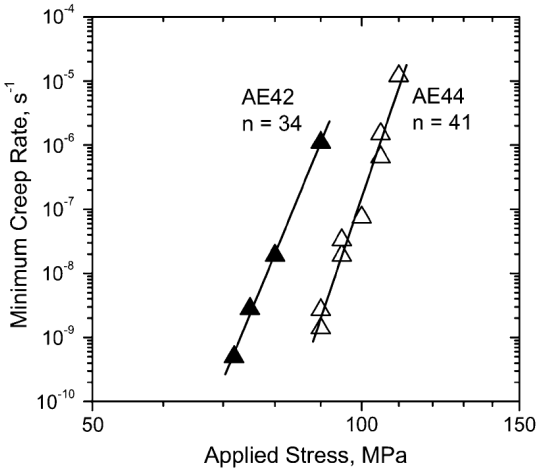

Figure 2.23: Minimum creep rate plotted against applied stress at 175°C for AE44 compared with AE42 [96].

In contrast, Zhu *et al.* [96] concluded that the improved creep properties of AE44 are related to the higher concentration of RE in solid solution in the α-Mg phase which, contributes to greater solid solution strengthening and/or precipitation hardening and also to the removal of Al from the matrix.

2.4.1.4 Mg-Zn-Al-RE Alloys

Additions of Zn to Mg-Al-RE alloys were used in an attempt to further improve their high temperature creep properties [113]. Zn was added to the HPDC Mg-4Al-4RE (wt.%) alloy due to its high solid solution strengthening effect in the α-Mg matrix (a reason for it being included in AZ91). Also, in alloys where Zn is the major alloying addition, fluidity is very good and the creep properties are improved, in comparison to Mg-Al, but they also have greater susceptibility to hot tearing [45, 114]. However, Xiao *et al*. [113] showed that increasing concentrations of Zn (from 1 wt.% to 4 wt.%) in a base AE44 alloy decreased the creep resistance of the alloy (Figure 2.24).

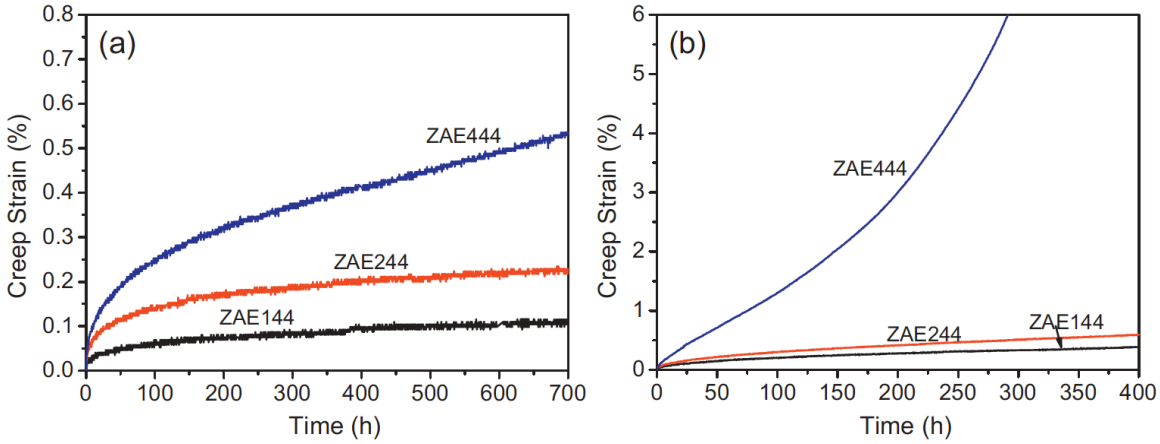

Figure 2.24: Creep curves for HPDC AE44-based alloys at 150°C under the applied stresses of a) 45 MPa and b) 60 MPa.

Following microstructure investigations, Xiao *et al.* [113] concluded that the reduction in creep strength was a result of the increase of Al_2REZn_2 phase in the expense of $Al_{11}RE$ and Al_4RE phases, which reduced the amount of dispersion strengthening of the eutectic. Additionally, Xiao *et al*. [113] concluded that the result could also be related to the fact that Zn has a relatively high solid solubility (2.4 at.% or 6.2 wt.% [115]) in Mg but also the relatively high diffusivity of Zn in Mg may assist in dislocation motion.

2.4.1.5 Mg-Al-Sr Alloys

The Mg-Al-Sr alloys were designed as viable alternatives to Mg-Al-RE alloys [116]. As with Mg-Al-Si and Mg-Al-RE alloys the formation of $Mg_{17}Al_{12}$ is reduced by the preferential formation of another phase, namely Al_4Sr. The superior creep resistance of AJ52 (Mg-5Al-2Sr wt.%) and AJ62 (Mg-6Al-2Sr wt.%) has been attributed to the presence of the Al_4Sr phase [117]. "In AJ-alloys the interdendritic network of Al_4Sr or bulky-phase is stable against coarsening at temperatures relevant for technical applications, since Sr is not dissolved in the matrix so that additional Al_4Sr or bulky-phase cannot be formed during creep or heat treatment" [116].

2.4.1.6 Mg-Al-Ca Alloys

More recently the Mg-Al-Ca based alloys such as AXJ530 (Mg-5Al-3Ca-0.15Sn wt.%) and MR1230D (Mg-6.5Al-2.25Ca-0.25Sr-0.8Sn) have shown excellent creep resistance at

temperatures of 150°C and applied stress above 90 MPa [118-120]. A third alloy that is also Mg-Al-Ca based, MRI153M (Mg-8Al-1Ca-0.27Sr wt.%) has significantly poorer elevated temperature creep properties in comparison to the other two alloys (Figure 2.25).

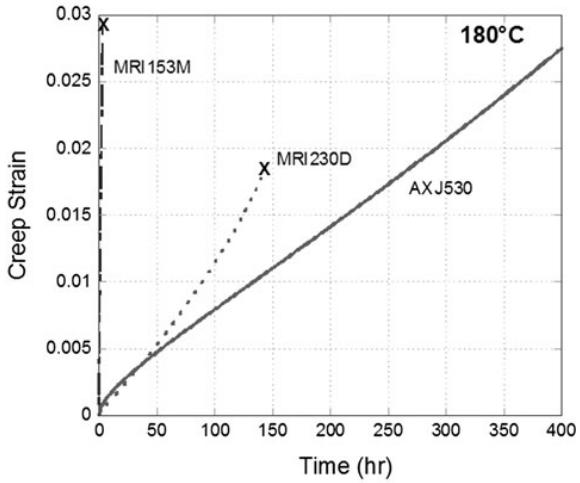

Figure 2.25: Tensile creep behaviour of AXJ530, MRI153M and MRI230D crept at 110 MPa at 180°C. Failed specimens are indicated by an 'x'. [22]

All the alloys attempt to improve the elevated temperature creep resistance of Mg-Al based alloys by introducing stable grain boundary phases and also reducing the amount of $Mg_{17}Al_{12}$ [95, 121]. The microstructure of the alloys is relatively similar (Figure 2.25). The primary α-Mg is surrounded by eutectic phases in the interdendritic regions, the average cell size is approximately 11µm and the grain size is on the order of 20µm for all the alloys [22].

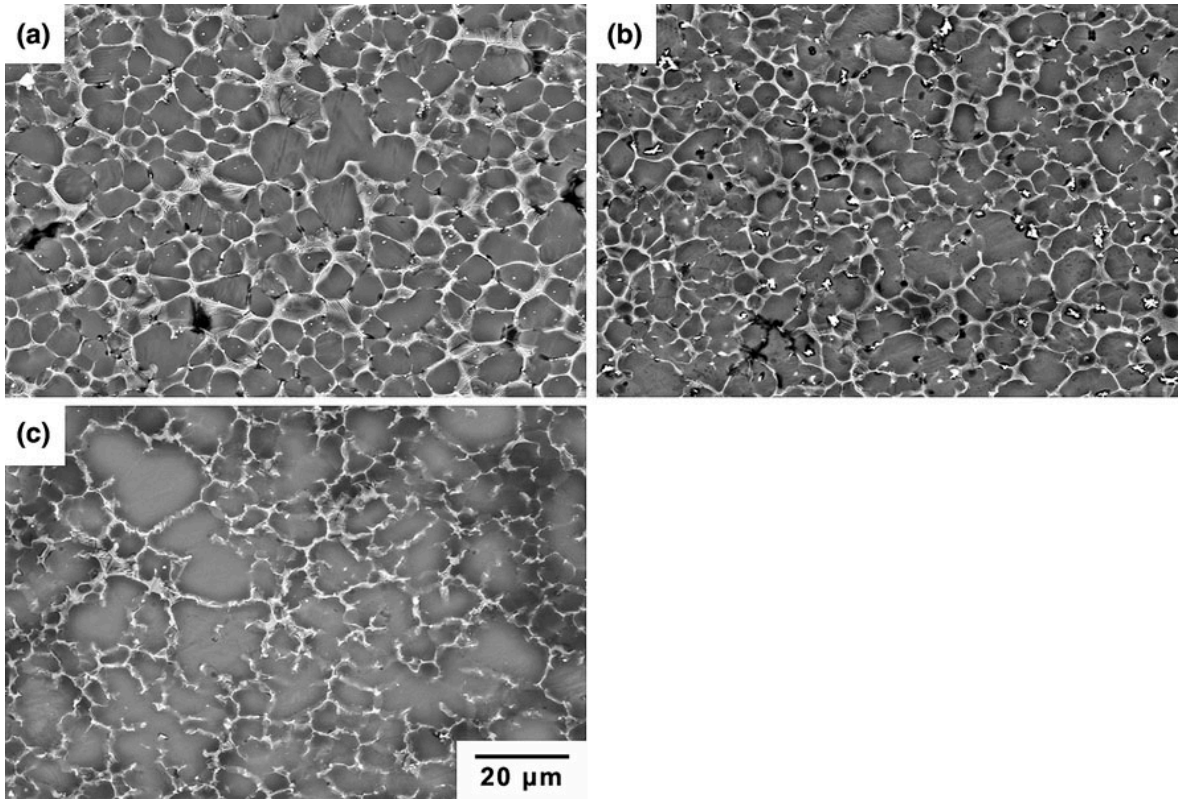

Figure 2.26: SEM (BSE) images of die-cast a) AXJ530, B) MRI230D and c) MR1153M. The darker grey regions are cells of primary α-Mg, while the brighter contrast features are intermetallic phases in the eutectic. [22]

Thus TerBush *et al.* [22] proposed that the variation in creep resistance could not be attributed to differences in microstructure. Rather, the differences in the partitioning of Al and Ca in the primary α-Mg phase during the non-equilibrium solidification was proposed as the likely reason for the difference in creep resistance. The segregation of solute in solid solution profiles of the three major elements of the alloys (Mg, Al and Ca) are shown in Figure 2.27 for MRI230D, MRI153M and AXJ530 and AX44 (Mg-3.8Al-3.5Ca wt.%) was included as a baseline Mg-Al-Ca comparison alloy.

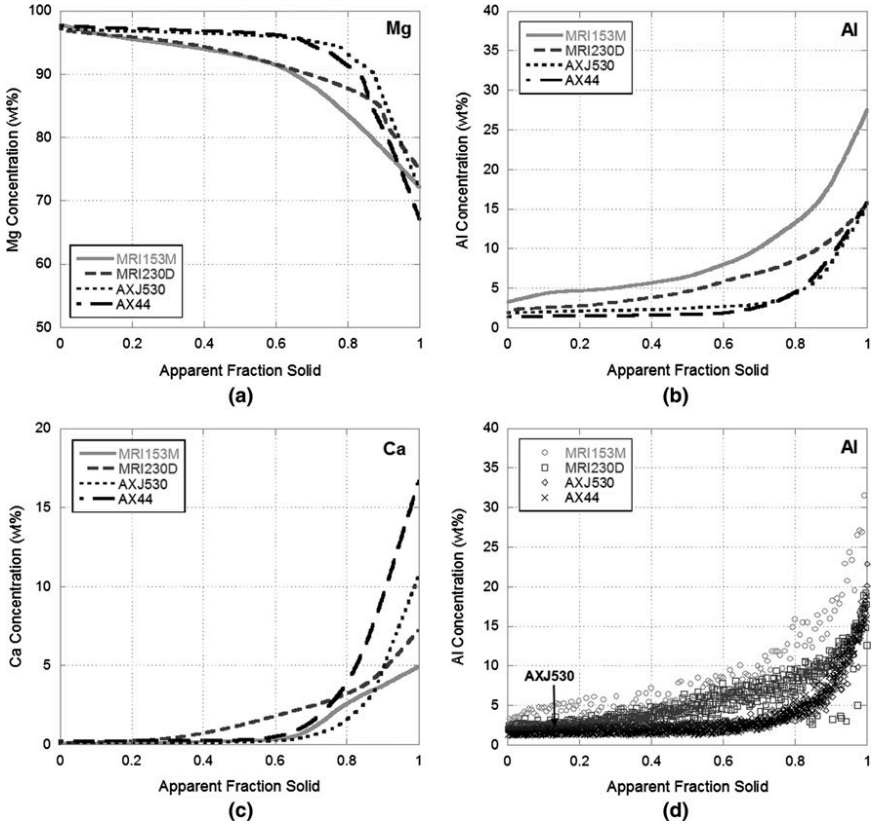

Figure 2.27: Least-mean-squares fit of concentration profiles for (a) Mg, (b) Al, and (c) Ca in MRI153M, MRI230D, AXJ530, and AX44, as measured by the electron microprobe. (d) Same as (b), except showing the scatter in the experimental data, which is caused by errors in the Mg concentrations used to sort the rest of the elements [118].

MRI230D had the greater level of Al and Ca in the primary α-Mg whilst MRI153D had a higher level of Al (Figure 2.27) compared to AX44 and AXJ530. The differences in the partitioning of the solute in solid solution were regarded to influence both the solid solution and precipitation strengthening, which could explain the differences in creep properties.

Although there has been significant advances in the creep resistance of Mg-Al based alloys (as shown by AXJ530) by the suppression of the $Mg_{17}Al_{12}$ phase, the creep resistance of Mg-RE (with no Al) such as the alloys based on the Mg-Y-Nd system [108] still have significantly better elevated temperature creep properties.

2.4.2 Creep of Mg-RE Alloys

An alternative method to overcome the detrimental effects of $Mg_{17}Al_{12}$ is to produce Mg alloys without any Al content. Mg-RE alloys, most notably WE54 (Mg-5.1wt.%Y-4wt.%RE-0.5wt.%Zr) and WE43 (Mg-4.0wt.%Y-3.3wt.%RE-0.5wt.%Zr) have excellent high temperature creep properties, minimum creep rate of 1.6 x 10^{-7} s^{-1} for WE54 at 300°C and 40 MPa and 7.34 x 10^{-10} s^{-1} for WE43 at 200°C and 60 MPa [58].

The instability of the price of RE elements has made alloys such as WE54 and WE43 economically unviable for the automotive industry (Figure 2.28).

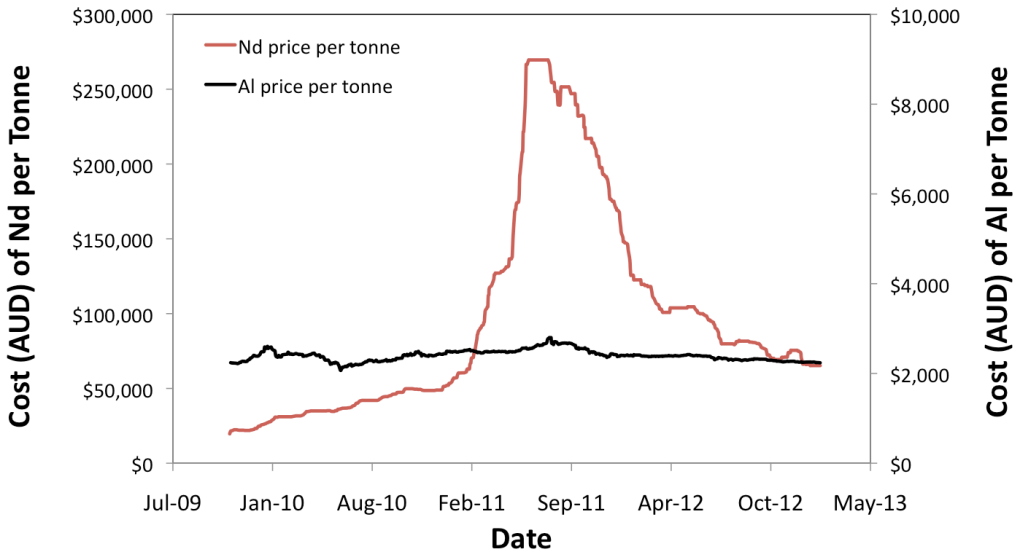

Figure 2.28: Cost of Nd per tonne also showing cost of Al for comparison [122].

Thus other Mg-RE alloys, with lower concentrations of RE, which still have good creep resistance have also been devised. Elektron 21 (Mg-2.7Nd-1.2Gd-0.49Zr-0.4Zn) and AM-SC1 (Mg-1.7Nd-0.5Zn-1.0Zr and 1.0 other RE wt.%) are some alternatives [123-125] that contain less RE, but due to being sand cast alloys they did not meet the industry requirement for rapid mass production. AM-HP2+ (a Mg-RE-Zn alloy) is an alternative to AM-SC1, which has both good creep resistance at temperatures of up to 177°C and can be mass-produced by high-pressure die-casting [7, 126]. The creep resistance of AM-HP2+ is shown to be at least as good as the commonly used Al alloy A380 and significantly better than some of the more commonly used Mg alloys such as AZ91 and creep resistant Mg-Al alloys such as AE42 and AXJ530 (Table 2.2).

Table 2.2: Typical secondary creep rates (minimum creep rates) and tensile 0.2 % proof strength of selected die-cast Mg alloys. The Al alloy A380 is also included for comparative purposes. [7, 12, 125, 127]

	Secondary creep rate (s^{-1})		0.2 % proof strength (MPa)	
Alloy	150°C and 100 MPa	175°C and 90 MPa	150°C	175°C
AZ91	1.1×10^{-6}	5.0×10^{-6}	107	88
AJ62	-	2.6×10^{-6}	-	93
AE42	-	1.1×10^{-6}	102	93
AJ52	-	9.4×10^{-9}	105	101
AE44	8.0×10^{-10}	2.7×10^{-9}	117	112
AXJ530	-	1.6×10^{-9}	-	146
AM-SC1	-	2.0×10^{-10}*	135	131
Elektron 21	-	1.7×10^{-8}‡	160	-
AM-HP2+	1.0×10^{-10}	1.0×10^{-10}	132	126
A380	1.0×10^{-10}	1.9×10^{-10}	166	166

*Creep tested at 177°C, ‡Creep tested at 250°C.

2.4.3 Influence of Different RE on Creep

Rare earth elements are commonly added to Mg alloys in the form of mischmetal, which is typically rich in Ce with lower concentrations of other RE elements such as La and still lower concentrations of Y, Nd, Pr etc. [9]. It has been shown that individual rare earth elements have significantly different effects on the properties and microstructure of the Mg alloy that it is alloyed with [16, 128-130]. The differences arise from the varying amount of precipitation strengthening and/or solid solution strengthening which is related to the solubility of the rare earth element in Mg.

The alloy system under investigation in this present work is based on the ternary Mg-La-RE system, which is discussed in more detail later in this section. RE additions that are commonly used are Ce, Nd, Y and Gd, which have larger atomic radii than Mg and have varying amounts of maximum solid solubility in Mg. Atomic radii and solubility data for the commonly used alloying additions are given in Table 2.3. The use of RE elements enables both solid solution hardening and precipitation hardening. The intermetallic phases exhibit little diffusivity and a good coherence to the matrix. [58]

Table 2.3: Radii of rare-earth elements and Mg and maximum solid solubility of Y, La, Ce, Nd and Gd in Mg [131].

Metal	Atomic number	Ion	Atomic radii, nm	Ionic radii, nm	Eutectic Temperature, °C	Max Solid Solubility, at.% (wt.%)
Mg	12	Mg^{+2}	0.16020	0.0720	-	-
Y	39	Y^{+3}	0.18012	0.0892	565	3.60 (12.0)
La	57	La^{+3}	0.18791	0.1061	612	0.04 (0.23)
Ce	58	Ce^{+3}	0.18247	0.1034	590	0.13 (0.74)
Nd	60	Nd^{+3}	0.18214	0.0995	552	0.63 (3.63)
Gd	64	Gd^{+3}	0.18013	0.0938	542	4.53 (23.48)

Recently, the ternary phase diagram determination for the Mg-La-Nd system have been reported by Gröbner *et al.* [132] at 500°C as shown in Figure 2.29.

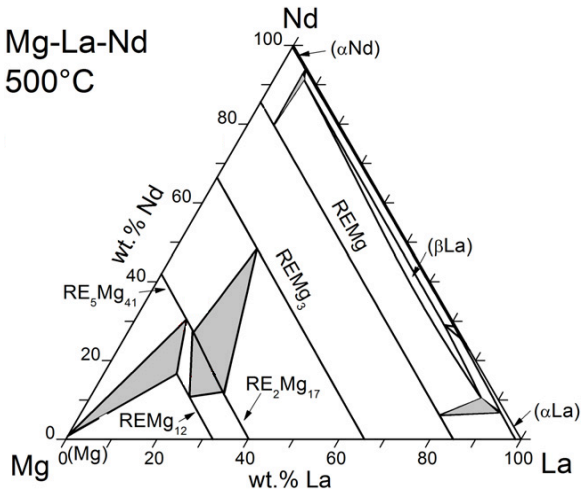

Figure 2.29: Calculated isothermal Mg-La-Nd phase diagram section at 500°C. Three-phase triangles are shaded in grey [132].

Following an extensive review of the literature, no ternary phase diagrams for Mg-La-Y or Mg-La-Gd could be found. Thus binary Mg-RE phase diagrams have been used to approximate solubility, possible intermetallic phases and melting temperatures for the RE elements in Mg which are the focus of the current work. Figures 2.30 to 2.34 show the binary phase diagrams for Mg-La, Mg-Nd, Mg-Y and Mg-Gd, respectively.

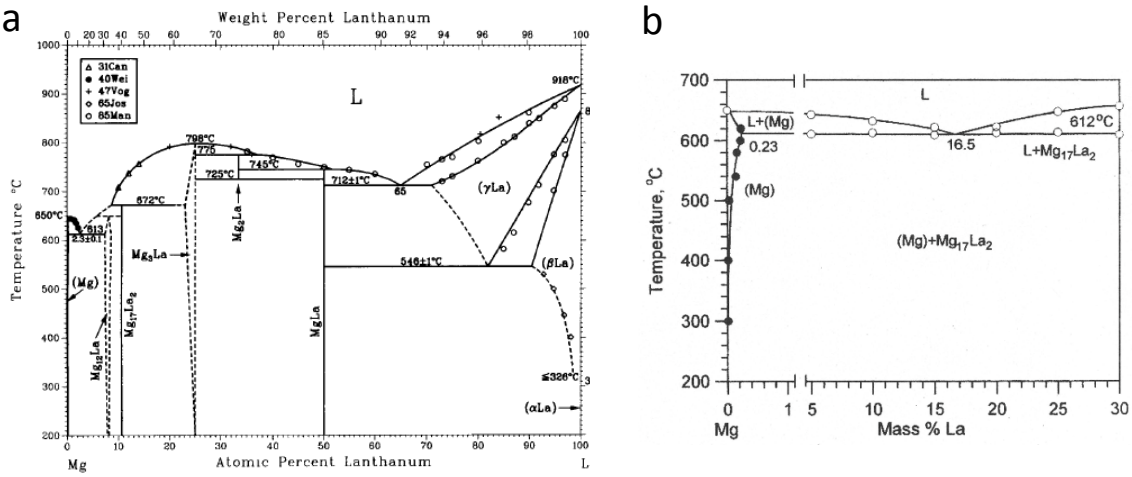

Figure 2.30: a) Full binary phase diagram for Mg-La in at.%, b) Mg-rich section of the phase diagram (wt.%) [131, 133].

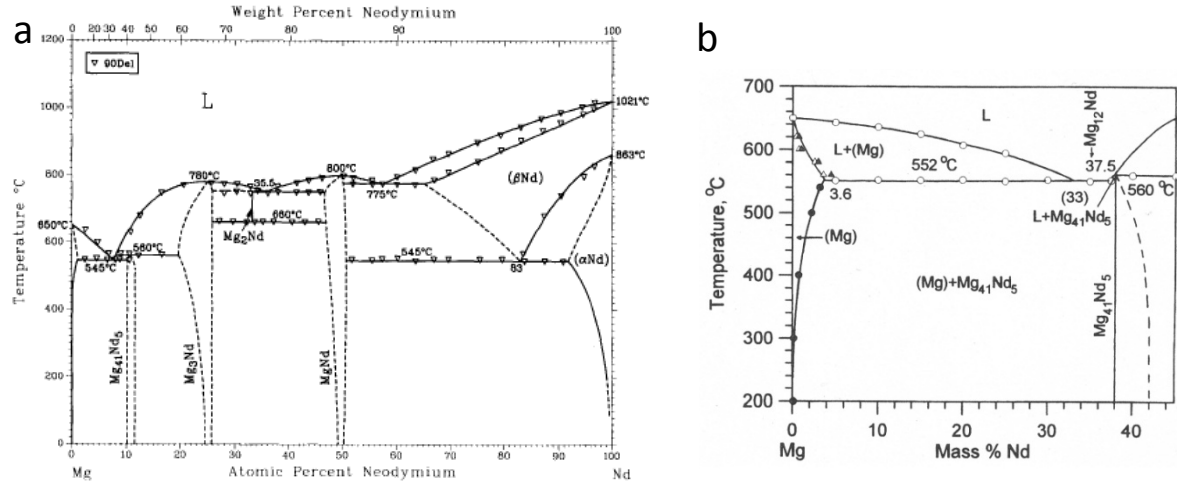

Figure 2.31: a) Full binary phase diagram for Mg-Nd, b) Mg-rich section of the phase diagram (wt.%) [131, 134].

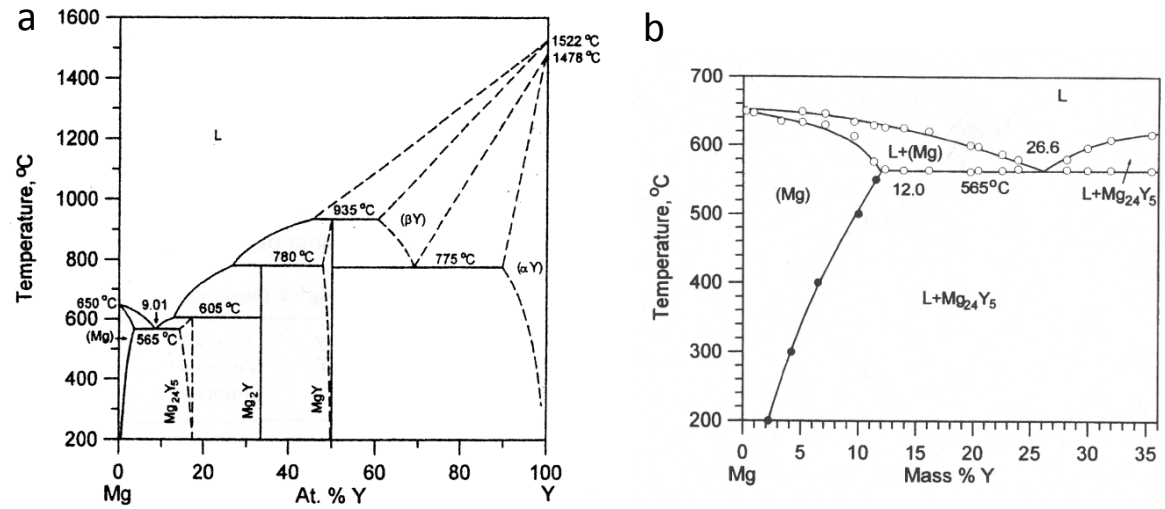

Figure 2.32: a) Full binary phase diagram for Mg-Y, b) Mg-rich section of the phase diagram (wt.%) [131].

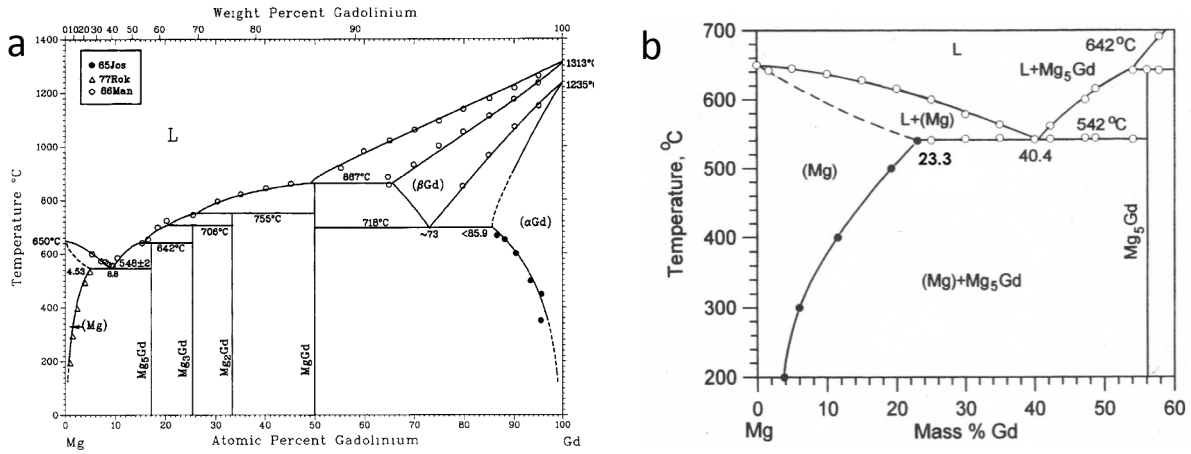

Figure 2.33: a) Full binary phase diagram for Mg-Gd, b) Mg-rich section of the phase diagram (wt.%) [131, 135].

There is general agreement on the form of the Mg-La [131, 133, 136], Mg-Y [131, 137] and Mg-Gd [131, 135] phase diagrams. There is still some debate as to the equilibrium intermetallic phase formed in the Mg-Nd system. Rokhlin *et al.* [131] and Okamoto [134] regard $Mg_{12}Nd$ to be a metastable phase and $Mg_{41}Nd_5$ as being the stable β phase for Nd in Mg. Zhu *et al.* [14], following TEM analysis of a binary HPDC Mg-Nd alloy, showed that intermetallic phase present in the interdendritic regions was Mg_3Nd. It was suggested that the Mg_3Nd intermetallic phase formed instead of $Mg_{12}Nd$ due to the non-equilibrium cooling conditions present for HPDC alloys.

In order to form solid-state precipitates required for precipitation hardening, the solid solubility of the alloying additions should decrease continuously with the decrease in temperature as is the case for Mg-Nd, Mg-Y and Mg-Gd alloys according to their respective phase diagrams, Figure 2.31 to Figure 2.33. During the ageing of Mg alloys, precipitation may occur by the formation of first Guinier-Preston (GP) zones and/or metastable phases prior to the formation of stable or equilibrium precipitate phase [9, 138]. The precipitation sequence of supersaturated binary solid solutions of Mg-Y, Mg-Nd and Mg-Gd as given in [139] are shown in Table 2.4.

Table 2.4: Precipitation sequences in individual magnesium alloy systems [139]. Note: * d is the separation distance of columns of RE atoms.

Mg-Nd

SSSS →	ordered G.P. zones zig-zag shape d = 0.37 nm *	→ β″ (Mg_3Nd) hcp, DO_{19} a = 0.64 nm c = 0.52 nm hexagonal prism	→ β′ (Mg_7Nd) orthorhombic a = 0.64 nm b = 1.14 nm c = 0.52 nm lenticular shape	→ β_1 (Mg_3Nd) fcc, $Fm\bar{3}m$ a = 0.74 nm $\{10\bar{1}0\}_\alpha$ plate	→ β ($Mg_{12}Nd$) tetragonal, I4/mmm c = 0.59 nm $[0001]_\alpha$ rod	→ β_e ($Mg_{41}Nd_5$) tetragonal, I4/m a = 1.47 nm c = 1.04 nm

Mg-Y

SSSS →	β′ (Mg_7Y) orthorhombic a = 0.65 nm b = 2.27 nm c = 0.52 nm globular shape	→ β ($Mg_{24}Y_5$) bcc, $I\bar{4}3m$ a = 1.13 nm $\{10\bar{1}0\}_\alpha$ or $\{31\bar{4}0\}_\alpha$ plate

Mg-Gd(-Y)

SSSS →	ordered G.P. zones zig-zag shape d = 0.37 nm *	→ β″ (Mg_3Gd) hcp, DO_{19} a = 0.64 nm c = 0.52 nm hexagonal prism	→ β′ (Mg_7Gd) orthorhombic a = 0.65 nm b = 2.27 nm c = 0.52 nm lenticular shape	→ β_1 (Mg_3Gd) fcc, $Fm\bar{3}m$ a = 0.73 nm $\{10\bar{1}0\}_\alpha$ plate	→ β (Mg_5Gd) fcc, $Fm\bar{3}m$ a = 2.23 nm $\{10\bar{1}0\}_\alpha$ plate

Due to the extremely low solid solubility of La in Mg, little research has been performed on the Mg-La ageing sequence. It is however generally accepted that the equilibrium intermetallic phase to form in the Mg-La is $Mg_{12}La$ which has a body-centred orthorhombic structure [140].

Dynamic precipitation, that is precipitation caused during deformation of an alloy as opposed to static precipitation, which occurs during prior heat treatments, has also been shown to influence the creep properties in certain Mg alloys [14, 141, 142]. In precipitation hardenable alloys that experience an applied stress, dynamic precipitates tend to preferentially nucleate on dislocations, due to the lower nucleation energy present at dislocations (Figure 2.34).

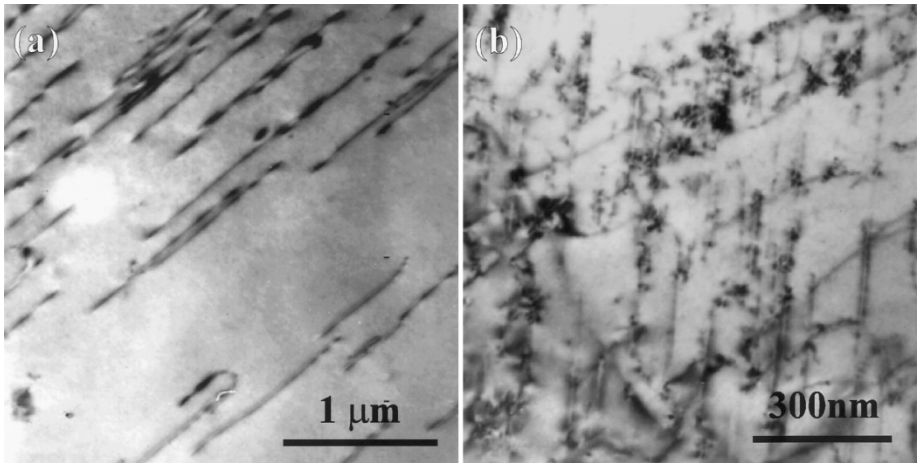

Figure 2.34: Dynamic precipitation during creep of Mg-2.4Y (wt.%) at 277°C and 100 MPa: a) Just after applying load and b) After creep for 20 h [13].

The dynamic precipitates also assist to impede the motion of dislocations through the alloy matrix and, in turn, this has been proposed to help improve creep properties [88]. Zhu *et al.* [14] showed that dynamic precipitation increased with increasing maximum solid solubility of alloying additions namely, La, Ce or Nd in Mg following creep testing (Figure 2.35).

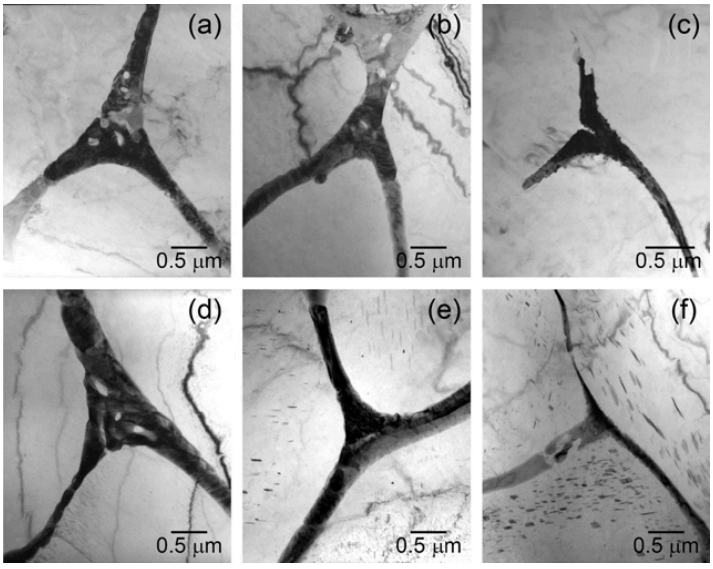

Figure 2.35: TEM micrographs showing microstructures of Mg-3.44La (wt.%) (a and d), Mg-2.87Ce (wt.%) (b and e) and Mg-2.60Nd (c and f) before and after creep testing at 177°C and 50 MPa for 300 h. Note the increased presence of precipitates in the Mg-2.87Ce and particularly Mg-2.60Nd alloys after creep [14].

In the current work, the differences in elevated temperature creep properties of three high-pressure die-cast Mg-rare earth (Mg-RE) alloy series, Mg-La-Nd, Mg-La-Y and Mg-La-

Gd have been determined. A consistent concentration of La (0.45at.%) was used to maintain similar grain boundary reinforcement for all the alloys and also to help reduce hot tearing susceptibility (Figure 2.8) and assist with castability. The ternary RE concentration was varied and the RE elements were chosen to have differing solubility in Mg. This was done to investigate the influence of solid solution strengthening and precipitation hardening on creep. If binary HPDC Mg-RE alloys were used to investigate creep properties instead of ternary Mg-La-RE alloys, it would be more difficult to isolate the effects of intermetallic at grain boundaries or the soluble RE since both are being influenced by the same alloying addition.

A significant improvement to creep resistance was also shown by Zhu *et al.* [14] with increasing solid solubility of RE in Mg (Figure 2.36). However, the authors [14] did not isolate the influence that precipitation hardening or solid solution strengthening had on the overall improvement to creep.

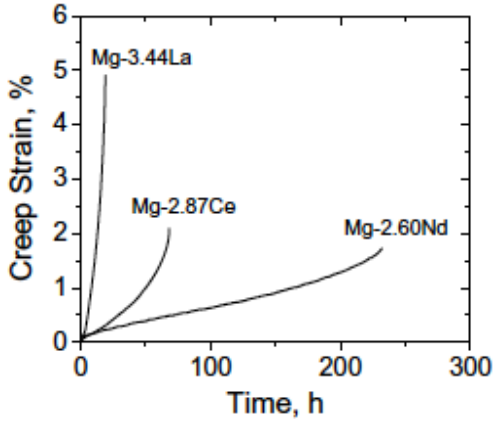

Figure 2.36: Creep curves for Mg-3.44La, Mg-2.87Ce and Mg-2.60Nd (wt.%) at 177°C and 90 MPa [14].

It should be noted that if precipitation hardening and/or solution strengthening are significant inhibitors of creep strain then solution treatment, quenching and then ageing of precipitation hardenable alloys, such as those used in the research by Zhu *et al.* [14] or Suzuki *et al.* [120] (for HPDC alloy AXJ530), may have further increased the precipitate volume fraction and thus may have further improved creep resistance. However, neither Zhu *et al.* [14] and Suzuki *et al.* [120] performed such heat treatments.

2.5 Effects of Microstructural Features on Creep

2.5.1 Grain Boundary Reinforcement

Over the last half century, grain-boundary sliding has been considered to be a major contributor to creep deformation of magnesium alloys [4, 11, 84, 99, 143-145]. In one of the earlier studies on creep of Mg alloys, Bell and Langdon [11] claimed that grain boundary sliding in Magnox Al 80 (Mg-0.78Al wt.%) caused up to 80% of the total creep deformation. More recently, Janik *et al.* [146] demonstrated that for a squeeze cast Mg-3Y-2Nd-1Zn-1Mn (wt.%) alloy the total creep deformation attributed to grain-boundary sliding was insignificant (no higher than 5.7 % of the total deformation). Rather they showed that the dominant creep mechanism was dislocation creep and that creep failure was the result of the nucleation, and coalescence of creep cavities present at grain boundaries.

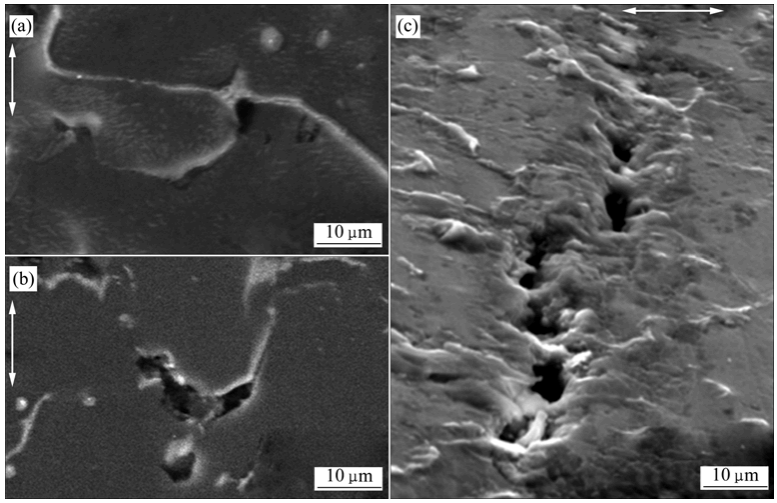

Figure 2.37: Detail of creep cavities on dendrite boundaries nucleated during exposure of Mg-3Y-2Nd-1Zn-1Mn at 300°C and 50 MPa: (a) Single creep cavity in earlier stage of creep exposure (relative time of test t/t_f=0.47); (b) Coalescence of cavities in later stages (relative time of test t/t_f=0.67); (c) Continuous crack in crept specimen [146].

Cavities formed at grain boundaries can grow causing weakening of the material [147]. Alloying additions that form intermetallic phases at grain boundaries are often used to act as barriers to the sliding of grains or to prevent dislocations that form within the grain to travel to neighbouring grains. It has been shown that a continuous intermetallic phase formed at grain boundaries can help to improve creep properties in Mg alloys [148]. Figure 2.38, compares the creep rate of different Mg alloys with varying degrees of

interconnected intermetallic at grain boundaries. AZ91 is shown to have the poorest creep rate properties at 200°C in comparison to MRI230D (which was cast in a plate with a depth of 6mm). The corresponding micrographs for these two alloys clearly shows that AZ91 (Figure 2.38h) has significantly less intermetallic present at grain boundaries while MRI230D (Figure 2.38n) has a continuous intermetallic phase present at grain boundaries that acts like a skeleton to improve the strength of the alloy. In addition, the intermetallic phase in MRI230D is more stable than the $Mg_{17}Al_{12}$ intermetallic phase (as mentioned in section 2.4.1).

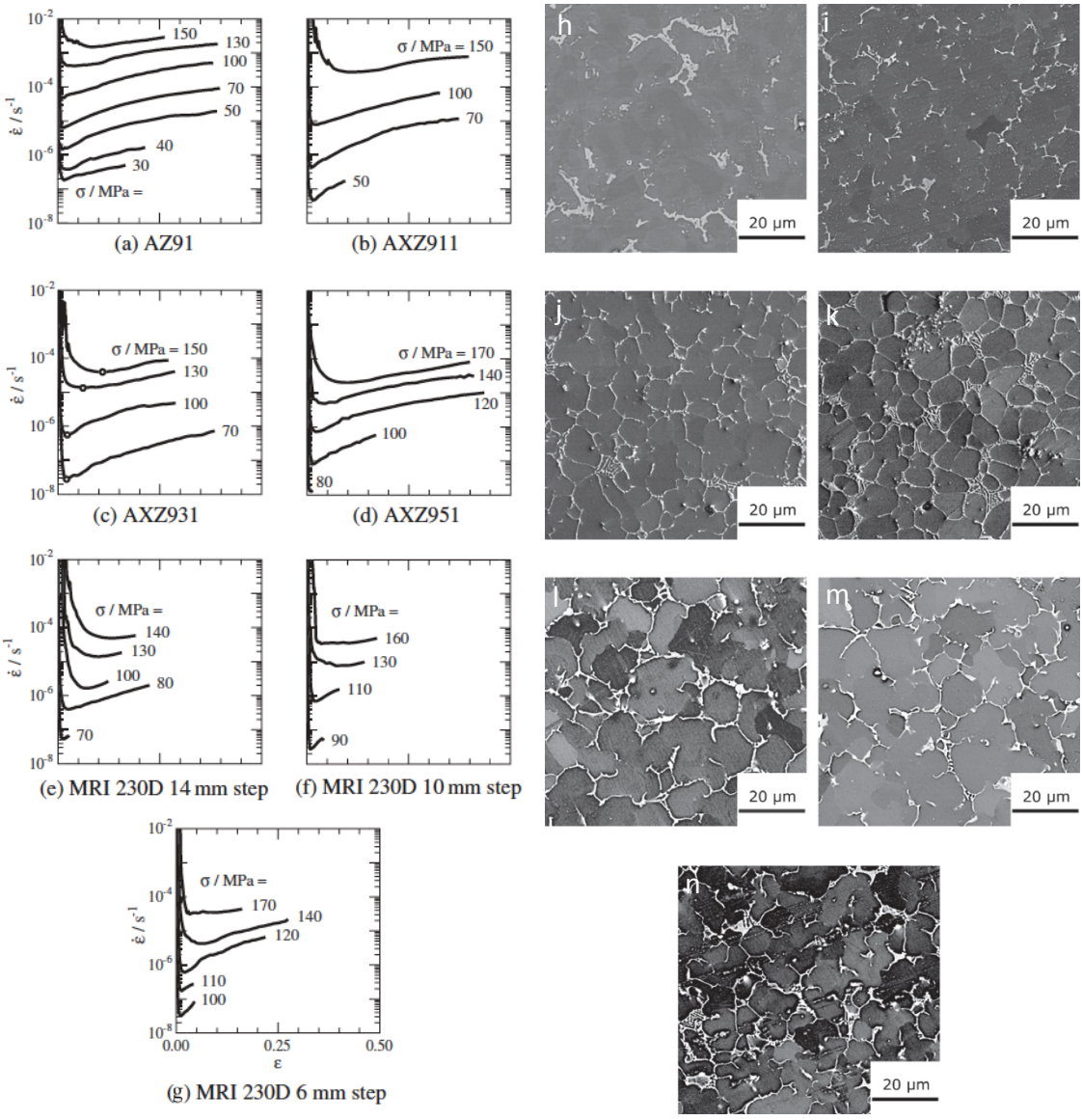

Figure 2.38: (a-g) Sets of creep rates at indicated stress levels at a testing temperature of 200°C. Open circles shown in (c) illustrate the evaluation of minimum creep rates. All graphs share the same axes. The corresponding SEM micrographs of the alloys are shown in (h - n). Note the step measurements indicate the depth of the stepped plate used during casting [148].

Zhang *et al.* [149] showed that yield strength is also influenced by the interconnectivity of eutectic or intermetallic phase at grain boundaries in HPDC Mg-RE alloys. 3D numerical images of Mg-0.62at.%La and Mg-0.6at.%Nd alloys created by dual beam FIB tomography (Figure 2.39) were incorporated into a finite element model code and used to model their tensile behaviour.

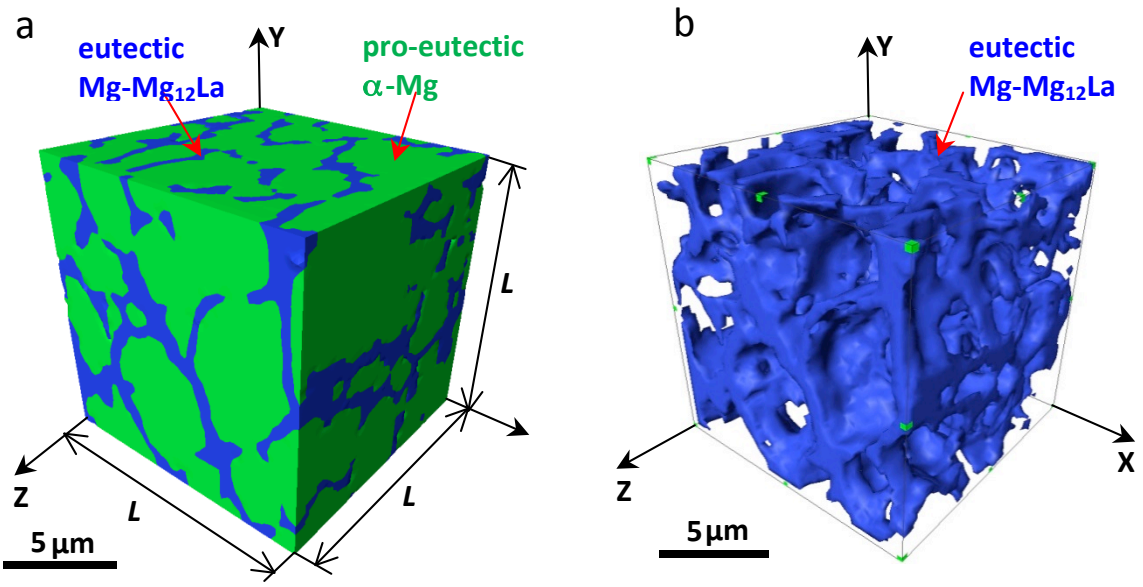

Figure 2.39: a) Cubic volume of the HPDC Mg-La alloy examined using FIB. The lighter phase is the pro-eutectic α-Mg whereas the darker one is the percolating 3D (α-Mg)-$Mg_{12}La$ eutectic. The latter is shown on its own in (b) [149].

The contribution to strength by individual components of the alloy morphology was then used to predict the overall yield strength of the alloy. The model used by Zhang *et al.* [149] predicted that the eutectic/intermetallic phase skeleton contributed 37 MPa to the yield strength of the Mg-La alloy. This value was closely matched to the drop in 0.2% PS in a HPDC Mg-0.45La-0.63Nd alloy following a flash anneal at 520°C for 1h (presented in the current work). The flash anneal did not significantly alter the rest of the microstructure of the alloy and thus demonstrated that a continuous eutectic or intermetallic phase at grain boundaries has a significant contribution to the yield strength of HPDC Mg-RE alloys. Further results on the effects of heat-treating ternary HPDC Mg-La-RE alloys are presented in Chapter 6.

2.5.2 Solute in Solid Solution and Its Effect on Creep

Solid solution strengthening is a method that can be used to strengthen metals by introducing impurities such as other atoms, which can be present as substitutional or interstitial positions in solid solution. The impurity atoms introduce a strain on the host atoms due to their difference in atomic size (this can occur if the impurity atoms are either larger or smaller than the host atoms). Solid solution strengthening in magnesium alloys depends on the solute atoms within the α-Mg phase interacting and impeding the movement of dislocations. Dislocations have associated stress fields, as do solute atoms. The stress fields from solute atoms can interact with dislocations and mutually exert forces between one another. Each of these interactions represents an energy barrier to dislocation motion thus causing a solid solution strengthening effect [65].

It has been shown that both Y and Gd have a considerably higher solid solution strengthening effect in Mg than either Al or Zn [150, 151]. Nie *et al.* [12] compared two Mg alloy systems with approximately equal concentrations of alloying additions, Mg-1.0Al (at.%) and Mg-1.1Y (at.%), in order to investigate the influence of solid solution strengthening and precipitation hardening on creep properties. The Mg-1.1Y alloy had superior creep resistance to the Mg-1.0Al alloy when tested at 277°C over a range of applied stress (Figure 2.40).

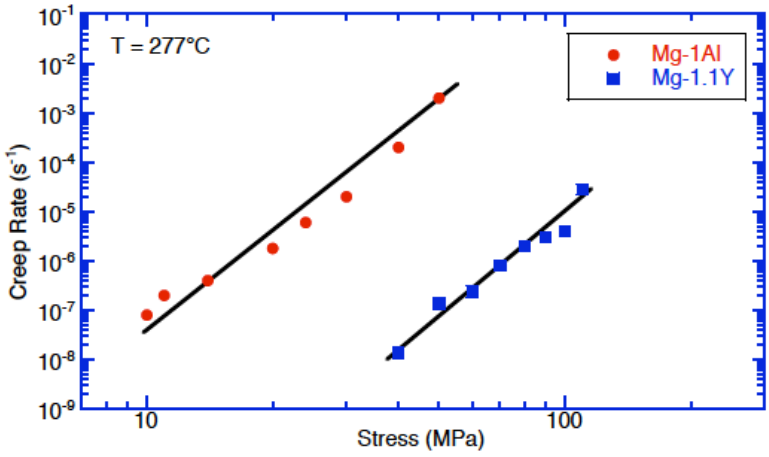

Figure 2.40: Comparison of the steady-state creep rates of Mg-1.0at.%Al and Mg-1.1at.%Y solid solution alloys subjected to different stresses at 277°C [12].

Solid solution strengthening was regarded to be approximately equal for the two alloys since both had approximately the same concentrations of alloying addition and both Al and Y have similar absolute atomic misfits when in solid solution, 11 % for Y and -14 % for Al [150]. By comparing the rate of diffusivity of Al in Mg and Ce (in place of Y due to the lack of sufficient Y diffusivity data) (Table 2.5) and the previous investigations on the morphology and evolution of precipitates in Mg-Al and Mg-RE alloys it was concluded that the faster diffusivity of Al in Mg was a determining factor between the creep resistance of the alloys.

Table 2.5: Solid diffusivity of Mg, Ce and Al in magnesium D_o = diffusion coefficient and Q = activation energy [12]. * Values of D_0 and Q for Zn were obtain from [152] for comparison.

Element	D_0 (m^2/s)	Q (kJ/mol)	D (m^2/s) at 150°C	D (m^2/s) at 175°C
Mg // c	0.0001	134.7	2.360×10^{-21}	1.999×10^{-20}
Mg $\perp$ c	0.00015	136	2.447×10^{-21}	2.115×10^{-20}
Ce	0.045	175.8	8.973×10^{-24}	1.458×10^{-22}
Al	0.0012	143	2.677×10^{-21}	2.586×10^{-20}
Zn*	0.00041	119.8	6.666×10^{-20}	4.455×10^{-19}

2.5.3 Precipitation and Its Effect on Mechanical Properties and Creep

Precipitation strengthening, also referred to as precipitation hardening, is another method that can be used to introduce an obstacle to prevent or reduce the motion of dislocations in alloys. In general, supersaturated solute in solid solution (α) is heated to a temperature that will allow precipitates to nucleate ($\alpha + \beta$ two phase region). The β precipitates increase the yield strength of the alloy by impeding the movement of dislocations in the material. The influence of precipitates on yield strength can be affected by the orientation, aspect ratio and number density of the precipitates.

Precipitation strengthening has been observed in a wide range of alloys particularly in Al alloys [153] and also Mg alloys such as WE54 (Mg-5.2Y-3RE-0.7Zr wt.%) [154], QE22 (Mg-2.5Ag-2.1Di-0.7Zr wt.%) [9] and AZ91 [101, 155]. Precipitates can act as obstacles to the motion of dislocations, which has been proposed as one of the key methods to improve creep resistance at elevated temperatures in Mg alloys [13, 16].

In HCP metals such as Mg alloys, two primary types of dislocations have been identified, <*a*> and <*c* + *a*> type dislocations [54]. The <*a*> type dislocations are the most commonly detected type of dislocations in Mg-alloys and glide along the basal plane. The <*a*> type dislocations can also glide on prismatic or pyramidal plane through thermally activated cross slip. The <*c* + *a*> type dislocations glide on second order pyramidal planes [54].

Sato *et al.* [156] showed, via EBSD microstructural evolution mapping of pure Mg during creep, that as steady state creep rates were reached an increasing amount of prismatic slip was detected. The orientation, morphology and number density of precipitates are important factors in determining how effective precipitates are in strengthening an alloy. Models have been proposed [157] showing that strengthening is achieved in precipitation hardenable Mg alloys that have a high density of intrinsically strong, plate-shaped precipitates with prismatic habit planes and large aspect ratios, as depicted in Figure 2.41. In Figure 2.41a, the cross-section of plate-like precipitates on the prismatic planes intersect the basal slip plane (0001) which can act to impede dislocation glide along that plane.

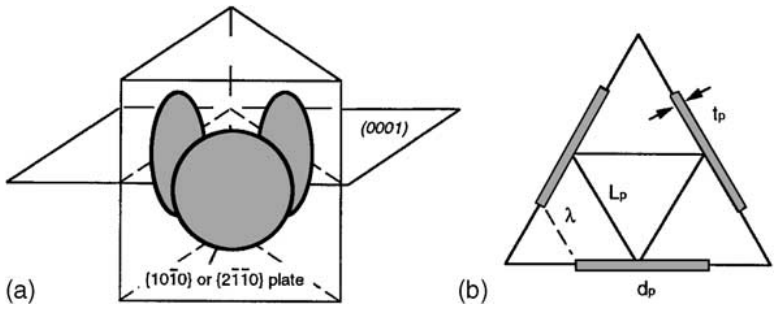

Figure 2.41: a) Arrangement of $\{10\bar{1}0\}_\alpha$ or $\{2\bar{1}\bar{1}0\}_\alpha$ precipitate plates in a triangular prismatic volume of α-Mg matrix, and b) projection of intersected prismatic plates in $(0001)_\alpha$ slip plane of α-Mg [157]. L_p is the mean planar centre-to-centre inter-precipitate spacing, d_p is the mean diameter of the plate, t_p is the mean planar thickness and λ is the effective planar inter-particle spacing.

Figure 2.42 shows the ratio of $\Delta\tau$ (Orowon stress increment required to force a dislocation past an obstacle) increases significantly for prismatic plane precipitates (Figure 2.42b) as the aspect ratio of precipitate plates/rods increases as opposed to basal plane precipitates (Figure 2.42a) or rod shaped precipitates (Figure 2.42c). It is important to

note that strengthening is only improved when the number density of the precipitates is large enough i.e. at least a volume fraction 0.04.

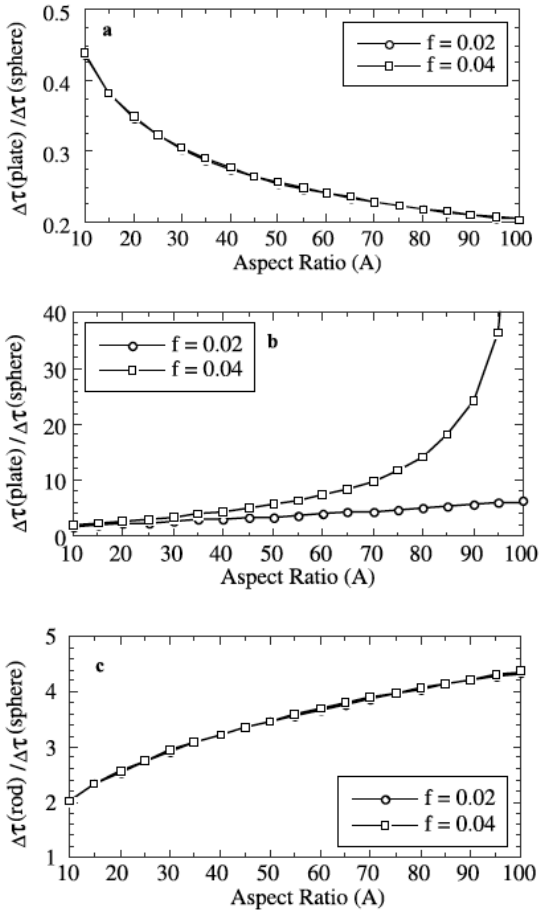

Figure 2.42: Variation of ratio Δτ(plate/rod)/Δτ(sphere) with plate/rod aspect ratio for strengthening attributing to a) (0001)$_\alpha$, b) $\{10\bar{1}0\}_\alpha$ or $\{2\bar{1}\bar{1}0\}_\alpha$ prismatic plates, and c) [0001]$_\alpha$ rods, at precipitate volume fractions of 0.02 and 0.04 [157].

When identical volume fractions and number densities of precipitates a compared, the effective inter-particle spacing of prismatic plates are more effective than either basal plates, [0001]$_\alpha$ rods or spherical particles (Figure 2.43).

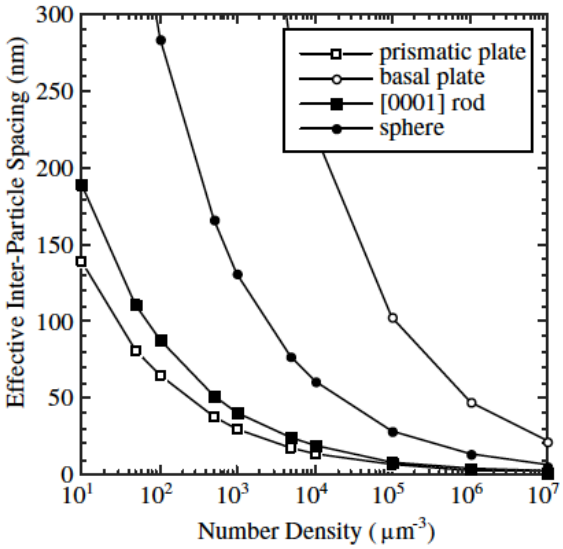

Figure 2.43: Variation of effective inter-particle spacing with number density of particles per unit volume of the magnesium matrix at a precipitate volume fraction of 0.04. Plate/rod aspect ratio is 40:1 [157].

Subsequently, it has been proposed that precipitate plates formed on the basal plane of the matrix phase provide the least effective barrier to gliding dislocations [157]. The precipitates present in AZ91 are regarded to be ineffective in impeding slip that occurs along the basal plane due to their orientation and their relatively low volume fraction [155, 158]. When a comparison is made between the minimum creep rates of AZ91 and WE54 (Table 2.6) it is clear that WE54 has significantly better creep properties.

Table 2.6: Minimum creep rates (compression tests) of AZ91 and WE54 alloys. Note: * indicates creep rate measured at a plastic strain of 4% [159].

Alloy	Temperature (°C)	Applied stress (MPa)	Minimal creep rate (10^{-8} s^{-1})
AZ91	25	250	0.4
	150	50	830*
WE54	150	235	3.4
	150	315	15
	200	165	250
	200	210	280*

This has been shown experimentally through the comparison of the precipitate morphology and orientation of poor creep resistant alloys such as AZ91 with those of superior creep resistance such as the RE-containing alloys WE54 and WE43 (Figure 2.44). In the case of AZ91, most continuous precipitates are orientated parallel to the basal

plane before they develop into lath-shaped precipitates on subsequent ageing and have a Burgers orientation relationship of $(0001)_m//(110)_p$ and $[1\bar{2}10]_m//[1\bar{1}1]_p$ [155] (Figure 2.44). AZ91 also has a small proportion of relatively coarse continuous precipitates perpendicular to the basal plane, which has an orientation relationship of $(0001)_m//(1\bar{1}1)_p$ and $[10\bar{1}0]_m//[1\bar{1}1]_p$. It is presumed that these precipitates are coarse as a result of the relatively high diffusion rate of Al atoms when in solid solution with magnesium [139] (Figure 2.44).

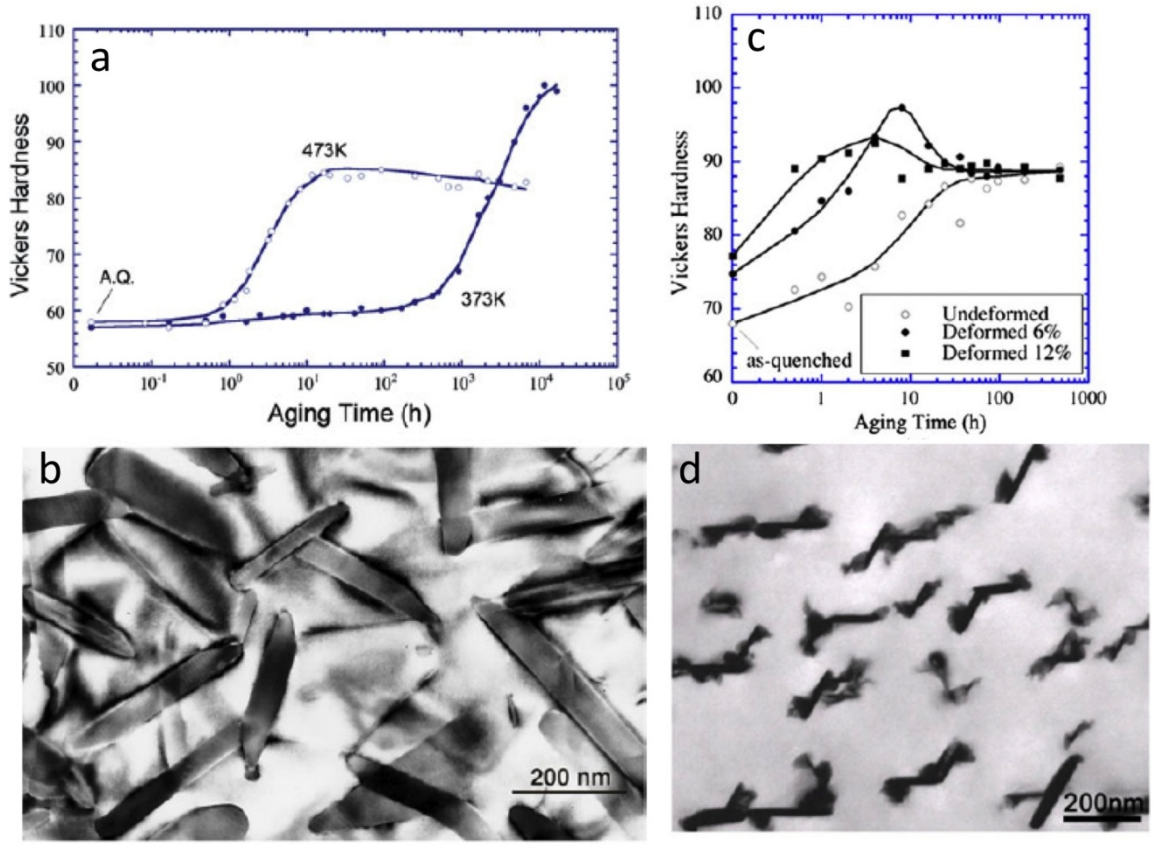

Figure 2.44: a) Isothermal ageing curves of magnesium alloy AZ91 at 373 K and 473 K (100°C and 200°C), b) Transmission electron micrograph showing the distribution and morphology of β precipitates in AZ91 aged for 8 h at 473 K (200 °C) with the electron beam parallel to $[0001]_\alpha$. Age-hardening response of WE54 alloy, c) at 523 K (250°C), d) Transmission electron micrograph showing distribution of precipitates in a WE54 sample peak-aged at 523 K (250°C) [139].

Precipitates in wrought Mg-RE alloys such as WE54 and WE43 have been extensively investigated [154, 157, 160, 161]. In comparison to the precipitates present in Mg-Al containing alloys such as AZ91, Mg-RE precipitates are more thermally stable and form on the prismatic planes of the Mg HCP crystal structure [139] (Figure 2.44). The evolution of

precipitates forming in a Mg-Gd-Zr alloy at an isothermal ageing temperature of 250°C starting with G-P zones and ending as stable β precipitates is shown schematically in Figure 2.45.

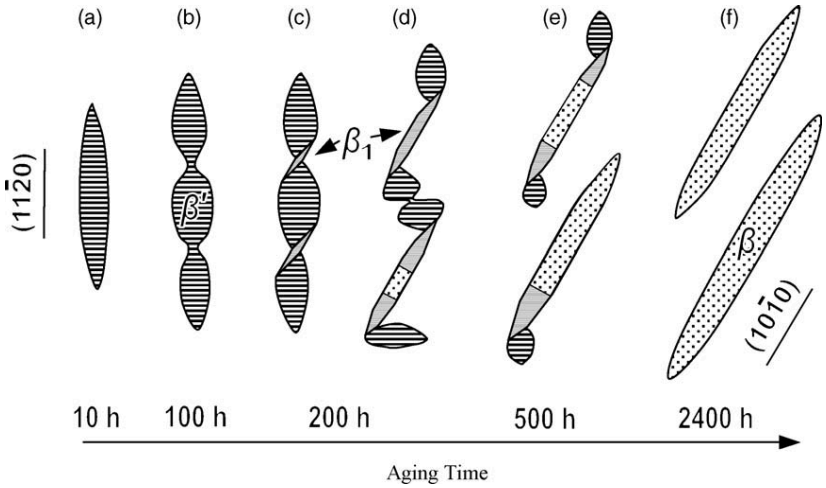

Figure 2.45: Schematic diagram showing the microstructural evolution from G-P zones to β′ then a combination of β′ and β_1 to the eventual formation of equilibrium β precipitates in Mg-15Gd-0.5Zr and Mg-10Gd-3Y-0.4Zr (wt.%) alloys at 250°C [162].

Improvements in creep properties in permanent mould cast Mg alloys have been observed following heat treatment to peak aged conditions [94, 163-165]. Precipitation of thermally stable solute and/or solid solution strengthening in Mg alloys has been attributed to the improvement of creep properties. Mg alloys are often aged to peak hardness and then crept in order to improve creep properties (Figure 2.46).

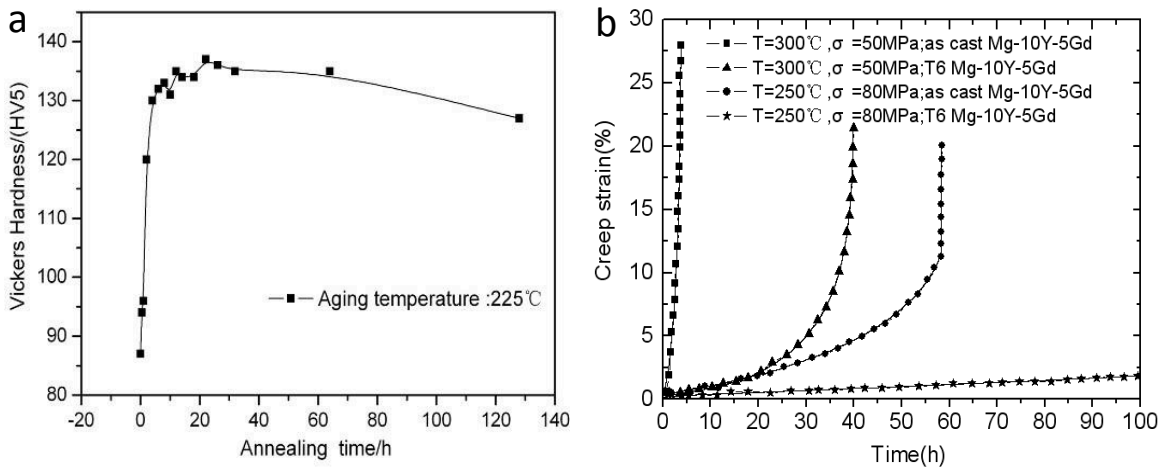

Figure 2.46: a) Age hardening response at 225°C for Mg-10Y-5Gd (wt.%) b) creep curves of Mg-10Y-5Gd alloys in as-cast and peak aged conditions tested at different temperatures and stress [163].

To a lesser extent, solution heat treatments have also been applied to Mg alloys including thixoformed AZ91 alloys [75] and permanent mould castings of AZ91D [102] in order to improve creep properties via solid solution strengthening. However, little research has been performed on the heat treatment of high-pressure die-cast (HPDC) alloys in particular HPDC Mg-alloys. HPDC alloys are usually not heat treated due to the presence of porosity throughout the casting, which may expand during heat treatment and cause damage to the casting.

Suzuki *et al.* [120] have shown that heat treatment may improve the creep properties of a Mg-Al-Ca HPDC alloy without surface blistering, however, this was at the comparatively low temperature of 250°C for 1h. Barbagallo *et al.* [166] had also shown that solution treatment of a HPDC AS21X (Mg-2.1Al-0.93Si-0.16Zn wt.%) at 415°C for durations of up to 48 h is possible without causing significant damage to the alloy. However, Barbagallo *et al.* [166] were more interested in the change in grain size during solution treatment thus nothing was mentioned on creep performance or anything specifically on the extent of blistering (if any) in the "skin" region of the alloys.

Gibson *et al.* [167] performed T6 solution treatment (solution treated at 525°C for 8h followed cold water quench, and then aged at 215°C for 4h) on two HPDC Mg-RE based alloys, Alloy A (Mg-0.10Nd-0.07Ce-0.06La-0.15Zn-0.14Y at.%) and Alloy B (Mg-0.09Nd-0.06Ce-0.06La-0.15Zn-0.05Y at.%). A comparison of the creep strain between the as-cast and T6 conditions is shown in Figure 2.47. It demonstrates that T6 has an influence on creep properties. However, it also demonstrated that the influence on creep of heat treatment is strongly dependent on alloying composition. In this case, Alloy B's creep resistance is more sensitive to heat treatment with respect to Alloy A.

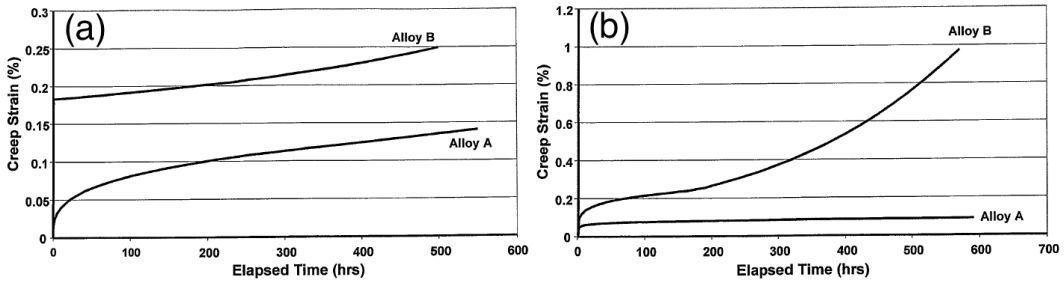

Figure 2.47: Creep curves for Alloy A and Alloy B for (a) as-cast and (b) T6 conditions tested at 177°C and 90MPa [167].

Gibson *et al.* [167] did not report on the condition of the HPDC sample surface (i.e. if blistering occurred). However, in subsequent personal correspondence with Dr. Gibson (February 2011) it was clarified that no significant blistering was detectable. Gavras *et al.* [168] showed that short-term solution treatments (1 h) at moderate temperatures (520°C) of HPDC Mg-2.70La-1.50Y wt.% (Mg-0.49La-0.42Y at.%) alloys caused no blistering damage to the surface to the alloy. The effects of hydrogen/gas porosity are not as severe for magnesium as they are for aluminium alloys [169, 170]. This may indicate that improvements to strength and creep resistance in Mg with sufficient RE alloying additions may be possible without causing blistering.

2.6 Summary

The review of the literature focused on creep properties of Mg alloys. Methods for improving the creep properties of Mg alloys were investigated. Particular attention was focussed on Mg-RE alloys due to their good elevated temperature creep properties. The castability of Mg-RE alloys was also investigated in order to ensure the viability of mass production and low cost which is required in the automotive industry**. In the current work an investigation on the castability of ternary HPDC Mg-La-RE alloys will be conducted since the addition of La to Mg improved castability as was indicated from previous Mg-La HTS results.** The ternary RE is of importance due to the poor elevated temperature creep resistance of Mg-La alloys

The literature review revealed that elevated temperature creep properties of Mg-alloys have been improved by a number of different methods. Key factors in the current literature, which will provide the guidance to the work undertaken in this thesis, are:

- grain boundary reinforcement
- precipitation hardening
- solid solution strengthening.

It was noted that there is still debate on the key creep mechanism and thus there is a variety of methods used to improve elevated temperature creep properties. More recently, less importance has been focussed on grain boundary strengthening for the improvement of creep properties in Mg alloys. However, it is still not clear whether one strengthening mechanism is more important than another or whether a combination of strengthening mechanisms is required. **It is therefore of great importance to determine what method or combination of methods improves the creep properties in HPDC Mg-RE alloys. In the current work the creep mechanism(s) of HPDC Mg-La-RE will be investigated.** This is achieved in the current work by primarily focusing on three groups of alloy concentrations:

1. Mg-La-RE alloys that are primarily strengthened by grain boundary reinforcement i.e. Mg-La-RE alloys with relatively low concentrations of ternary RE (approximately 0.1 at.%) but have the majority of the La addition present as intermetallic at grain boundaries due to the low solid solubility in Mg.
2. Mg-La-RE alloys with concentrations of ternary RE where the minimum creep rate of the alloy series is first reached (approximately 0.2 at.%).
3. Mg-La-RE alloys with sufficient ternary alloying addition for precipitation to occur at the creep testing temperature.

The literature has shown that different RE elements can have varying amounts of influence on creep properties in Mg-alloys. This is related to the solid solubility of the RE in Mg, the rate of solute diffusion in the matrix and also the concentration of RE. A

combination of various RE elements in Mg will thus be used to address the different creep strengthening methods in Mg such as:

- Nd, Y and Gd have significantly higher solid solubility in Mg compared with La and also have notably different solubility in Mg with respect to each other. The influence of different amounts of solid solution strengthening and in turn precipitation hardening can thus be determined by alloying this set of elements to a base Mg-La alloy.

Research into heat treatment of HPDC alloys has shown that it may be possible to improve tensile and creep properties without causing any damage to the casting. It is therefore important to determine if heat-treatment of HPDC Mg-RE alloys can be used to capitalise on the strengthening mechanisms such as solid solution strengthening or precipitation hardening. **Hence the project will focus on understanding the microstructural effects on the creep properties of Mg-La-RE alloys with RE elements that have relatively high but different solubility in Mg such as Nd, Y or Gd and also on the prospects of using heat treatment to further improve the properties.**

3 Experimental Procedures

3.1 Introduction 61

3.2 HPDC of Experimental Materials 62

3.3 Hot Tearing 64

3.4 Mechanical Testing 65
3.4.1 Hardness Testing 65
3.4.2 Heat Treatment 66
3.4.2.1 T4 (Solution treatment and water quenching) 66
3.4.2.2 T5 (Ageing and water quenching) 66
3.4.2.3 T6 (Solution treatment, water quenching and ageing) 67
3.4.3 Tensile Testing 67
3.4.4 Creep Testing 68

3.5 Microstructural Analysis 73
3.5.1 Scanning Electron Microscopy 74
3.5.2 Transmission Electron Microscopy 76

3.1 Introduction

There are two main points in this work: one is to identify the influence of different RE elements on the mechanical properties of HPDC Mg-La-RE alloys, and the second is to examine the effect of heat treatment on the mechanical properties of HPDC Mg-La-RE alloys. The following tests were conducted on the HPDC Mg-La-RE alloys:

- Heat treatment – to identify the feasibility of heat treating HPDC Mg-La-RE alloys and to determine if solid solution strengthening or solid solution strengthening and peak ageing would improve alloy properties.
- Hardness measurements – to determine peak ageing conditions and also to indicate the thermal stability of the alloying additions.
- Tensile and compression tests at room temperature and elevated temperature – to determine the influence of grain boundary reinforcement from eutectic or intermetallic on the strength of the alloys. This is also used to determine if the applied creep stress is above or below the yield strength of the alloy.
- Creep testing (in both tension and compression) – to compare the influence of different ternary RE additions and concentrations on creep properties and to assist with the identification of creep mechanisms.
- Microstructural characterisation using scanning electron microscopy (SEM), electron backscatter diffraction (EBSD), energy-dispersive x-ray spectroscopy (EDS) and transmission electron microscopy (TEM) – to help determine if there are any differences in grain boundary reinforcement, grain size, solute distribution or precipitate morphology following creep testing.

This is required in order to examine the changes to the as-cast condition (Chapter 4), following elevated temperature mechanical and creep testing (Chapter 5) and following heat treatment and mechanical and creep testing (Chapter 6).

3.2 HPDC of Experimental Materials

A series of ternary Mg-La-Nd, Mg-La-Y and Mg-La-Gd alloys were cast from commercially pure Mg and RE elements La, Nd, Y and Gd using a 250 tonne Toshiba cold chamber HPDC machine. The casting parameters are given in Table 3.1:

Table 3.1: Casting parameters for HPDC of alloys in this project.

Casting Parameter	Parameter Value
Melt temperature	740°C
Oil heaters in both halves of the die	250°C
Accumulator pressure	110 kg/cm^2
Ram velocities, slow speed	Approximately 0.36 ms^{-1}
Ram velocities, high speed	Approximately 2.2 ms^{-1}
Average die fill time	600 ms
Die open time	4 s

AM-cover (tetrafluoroethane 0.2wt.% and 99.8wt.% nitrogen gas) was used to protect the melt. The compositions of the alloys are measured using inductively coupled plasma atomic emission spectroscopy (ICP-AES) and shown in Table 3.2 (all compositions are given in at.% unless otherwise stated). All alloys used a La content close to 0.45 at.% in order to maintain similar amounts of intermetallic at grain boundaries and also to assist with castability. Nd, Y and Gd contents were chosen in order to investigate the influence of solid solution strengthening and also precipitation hardening of relatively soluble RE elements in Mg on creep and mechanical properties.

Table 3.2: Actual alloy compositions determined by inductively coupled plasma atomic emission spectroscopy (ICP-AES).

Alloy (at.%)	La (at.%)	Nd (at.%)	Y (at.%)	Gd (at.%)	Mg
Mg-0.46La-0.002Nd	0.456	0.002	-	-	Bal.
Mg-0.46La-0.02Nd	0.456	0.016	-	-	Bal.
Mg-0.45La-0.03Nd	0.451	0.031	-	-	Bal.
Mg-0.46La-0.06Nd	0.459	0.060	-	-	Bal.
Mg-0.47La-0.10Nd	0.469	0.104	-	-	Bal.
Mg-0.47La-0.14Nd	0.466	0.144	-	-	Bal.
Mg-0.43La-0.18Nd	0.430	0.175	-	-	Bal.
Mg-0.45La-0.63Nd	0.453	0.630	-	-	Bal.
Mg-0.49La-0.003Y	0.487	-	0.003	-	Bal.
Mg-0.49La-0.02Y	0.485	-	0.017	-	Bal.
Mg-0.48-0.05Y	0.477	-	0.045	-	Bal.
Mg-0.48-0.12Y	0.477	-	0.121	-	Bal.
Mg-0.49La-0.24Y	0.488	-	0.236	-	Bal.
Mg-0.49La-0.31Y	0.493	-	0.305	-	Bal.
Mg-0.49La-0.42Y	0.491	-	0.421	-	Bal.
Mg-0.44La-0.70Y	0.435	-	0.699	-	Bal.
Mg-0.45La-1.18	0.451	-	1.183	-	Bal.
Mg-0.48La-0.003Gd	0.480	-	-	0.003	Bal.
Mg-0.45La-0.01Gd	0.452	-	-	0.005	Bal.
Mg-0.45La-0.04Gd	0.453	-	-	0.041	Bal.
Mg-0.45La-0.10Gd	0.450	-	-	0.102	Bal.
Mg-0.46La-0.21Gd	0.463	-	-	0.214	Bal.
Mg-0.46La-0.60Gd	0.463	-	-	0.592	Bal.
Mg-0.45La-0.87Gd	0.449	-	-	0.872	Bal.

For each alloy, approximately 40 castings were made. Each casting consists of 2 round "dog-bone" shaped tensile bars and one flat tensile bar (Figure 3.1).

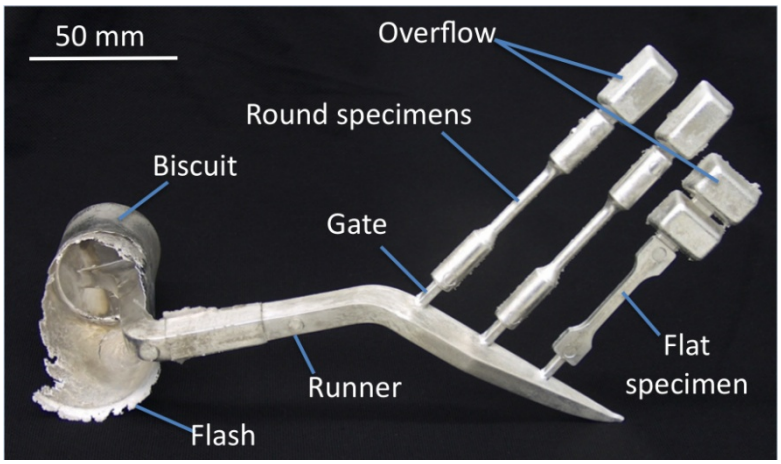

Figure 3.1 A HPDC casting showing two round and one flat tensile sample. [45].

Round “dog-bone” tensile bars have an average diameter of 5.64 mm in the gauge length section and flat “dog-bone” shaped tensile bars with a thickness of 3 mm were cast for the mechanical testing in this work (Figure 3.2).

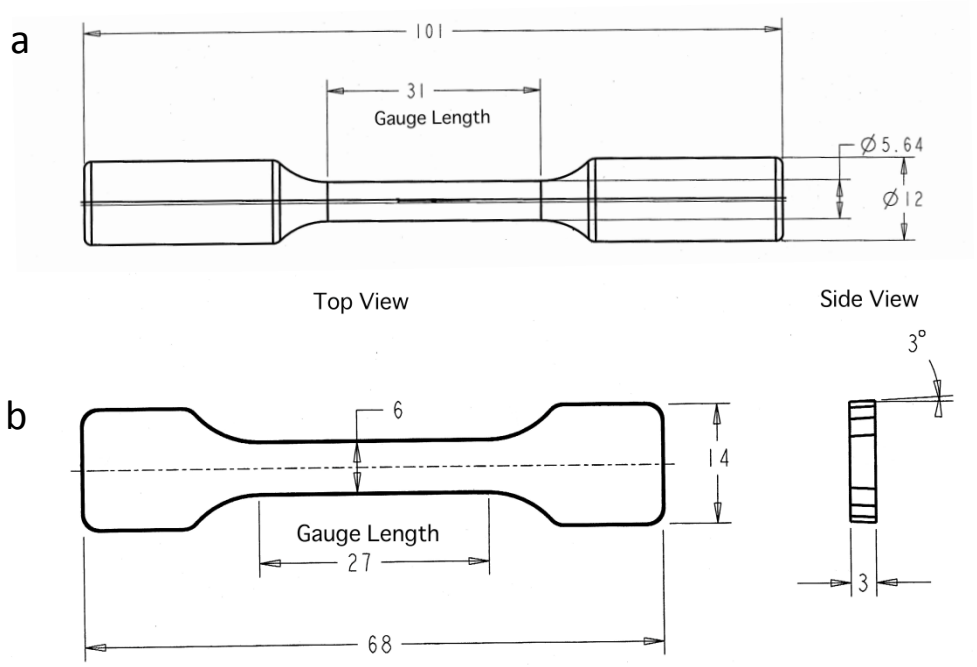

Figure 3.2: Schematic diagram of a) round and b) flat “dog-bone” shaped tensile bars used in this work. Note: Dimensions are in mm.

3.3 Hot Tearing

A visual inspection of the surface of flat tensile samples is used to provide the hot tearing criterion proposed by Easton *et al*. [171] (Figure 2.6). For convenience, the rating scale for the hot tearing index (HTI) that was used to assess the casting quality of a particular specimen is given below:

0 = No cracks/dimples in the specimen observed by the naked eye.

1 = Small observable dimple/s that require close examination to see.

2 = Dimple/s easily seen by the naked eye.

3 = Crack/s observed on the surface of the specimen, but the specimen remained intact.

4 = Specimen is fractured.

Whilst fine cracks were not able to be observed by the naked eye and cannot be identified by this evaluation, the test is able to select out alloys that have a high susceptibility to hot tearing and consequently decrease the amount of detailed metallography required. In most cases 25-30 samples were available for analysis, producing a statistically useful set of data. The hot tearing index is determined by the mean of the ratings given for each individual specimen of a particular alloy and the standard error was determined to give a measurement of the uncertainty.

Hot tearing is also predicted qualitatively using a hot tearing model based on the temperature-fraction solid behaviour, and the coherency and coalescence points of an alloy could be used to indicate hot tearing susceptibly (HTS) [171]. As the temperature-fraction solid curves for the alloys investigated are mathematically difficult to describe, the integral between the coherency and coalescence points is approximated using the trapezoidal method for area determination. Pandat™ software and a Mg-RE database developed by Gröbner *et al.* [132] are used to produce the temperature - fraction solid curves. Ternary phase diagrams for Mg-La-Y or Mg-La-Gd are not available and thus only the Mg-La-Nd system could be simulated. However, an indication of the HTS for Mg-La-Y and Mg-La-Gd alloys is obtained by using the predicted HTS of binary Mg-Y and Mg-Gd alloys.

3.4 Mechanical Testing

3.4.1 Hardness Testing

Vickers microhardness measurements on flat ‘dog bone’ shaped tensile bars are obtained using a Duramin A-300 hardness-testing machine with a 1 kg indentation. Interrupted age hardening tests are performed in silicon oil baths where the samples are removed at the appropriate measurement time and water quenched in room temperature water. Measurements are recorded after 1 h, 2h, 4h, 8h, 16h, 24h and then for twice the length of time as the previous ageing duration until peak hardness has been reached. A minimum of 5 indentations are made per sample in the as-cast condition and at each

ageing measurement. Each indentation is made a distance of at least two times the width of an indentation mark (approximately 0.5 mm) apart from each other in order to minimise the influence of neighbouring indentations on the hardness of the material.

3.4.2 Heat Treatment

3.4.2.1 T4 (Solution treatment and water quenching)

Solution treatments are performed at 520°C for 1 h immediately followed by room temperature water quenching for all the alloys tested in this work. The temperature is selected in order to allow for the solute in solid solution to be distributed homogeneously throughout the grains relatively quickly whilst minimising the possibility of melting the eutectic. Samples are completely buried in alumina powder and solution treated in a Tetlow furnace. The solution treatment temperature is monitored by a thermocouple built into the furnace and by a second thermocouple placed beside the samples being solution treated. Samples are immediately quenched in a large bucket filled with room temperature water after being removed from the furnace.

3.4.2.2 T5 (Ageing and water quenching)

The samples are aged in silicon oil baths without being covered and then quenched in a large bucket filled with room temperature water. The ageing temperatures are chosen to investigate the influence of relatively low (160°C) and relatively high (200°C) ageing temperatures on HPDC Mg-La-RE alloys. Ageing is also performed at a third, intermediate temperature (177°C) that is also the temperature used during creep testing (Table 3.3).

Table 3.3: T5 peak ageing heat treatment for the three alloy series investigated.

Alloy Series	Temperature	Duration (h)
Mg-La-Nd	160°C	20
	177°C	10
	200°C	1
Mg-La-Y	160°C	1000
	177°C	400
	200°C	200
Mg-La-Gd	160°C	1000
	177°C	400
	200°C	50

3.4.2.3 T6 (Solution treatment, water quenching and ageing)

T6 heat treatments are comprised of a combination of solution treatment in the Tetlow muffle furnace, room temperature water quenching and peak ageing in an oil bath. Once again, solution treatment is performed at 520°C for 1 h with the samples completely buried in alumina powder to protect them from oxidation. The samples are then quenched in room temperature water and then aged in oil baths at either 160°C, 177°C or 200°C until peak ageing conditions are reached followed by a final water quenching in room temperature water (Table 3.4).

Table 3.4: T6 heat treatment for the three alloy series investigated

Alloy Series	Solution Treatment	Peak Ageing Temperature
Mg-La-Nd	520°C/1 h	160°C/ 100 h
	520°C/1 h	177°C/ 16 h
Mg-La-Y	520°C/1 h	160°C/ 1700 h
	520°C/1 h	177°C/ 4000 h
Mg-La-Gd	520°C/1 h	160°C/ 1100 h
	520°C/1 h	177°C/ 400 h

3.4.3 Tensile Testing

Tensile tests are conducted on as-cast round "dumb-bell" specimens at room temperature and 177°C (creep testing temperature) using a screw-driven Instron 4505 with a 100kN load cell. The round specimens are chosen for testing since they are also used for creep testing. For both room temperature and 177°C tensile tests, a cross-head speed of 5mm/min and an extensometer gauge length of 25mm are used. An Instron 2630-106 extensometer is used to record the extension of the specimens during tensile tests. Round tensile samples are secured in tensile clamps and a preload of 20 N is applied to ensure any slack in the clamps is removed. Four samples are tested for each tensile testing condition and an average of these results are used to determine the key parameters such as 0.2% proof stress (0.2% PS), ultimate tensile strength (UTS) and elongation to fracture.

An environmental chamber is used in order to perform tensile tests at 177°C. For elevated temperature testing, samples are placed into the tensile clamps once the environmental chamber has reached the testing temperature. A thermocouple placed at one of the tensile grips is used to monitor the temperature. Once the sample is placed in the grips it is held for approximately 5 minutes for the sample to reach the testing temperature. A preload of 50 N is then applied to remove any slack from the clamps before tensile testing begins.

3.4.4 Creep Testing

Constant load tensile creep tests are performed on as-cast and heat treated Mg-La-Nd, Mg-La-Y and Mg-La-Gd alloys predominately at 177°C and 90 MPa. However, some tests are also performed at lower and higher stresses. A list of all the testing conditions can be found in Table 3.5. A minimum of two samples are tested for each alloy and testing conditions.

Table 3.5: Test conditions for each alloy that are tensile creep tested. Note * indicates tests performed by Dr. Mark Gibson at CSIRO.

Composition (at.%)	Testing Conditions		Alloy Conditions
	Temp (°C)	Stress (MPa)	
Mg-0.46La-0.002Nd	177	90	As-Cast
Mg-0.46La-0.02Nd	177	90	As-Cast
Mg-0.45La-0.03Nd	177	90	As-Cast
Mg-0.46La-0.06Nd	177	90	As-Cast
Mg-0.47La-0.10Nd	177	90	As-Cast
	177	90	T4 (520C/1h)
	177	90	T6 (520C/1h and 177C/16h)
Mg-0.47La-0.14Nd	177	90	As-Cast
Mg-0.43La-0.18Nd	177	90	As-Cast
	177	90	T4 (520C/1h)
	177	90	T6 (520C/1h and 177C/16h)
Mg-0.45La-0.63Nd	177	70	As-Cast
	177	90	As-Cast
	177	110	As-Cast
	177	90	T4 (520C/1h)
	177	90	T6 (520C/1h and 177C/16h)

Table 3.5 cont.

Composition (at.%)	Testing Conditions		Alloy Conditions
	Temp (°C)	Stress (MPa)	
Mg-0.49La-0.003Y	177	90	As-Cast*
Mg-0.49La-0.02Y	177	90	As-Cast*
Mg-0.48La-0.04Y	177	90	As-Cast*
Mg-0.48La-0.12Y	177	90	As-Cast
	177	90	T4 (520C/1h)
	177	90	T6 (520C/1h and 160C/1700h)
Mg-0.49La-0.24Y	177	90	As-Cast
	177	90	T4 (520C/1h)
	177	90	T6 (520C/1h and 160C/1700h)
Mg-0.49La-0.30Y	177	90	As-Cast
Mg-0.49La-0.42Y	177	90	As-Cast
Mg-0.43La-0.70Y	177	90	As-Cast
Mg-0.45La-1.18Y	177	90	As-Cast
	177	110	As-Cast
	177	90	T4 (520C/1h)
	177	90	T6 (520C/1h and 160C/1700h)
Mg-0.48La-0.003Gd	177	90	As-Cast*
Mg-0.45La-0.005Gd	177	90	As-Cast*
Mg-0.45La-0.04Gd	177	90	As-Cast*
Mg-0.45La-0.10Gd	177	90	As-Cast
	177	90	T4 (520C/1h)
	177	90	T6 (520C/1h and 177C/400h)
Mg-0.46La-0.21Gd	177	90	As-Cast
	177	90	T4 (520C/1h)
	177	90	T6 (520C/1h and 177C/400h)
Mg-0.46La-0.59Gd	177	90	As-Cast
	177	110	As-Cast
	177	90	T6 (520C/1h and 160C/1700h)
Mg-0.45La-0.87Gd	177	90	As-Cast
	177	90	T4 (520C/1h)
	177	90	T6 (520C/1h and 177C/400h)

Creep tests are performed in purpose built constant load tensile creep testing rigs. The key components of the rigs are a silicon oil bath, which can be raised to envelop the test specimens in the specimen holders, which are connected to arms, to which weight is applied to produce the required stress for the test (Figure 3.3).

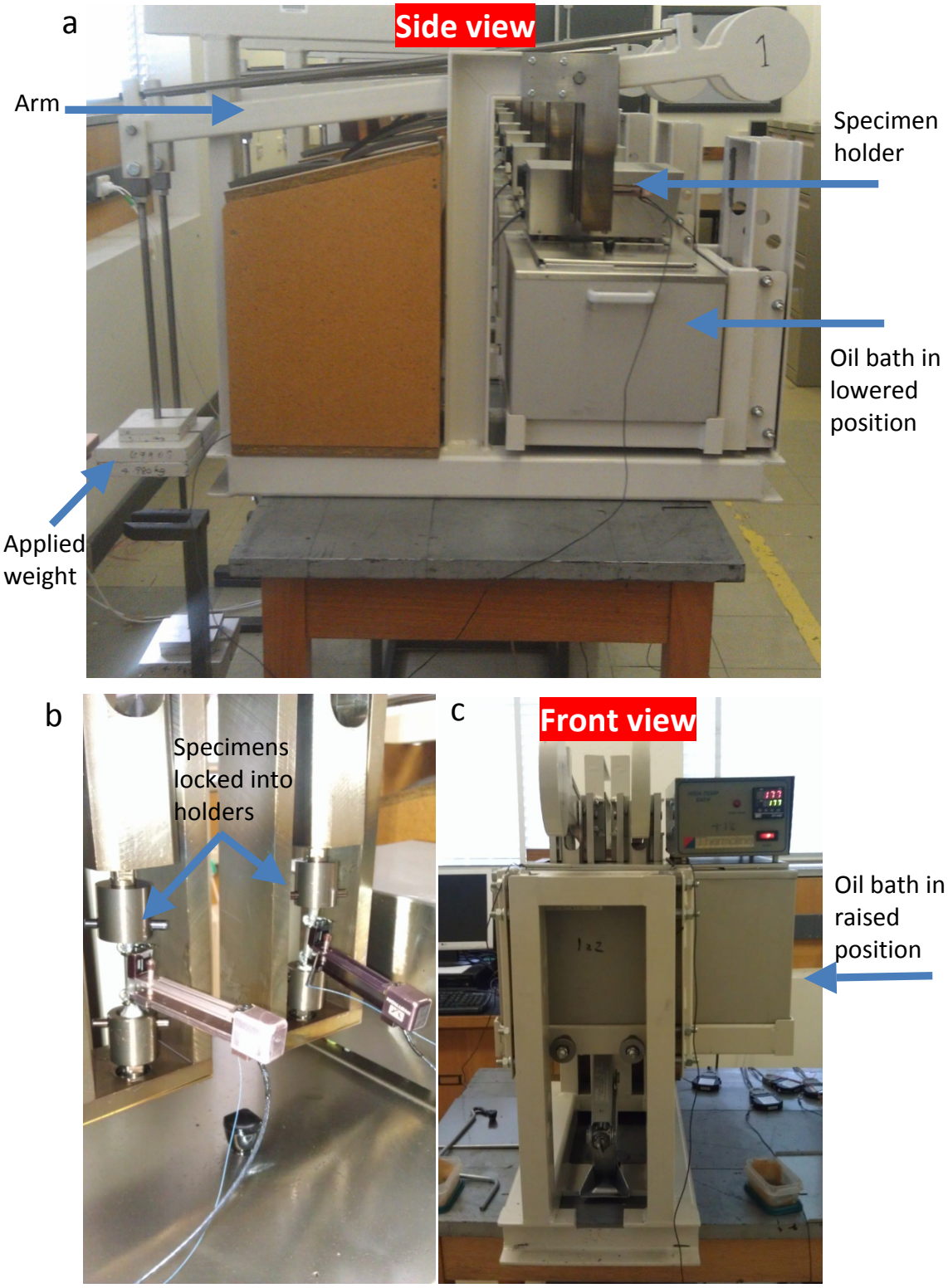

Figure 3.3: a) Side view of the creep rig, b) samples locked into the holders, c) oil bath in raised position, completely immersing the creep samples in silicon oil which is at the testing temperature of 177°C.

Two samples can be tested per creep rig (Figure 3.3). Round tensile sample required approximately 10mm to be cut off from the top and bottom ends of the grip ends of the

castings and holes drilled into the grip ends to allow the samples to be locked into the creep rig "arms" (Figure 3.3b). Round tensile samples with an Instron extensometer attached to every sample are used for creep testing (Figure 3.4). The extensometer is connected to a data logger which then displays the extension measurements on a computer using the software DeLogger produced by dataTaker®.

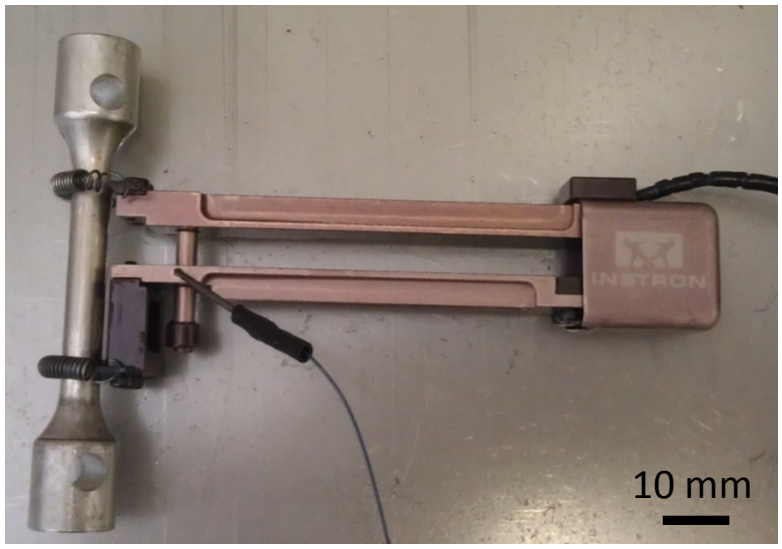

Figure 3.4: Photo of Mg-0.45La-1.18Y in as-cast condition cut and drilled for creep testing with an Instron extensometer attached to it.

An oil bath filled with silicon oil is preheated to the appropriate testing temperature (177°C). An oil bath is used to help maintain an accurate temperature on the samples tested. Once the temperature is reached the oil bath is raised to completely cover the samples (Figure 3.3c). There is a drop in temperature of the silicon oil after the bath is raised. Testing begins once the temperature of the oil reaches 177°C again, this takes between 5 to 10 minutes. Weights are added to the rear end of the testing arm to apply the required testing stress.

Upon applying the load, measurements are recorded initially every 10 seconds. This is done to ensure an accurate measurement of the initial stages of creep. Once the strain experienced by the initial application of the load stabilises (after approximately 10 minutes) i.e. extensometer measurements do not change significantly, the measurement duration is changed to once every 15 minutes. Measurements over this interval are maintained until the sample fails or the duration of the experiment reaches 600 h.

In order to perform creep tests at higher temperatures and stresses an alternative creep-testing device was required. This was necessary since the tensile creep rigs and extensometers at Monash University (Figure 3.3) have a maximum practical testing temperature of 200°C and stress of 110 MPa. At higher temperatures or stresses damage could occur to the extensometer or creep arm, respectively. Applied Test System (ATS) (model number 2330) lever arm compression creep testing machines at the Helmholtz Zentrum in Geesthacht (HZG), Germany were used to perform creep tests at higher temperatures and stresses under the supervision of Dr. Hajo Dieringa (Figure 3.5).

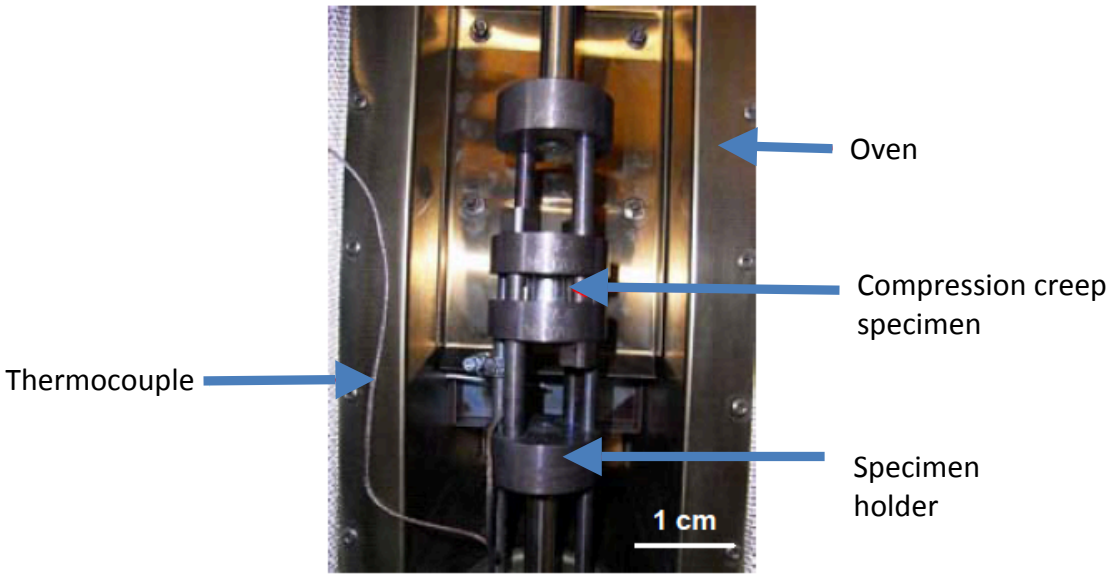

Figure 3.5: Photo of an ATS compression creep machine showing the components of the rig inside the oven [172].

Specimens that are 15mm long are cut from the gauge length of round tensile samples. It is critical that the top and bottom edges of the sample are parallel for accurate compression measurements. Some light polishing using 2500 grit silicon carbide paper is used to ensure that the top and bottom surfaces of the sample that mate with the compression platens are flat. A minimum of 2 specimens are compressed for each alloy condition.

Constant temperatures and constant stresses are selected in order to be able to determine the stress exponent of creep (n) and the activation energy (Q) (Table 3.6).

Table 3.6: Test conditions for each alloy that was compression creep tested.

Alloy (at.%)	Temperature (°C)	Stress (MPa)
Mg-0.45La-0.63Nd	177	30
		90
	225	90
	275	30
		50
		90
Mg-0.45La-1.18Y	177	90
		130
		150
	225	90
	275	90
		130

Creep strain is recorded as a function of testing time and plotted using Origin® 8.1 software. The creep strain data is differentiated over time using Origin® in order to determine the creep rate of the alloys tested for both tension and compression creep tests.

3.5 Microstructural Analysis

Electron microscopes are used to examine the alloys in the as-cast condition as well as following creep testing in the as-cast and heat treated conditions. This includes the examination of:

- Pores present at the surface or “skin” region of the specimen (SEM).
- Characterisation of the eutectic at grain boundaries (SEM).
- Confirmation of intermetallic phase present in the eutectic (EBSD).
- Average grain size determination (EBSD).
- Investigation of static or dynamic precipitates in the α-Mg phase (TEM).
- Characterisation of the distribution of solute in solid solution from the grain boundary to the “core” of a grain (EDS on TEM).

3.5.1 Scanning Electron Microscopy

Samples are cut from the gauge length of round tensile specimens using a Buehler Isomet slow speed saw. Typically the specimen would be approximately 10 mm long. Metallographic preparation consists of grinding the specimen using silicon carbide paper with successively finer grit finishing at 2500 grit paper. Polishing then continues with 3 μm and then finally 1 μm diamond suspension solution on a neoprene polishing pad.

A JEOL JSM 7001F field emission SEM (Figure 3.7a), equipped with an EBSD detector is used to investigate the microstructure of the metallographically prepared specimens. Back scattered electron (BSE) mode with an accelerating voltage of 15 kV and a working distance of 10 mm is used to image the specimens. Volume fraction analysis of the eutectic in a specimen is determined using the image analysis with ImageJ software. The original micrographs are colour inverted and the threshold/contrast is adjusted to produce a high contrast between the eutectic regions of the sample and the matrix. Using the ImageJ “measure” option, the amount of black and white (i.e. eutectic and matrix) in the image is measured. A minimum of 5 high contrast BSE SEM images from the “core” region of each specimen are used to calculate the average volume fraction of eutectic.

Specimens approximately 100 μm thick are used for both grain size determination and phase confirmation by EBSD. The specimens are prepared similarly to TEM foils (described in 3.5.2). Relatively thin slices (approximately 400 μm) are cut from a round tensile specimen using a Buehler IsoMet low speed saw, punched into 3 mm diameter discs and polished to approximately 100 μm using 2500 grit silicon carbide paper. The specimen is then ion milled for 1 hour using a Gatan 691 Precision Ion Polishing System (PIPS) with an ion gun angle of 4° and current of 5 keV. The PIPS process is excellent in removing the strain layer in the surface of the specimen that is introduced during mechanical polishing which can cause poor results [173, 174].

EBSD is used in order to confirm the identity of the intermetallic phase present in the alloys. The sample (and sample stage) is tilted to 70° at a working distance of 15 mm inside the SEM column and the accelerating voltage of 15 kV. Only Kikuchi patterns obtained from EBSD with a mean angular deviation (MAD) value of less than 0.5° (ideal MAD for accurate phase confirmation) are considered for phase identification (Figure 3.6a). Kikuchi maps with poor MAD values (approximately 1° or greater) have poorly defined Kikuchi patterns, which cause incorrect phase identifications (Figure 3.6b).

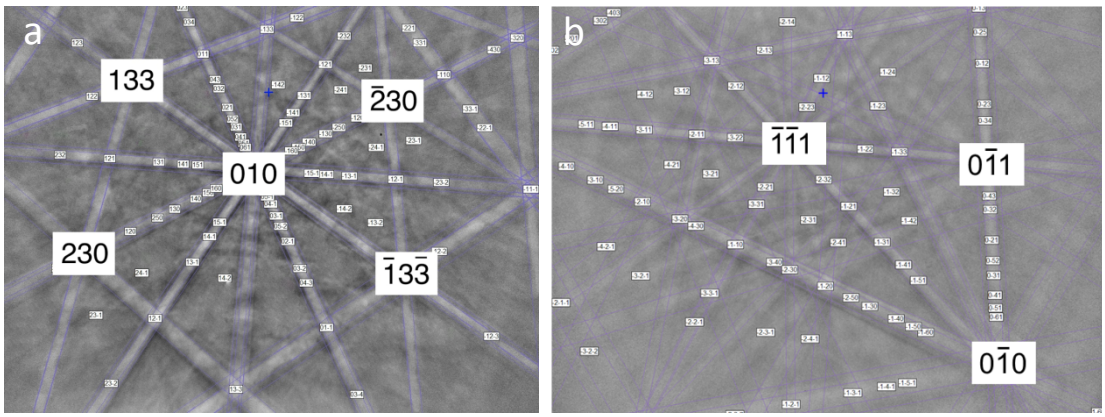

Figure 3.6: Kikuchi map overlaid with identification lines from EBSD phase identification for Mg-0.49La-0.24Y for a map with an MAD of a) less than 0.5° and b) of approximately 1°.

Average grain size measurements in the "core" and "skin" regions of round tensile samples are obtained from EBSD maps using Aztec software and the data is processed using HKL Channel5 software. The EBSD maps are noise reduced in HKL's Tango software using "standard noise reduction" where unindexable points are corrected if they had 4 neighbouring points that were indexable. A step size of 0.5 μm is used and a magnification was chosen to allow at least 100 grains to be present within the EBSD scanning window. A minimum of 5 EBSD maps are used per alloy and the average grain size is determined from a combination of all the maps.

Qualitative measurements of the concentration of alloying additions present in the eutectic are recorded from energy-dispersive x-ray spectroscopy (EDS) using a FEI Quanta 3D FEG FIB (Figure 3.7b). An accelerating voltage of 15kV at a working distance of 10mm is used for each point scan. A single point measurement is recorded for a local region

containing the eutectic and also per cell in a grain. A minimum of 15 EDS point measurements are made per specimen and per region i.e. eutectic or α-Mg matrix.

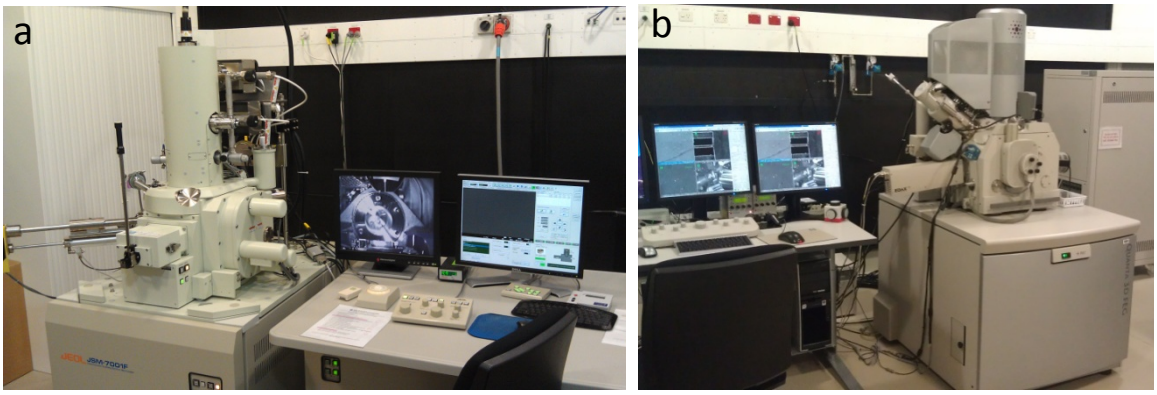

Figure 3.7: Scanning electron microscopes used in the current studies a) JEOL JSM 7001F field emission scanning electron microscope and b) FEI Quanta 3D FEG FIB.

3.5.2 Transmission Electron Microscopy

All specimens used for transmission electron microscopy (TEM) are cut into 0.3 mm thick slices using a Buehler IsoMet low speed saw from round tensile samples. The slices are then cut into 3 mm diameter discs using a Gatan precision 3 mm punch. The 3 mm discs are polished using 2500 grit silicon carbide paper to a thickness of approximately 60 μm. The foil is then ion milled using PIPS with ion guns tilted to 4° at 5 keV until a hole with sufficient electron transparent area around the edge of hole is formed. The angle of the ion guns is reduced to 2° and the electron voltage reduced to 2.5 keV for 30 minutes.

A FEI Tecnai G2 T20 TWIN LaB6 TEM (Figure 3.8a) is used for the majority of the TEM microscopy in this work. However, a Philips CM20 TEM (Figure 3.8b) was also used for some of the work in this thesis. An operating voltage of 200 kV is used for all TEM observations. TEM was primarily used to determine any changes in the microstructure of specimens from their as-cast condition to their post-crept condition. This includes bright field (BF) multi-beam imaging, using a 20 μm objective aperture, to observe the presence of any precipitates formed before creep testing during the ageing (static precipitates) or during creep testing (dynamic precipitates). A selected area aperture of 10 μm is used for selected area electron diffraction (SAED) to determine the orientation of the grain under

investigation and to identify precipitate phases. A double tilt holder with an allowable α tilt range of ±50° and β of ± 25° is used. SAED diffraction patterns are recorded onto a Gatan SC200D Orius CCD camera (2k x 2k) and micrographs are recorded using a Gatan 831 SC600 Orius CCD camera (2.7k x 2.7k).

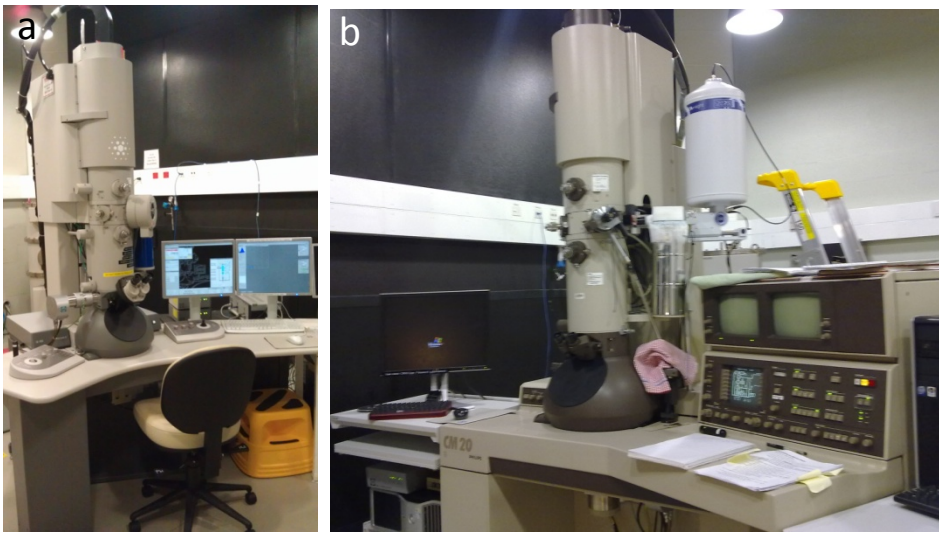

Figure 3.8 Transmission electron microscopes used in this work a) FEI Tecnai G2 T20 TWIN LaB6 TEM, and b) Philips CM20.

Table 3.7 summaries the techniques used in the respective chapters of the present work.

Table 3.7: Summary of the techniques used and their application in the results chapters (Chapters 4 – 6).

	Chapter 4	Chapter 5	Chapter 6
Hardness Measurement		Identify the influence of different ternary RE additions on precipitation hardening.	Age hardness testing of solution treated alloys to determine if increases in the concentration of solute in solid solution improve the ageing response of the alloys.
Scanning Electron Microscopy	Morphology characterisation and eutectic volume fraction measurements.		Surface characterisation of the alloys following heat treatment and also characterisation of the morphology change of the alloys compared to the as-cast condition.
Transmission Electron Microscopy	EDS line scan to identify the inhomogeneous distribution of solute in solid solution.	BSE micrographs and SAED are used to characterise the microstructure of the alloys following creep testing.	BSE and SAED are used to help characterise changes in precipitate formation in comparison to the as-cast condition of T4 and T6 alloys following creep testing.
Castability	Hot tearing index determination		
Microstructure Simulation using Pandat™	Intermetallic volume fraction predictions using Mg-La-Nd ternary phase diagram information in Pandat™		
Tensile Testing		Room and elevated temperature tensile testing to determine the effects of varying concentrations of ternary RE and varying ternary RE elements on tensile properties.	Testing of T4 and T6 alloys at room temperature and 177°C to see if solid solution strengthening or precipitation hardening improves as-cast tensile properties.
Creep Testing		Determine how varying ternary RE additions and concentrations of RE influence elevated temperature creep properties of as-cast HPDC Mg-La-RE alloys. Compressive creep tests are performed to indicate creep mechanisms.	Testing of T4 and T6 alloys is also performed to help to determine if solid solution strengthening or precipitation hardening improves the as-cast tensile properties of the alloys.

4 As-Cast Microstructure and Castability of Mg-La-RE Alloys

4.1 Introduction 80

4.2 Experimental Results on Microstructure 80
4.2.1 Microstructure of As-Cast Mg-La-RE Alloys 80
4.2.2 Eutectic and Intermetallic Characterisation 82

4.3 Castability 88

4.4 Discussion 90
4.4.1 Effects of alloying elements on microstructure 90
4.4.2 Modelling the castability of alloys with different alloying elements 92

4.5 Conclusions 99

4.1 Introduction

In this chapter the microstructure, castability and mechanical properties of three Mg-La-RE alloy series, namely Mg-La-Nd, Mg-La-Y and Mg-La-Gd are investigated. The focus here is to identify what influence different ternary RE elements have on microstructure and castability at room temperature for alloys in the as-cast condition. The influence of varying the concentration of the ternary alloying addition is also investigated. The morphology of the eutectic present at grain boundaries is presented and the effect of different concentrations of ternary RE on the morphology is shown. The Scheil-Gulliver equation is used to produce the temperature-fraction solid curves for the alloys. This information is then used as input parameters into a simple model that predicts hot tearing susceptibility. An attempt to relate castability with microstructure is also made.

4.2 Experimental Results on Microstructure

4.2.1 Microstructure of As-Cast Mg-La-RE Alloys

The microstructure of all the alloys investigated consists of an α-Mg matrix with a dendritic morphology and a eutectic composed of α-Mg and a La-rich intermetallic, formed at the grain/cell boundaries (Figure 4.1). The eutectic creates a skeleton-like structure that is present throughout the alloy. Gas pores formed during solidification are also detected in the microstructure.

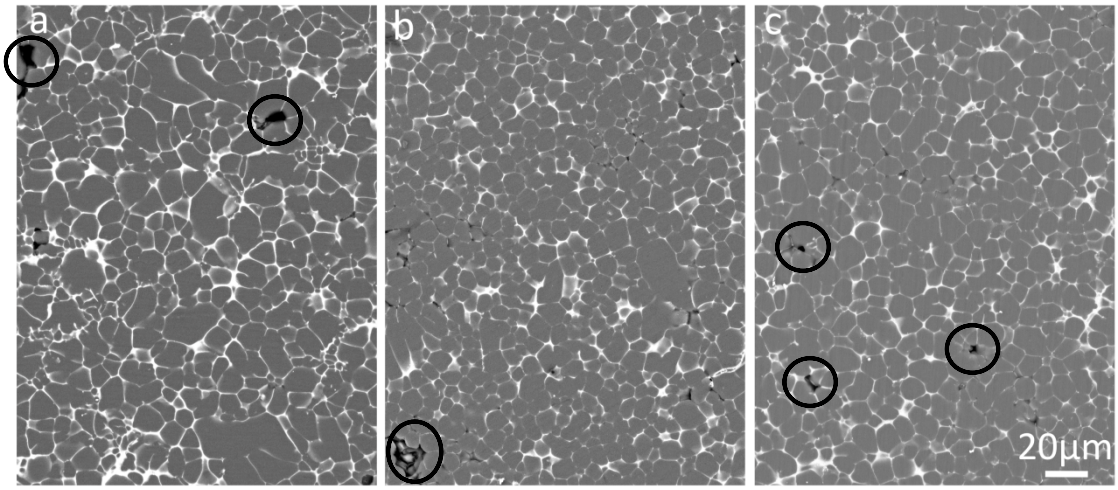

Figure 4.1: SEM BSE micrographs of the dendritic morphology of the "core" region of Mg-0.43La-0.18Nd, Mg-0.49La-0.24Y and Mg-0.46La-0.21Gd (at.%) are shown in images a), b) and c) respectively. The brighter feature in the microstructure is the eutectic and the darker grey feature is the α-Mg matrix. Gas pores (dark/black features) are circled.

The average grain size of grains near the "core" region of a round tensile sample is determined by EBSD (Figure 4.2) to be approximately 9-10 µm for each of the alloy series (Table 4.1). However, the few externally solidified grains [175], present in the "core" region of the samples, can be as large as 20 - 30 µm. Grains present near the surface or "skin" region of the castings are smaller (approximately 6 µm) as solidification is more rapid near the mould wall [25] (Figure 4.3).

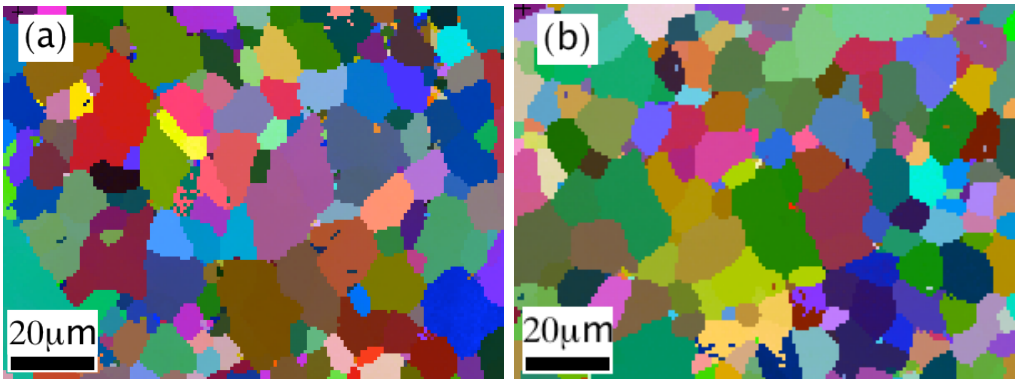

Figure 4.2: EBSD maps showing grains in (a) Mg-0.45La-1.18Y and (b) Mg-0.45La-0.63Nd alloys in the as-cast condition [130].

Table 4.1: Average grain sizes in "core" and "skin" regions for Mg-La-RE alloys.

Alloy Composition, at.%	Average Grain Size at "Core", μm (±SD)	Average Grain Size at "Skin", μm (±SD)
Mg-0.47La-0.10Nd	9.9 (± 1.0)	
Mg-0.43La-0.18Nd	9.1 (± 0.5)	5.8 (± 0.4)
Mg-0.45La-0.63Nd	9.4 (± 0.8)	
Mg-0.48La-0.12Y	10.0 (± 1.1)	
Mg-0.49La-0.24Y	9.8 (± 1.1)	6.1 (± 0.3)
Mg-0.45La-1.18Y	8.5 (± 0.6)	
Mg-0.45La-0.10Gd	9.9 (± 1.2)	
Mg-0.46La-0.21Gd	9.0 (± 1.1)	7.0 (± 0.1)
Mg-0.45La-0.87Gd	9.0 (± 0.5)	

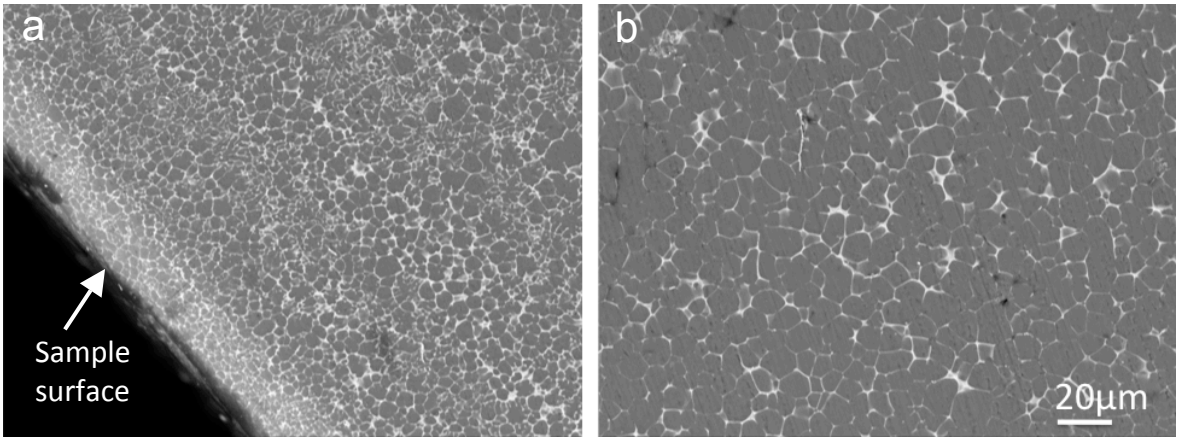

Figure 4.3: SEM BSE micrographs of a) "skin" region and b) "core" region of Mg-0.49La-0.24Y.

4.2.2 Eutectic and Intermetallic Characterisation

The volume fraction of eutectic was determined from BSE micrographs of Mg-La-RE alloys (Figure 4.4). The BSE micrographs were converted into high contrast images in order to help determine the amount of α-Mg and eutectic present in the image using image analysis software (ImageJ). A minimum of four high contrast images are obtained for each alloy under investigation in this chapter and an example of this shown in Figure 4.4.

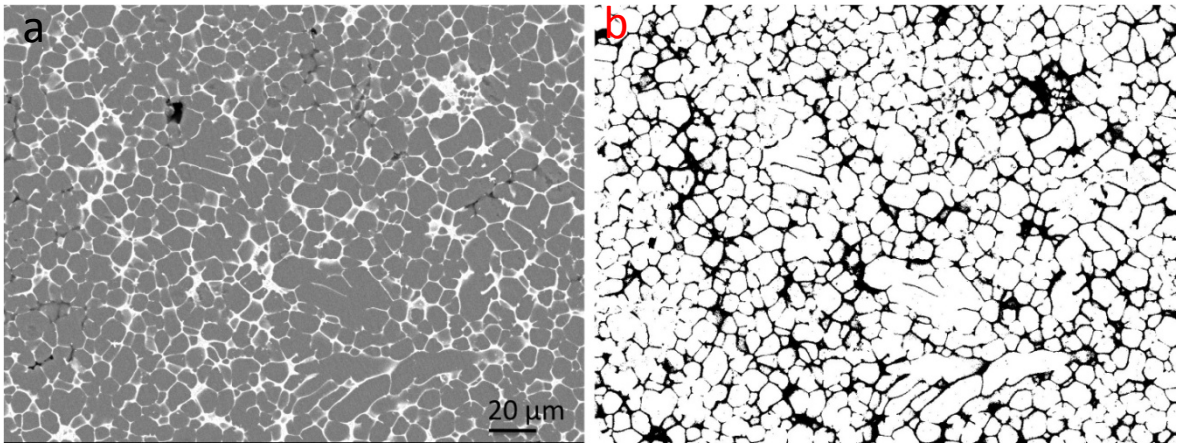

Figure 4.4: An example SEM BSE micrograph used to determine the amount of eutectic present in an alloy of as-cast Mg-0.45La-0.63Nd a) original image from SEM and b) inverted high contrast image to isolate eutectic.

The average volume fraction of eutectic is determined for the alloys within each series and is compared to a binary Mg-La alloy from BSE micrograph analysis (Table 4.2). The eutectic volume fraction for the binary Mg-0.46La alloy is determined to be approximately 14% and the volume fraction of eutectic is observed to increase with ternary alloying content.

Table 4.2: Average volume fraction of eutectic for Mg-La-Nd, Mg-La-Y and Mg-La-Gd with similar concentrations of La but with varying concentrations of ternary RE. The average volume fraction of binary Mg-0.46La is also included for comparison.

Alloy Composition, at.%	Eutectic Volume Fraction, % (±SD)
Mg-0.46La	14.1 (± 1.0)
Mg-0.47La-0.10Nd	16.7 (± 1.5)
Mg-0.43La-0.18Nd	18.9 (± 1.3)
Mg-0.45La-0.63Nd	24.7 (± 1.1)
Mg-0.48La-0.12Y	18.3 (± 1.6)
Mg-0.49La-0.24Y	18.1 (± 0.8)
Mg-0.45La-1.18Y	26.4 (± 1.1)
Mg-0.45La-0.10Gd	17.3 (± 1.5)
Mg-0.46La-0.21Gd	18.0 (± 0.6)
Mg-0.45La-0.87Gd	31.8 (± 2.0)

The morphology of the eutectic phase changes relative to ternary alloying addition (Figure 4.5, a micrograph of the binary Mg-0.46La alloy is also shown for comparison). For relatively low concentrations of Nd, Y or Gd (approximately 0.2 at.%) the eutectic has a well-defined lamellar morphology similar to the binary Mg-0.46La alloy [18]. When the concentration of the ternary addition is increased (greater than 0.2 at.%) the eutectic becomes less lamellar and increasingly more divorced. This is less evident in the alloy containing Nd, which has a more complex regular morphology as the proportion of continuous intermetallic phase in the eutectic increases.

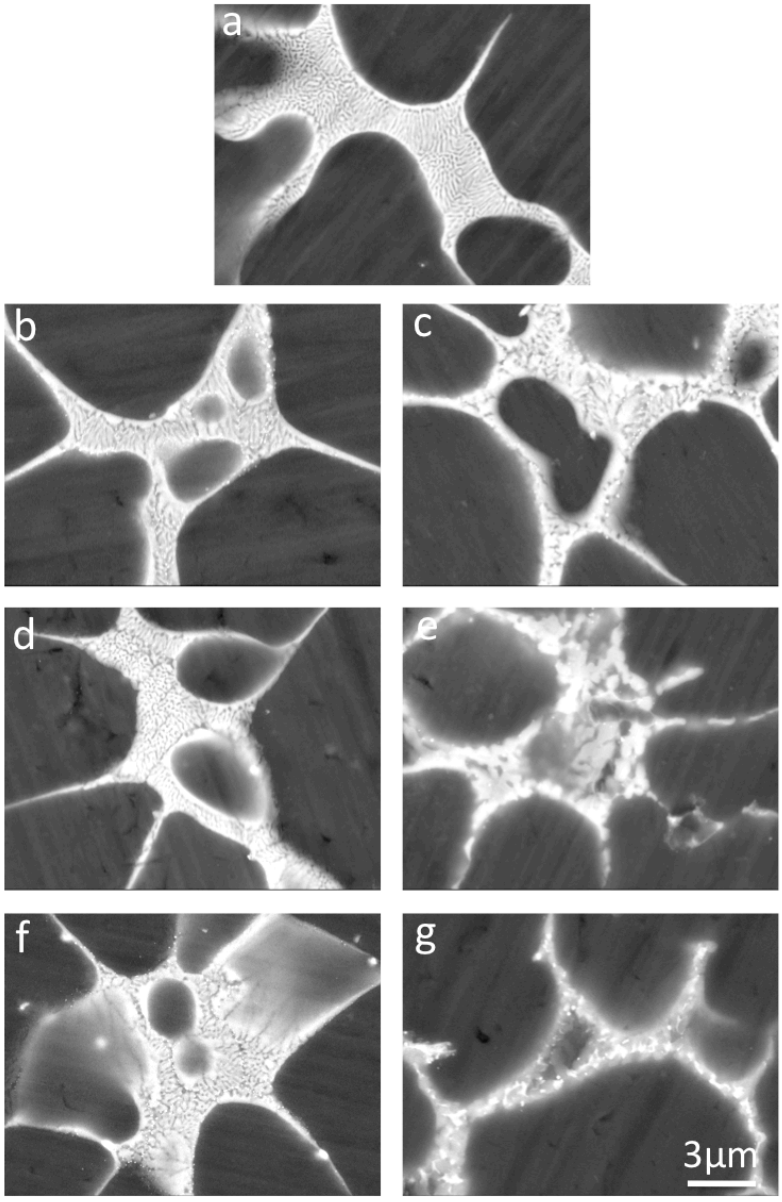

Figure 4.5: SEM BSE micrographs showing eutectic morphologies in a) Mg-0.46La, b) Mg-0.43La-0.18Nd, c) Mg-0.45La-0.63Nd, d) Mg-0.49La-0.24Y, e) Mg-0.45La-1.18Y, f) Mg-0.46La-0.21Gd and g) Mg-0.45La-0.87Gd alloys.

Using EDS the atomic ratio of the ternary alloying element to La in the eutectic, the intermetallic phase present in the eutectic is found to increase with the total increase of ternary alloying addition (Figure 4.6). The ratio of Nd to La in the eutectic is higher than either the ratio of Y to La or Gd to La i.e. more Nd is present in the eutectic in comparison to Y or Gd at similar concentrations. In an attempt to simulate the microstructure, the temperature - fraction solid curves of Mg-La-Nd alloys are determined using the non-equilibrium solidification setting in Pandat^{TM}. The ternary phase diagram database for Mg-La-Nd was obtained from Gröbner *et al.* [132]. From the fraction solid curves, the temperature at which the eutectic begins to solidify and also at which is it completely solid are determined. Using the equivalent of the lever rule for ternary phase diagrams or alternatively the point calculation feature in Pandat^{TM}, the concentrations of La and Nd in the eutectic at these temperatures can be determined. The ratio of ternary RE to La is then plotted and compared with the experimentally determined ratios (Figure 4.6). A lower bound (lower dashed curve in Figure 4.6) to the predicted Nd to La ratio is calculated by using the concentrations of Nd and La that are predicted to be present as the eutectic begins to form (this is obtained from the temperature - fraction solid curves for each Mg-La-Nd alloy). The upper bound (top dashed curve in Figure 4.6) for the predicted Nd to La ratio is calculated in the same way but with the use of the concentrations of Nd and La in the eutectic following complete solidification. However, the predicted values underestimate the values determined by EDS. It is interesting to note that there appears to be a slightly greater amount of Gd in the eutectic than Y. The opposite result would have been expected due to the lower solid solubility of Y in Mg in comparison to Gd in Mg (3.60 at.% and 4.53 at.% for Y or Gd in Mg respectively) [131].

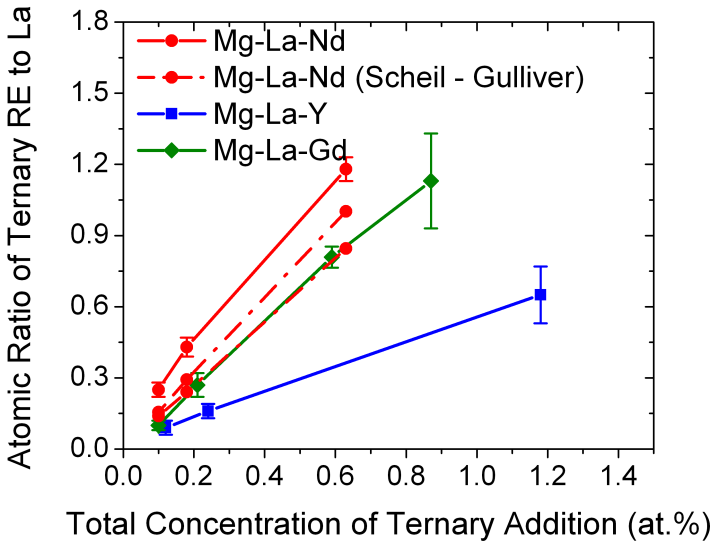

Figure 4.6: Atomic ratio of total ternary alloying addition to La present in the eutectic for alloys with relatively low, medium and high concentrations of Nd, Y or Gd determined from EDS and predicted from the Scheil-Gulliver equation. The dashed lines indicate upper and lower bounds of the predicted Nd to La ratio predicted by the Scheil-Gulliver equation.

The $Mg_{12}RE$ phase is the most commonly found intermetallic phase in the as-solidified microstructure of Mg-La, Mg-Ce or Mg-Nd alloys [16, 132] due to its combination of a relatively low barrier to nucleation and relative thermodynamic stability [176]. Kikuchi maps taken from the intermetallic phase in Mg-La-Nd, Mg-La-Y and Mg-La-Gd alloys obtained using EBSD are used to confirm the phase identity of the intermetallic to be $Mg_{12}RE$. Figure 4.7 shows the Kikuchi maps from the intermetallic present in Mg-0.45La-0.63Nd, Mg-0.45La-1.18Y and Mg-0.45La-0.87Gd with the $Mg_{12}RE$ Kikuchi map outlines overlaid on top indicating a close correlation between the two (mean angular deviation (MAD) < 0.5°).

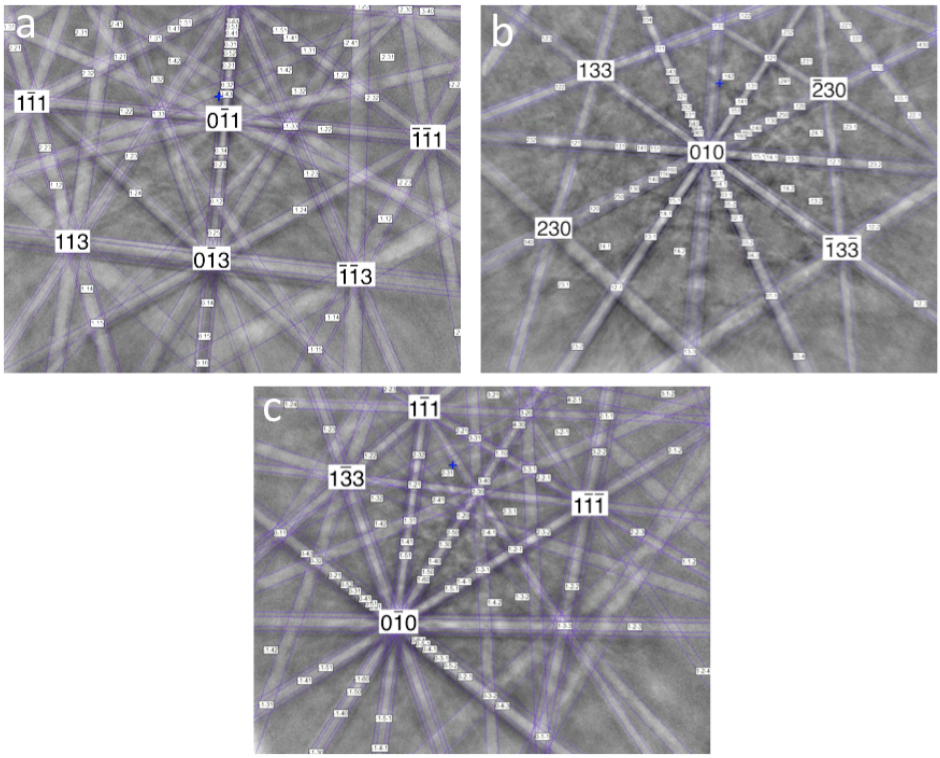

Figure 4.7: Kikuchi maps obtained from the intermetallic present in the eutectic are overlaid with identification lines from EBSD phase identification for $Mg_{12}RE$ a) Mg-0.45La-0.63Nd b) Mg-0.45La-1.18Y and c) Mg-0.45La-0.87Gd alloys.

The concentration profile of solute in solid solution across the grain of an as-cast HPDC alloy (Mg-0.45La-1.18Y) is obtained from an EDS line scan using TEM (Figure 4.8). The line scan shows that the concentration of the ternary alloying addition (in this case Y) decreases rapidly from a point near the grain boundary towards the centre of the grain.

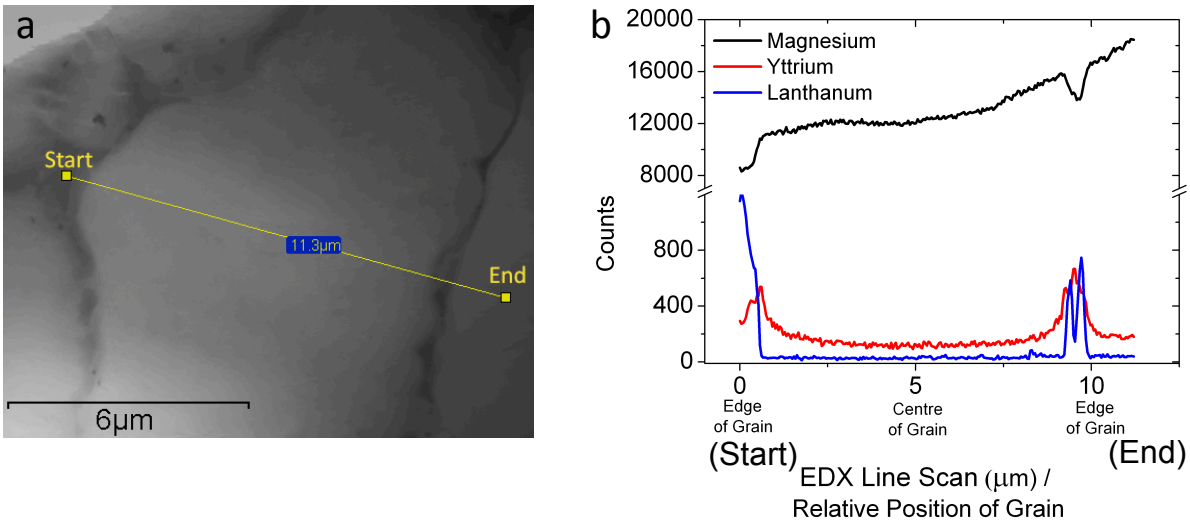

Figure 4.8: a) STEM micrograph of Mg-0.45La-1.18Y grain in as-cast condition showing where the EDS line scan is recorded and b) the corresponding EDS line scan measurements for Mg, La and Y across the grain.

This is as a result of the rapid solidification that occurs during HPDC and the solute distribution can thus be more accurately modelled using the Scheil-Gulliver rule, Eq. (2.1), rather than the lever rule.

4.3 Castability

The hot tearing index, which was detailed in Section 3.3, is used to rate susceptibility to hot tearing for each alloy. Table 4.3 shows the number of specimens per alloy that obtained a particular hot tearing rating.

All of the ternary RE elements increase the HTS, even for relatively low ternary alloying additions (Figure 4.9). Y and Gd appeared to have the greatest negative effect on hot tearing susceptibility but both show a substantial improvement in the hot tearing index above 0.1 and 0.2 at.%, respectively. At concentrations above 0.6 – 0.7 at.% there is little further increase in hot tearing observed. Nd additions show a less steep increase in hot tearing susceptibility for relatively small additions but at 0.6 at.% there is still no significant decrease in the HTS. These results are typical of the hot tearing Λ-curve [37, 43, 177, 178], where small amounts of a secondary or in this case, ternary element, increase the hot tearing whilst greater levels of addition result in a reduction HTS.

Table 4.3: List of alloys used to determine hot tearing susceptibility. The number of samples per alloy that received a particular hot tearing rating and the hot tearing index (HTI) and standard error (SE) are included.

	Hot Tearing Rating Scale							
Alloy	0	1	2	3	4	Total Samples	HTI	SE
Mg-0.46La-0.002Nd	30	0	0	0	0	30	0.0	0.00
Mg-0.46La-0.02Nd	24	6	0	0	0	30	0.2	0.09
Mg-0.45La-0.03Nd	16	12	0	0	0	28	0.4	0.07
Mg-0.46La-0.06Nd	19	11	0	0	0	30	0.4	0.08
Mg-0.47La-0.10Nd	10	20	0	0	0	30	0.7	0.09
Mg-0.47La-0.14Nd	18	12	0	0	0	30	0.4	0.09
Mg-0.43La-0.18Nd	11	19	0	0	0	30	0.6	0.09
Mg-0.45La-0.63Nd	41	35	4	0	0	80	0.5	0.03
Mg-0.49La-0.003Y	30	0	0	0	0	30	0.0	0.00
Mg-0.49La-0.02Y	9	21	0	0	0	30	0.7	0.07
Mg-0.48La-0.05Y	5	25	0	0	0	30	0.8	0.10
Mg-0.48La-0.12Y	7	23	0	0	0	30	0.8	0.09
Mg-0.49La-0.24Y	16	14	0	0	0	30	0.5	0.09
Mg-0.49La-0.31Y	18	12	0	0	0	30	0.4	0.09
Mg-0.49La-0.42Y	16	14	0	0	0	30	0.5	0.09
Mg-0.44La-0.70Y	75	5	0	0	0	80	0.1	0.07
Mg-0.45La-1.18Y	74	6	0	0	0	80	0.1	0.00
Mg-0.48La-0.003Gd	30	0	0	0	0	30	0.3	0.09
Mg-0.45La-0.01Gd	15	15	0	0	0	30	0.5	0.09
Mg-0.45La-0.04Gd	10	20	0	0	0	30	0.7	0.09
Mg-0.45La-0.10Gd	4	26	0	0	0	30	0.9	0.06
Mg-0.46La-0.21Gd	6	24	0	0	0	30	0.8	0.07
Mg-0.46La-0.60Gd	74	6	0	0	0	80	0.1	0.03
Mg-0.45La-0.87Gd	56	4	0	0	0	60	0.1	0.03

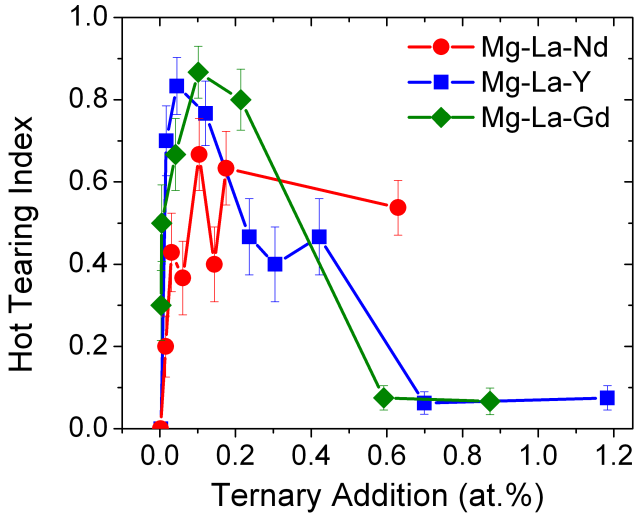

Figure 4.9: Hot tearing index as a function of total ternary alloying addition for Mg-La-Nd, Mg-La-Y and Mg-La-Gd alloy series. Note: lower hot tearing indices indicate better castability.

4.4 Discussion

4.4.1 Effects of Alloying Elements on Microstructure

The alloys investigated had similar average grain sizes and an identical intermetallic phase. The intermetallic phase had higher concentrations of La in comparison to the ternary RE content due to the lower solid solubility of La in Mg (0.04 at.%). In Chia *et al.* [18] the intermetallic phase in a binary HPDC Mg-La was shown to be $Mg_{12}La$. This is due to a combination of relatively low nucleation barrier and thermodynamic stability. Using Kikuchi maps obtained via EBSD (Figure 4.7) this current research was able to confirm that the intermetallic phase in ternary Mg-La-RE alloys is also $Mg_{12}RE$.

The fraction of the α-Mg eutectic and intermetallic in at.% was obtained from the temperature – fraction solid curves and then converted into volume fractions assuming that the density of the intermetallic was equal to the density of $Mg_{12}La$ (ρ_{int}), 2.27 g/cm^3 [18] and the density of the α-Mg eutectic was equal to the density of Mg (ρ_α), 1.738 g/cm^3. Thus the total volume fraction of the intermetallic in the eutectic (vol_{int}) could be determined from Eq. (4.1).

$$vol_{\text{int}} = \frac{m_{\text{int}}/\rho_{\text{int}}}{m_\alpha/\rho_\alpha + m_{\text{int}}/\rho_{\text{int}}} \qquad \textbf{(4.1)}$$

where m_{int} and m_α are the weight fraction of the intermetallic and α-Mg respectively (Figure 4.10).

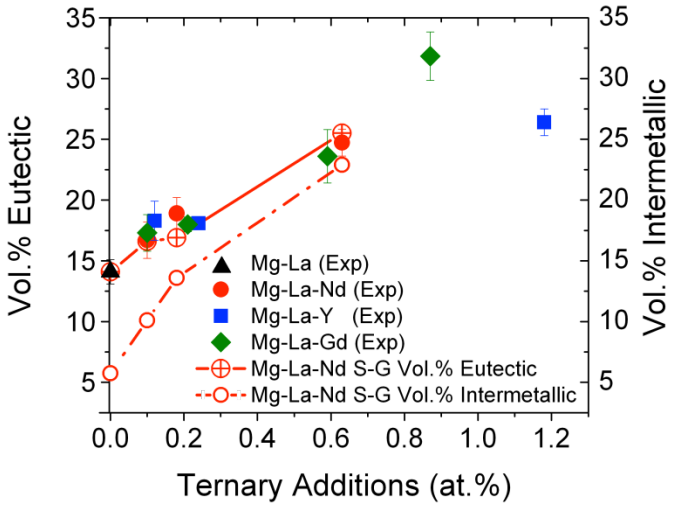

Figure 4.10: Comparison between experimentally determined eutectic volume fraction (Exp) and Scheil-Gulliver (S-G) equation calculations for the volume fraction of eutectic as a function of total ternary alloying concentration for each alloy series and a binary Mg-0.46La alloy. The Scheil-Gulliver (S-G) equation predicted volume fraction of intermetallic in Mg-La-Nd alloys is also included for comparison.

Due to the unavailability of ternary Mg-La-Y or Mg-La-Gd thermodynamic data, a comparison of the volume fraction of intermetallic in Mg-La-Y or Mg-La-Gd cannot be made. However, due to the high solubility of Y or Gd in Mg (3.60 at.% and 4.53 at.% respectively) in a binary alloy it would be expected that more Y and Gd would be soluble in α-Mg in ternary alloys and thus less present in the intermetallic phase (Figure 4.6).

A majority of the volume fraction of the eutectic was shown to be composed of $Mg_{12}La$ with ternary RE dissolved in the intermetallic phase (Figure 4.10). The volume fraction of eutectic did not increase significantly with the addition of ternary RE until relatively high concentrations (greater than 0.2 at.%) were added to the alloy. This can be attributed to the ternary RE going into solid solution due to their higher solid solubility than that of La in Mg.

Increasing the ternary alloying content resulted in the morphology of the eutectic changing gradually from a lamellar form, to one with a fibrous α-Mg phase within a matrix of intermetallic phase, to an increasingly divorced, discontinuous eutectic (Figure 4.5). This was, however, more apparent for alloys containing either Y or Gd, particularly above 0.2 at% as opposed to Nd, where the eutectic remained fibrous up to 0.63 at.%. Based on surface energy minimisation for eutectic phases with similar surface energy if

the volume fraction of one phase in the eutectic is less than approximately 10 % (0.1) it is divorced, between 10 % (0.1) and 28 % (0.28) the eutectic will be fibrous and if it is between 28 % (0.28) to 50 % (0.5) the eutectic will have a lamellar morphology [179]. In the case of the alloys being studied, the α-Mg is in general the minor phase.

$Mg_{12}RE$ is a metastable phase in Mg-Nd alloys but is often found in cast alloys due to its combination of reasonably low nucleation barrier and relative thermodynamic stability [176]. Mg_{12}(La,Nd) forms a continuous solid solution for the rare earth elements [180]. Hence, as the alloy becomes richer in Nd, the proportion of $Mg_{12}RE$ in the eutectic will increase leading to the change in eutectic morphology.

$Mg_{12}RE$ is not a stable phase in either binary Mg-Y nor Mg-Gd alloys. In fact the equilibrium eutectic concentrations are above that to form $Mg_{12}RE$ hence such a eutectic will not be able to form even under non-equilibrium conditions (Table 4.4). In the case of the alloys considered here, there is a continuous solid solution for the rare earths in the $Mg_{12}RE$ phase [18], which was confirmed to be the intermetallic in all cases (Figure 4.7). This means that Y and Gd can be expected to have a similar but more dramatic effect than Nd on the eutectic morphology, with the eutectic becoming divorced at lower concentrations than for the Nd containing alloys (Figure 4.5).

Table 4.4: Eutectic concentration [131] and concentration of $Mg_{12}RE$ in binary Mg-RE alloys with the ratio of the two concentrations where greater than 1 means the eutectic composition is less than the $Mg_{12}RE$ phase. Mg-La is shown for comparative purposes.

	C_{eut} (wt.%)	C_{Mg12RE} (wt.%)	$C_{eut} : C_{Mg12RE}$
Mg-La	16.5	32.3	0.51
Mg-Nd	33.0	33.1	0.99
Mg-Y	26.6	12.4	2.14
Mg-Gd	40.4	35.0	1.15

4.4.2 Modelling the Castability of Alloys with Different Alloying Elements

Hot tearing is a major defect that can form during casting when the cast piece is still in a semi-solid state and is often a key defect related to the rejection of castings and imposes

a limitation to the use of alloys [31]. Hot tearing is linked to the lack of sufficient compensation for solidification shrinkage by liquid flow in the presence of thermal stress due to solidification shrinkage [31, 35]. This indicates that the final stages of solidification are the most critical. A simple hot tearing model proposed by Easton *et al.* [39] was used to help model the hot tearing susceptibly from the temperature-fraction solid curve of binary HPDC Mg-RE alloys can accurately predict HTS of the alloys. The model predicts hot tearing susceptibility from the integral of the temperature-fraction of solid curve from the coherency (the temperature when feeding becomes interdendritic) to the coalescence (the temperature at which the metal has solidified sufficiently to act as a solid) points (Eq. (4.2)),

$$S_{ht2} = \int_{T_0}^{T_{co}} f_s(T)\, dT \qquad (4.2)$$

where $f_s(T)$ is the fraction of solid at temperature T, T_0 is the temperature at which coherency occurs, T_{co} is the temperature at which coalescence has been achieved. The area under the temperature – fraction of phase curve between the coherency and coalescence points is used to approximate the integral (Figure 4.11).

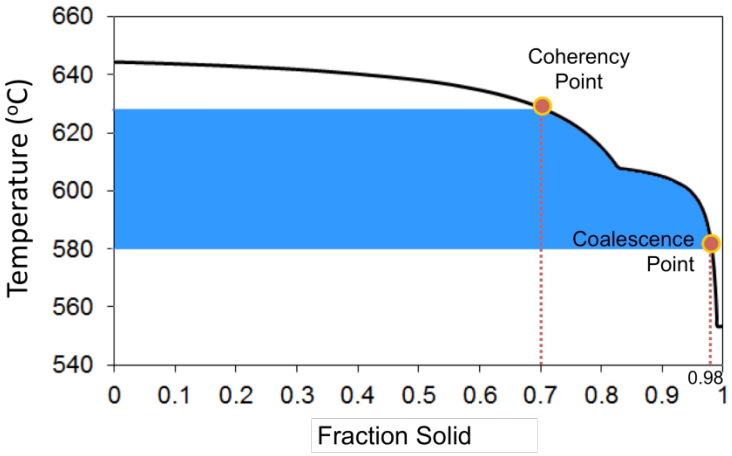

Figure 4.11: Temperature – fraction solid curve for Mg-0.49La-0.18Nd. The blue highlighted area indicates the region of the curve between the points of coherency and coalescence, which were chosen to be 0.7 and 0.98 respectively.

The Mg-La-Y and Mg-La-Gd alloy series have a Λ-shaped HTS curve with a peak in HTS occurring at ternary concentrations of approximately 0.05 and 0.1 at.%, respectively. Above this concentration, there was a significant improvement to HTS at higher alloying concentrations (Figure 4.9). This result is commonly observed in Mg alloys where alloying

additions of approximately 0.1 at.% begin to improve HTS [37, 39, 181, 182]. The Mg-La-Nd alloy series did not experience the same degree of improvement. Rather, a relatively minor yet steady rate of improvement in HTS was measured for Nd concentrations of greater than 0.2 at.%. In terms of castability, a hot tearing index greater than 0.2–0.4 is problematic, that is, hot tearing is still prevalent throughout the casting. Easton *et al.* [45] have previously mentioned that binary Mg-Al alloys are less prone to HTS than a number of Mg-Zn-Al and Mg-Zn-Al-RE alloys and in fact show little to no signs of hot tearing (i.e. hot tearing index well below 0.2 – 0.4 range). Thus in relation to castability, only alloys with virtually no ternary RE or alloys with Y or Gd additions of greater than 0.6 – 1.2 at.% have relatively good castability.

It has been shown that hot tearing susceptibility can be influenced by grain morphology and size, solidification range and the amount of eutectic [31, 38, 40]. The eutectic temperatures of the binary Mg-Nd, Mg-Y and Mg-Gd alloys (Table 4.5) are all relatively similar when compared with Mg-La, which has a significantly higher eutectic temperature. Hence the solidification range of the three alloy series investigated may also be assumed to be similar.

Table 4.5: Eutectic temperatures of RE elements in Mg at the Mg-rich side of the phase diagram [131].

Alloy System	Eutectic Temperature (°C)
Mg-La	612
Mg-Nd	552
Mg-Y	565
Mg-Gd	542

Grain size is also similar between all alloys investigated (Table 4.1). The total volume fraction of eutectic is relatively similar between all the alloys investigated (Figure 4.10). There is however a difference in the morphology of the eutectic between the Y or Gd-containing alloys and the Nd-containing alloys. This is most apparent at ternary concentrations greater than 0.2 at.% (Figure 4.5). Feeding channels allow for the flow of the molten component of the alloy during final stages of solidification to fill the voids in the castings and prevent hot tearing [37]. The difference in the morphology of the

eutectic for higher concentrated Y or Gd to Nd containing alloys may influence the feeding channels during solidification. However, further analysis of the morphology of the eutectic is required to confirm this.

The temperature – fraction solid curves for Mg-La-Nd alloys were modelled using the non-equilibrium solidification simulation feature in Pandat™ with Mg-La-Nd phase information from Gröbner *et al.* [132] for Mg-La-Nd alloys (Figure 4.12).

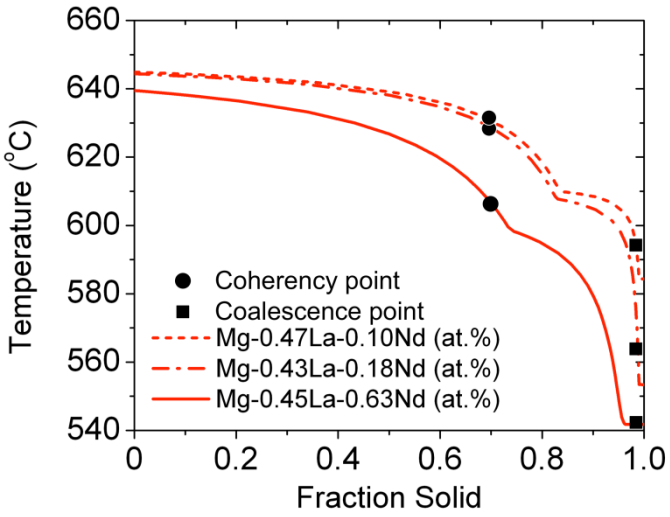

Figure 4.12: Temperature-fraction solid curves determined using Scheil-Gulliver equation for Mg-La-Nd alloys with varying concentrations of Nd alloying addition.

The integral between the point of coherency (when the fraction solid is 0.7) to the point of coalescence (when the fraction solid is 0.98) of the temperature-fraction solid curves for Mg-La-Nd alloys is used to provide an indication of castability [39] (Figure 4.13). However the S_{ht2} values can show a similar trend in HTS for an alloy series and can be used to qualitatively compare the HTS of different alloys. Thus it can be deduced from this comparison that the final stages of solidification are critical to the HTS of the alloys. Furthermore, the solidification temperature of the eutectic can be used as an approximate indication for the relative HTS of the alloy series, as has been found elsewhere [39, 183].

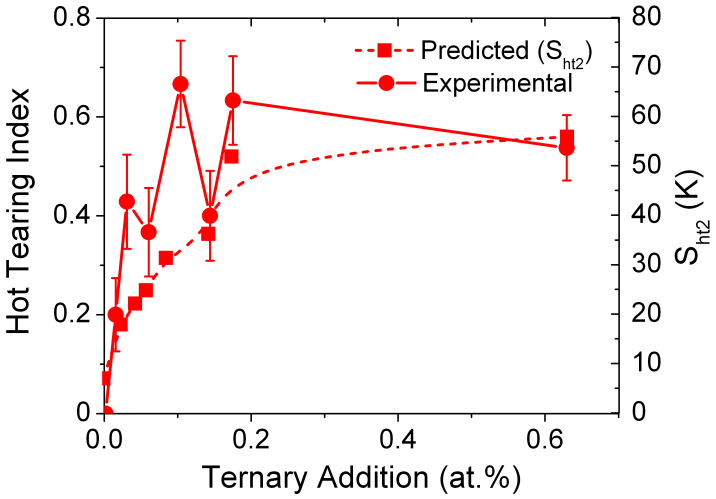

Figure 4.13: Comparison between experimentally determined HTS and predicted HTS for the Mg-La-Nd alloy system (compositions given in Table 4.3). Note: lower hot tearing indices indicate better castability.

An indication of the HTS of Mg-La-Y and Mg-La-Gd is made from the temperature-fraction solid curves for the equivalent binary Mg-Y and Mg-Gd, i.e. with the concentration of Y or Gd that is present in the ternary Mg-La-RE alloys. In this instance, the influence of La on HTS can be ignored due to the eutectic temperature of Mg-La being significantly higher than the eutectic temperatures of Mg-Nd, Mg-Y or Mg-Gd and hence does not have a major effect on the final stages of solidification (Table 4.5). Figure 4.14a compares the predicted HTS of Mg-La-Nd alloys with Mg-Nd alloys with identical concentrations of Nd. The predicted hot tearing curves for the binary alloys were produced in the same way as for the Mg-La-Nd alloys i.e. the HTS predicted by S_{ht2} (Eq. (4.2)). The corresponding temperatures for the coherency and coalescence points for each alloy are presented in Appendix A. It is obvious that although the magnitude of the predicted HTS for Mg-Nd alloys is higher than that for the Mg-La-Nd alloys, the point at which hot tear susceptibility peaks or begins to reach the plateau (as is the case for the Mg-La-Nd S_{ht2} curve) correlate well. Thus an attempt to predict HTS from the Mg-Y and Mg-Gd systems can be used to make a qualitative estimate of HTS for the Mg-La-Y and Mg-La-Gd alloys. Figure 4.14b shows that a similar trend in relation to the peaks in hot tearing susceptibility of the experimentally determined hot tearing index of Mg-La-Y and Mg-La-Gd alloys and that of the S_{ht2} indicator for HTS for Mg-Y and Mg-Gd. However, the concentration of Y or Gd at which the peaks are reached in the Mg-Y and Mg-Gd S_{ht2}

simulations do not match those of the equivalent ternary RE alloys. Thus the binary Mg-RE cannot be used to perfectly substitute the Mg-La-RE hot tearing susceptibility simulations.

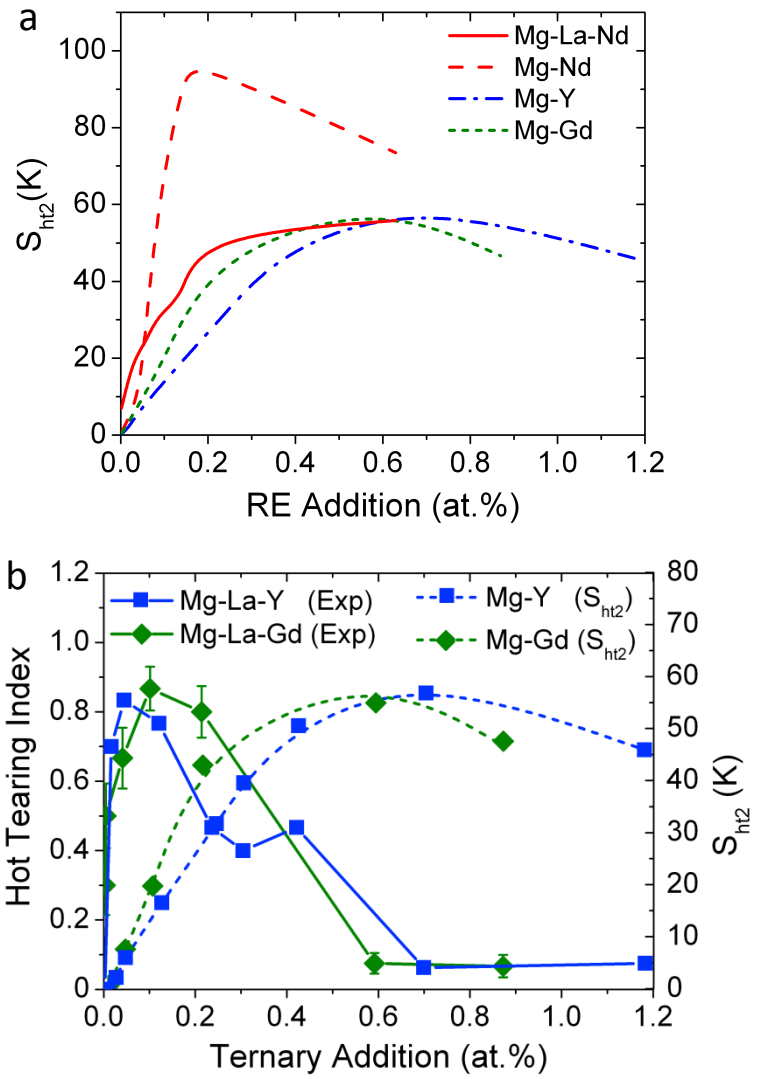

Figure 4.14: a) HTS predictions for Mg-Y and Mg-Gd. The predicted HTS for Mg-La-Nd and the binary equivalent alloys Mg-Nd is included for comparison and b) comparison between experimentally (Exp) determined HTS and predicted HTS using binary Mg-Y and Mg-Gd equivalent alloys for the Mg-La-Y and Mg-La-Gd alloy systems when the point of coherency is 0.7f_s and the point of coalescence is 0.98f_s.

By changing the value of the point of coherency (from 0.7f_s to 0.9f_s) and coalescence (from 0.98f_s to 0.99f_s) the binary alloy (Mg-Y and Mg-Gd) simulations can be improved (Figure 4.15). However, there are still significant differences in the simulated hot tearing curves in comparison to the experimentally determined values.

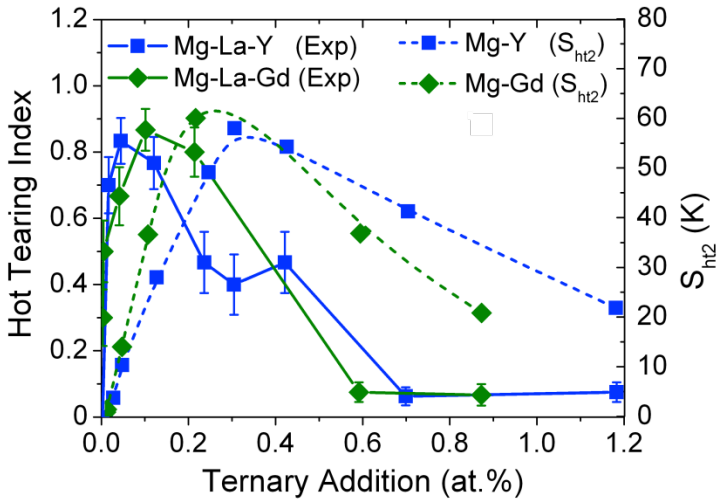

Figure 4.15: Comparison between experimentally (Exp) determined HTS and predicted HTS using binary Mg-Y and Mg-Gd equivalent alloys for the Mg-La-Y and Mg-La-Gd alloy systems when the point of coherency is 0.9f_s and the point of coalescence is 0.99f_s.

According to Easton *et al.* [171] the selection of the coherency point is not as critical as the selection of the coalescence point since hot tearing is significantly influenced by the final stages of solidification. This is related to feeding constrictions and strain accumulation occurs during the final 10 % of solidification [171]. However, changing the coherency point and the coalescence points assisted in producing an improved hot tearing simulation for Mg-Y and Mg-Gd alloys. It has been shown in [46, 47] that the composition of more complex alloy systems can cause significant changes to hot tearing susceptibility. Figure 4.5 shows that increasing the concentration of ternary RE causes the eutectic morphology to become increasingly divorced. This is more apparent in the Y or Gd-containing alloys than the Nd-containing alloys. The change in morphology could influence the feeding of liquid metal during solidification and thus could also change the points of coherency and/or coalescence. The influence of the more complex composition may however be more apparent nearer its final stages of solidification. Thus choosing a coherency point at a point later than 0.7f_s produce a more accurate model. This may explain the differences in the simulated HTS of the binary and ternary Mg-rare earth alloys.

4.5 Conclusions

The as-cast Mg-La-RE alloys studied here share similar grain sizes, intermetallic phase and grain boundary reinforcement. The greatest difference between the alloys arises from the solid solubility of the ternary additions in Mg, which in turn influence the volume fraction of intermetallic phase in the eutectic. The influence of different ternary rare earth elements and concentrations on microstructure and castability were examined and the following trends were established.

- Each alloy series had similar average grain sizes and percentage volume fraction of eutectic. The intermetallic phase present in the eutectic in each alloy series was confirmed to be $Mg_{12}RE$. However, as the ternary concentration increased the eutectic morphology changed from largely lamellar to one increasingly more divorced. This was more apparent in the Mg-La-Y and Mg-La-Gd alloys than Mg-La-Nd alloys.

- It was found that micro-alloying additions of Nd, Y or Gd to a base Mg-La alloy increases hot tearing susceptibility significantly. However, Y or Gd alloying additions of greater than approximately 0.1 or 0.2 at.%, respectively, decreases hot tearing susceptibility. Furthermore, Mg-La-Y and Mg-La-Gd alloys with ternary RE concentrations greater than 0.6 at.% had very good castability.

- No significant improvement to hot tearing susceptibility was detected in Nd-containing alloys for concentrations of Nd up to 0.63 at.%. This may be related to the difference in the morphology of the eutectic for higher concentrated Y or Gd to Nd containing alloys, which in turn may influence the feeding channels during solidification.

- Temperature-fraction solid curves (from 0.7 to 0.98 fraction solid) were used as input parameters into a simple equation to indicate HTS. The experimental results closely matched the trend in HTS produced from the model for the Mg-La-Nd

alloy system. The use of binary Mg-RE HTS simulations to predict HTS for Mg-La-RE could only be used to broadly estimate HTS. Binary HTS simulations could be improved if coherency and coalescence points were adjusted.

5 Effects of Alloying Elements on As-Cast Mechanical Properties and Microstructure

5.1 Introduction 102

5.2 Tensile Properties of As-die-cast Mg-La-RE Alloys 103

5.3 Age Hardening of Mg-La-RE Alloys 108

5.4 Creep Properties of HPDC Mg-La-RE Alloys 112

5.4.1 Tensile Creep 112

5.4.2 Compression Creep 113

5.5 Microstructure of HPDC Mg-La-RE Alloys Following Creep Testing 118

5.6 Discussion 127

5.6.1 Effect of Alloying Elements on Tensile Properties 127

5.6.2 Effect of Alloying Elements on Hardening Response of As-Cast Alloys 130

5.6.3 Effect of Alloying Elements on Creep Properties and Microstructure 131

5.7 Conclusions 133

5.1 Introduction

In Chapter 4 it was shown that different ternary RE alloying elements and concentrations in a Mg-La alloy have notable differences in the microstructure and castability of as-cast alloys. The average grain size of each alloy series was not significantly affected by the different ternary RE additions. The eutectic morphology and the castability of the alloys were, however, influenced by the selection and concentration of the ternary RE. With increasing concentration of ternary RE the intermetallic phase in the eutectic became less continuous and the castability also began to improve in the Mg-La-Y and Mg-La-Gd alloy series, there was less of an improvement for the Mg-La-Nd alloys.

Chapter 5 investigates further the influence of different ternary RE element additions on the properties of Mg-La-RE alloys such as tensile and creep properties. Zhu *et al.* [88] suggests that the concentration of solute in solid solution and/or dynamic precipitation are significant factors that influence the creep resistance of HPDC Mg-RE alloys at elevated temperatures. In this chapter the properties of as-cast HPDC Mg-La-RE alloys at room temperature and elevated temperatures are investigated. The aims of this chapter are to:

- Identify the influence of ternary RE (Nd, Y and Gd) additions on creep properties.
- Determine the effectiveness of solute in solid solution and dynamic precipitation on creep resistance.
- Identify the likely creep mechanisms in HPDC Mg-La-RE alloys at elevated temperatures.

These points will be addressed by:

- Examining the age hardening response to determine the thermal stability of the alloys, which is used as an indication to the diffusion rate of solute in solid solution.
- Creep testing at 177°C and 90 MPa to compare the influence of ternary RE additions with varying amounts of solubility in Mg.

- Using creep tests over a range of temperatures and stresses in combination with microstructure analysis (TEM) of crept alloys to deduce the likely creep mechanism.

5.2 Tensile Properties of As-die-cast Mg-La-RE Alloys

Room temperature tensile properties are measured for each alloy series over a range of relatively low to high ternary alloying additions. There is no well-defined yield point in the alloys (Figure 5.1). Instead of a well-defined yield point there is a gradual increase in stress followed by a dip and then either a relatively constant amount of stress or another gradual increase in stress until failure occurs. This is more clearly defined as the concentration of ternary RE is increased in each alloy series. Thus a 0.2% proof stress is used for the alloys tested. There is a significant increase in 0.2% PS with increasing alloy addition (Table 5.1).

Table 5.1: Average tensile properties at room temperature for Mg-La-Nd, Mg-La-Y and Mg-La-Gd alloys in the as-cast condition.

Alloy Composition (at.%)	0.2% PS ±SD (MPa)	UTS ±SD (MPa)	Elong. ±SD (%)
Mg-0.47La-0.10Nd	146.7 (± 3.0)	166.7 (± 2.3)	2.7 (± 0.3)
Mg-0.43La-0.18Nd	151.6 (± 3.2)	167.1 (± 4.5)	2.3 (± 0.7)
Mg-0.45La-0.63Nd	196.9 (± 4.2)	198.6 (± 4.2)	2.1 (± 0.7)
Mg-0.48La-0.12Y	155.2 (± 1.6)	175.8 (± 1.0)	3.9 (± 0.4)
Mg-0.49La-0.24Y	158.7 (± 1.6)	180.4 (± 3.9)	4.4 (± 0.4)
Mg-0.45La-1.18Y	186.4 (± 2.1)	213.6 (± 5.8)	4.0 (± 0.7)
Mg-0.45La-0.10Gd	145.7 (± 5.1)	169.4 (± 8.7)	3.4 (± 0.9)
Mg-0.46La-0.21Gd	159.6 (± 2.4)	180.2 (± 7.9)	4.7 (± 0.8)
Mg-0.45La-0.87Gd	182.3 (± 3.1)	200.2 (± 5.6)	3.8 (± 0.3)

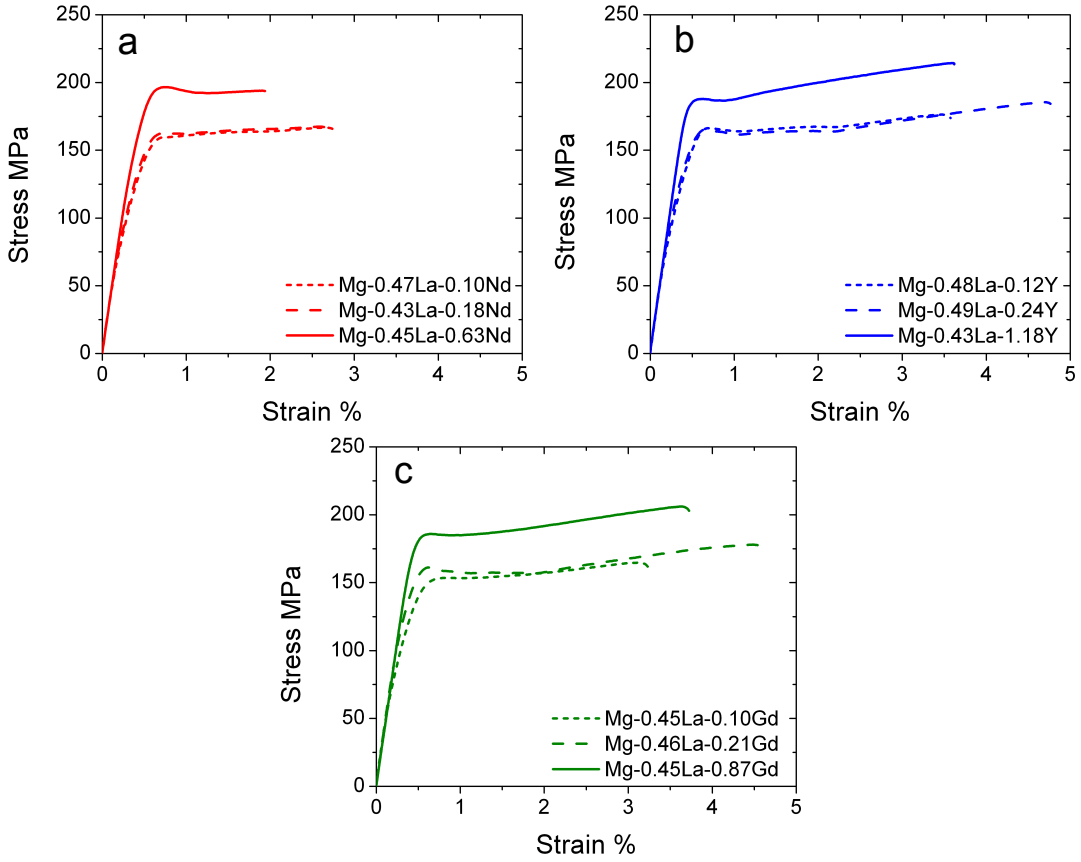

Figure 5.1: Stress-strain curves at room temperature for as-cast alloys with ternary RE additions of a) Nd, b) Y and c) Gd.

As can be seen in Figure 5.2a, the 0.2% PS increases with increasing ternary alloying addition in each alloy series. At concentrations less than 0.1 at.% the Mg-La-Nd alloy series has the lowest 0.2 % PS at room temperature. At approximately 0.2 at.% of ternary alloy addition all three alloy series have comparable 0.2 % PS. Above this concentration of ternary alloying addition, the Nd containing alloys have a higher 0.2 % PS than either Y or Gd-containing alloys. Specifically, the Mg-0.45La-0.63Nd alloy has a 0.2 % PS of 195 MPa, whereas Gd or Y containing alloys with similar additions would have a 0.2 % PS of less than 180 MPa. Elongation to fracture (Figure 5.2b) is reduced for all alloy series but the most significant decrease in elongation occurs in the Mg-La-Nd alloy series. There is a reduction in the elongation in the Nd containing alloys at concentrations greater than 0.1 at.% Nd.

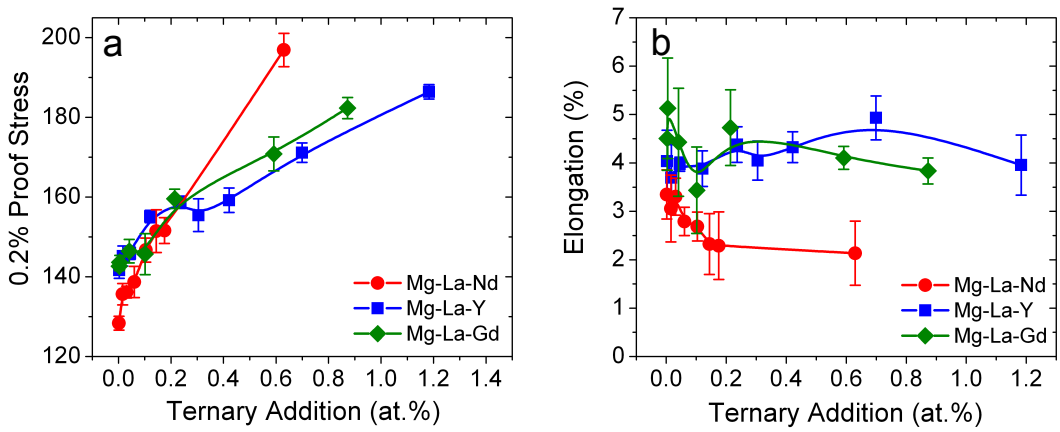

Figure 5.2: a) 0.2% proof stress and b) elongation for Mg-La-Nd, Mg-La-Y and Mg-La-Gd alloys, tested at room temperature.

Similar to the room temperature as-cast tensile strength, the alloys with higher concentrations of ternary alloying additions have better strength properties (Table 5.2). There is a yield "plateau" or yield point elongation [184] present in the highest concentrated alloys in each alloy series immediately following the elastic region of the stress-strain curve. This is then followed by an increase in stress due to work hardening (Figure 5.3).

Table 5.2: Average tensile properties at 177°C for Mg-La-Nd, Mg-La-Y and Mg-La-Gd alloys in the as-cast condition.

Alloy Composition (at.%)	0.2% PS ±SD (MPa)	UTS ±SD (MPa)	Elong. ±SD (%)
Mg-0.47La-0.10Nd	103.4 (± 0.9)	126.5 (± 1.6)	11.9 (± 2.2)
Mg-0.43La-0.18Nd	111.2 (± 2.3)	143.4 (± 1.9)	19.1 (± 1.8)
Mg-0.45La-0.63Nd	134.4 (± 2.0)	175.8 (± 4.1)	5.6 (± 1.0)
Mg-0.48La-0.12Y	108.0 (± 1.0)	137.7 (± 2.2)	19.8 (± 2.0)
Mg-0.49La-0.24Y	112.8 (± 1.5)	153.0 (± 2.5)	14.2 (± 2.3)
Mg-0.45La-1.18Y	150.6 (± 1.4)	205.7 (± 3.6)	5.3 (± 0.8)
Mg-0.45La-0.10Gd	100.6 (± 1.4)	129.3 (± 3.0)	16.2 (± 4.6)
Mg-0.46La-0.21Gd	110.9 (± 1.7)	151.1 (± 2.5)	12.3 (± 0.8)
Mg-0.45La-0.87Gd	140.2 (± 4.6)	192.9 (± 2.1)	5.4 (± 0.4)

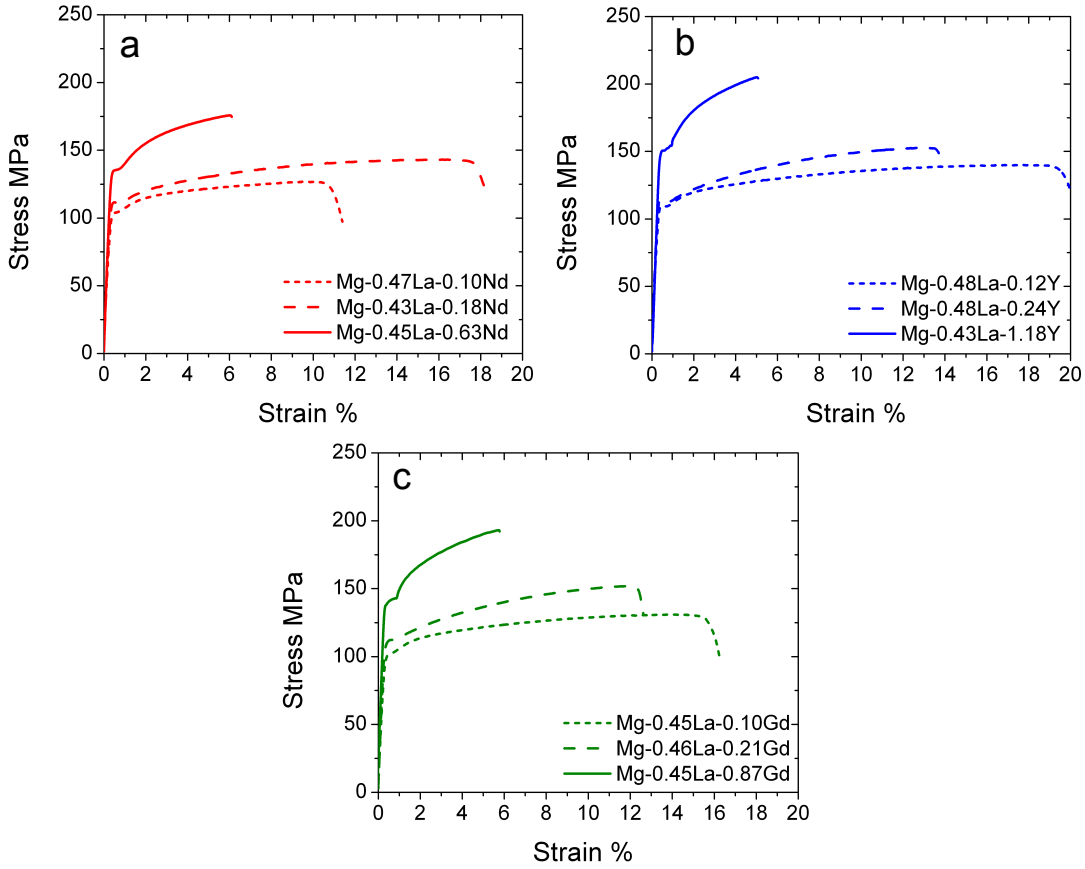

Figure 5.3: Stress-Strain curves at 177°C for as-cast alloys with ternary RE additions of a) Nd, b) Y and c) Gd.

All three alloy series appear to have comparable 0.2% PS for a given ternary RE concentration, which is different to the results at room temperature (Figure 5.1). At 177°C, the highest concentrated Nd-containing alloy (Mg-0.45La-0.63Nd) does not have a significantly higher 0.2 % PS when compared with comparable Y or Gd-containing alloys (Figure 5.4). The total elongation to failure is similar for each of the three alloy series. The 0.2% PS of the lowest concentrated ternary alloys is approximately 98 MPa and there is a near linear increase in strength with increasing concentration of ternary alloying addition for all three alloy series.

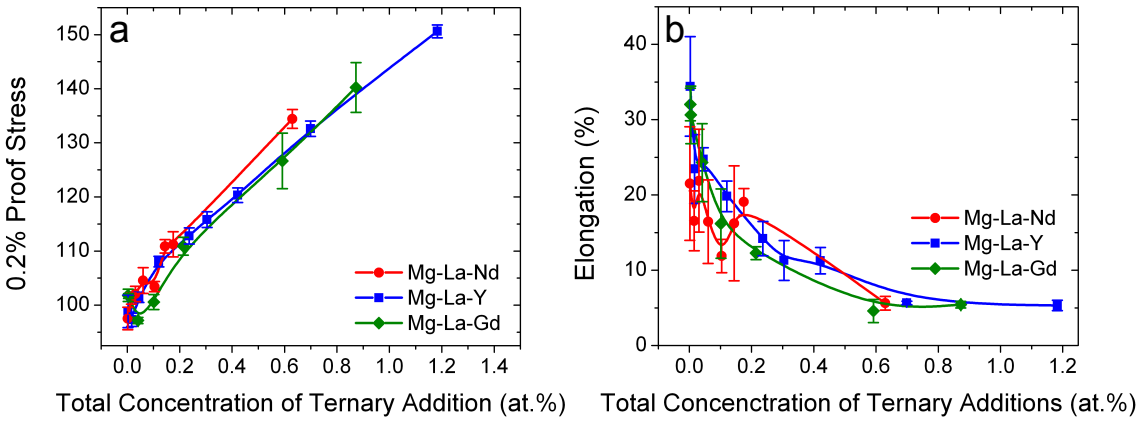

Figure 5.4: a) 0.2% proof stress and b) elongation for Mg-La-Nd, Mg-La-Y and Mg-La-Gd alloy series, tested at 177°C in as-cast condition.

In addition to tensile creep testing at 177°C of all the alloys investigated in this section, Mg-0.45La-0.63Nd and Mg-0.45La-1.18Y are also compression creep tested at 177°C, 225°C and 275°C, shown in Section 5.4.2. It is thus important to determine the compression properties of Mg-0.45La-0.63Nd and Mg-0.45La-1.18Y at 177°C, 225°C and 275°C (Table 5.3).

Table 5.3: Compression properties of Mg-0.45La-0.63Nd and Mg-0.45La-1.18Y in as-cast condition.

Alloy	Temp (°C)	0.2% PS (MPa)	UCS (MPa)	Compression (%)
Mg-0.45La-0.63Nd	225	167.3 (± 2.5)	248.4 (± 2.9)	39.5 (± 5.6)
Mg-0.45La-0.63Nd	275	150.0 (± 1.5)	210.0 (± 1.1)	48.6 (± 5.7)
Mg-0.45La-1.18Y	225	169.0 (± 16.5)	292.5 (± 7.7)	41.9 (± 12.0)
Mg-0.45La-1.18Y	275	176.7 (± 2.9)	271.3 (± 2.5)	37.6 (± 1.9)

The Mg-0.45La-0.63Nd has poorer 0.2 % PS under compression than Mg-0.45La-1.18Y. This is unlike the tensile properties of these two alloys at the lower testing temperature of 177°C where the highest concentrated Nd-containing alloy has the highest 0.2 % PS under tension. Mg-0.45La-0.63Nd does however have greater compression strain to failure than Mg-0.45La-1.18Y at both 225°C and 275°C.

5.3 Age Hardening of Mg-La-RE Alloys

The solubility of the ternary alloying elements in Mg at 160°C, 177°C and 200°C spanned the range, which produces castings that are likely to experience an age hardening response. Ageing at 177°C was performed since the majority of creep testing is performed at this temperature and it also compliments the age hardness results of the relatively low and high ageing temperatures of 160°C and 200°C, respectively. In the absence of ternary Mg-La-Y and Mg-La-Gd phase diagrams, binary phase diagram information was used. The solubilities of Y, Nd and Gd in Mg at the ageing and testing temperatures (160°C, 177°C and 200°C) are shown in Table 5.4.

Table 5.4: Solubilities of Y, Nd and Gd in Mg at 160°C, 177°C and 200°C. Note: Nd solubility values were taken from the Mg-La-Nd ternary phase diagram and Y and Gd solubility in Mg were determined from solvus line projections of binary phase diagrams, [135] and [131] respectively.

Element	Solubility in Mg at		
	160°C	177°C	200°C
Nd	0.008at.% (0.045wt.%)	0.008at.% (0.045wt.%)	0.008at.% (0.045wt.%)
Y	0.45at.% (1.62wt.%)	0.52at.% (1.86wt.%)	0.61at.% (2.21wt.%)
Gd	0.51at.% (3.22wt.%)	0.56at.% (3.50wt.%)	0.61at.% (3.82wt.%)

The Nd solubility in Mg is taken from the Mg-La-Nd ternary phase diagram produced by Gröbner *et al.* [132] and Y or Gd solubility in Mg are from binary phase diagrams or approximations taken from solvus line projections of existing binary phase diagrams extended to cover the ageing temperatures (Figure 5.5).

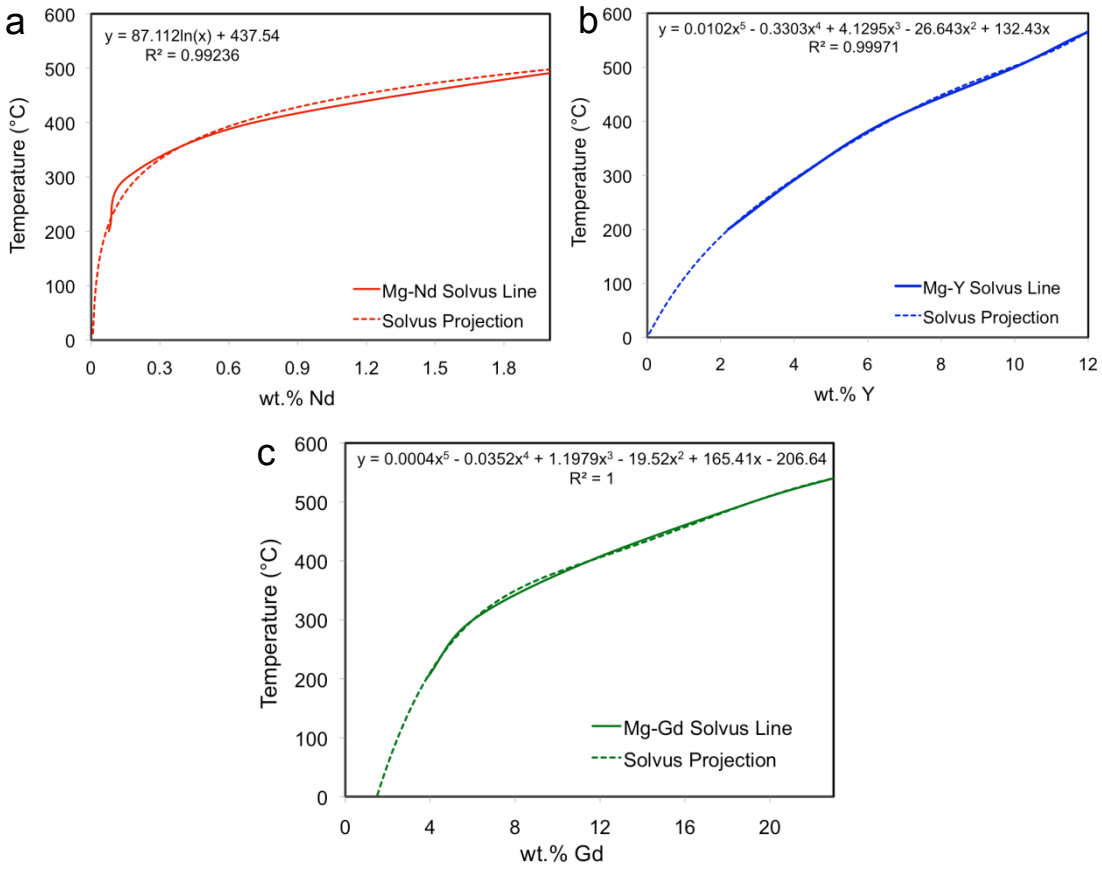

Figure 5.5: Solvus line projections for a) Mg-Nd, b) Mg-Y and c) Mg-Gd constructed from binary phase diagram data from [131] for Mg-Nd and Mg-Y and [135] for Mg-Gd.

There is good correlation between the solubility of Nd in Mg determined from the Mg-La-Nd ternary phase diagram and the from the solvus line projection of the Mg-Nd binary phase diagram (Table 5.5).

Table 5.5: Comparison of the solubility of Nd in Mg determined from solvus line projections of the Mg-Nd phase diagram [131] and ternary Mg-La-Nd phase diagram [132].

	Solubility of Nd in Mg at		
	160°C	177°C	200°C
From Solvus Projection	0.007at.% (0.04wt.%)	0.008at.% (0.05wt.%)	0.013at.% (0.077wt.%)
Ternary Phase Diagram	0.008at.% (0.045wt.%)	0.008at.% (0.045wt.%)	0.008at.% (0.045wt.%)

When the concentrations of the ternary alloying additions are increased above the solubility limit at 200°C an age hardening response is observed at 160°C, 177°C and 200°C

(Figure 5.6), as would be expected. Since, Mg-0.43La-0.18Nd already has a Nd concentration greater than the solubility limit at these ageing temperatures it was decided to produce an Mg-La-Nd alloy where the concentration of Nd was equal to maximum solid solubility of Nd in Mg (0.63 at.%). The alloy series containing the least soluble ternary alloying addition (Nd) reaches peak aged conditions before either the Mg-La-Y or Mg-La-Gd when aged at 160°C, 177°C or 200°C, (Table 5.6). Mg-0.45La-0.63Nd begins to overage far more rapidly, particularly at 160°C and 177°C, than Mg-0.45La-1.18Y or Mg-0.45La-0.87Gd. At 177°C (the creep testing temperature) both Y- and Gd-containing alloys appear to have relatively slow ageing kinetics, reaching peak hardness after approximately 1000 h of ageing.

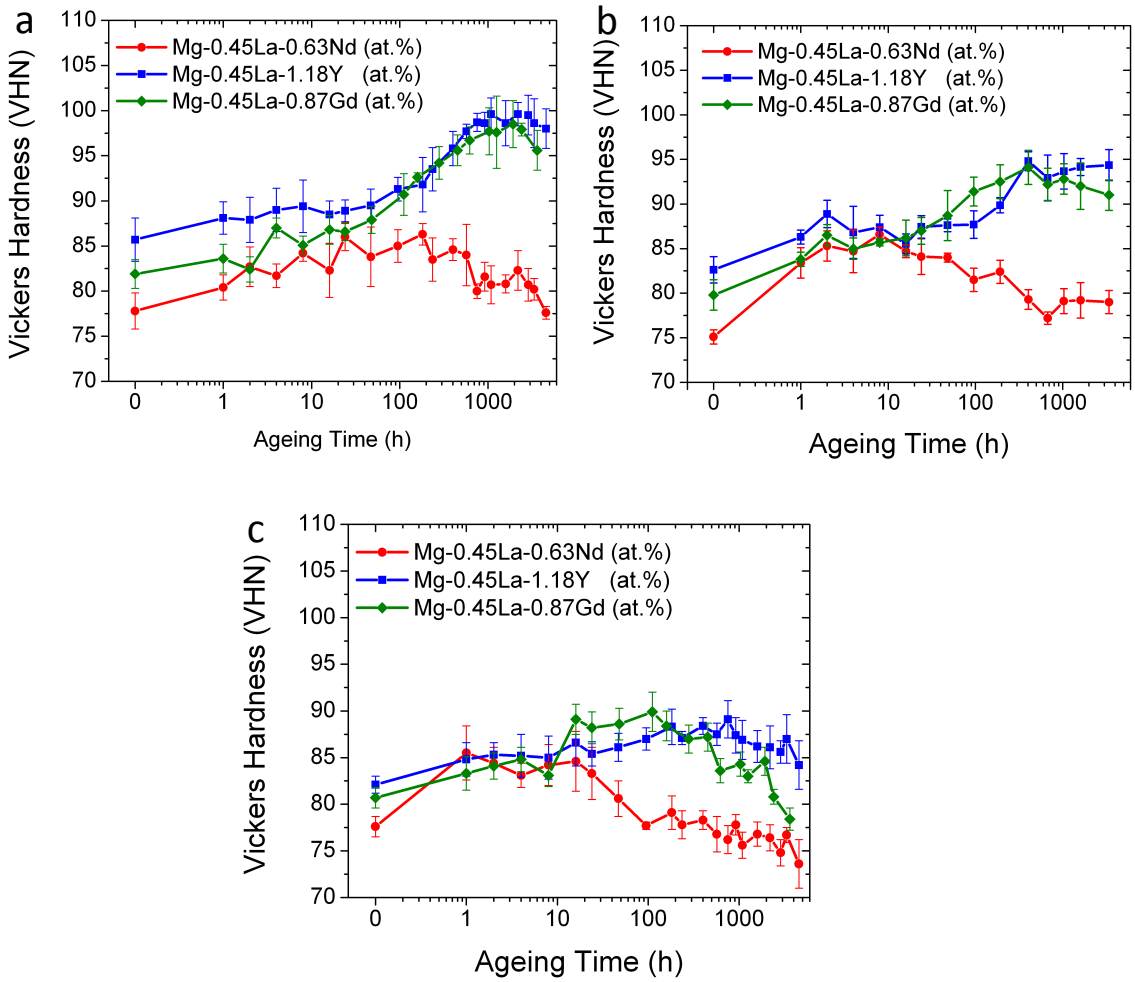

Figure 5.6: Age hardening response of Mg-0.45La-0.63Nd, Mg-0.45La-1.18Y and Mg-0.45La-0.87Gd at a) 160°C, b) 177°C and c) 200°C.

Table 5.6: Approximate peak ageing duration for Mg-0.45La-0.63Nd, Mg-0.45La-1.18Y and Mg-0.45La-0.87Gd at 160, 177 and 200°C.

Ageing Temperature, °C	Mg-0.45La-0.63Nd Peak Ageing Time, h	Mg-0.45La-1.18Y Peak Ageing Time, h	Mg-0.45La-0.87Gd Peak Ageing Time, h
160	20	1000	1000
177	10	400	400
200	1	200	50

However, due to the inhomogeneous distribution of solute in solid solution as a result of rapid solidification during casting (Figure 4.8) there is still a supersaturated region of solute near the grain boundary in alloys with significantly less ternary alloy concentrations.

In order to determine the influence of the supersaturated region of solute in the as-cast alloys on age hardening, alloys with less ternary RE than those used in Figure 5.6 are also heat-treated. Three alloys with approximately 0.2 at.% ternary RE are aged at 160°C and 200°C. The Mg-0.43La-0.18Nd alloy still contains a ternary concentration that is above the solid solubility of Nd in Mg at 200°C (Table 5.4) but both Mg-0.49La-0.24Y and Mg-0.46La-0.21Gd are not supersaturated. However, due to the non-equilibrium solidification of all the alloys a region of supersaturated solute near the grain/cell boundaries in each of the three alloys with approximately 0.2 at.% ternary RE is present. This region however is not substantial enough to produce an age hardening response at 160°C or 200°C (Figure 5.7).

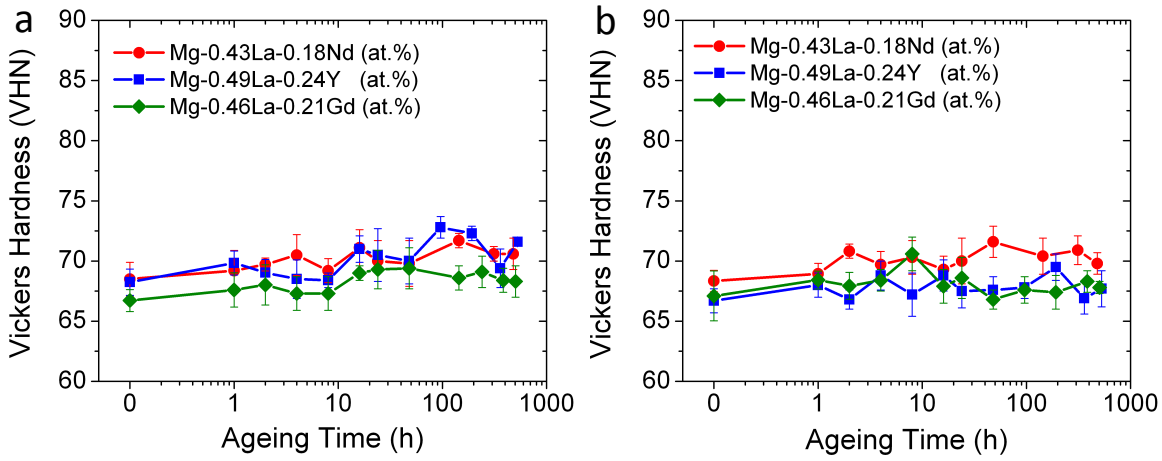

Figure 5.7: Age hardening response of Mg-0.43La-0.18Nd, Mg-0.49La-0.24Y and Mg-0.46La-0.21Gd during isothermal ageing at a) 160°C and b) 200°C.

5.4 Creep Properties of HPDC Mg-La-RE Alloys

5.4.1 Tensile Creep

Increasing the ternary alloying concentration from approximately 0.1 at.% to 0.2 at.% in all alloy series improves primary creep significantly (Figure 5.8). Since it is not always clear when primary creep ends and steady state creep begins a value of 5 h of creep testing is chosen to be the end point of primary creep. This point was chosen as it generally fell within the region of pronounced initial creep strain and allows for more meaningful and direct comparisons of primary creep strain between alloys. An improvement in steady-state creep also occurs for ternary alloying additions up to 0.2 at.%. This however, is more pronounced in the Mg-La-Y and Mg-La-Gd alloys where 0.1% creep strain is reached after approximately 600 h compared to the Mg-La-Nd alloy, which reaches tertiary creep in less than 50 h (Figure 5.8).

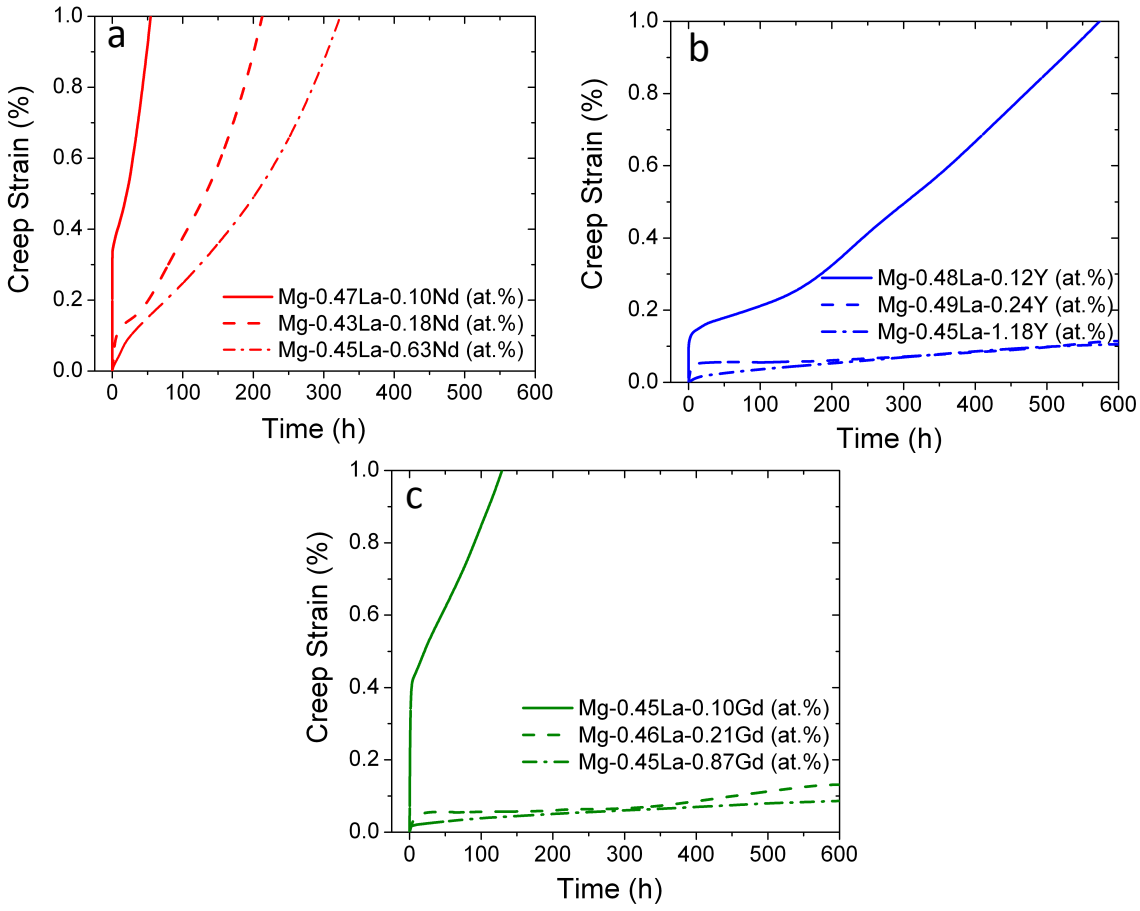

Figure 5.8: Creep strain curves for three as-cast a) Mg-La-Nd b) Mg-La-Y and c) Mg-La-Gd alloys tested at 177°C and 90MPa.

Additions of ternary alloying elements greater than 0.2 at.% do little to further improve steady-state creep (Figure 5.9). However, it may assist to prolong the onset of tertiary creep as is demonstrated by the delayed onset of tertiary creep in the Mg-0.45La-0.63Nd alloy (Figure 5.8a). The minimum creep rate (MCR) decreases with increasing concentration of ternary alloying addition and reaches a plateau after approximately 0.2 at.% of ternary addition in all three alloy series. A difference between the MCR of the Nd containing alloys with the Gd and Y containing alloys is also observed. The Nd-containing alloys reach a MCR of approximately 1×10^{-8} s^{-1} at 0.2 at.% in comparison with the Gd and Y containing alloys that plateau at approximately 8×10^{-10} s^{-1}. The Y-containing alloys have a slightly lower MCR than the Gd-containing alloys at lower concentrations of ternary addition (i.e. less than 0.2 at.%) but at lower concentrations the Y-containing alloys have approximately equal MCRs to the Gd-containing alloys for a similar solute content. The Nd-containing alloys generally have the same MCR at the lower concentrations as the Y and Gd containing alloys.

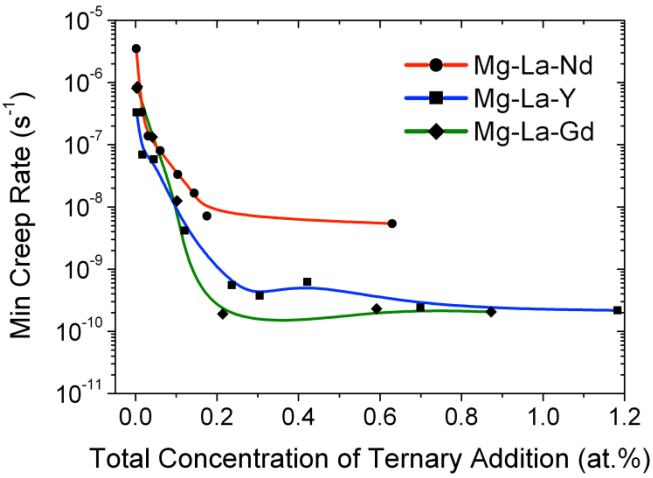

Figure 5.9: Minimum creep rate as a function of total ternary alloying addition concentration for Mg-La-Nd, Mg-La-Y and Mg-La-Gd alloy series tested at 177°C and 90MPa.

5.4.2 Compression Creep

The creep results in this section are obtained from compression creep testing rather than tension creep testing (which was the case for the creep tests in section 5.4.1). This is done due to the limitations in both temperature (maximum of 200°C) and applied stress (maximum 110 MPa) that could be used in the tension creep apparatus at Monash

University without causing damage to the rig. The minimum compression creep rates for all the alloys and conditions are given in Table 5.7.

Table 5.7: Average minimum (±SD) creep rate of Mg-0.45La-0.63Nd and Mg-0.45La-1.18Y specimens compression creep tested over a number of temperatures and stresses. Tests were performed at HZG, Germany.

Alloy	Testing Condition	Min. Creep Rate (s^{-1})
Mg-0.45La-0.63Nd	177°C/30MPa	6.2×10^{-11} ($\pm 3.6 \times 10^{-11}$)
	177°C/90MPa	9.4×10^{-9} ($\pm 1.8 \times 10^{-9}$)
	225°C/90MPa	9.3×10^{-7} ($\pm 3.0 \times 10^{-7}$)
	275°C/30MPa	9.6×10^{-8} ($\pm 9.6 \times 10^{-11}$)
	275°C/50MPa	3.8×10^{-6} ($\pm 2.0 \times 10^{-7}$)
	275°C/90MPa	2.5×10^{-4} ($\pm 1.2 \times 10^{-4}$)
Mg-0.45La-1.18Y	177°C/90MPa	1.7×10^{-10} ($\pm 9.3 \times 10^{-12}$)
	177°C/130MPa	3.4×10^{-10} ($\pm 7.0 \times 10^{-11}$)
	177°C/150MPa	9.2×10^{-10} ($\pm 1.0 \times 10^{-10}$)
	225°C/90MPa	5.0×10^{-9} ($\pm 6.3 \times 10^{-10}$)
	275°C/70MPa	5.2×10^{-7} ($\pm 3.3 \times 10^{-8}$)
	275°C/90MPa	3.4×10^{-6} ($\pm 3.7 \times 10^{-7}$)
	275°C/130MPa	5.0×10^{-5} ($\pm 2.4 \times 10^{-6}$)

When a comparison is made between alloys tested in compression and tensile creep under the same stress and temperature conditions there is no significant difference between the creep response during primary and secondary creep (Figure 5.10). There is typically a difference between tensile creep properties and compression creep properties in Al containing Mg alloys [185-187].

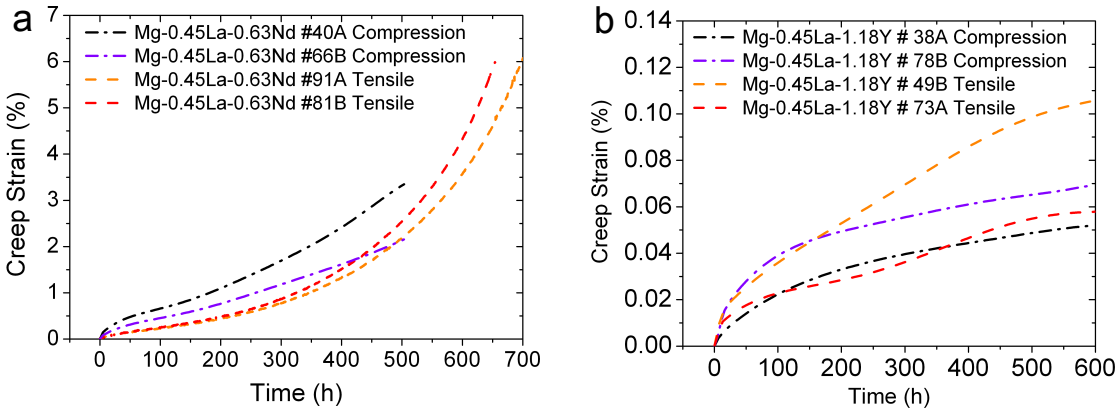

Figure 5.10: Comparison between compression and tensile creep for a) Mg-0.45La-0.63Nd and b) Mg-0.45La-1.18Y creep tested at 177°C and 90 MPa.

Compression creep testing was used to determine the creep strength of the material over a greater range of temperatures and stresses. Due to the limited number of available of

compression creep testing machines at the Helmholtz Zentrum Geesthacht (HZG), Germany only two alloys were tested. One was the highest concentrated Nd containing alloy investigated in this work and the other was the highest concentrated Y containing alloy (Figure 5.11). No Gd-containing alloy was tested since both Y and Gd containing alloys have similar creep responses.

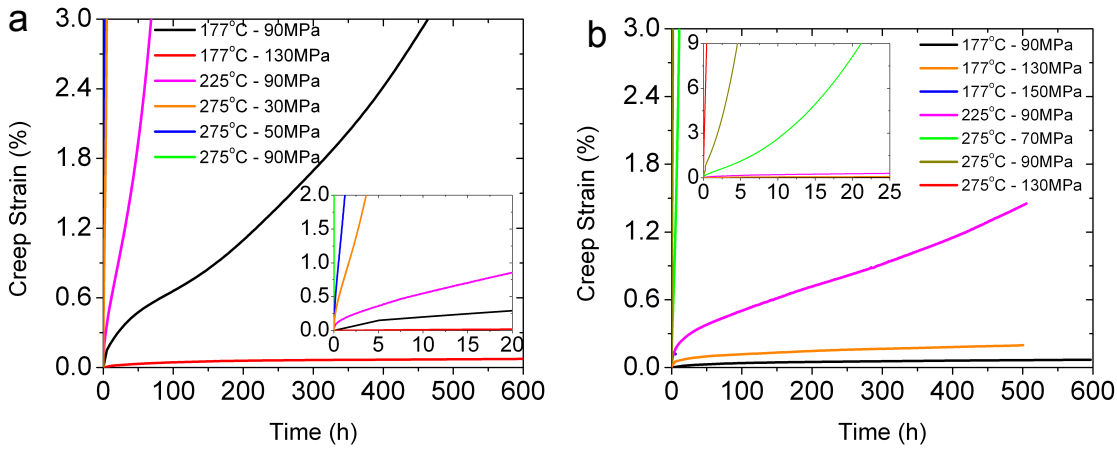

Figure 5.11: Compression creep curves for a) Mg-0.45La-0.63Nd and b) Mg-0.45La-1.18Y alloys tested over a range of temperatures and stresses.

The compression properties of Mg-0.45La-0.63Nd (Table 5.3) show that the 0.2% PS (under compression) is approximately 150 MPa at 275°C. All compression tests for Mg-0.45La-0.63Nd are performed with an applied stress 110MPa or lower at 177°C and 275°C. The stress exponent at 275°C for Mg-0.45La-0.63Nd is almost identical to that of the Mg-0.45La-1.18Y alloy at the same temperature, n = 7.3. It is difficult to determine the n value at 177°C because it is not clear if there is a "mechanism" change between 30 – 70 MPa and 70 - 110MPa. If there is a change then the n value between 30 - 70MPa is 3.3 and that between 70 – 110MPa is 14.7 (Figure 5.12). Minimum creep rates of Mg-0.45La-0.63Nd at 177°C and 90MPa in compression and tensile creep tests are available. A comparison between the two sets of data is included in Figure 5.10.

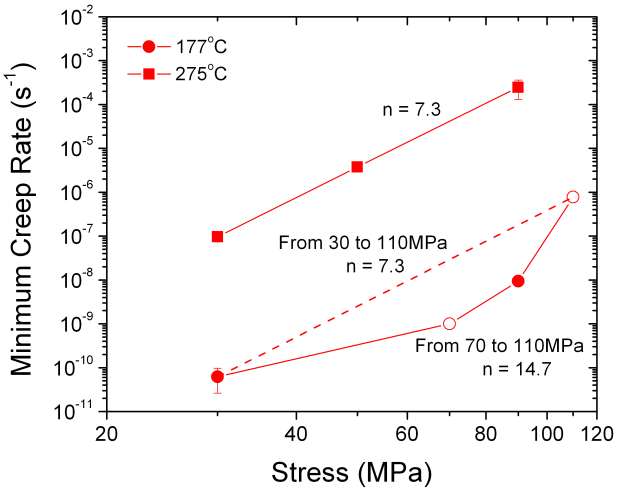

Figure 5.12: Creep rate versus stress for Mg-0.45La-0.63Nd at 177°C and 275°C. Note the open symbol indicates tensile creep data.

The activation energy at 30MPa was Q = 147.9 kJ/mol and at 90MPa Q = 201.9kJ/mol as shown in Figure 5.13. The activation energy determined at 30 MPa should only be regarded as an estimate since only two temperatures are used to calculate the value.

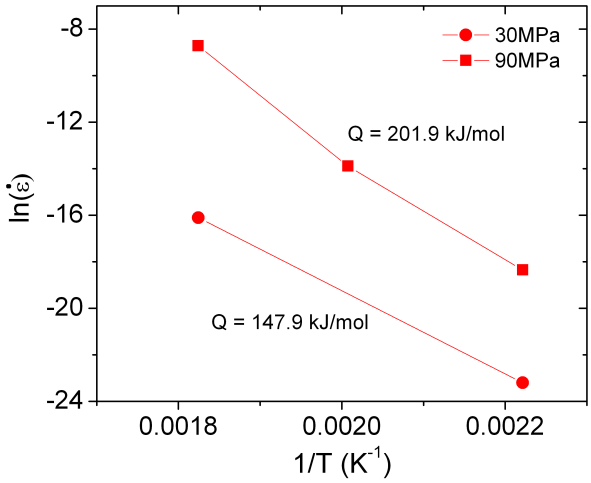

Figure 5.13: Creep strain rate vs. 1/T with activation energies (Q) for Mg-0.45La-0.63Nd at 30 and 90MPa.

The compression properties of Mg-0.45La-1.18Y (Table 5.3) show that the 0.2% PS (under compression) is approximately 185 MPa at 275°C. All compression tests for Mg-0.45La-1.18Y are performed with an applied stress 150MPa or lower at 177°C and 275°C. Using both compression and tensile minimum creep rate values for Mg-0.45La-1.18Y at 177°C, a stress exponent n = 3.4 was calculated (Figure 5.14). Due to high creep resistance of this alloy at 177°C there is little change in MCR between 90 and 110 MPa. Once again, this

makes it difficult to determine if steady state creep has been reached. Thus the n values obtained at 177°C from 90 to 150 MPa or 110 to 150 MPa should only be used to indicate the creep mechanism.

The stress exponent at 275°C is found to be n= 7.4 which indicates that the creep mechanism is related to diffusion controlled dislocation motion [94]. This value should be regarded to be more reliable than the n-value determined at 177°C.

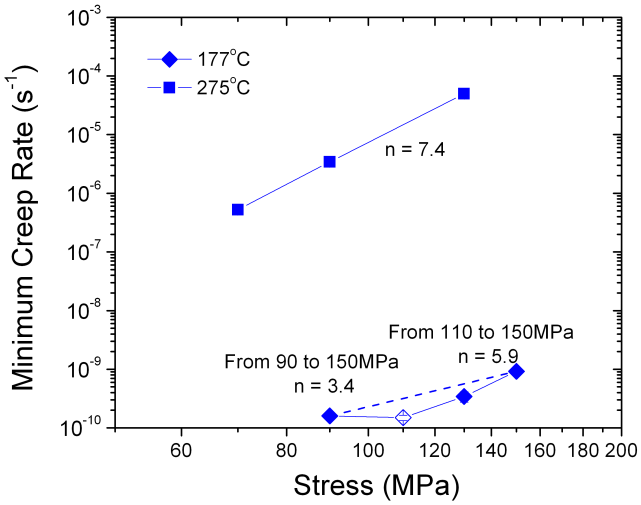

Figure 5.14: Creep rate versus stress for Mg-0.45La-1.18Y at 177°C and 275°C to determine the n-values. Note the open symbol indicates tensile creep data.

The activation energy (Q) at 90 and 130MPa is also determined for Mg-0.45La-1.18Y. However the Q values should only be regarded as a broad indication of the true activation energy at 130 MPa since only two temperatures are used. At 90MPa, Q = 211.1 kJ/mol and at 130MPa, Q = 250.1 kJ/mol (Figure 5.15).

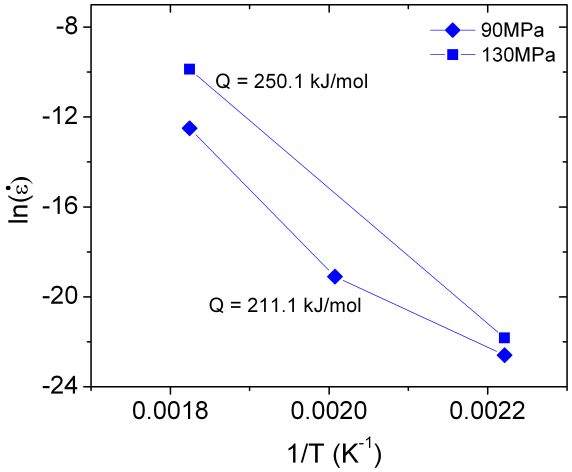

Figure 5.15: Creep strain rate vs. 1/T with activation energies (Q) for Mg-0.45La-1.18Y at 90 and 130MPa.

5.5 Microstructure of HPDC Mg-La-RE Alloys Following Creep Testing

Comparable precipitate morphology and distribution are also observed in compression crept and tensile crept alloys at 177°C and 90 MPa as will be shown further in this chapter.

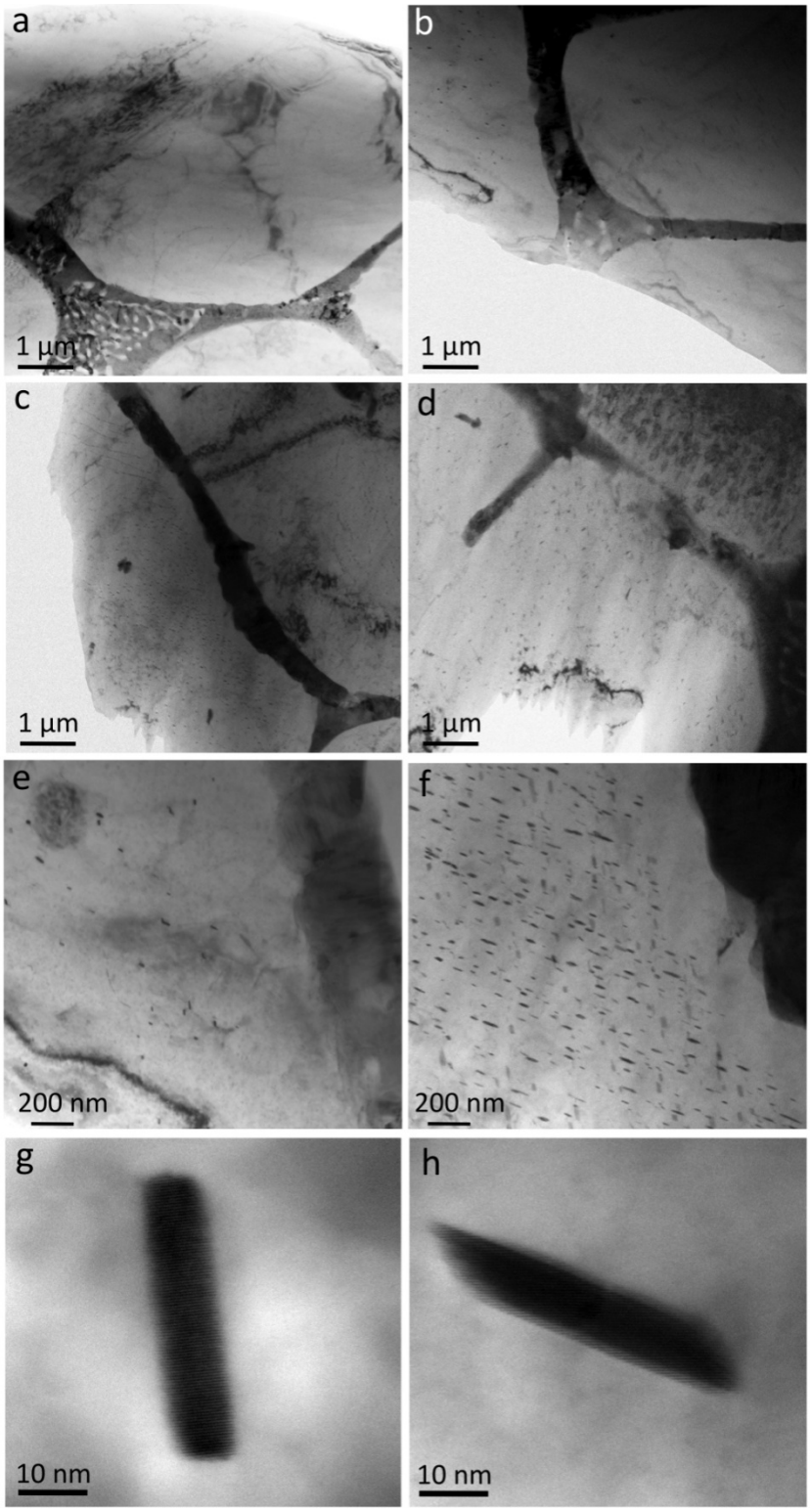

Figure 5.16: $[0001]_{\alpha}$ Bright field (BF) TEM micrographs following creep testing at 177°C and 90 MPa in the as-cast condition of a) Mg-0.47La-0.10Nd, b) Mg-0.43La-0.18Nd, c) Mg-0.45La-0.63Nd following tensile creep, d) Mg-0.45La-0.63Nd following compression creep. Higher resolution micrographs more clearly showing precipitates are also included for tensile crept e) Mg-0.43La-0.18Nd and f) Mg-0.45La-0.63Nd and precipitate morphology g) Mg-0.43La-0.18Nd and h) Mg-0.45La-0.63Nd.

Continuous dynamic precipitates are detected in the α-Mg phase of Mg-0.43La-0.18Nd and Mg-0.45La-0.63Nd alloys but not in Mg-0.47La-0.10Nd. When viewed along the $[0001]_\alpha$ direction, the precipitates present in the higher concentrated Nd-containing alloy (Figure 5.16e and f) have a plate-like morphology and lie on the basal plane (Figure 5.16g and h). Only two of the three precipitate variants, which have their long axis parallel to the $\langle 1\bar{1}00 \rangle_\alpha$ directions, are observed.

Figure 5.17 shows the morphology of the microstructure in Mg-La-Y alloys following creep. Similar to the Mg-La-Nd alloys, the Mg-La-Y alloy with the lowest concentration of ternary alloying addition, Mg-0.48La-0.12Y, does not have any observable dynamic precipitates. The precipitates in the Mg-0.49La-0.24Y and Mg-0.45La-1.18Y alloys have a greater number density near grain boundary regions. However, the precipitates in alloy Mg-0.45La-1.18Y are significantly finer than those of Mg-0.49La-0.24Y.

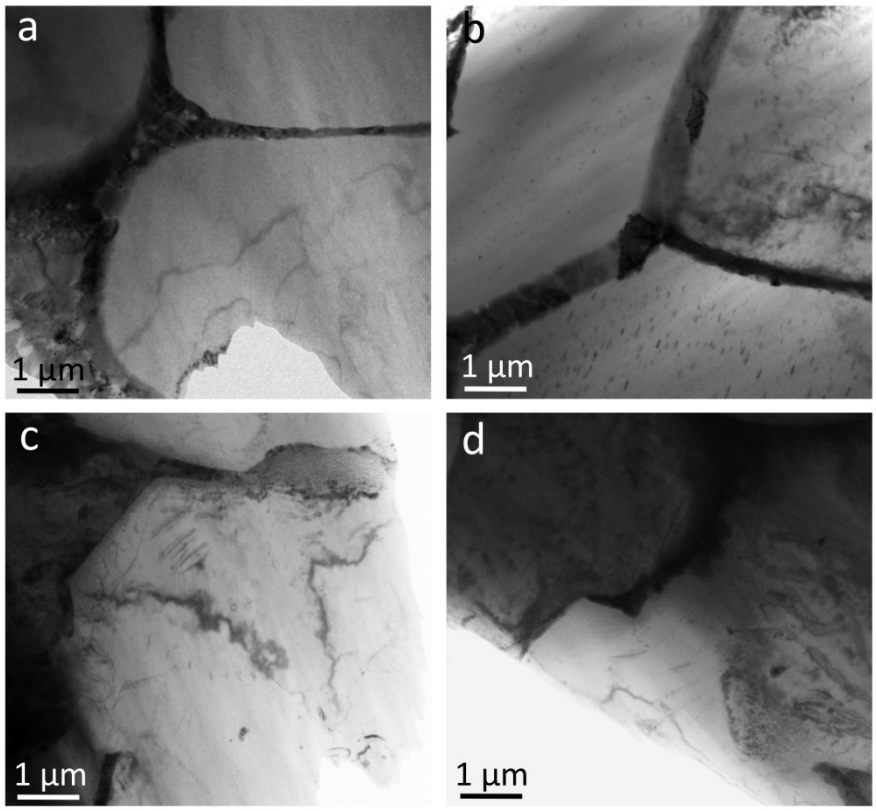

Figure 5.17: $[0001]_\alpha$ BF TEM micrographs following tensile creep testing at 177°C and 90 MPa a) Mg-0.48La-0.12Y, b) Mg-0.49La-0.24Y and c) Mg-0.45La-1.18Y following tensile creep and d) Mg-0.45La-1.18Y following compression creep.

However, unlike the precipitates present in the Nd-containing alloys the precipitates in the Y-containing alloys do not appear as plates along the $[0001]_\alpha$ direction (Figure 5.18). The precipitates in the Mg-0.49La-0.24Y alloy have an irregular elongated morphology while the precipitates in the Mg-0.45La-1.18Y alloy are relatively fine β' precipitates, in both tensile and compression crept samples (Figure 5.19).

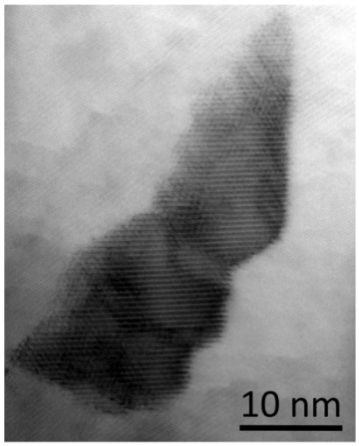

Figure 5.18: Precipitate in Mg-0.49La-0.24Y alloy following creep testing at 177°C and 90 MPa for 600 h in the as-cast condition.

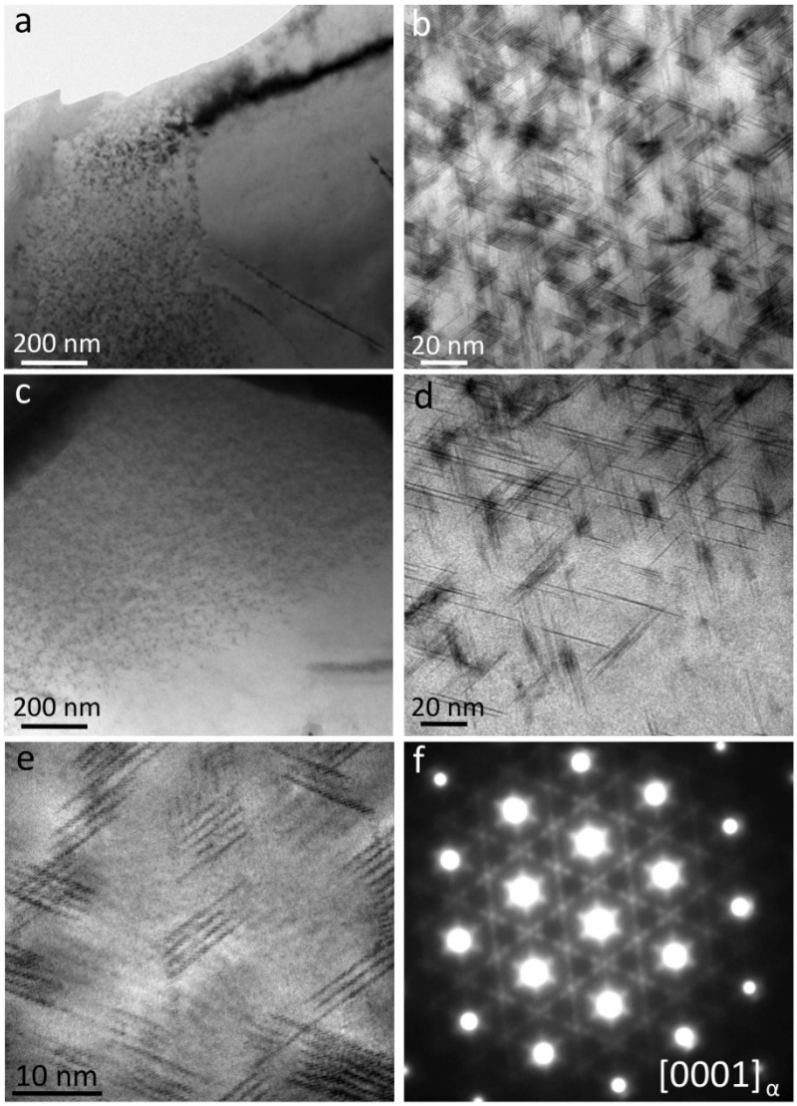

Figure 5.19: a) and b) Region of a Mg-0.45La-1.18Y specimen densely populated with β' precipitates tensile crept at 177°C and 90 MPa, c and d) comparable region of precipitates in a compression crept sample at 177°C and 90 MPa, e) higher resolution micrograph of the β' precipitates from tensile crept sample and f) diffraction pattern from the region which identifies the precipitates as β'.

Similarly to the Mg-La-Nd and Mg-La-Y alloys, the Mg-La-Gd with less than 0.2 at.% ternary RE addition do not have any observable precipitates nucleating dynamically during creep (Figure 5.20a). It is only at ternary concentrations of approximately 0.2 at.% or greater that dynamic precipitates become resolvable (Figure 5.20b and c).

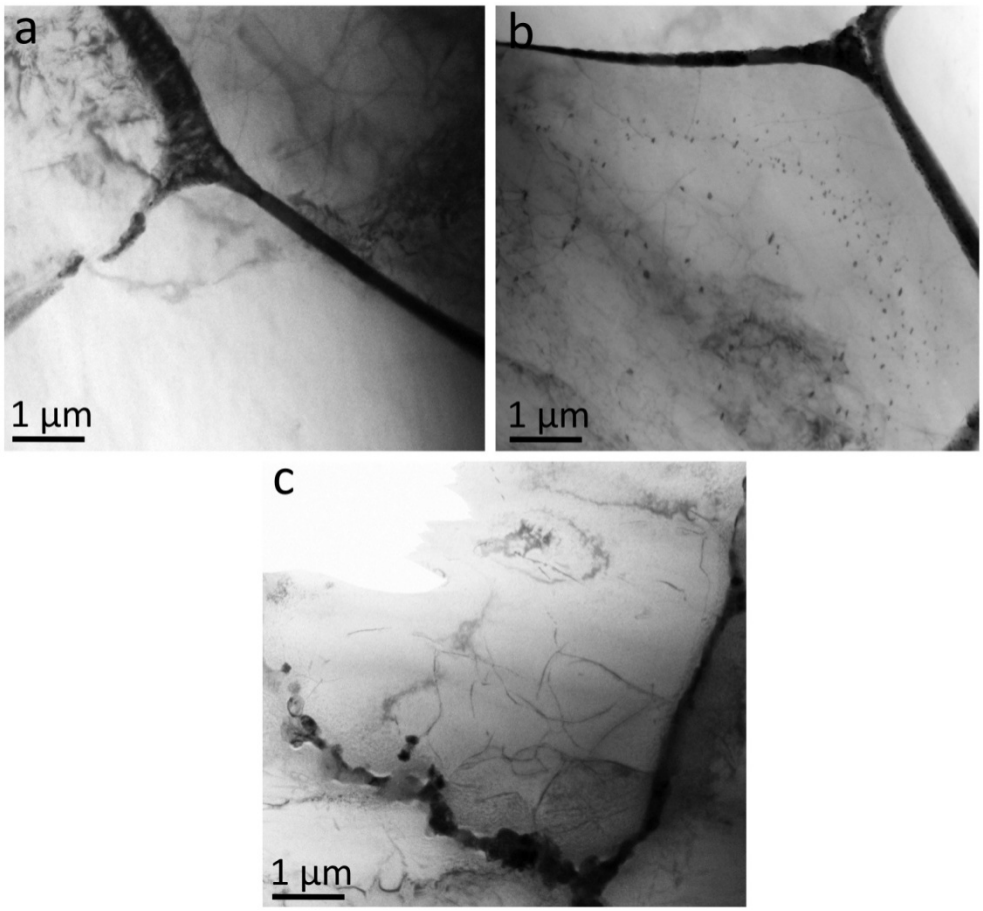

Figure 5.20: BF TEM micrographs of as-cast a) Mg-0.45La-0.10Gd, b) Mg-0.46La-0.21Gd c) Mg-0.45La-0.87Gd following creep testing at 177°C and 90 MPa.

Similar to the Mg-0.49La-0.24Y alloy following creep testing the precipitates in the Mg-0.46La-0.21Gd alloy also have an irregular shaped morphology (Figure 5.21). The irregular shaped precipitates appear to be have a similar appearance to the β'- β_1 precipitates found in Mg-Gd alloys [162].

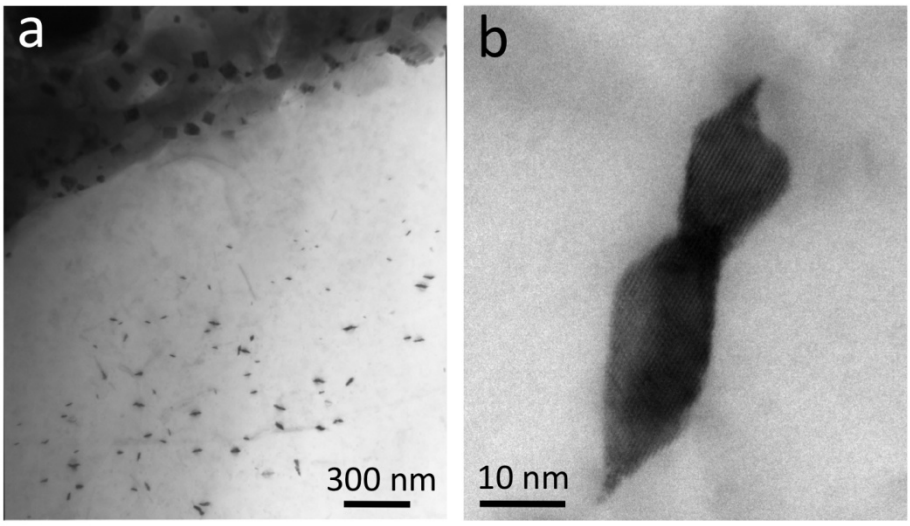

Figure 5.21: Dynamic precipitates of Mg-0.46La-0.21Gd a) nucleating near grain boundary and b) higher resolution micrograph of precipitates. Micrographs recorded along the $[0001]_\alpha$ direction.

A highly concentrated region of dynamic precipitates situated very near to the grain boundaries are observed in as-cast Mg-0.45La-0.87Gd following creep testing at 177°C and 90 MPa after 600 h. Precipitates of β' connected to β_1 (as previously shown in [188] and [139]) are present in the localised region with high precipitation number density along β' precipitates on their own (Figure 5.22).

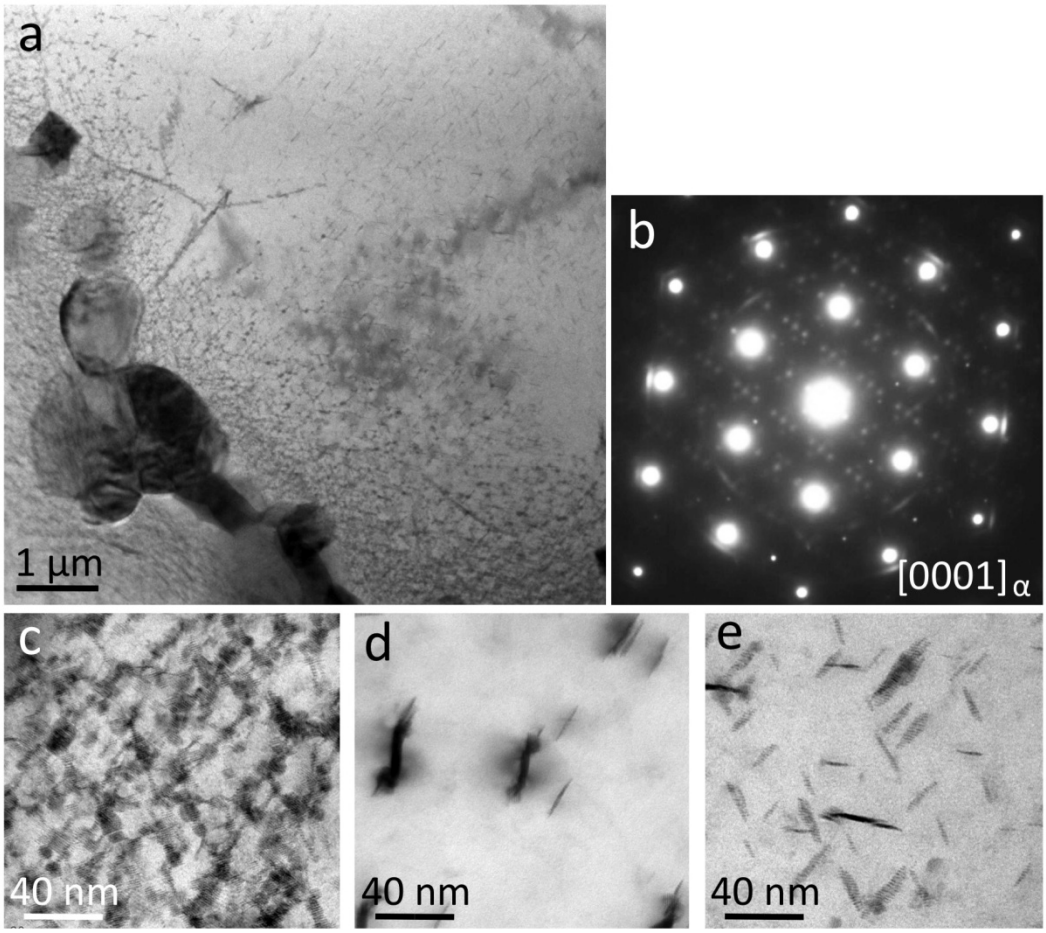

Figure 5.22: Dynamic precipitates observed in alloy Mg-0.45La-0.87Gd a) Dynamic precipitates nucleating throughout grain b) diffraction pattern from densely populated region of precipitates aligned along [0001] showing β' precipitates, c) dense concentration of β' precipitates near grain boundary d) outer region of densely concentrated precipitate region showing a combination of β' and β'+ β_1 precipitates and e) elongated β' precipitates near grain centre.

Dislocations with dynamic precipitates nucleating on them are also clearly observed in Mg-La-Nd, Mg-La-Y and Mg-La-Gd alloys (Figure 5.23). Dislocations are present throughout the grains in each alloy investigated but also appear to pile-up near grain boundaries.

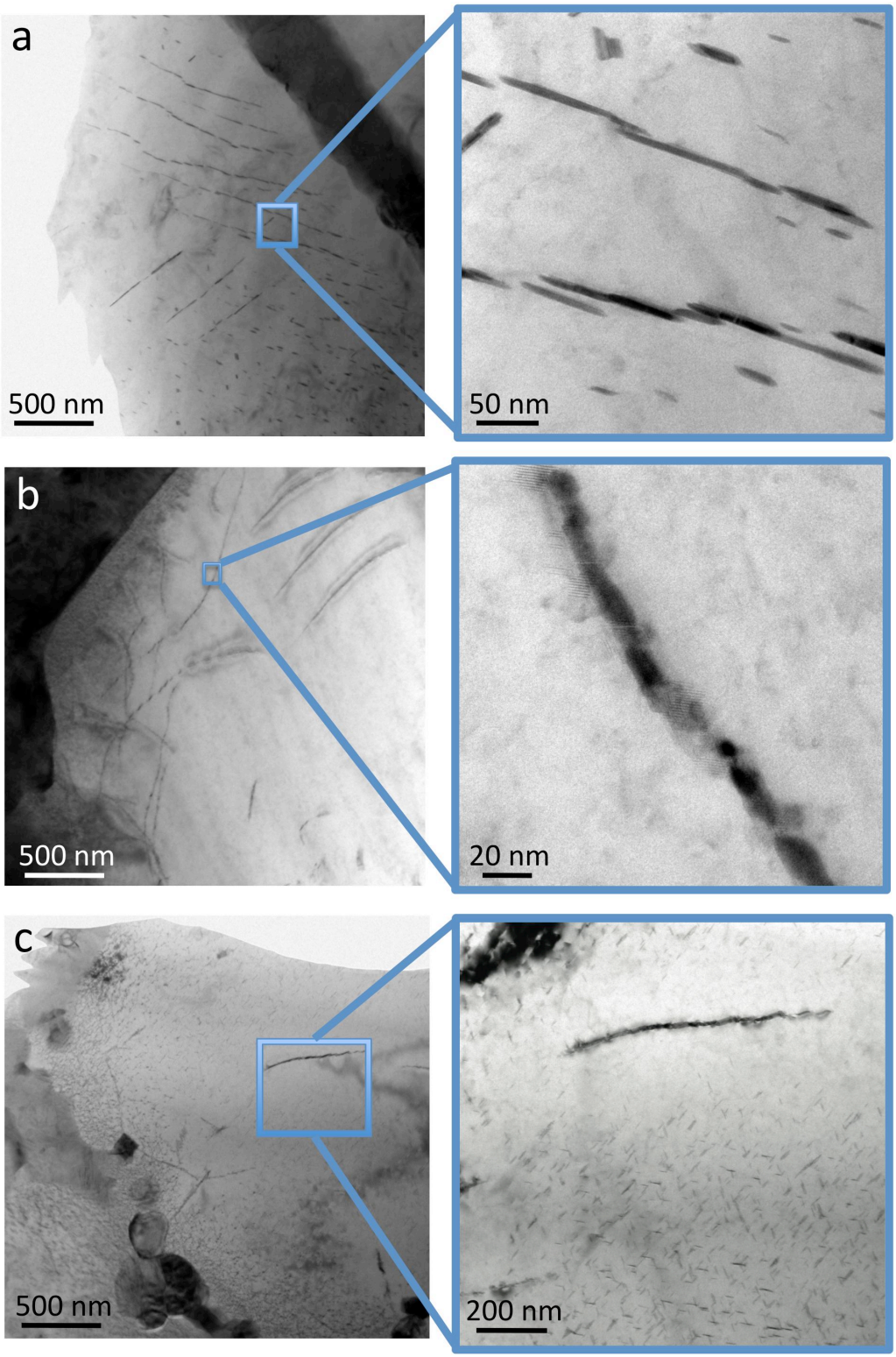

Figure 5.23: Dislocations in a) Mg-0.45La-0.63Nd and b) Mg-0.45La-1.18Y and c) Mg-0.45La-0.87Gd with higher resolution localised micrographs.

5.6 Discussion

5.6.1 Effect of Alloying Elements on Tensile Properties

At ternary concentrations greater than approximately 0.2 at.%, the 0.2 % PS of Mg-La-Nd alloys is greater than the two other alloy series. Caceres *et al.* [189] have modelled the yield strength (YS) of HPDC Mg alloys by attempting to determine the contribution to strength from key strengthening components in the alloys. The components include solid solution strengthening (σ_{ss}), grain boundary strengthening that is related to the Hall-Petch relationship (σ_{gb}) and grain boundary reinforcement present at grain and cell boundaries (referred to as dispersion strengthening by Caceres *et al.* [189]) from the intermetallic phase ($\Delta\sigma_{Mg\text{-}RE}$). Thus the following equation can be used to model the YS of the Mg-La-RE alloys:

$$\sigma_{Mg-La-RE} = \sigma_{ss} + \sigma_{gb} + \Delta\sigma_{Mg-RE} \quad \textbf{(5.1)}$$

Although modelling the contribution from each strengthening component is useful, this current work only intends to use the model given in Eq. (5.1) for qualitative analysis. The eutectic volume fraction of the three alloy series are relatively similar for a given ternary alloying addition (Figure 4.10), as is the average grain size and the intermetallic phase present in the eutectic in all three alloy series was confirmed to be predominantly $Mg_{12}RE$. However, there is a difference between the ratio of ternary RE to La in the eutectic where the Nd-containing alloys had the highest ratio of ternary RE to La (Figure 4.6). This information, in combination with the comparison of solid solubilities of Nd, Y or Gd in Mg (Table 2.3), can be used to indicate that Mg-La-Nd alloys have higher volume fractions of intermetallic phase than Mg-La-Y and Mg-La-Gd. Moreover, it has been shown by Zhang *et al.* [149] that a continuous intermetallic phase at grain boundaries may contribute between 20-30 MPa of strength to the yield strength of HPDC Mg-RE alloys. The highest concentrated Mg-La-Nd alloy has a greater degree of intermetallic phase connectivity between grains (Figure 4.1). Thus the greater amount of solid solution strengthening present in the Mg-La-Y and Mg-La-Gd alloys appear to be not as significant to the improvement of yield strength as the grain boundary strengthening in the Mg-La-Nd alloys from the increased concentration of Nd in the eutectic (Figure 4.6).

Using the predicted intermetallic phase volume fraction of Mg-La-Nd alloys (Figure 4.10), Figure 5.24 shows that 0.2% proof stress increases in Mg-La-Nd alloys with the increase in the volume fraction of intermetallic phase and elongation to fracture steadily decreases. From Chia *et al.* [18] a comparison can be made between the influence of the intermetallic phase in binary HPDC Mg-La and that of ternary HPDC Mg-La-Nd alloys on 0.2% proof stress and elongation. There is good correlation between the volume fraction of intermetallic phase in the binary Mg-La series and the Mg-La-Nd series with respect to 0.2% proof stress. However, the elongation to fracture values for Mg-La with greater than approximately 5 volume percent intermetallic phase are significantly lower than Mg-La-Nd alloys with comparable volume fractions of intermetallic phase.

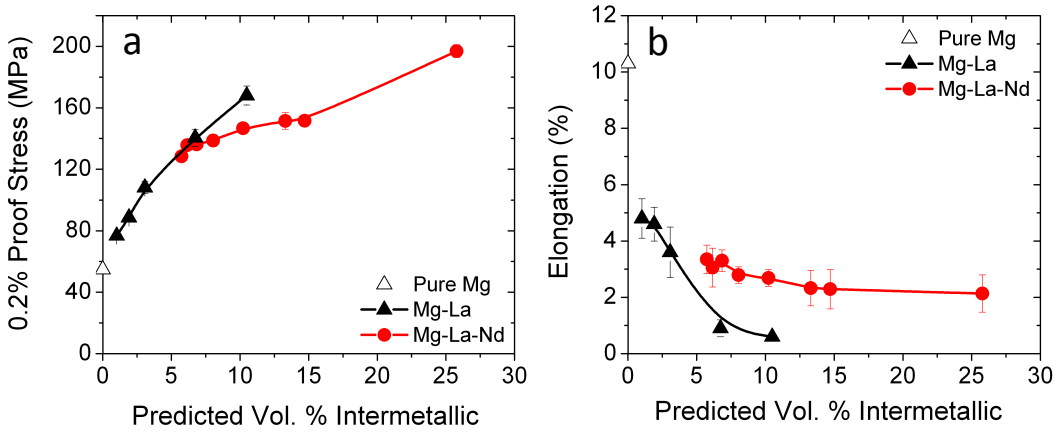

Figure 5.24: a) 0.2% proof stress and b) elongation at room temperature as a function of predicted volume fractions of eutectic or intermetallic phase in pure Mg, Mg-La from Chia *et al.* [18] and Mg-La-Nd alloys from the current work.

Chia *et al.* [18] concluded that yield strength and elongation in binary HPDC Mg-RE alloys are dependent on volume fraction and type of intermetallic phase. The increased 0.2% proof strength at room temperature in the Nd containing alloys, especially for concentrations of Nd greater than 0.2 at.%, can be attributed to the increased grain boundary reinforcement achieved from increased amounts of intermetallic phase [18, 190].

Elongation to fracture is shown to decrease with increasing fraction of intermetallic phase in the eutectic (Figure 5.24b). There does, however, appear to be some other influence on

elongation besides the volume fraction of intermetallic phase because the Mg-La-Nd alloys, with greater than 5 % volume fraction of intermetallic phase, have almost twice the elongation to fracture than the Mg-La alloys, with comparable volume fractions of intermetallic phase. This may simply be related to the variance in metal quality or casting defects between different cast batches, which has also been shown to cause other properties such as impact toughness to vary in binary HPDC Mg-Nd alloys [191]. Several authors have also noted that oxide bifilms [192, 193] or variations in porosity decrease elongation [194].

At 177°C, the as-cast 0.2% proof stress and elongation of Mg-La-Nd, Mg-La-Y and Mg-La-Gd alloys appear to be proportional to the concentration of ternary alloying additions. This is irrespective of what particular ternary RE element is used (Figure 5.4). This differs from the as-cast room temperature 0.2 % proof stress results (Figure 5.2), where the highest concentrated Nd alloy had a significantly higher 0.2 % proof stress than Mg-La-Y or Mg-La-Gd alloys, with comparable ternary RE concentrations. Zhang *et al.* [149] have shown that the morphology of the eutectic can play a significant role with respect to yield strength for Mg-RE alloys. From the morphology of the microstructure of the three relatively high concentrated alloys (Figure 4.5), the Mg-0.45La-0.63Nd alloy has a more continuous intermetallic phase in the eutectic than either Mg-0.45La-1.18Y or Mg-0.45La-0.87Gd. Thus the continuous intermetallic phase can lead to easier propagation of cracks throughout the alloy causing it to have lower yield strength.

The elevated temperature stress-strain curves of the three alloy series tested have a yield point elongation region (i.e. following yielding there is a plateau in the stress-strain curve [195]) (Figure 5.3). The yield point elongation is more clearly defined as the concentration of the ternary alloying addition increases and thus is more apparent in the Mg-0.45La-1.18Y and Mg-0.45La-0.87Gd alloys rather than in Mg-0.45La-0.63Nd. This feature is often present in stress-strain curves of low carbon steels and is attributed to Lüders band formation. The mechanism that produces this is dynamic strain ageing which is where dislocations are pinned by the “atmospheres” around interstitial atoms in the matrix of

the material. However, the cause of the yield point elongation is not completely understood in Mg alloys [184, 196]. Barnett *et al.* [184] have attempted to explain this phenomenon by attributing it to the formation of twins which propagate over the sample in a Lüders front. A relationship between grain size and the presence of yield point elongation has also been proposed in Al alloys [195, 197]. However, the alloys used in the present research have approximately equal average grain sizes but yield point elongation is more clearly defined in higher concentrated alloys. The classical understanding for the cause in Mg alloys, described by Kent and Kelly [198] using a Mg-0.5wt.%Th alloy, attributed the yield point elongation to "various forms of interaction between solute atoms and dislocations." This appears to be the most likely reason for the presence of elongated yield strength in the alloys investigated in the current work. Only alloys with relatively large amounts of solute in solid solution appear to have yield point elongations. However, further work is required to fully understand this phenomenon in the current set of alloys.

5.6.2 Effect of Alloying Elements on Hardening Response of As-Cast Alloys

The alloys with approximately 0.2 at.% ternary RE did not produce age hardening at ageing temperatures of 160°C or 200°C (Figure 5.7). Due to the relatively small amount precipitation in the alloys it is possible that there was an insufficient increase in hardness to distinguish from the relatively hard Mg-RE rich eutectic present at grain/cell boundaries. Yin *et al.* [199] demonstrated in another Mg-RE rich alloy (Mg-11Y-5Gd-2Zn-0.5Zr wt.%) that there was a difference of approximately 35 Vickers hardness between the eutectic (146.4 ± 5.4 HV) and the α-Mg matrix (111.2 ± 5.0 HV) in the as-cast condition. The increased amount of detectable precipitates in the alloys with greater than 0.2 at.% ternary RE do have an appreciable age hardness response, enough to become measureable even in the presence of a relatively hard Mg-La rich intermetallic.

The age hardening results of the alloys with relatively high concentrations of Nd, Y or Gd (Mg-0.45La-0.63Nd, Mg-0.45La-1.18Y and Mg-0.45La-0.87Gd) indicate that the Mg-La-Nd alloys reach peak ageing conditions before Mg-La-Y or Mg-La-Gd alloys but begin to overage relatively quickly soon after that point. This can be used as an indication that the

thermal diffusivity of Nd in solid solution is greater than Y or Gd in Mg. Whilst this did not appear to have a significant influence on the tensile properties at 177°C (Figure 5.4) there was a noticeable difference between the creep properties of Mg-La-Nd and Mg-La-Y or Mg-La-Gd alloys (Figure 5.8).

5.6.3 Effect of Alloying Elements on Creep Properties and Microstructure

For each alloy series creep tested, a clear improvement in creep properties (both time to failure and creep strain) was achieved with increasing concentration of the ternary alloying addition, up to approximately 0.2 at.% (Figure 5.9). In general, the Mg-La-Gd and Mg-La-Y alloys had similar creep properties with the exception of the low concentrated Mg-La-Gd, which failed prior to 400h when tested at 177°C and 90MPa. This is despite the difference in the morphology of the precipitates between Mg-La-Y and Mg-La-Gd alloys. The Mg-La-Nd alloy series was the least creep resistant when compared to the other two alloy series tested. None of the alloys with relatively low ternary alloying additions appear to have any resolvable precipitates dynamically nucleating from the matrix. There is also no evidence of precipitates nucleating on dislocations for the alloys with relatively low ternary alloying additions.

Zhu *et al.* [14] have previously shown for binary HPDC Mg-RE alloys that RE additions with higher solid solubility in Mg improve creep resistance. The results shown in the current work indicated that once a certain concentration of ternary RE is present any further increase in ternary RE does little to further improve creep properties (Figure 5.9). Gd has a significantly higher maximum solid solubility in Mg than Y (4.53 at.% and 3.60 at.%, respectively). However, both alloy series have very similar creep properties particularly for alloys with approximately 0.2 at.% or greater ternary alloying addition. Since there is a greater amount of solute in solid solution in the higher concentrated alloys, this indicates a limit to the strengthening that is achieved by solid solution strengthening. There is also a limit to the strengthening achieved by precipitation hardening. Precipitates also appear to improve creep properties but once again they also appear to reach a limit to their

ability to further improve properties. This is shown when a comparison is made between the creep properties and microstructure following creep testing. Both alloys with approximately 0.2 at.% ternary RE and those with much greater concentrations of ternary RE have similar creep properties even though the distribution of precipitates differs significantly (Section 5.5). The rate of the diffusion of the solute in solid solution, however, is shown to be of significant importance since the Mg-La-Nd alloys have the poorest creep properties and from the fast age hardness response of Mg-La-Nd alloys (Figure 5.6), Nd can be inferred to have a higher diffusion coefficient than either Y or Gd in Mg.

The volume fraction of eutectic was also relatively consistent between alloy series (Figure 4.10) for comparable ternary RE additions. Within individual series a relatively small difference between the volume fraction of eutectic in the least concentrated alloys and the medium or high concentrated alloys was detected. The results from the Mg-La-Nd alloys indicate that the improvement in creep resistance with increasing Nd concentration is independent of the volume fraction of eutectic. The creep properties continue to improve with increasing Nd concentration but the volume fraction of eutectic only increases from the low to medium concentrated alloys and remains approximately the same for the highly concentrated alloy.

Using the compression and tensile creep results, the stress exponent (n) was determined for the Mg-La-Nd and Mg-La-Y alloys. Stress exponents of 7.3 and 7.4 were determined for Mg-0.45La-0.63Nd and Mg-0.45La-1.18Y alloys, respectively. This indicates that the dislocation motion is a likely creep mechanism, in particular lattice diffusion-controlled dislocation climb as was similarly shown for Mg–1Ca–1Zn–0.6Zr (n = 7.2) [94]. Typically, minimum creep rates from compression and tensile experiments are not used in combination to determine stress exponents due to the difference in creep properties of the alloy when tested under compression in comparison to tension. In HPDC Mg-Al alloys such as AM60, Agnew *et al.* [186], and AM50, Xu *et al.* [185], compression creep results were shown to differ from tensile creep results when the alloys were tested under the

same conditions. They proposed that compression creep tests resulted in minimising the precipitation of the thermally unstable β-$Mg_{17}Al_{12}$ phase, which has been attributed to poor elevated temperature creep properties. However due to the good correlation between compressive and tensile creep results in the current work, both sets of data were used. This is likely due to the similarity of the microstructure, in particular eutectic volume fraction and precipitate phase and distribution within the alloys tested under compression or tension Figures 5.16 and 5.17.

5.7 Conclusions

There is a significant effect on the creep properties of Mg-La based alloys in relation to which ternary RE is added to the Mg-0.45La base alloy.

- The relatively fast diffusion of Nd in the α-Mg matrix contributes to the poor creep resistance of the Mg-La-Nd alloys in comparison to Mg-La-Y and Mg-La-Gd alloys. This results in larger precipitates in Mg-La-Nd alloys than Mg-La-Y or Mg-La-Gd alloy with comparable ternary RE additions.
- The microstructure observations following creep testing of the alloys reveal that all alloys with approximately 0.2 at.% (or greater) ternary RE can form dynamic precipitates. This helps to show that it is not only the mere presence of dynamic precipitates that is important for creep resistance but rather thermal stability of the precipitates and ultimately of the solute in solid solution that is important.
- The thermal stability of the solute is solid solution is particularly important since the creep mechanism was indicated to be related to diffusion-controlled dislocation climb.

6 Effects of Heat Treatment on Mechanical Properties and Creep on Mg-La-RE Alloys

6.1 Introduction 135

6.2 Ageing Response of Solution Treated HPDC Mg-La-RE Alloys 136

6.3 Tensile Properties of Heat Treated HPDC Mg-La-RE Alloys 138

6.4 Creep Properties of Heat Treated HPDC Mg-La-RE Alloys 144

6.5 Microstructures of Heat Treated HPDC Mg-La-RE Alloys 150
6.5.1 Surface After Solution Treatment 150
6.5.2 Microstructure After Heat Treatment 151
6.5.3 Microstructure After Heat Treatment and Creep Testing 153

6.6 Discussion 166
6.6.1 Heat Treatment of HPDC Mg-La-RE Alloys 166
6.6.2 Age Hardening Response 167
6.6.3 Influence of Heat-Treatment on Tensile Properties of HPDC Mg-La-RE Alloys 168
6.6.4 Precipitates in Mg-La-RE Alloys following Heat Treatment and Creep 170
6.6.5 Influence of Heat Treatment on Creep Properties and Microstructure 171

6.7 Conclusions 174

6.1 Introduction

In Chapter 5, three Mg-La-RE alloy series were mechanically tested in the as-cast condition and their microstructures were investigated following creep testing. The effect of alloying additions and their concentration was the primary focus of the chapter. The thermal stability of dynamic precipitates was concluded to be an important factor on creep properties of the Mg-La-Nd alloys and Mg-La-Y and Mg-La-Gd alloys, which had more thermally stable precipitates.

Further work is required to attempt to isolate the influences from other microstructural features/components/properties of the alloys. This includes:

- What influence does the strength of the continuous intermetallic phase present in the eutectic at grain boundaries play on creep properties?
- Can solid solution strengthening be used as the primary method to improve creep properties?
- Can static precipitates improve creep properties when there is little to no grain boundary reinforcement from the eutectic?

These points will be addressed by heat-treating alloys in each alloy series in order to isolate the influences of precipitation hardening, solid solution strengthening or grain boundary reinforcement. In Chapter 5, it was shown that even though the Mg-La-RE alloys with approximately 0.2 at.% ternary RE did not show an age hardness response they did still form dynamic precipitates during creep testing. Alloys with greater ternary RE concentrations showed both an age hardness response and the presence of dynamic precipitates. Consequently, three levels of ternary RE were investigated:

- A relatively low concentration of ternary RE (approximately 0.1 at.%).
- A medium level concentration that correlated with ternary RE concentration where the minimum creep rate in the three alloy series reached its minimum (approximately 0.2 at.%).
- Finally, a relatively high concentration of ternary RE (approximate or greater than the solubility limit at 177°C in Mg).

These ternary RE concentrations were chosen in order to identify the influence of solid solution strengthening and/or precipitation hardening on mechanical and creep properties. The alloys with less than 0.2 at.% ternary RE alloys are ideal for determining the influence of eutectic/intermetallic phase at grain boundaries with regards to mechanical and creep properties because they contain a minimal amount of RE in solid solution. They can also be used to compare the influence of a lack of precipitation hardening and/or solid solution strengthening has on the properties of the alloys.

6.2 Ageing Response of Solution Treated HPDC Mg-La-RE Alloys

In Chapter 5 it was shown that no age hardening response occurred in Mg-La-RE alloys with approximately 0.2 at.% ternary RE at 160°C or 200°C (Figure 5.7). As a result of this, heat treatments in this chapter are concentrated on alloys with higher concentrations of ternary RE. Specifically, the age hardness response of the alloys with the higher ternary concentration, Mg-0.45La-0.63Nd, Mg-La-0.45La-1.18Y and Mg-0.45La-0.87Gd following solution treatment at 520°C for 1 h will be investigated in this section. The duration of the solution treatment was determined using the approximation for diffusion from Fick's 1st Law [20],

$$x \approx \sqrt{Dt} \qquad \textbf{(6.1)}$$

where x = diffusion distance (m),

D = diffusion rate (m^2/s), and

t = time (s).

An estimate of the time required for diffusion at 520°C throughout an entire grain is made. No information in the literature was found for the diffusion of Nd, Y and Gd in Mg so the diffusion coefficient (D_o) and activation energy (Q) of Ce in Mg (0.045 m^2/s, 175.8kJ/mol respectively [12]) were used to estimate the diffusion rate at 520°C to be 1.168×10^{-13} m^2/s using the Arrhenius type equation for diffusivity shown below

$$D = D_o \exp\left(-\frac{Q_c}{RT}\right) \qquad \textbf{(6.2)}$$

This is an acceptable approximation for the diffusion of Nd, Y or Gd in Mg since Ce has approximately the same atomic radii, 0.18247 nm for Ce and 0.18214 nm, 0.18012 nm and 0.18013 nm for Nd, Y and Gd, respectively [131]. Using 10 µm as the average cell (dendrite size), the diffusion time was calculated to be ≈ 0.25 h. To take into account the difference (increase) in cell size closer to the 'core' of the sample a solution treatment time of 1 h was used**.**

Mg-0.45La-0.63Nd, Mg-0.45La-1.18Y and Mg-0.45La-0.87Gd alloys were aged at 160°C or 177°C following solution treatment at 520°C for 1 h and water quenching. It is surprising that the Mg-0.45La-1.18Y alloy took approximately 2300 h longer to reach peak hardness at 177°C than it did at 160°C. The age hardening tests were repeated for Mg-0.45La-1.18Y at both 160°C and 177°C following solution treatment at 520°C for 1 h and water quenching in order to confirm the unexpected ageing response (Figure 6.1) i.e. the earlier onset of peak hardness at 160°C.

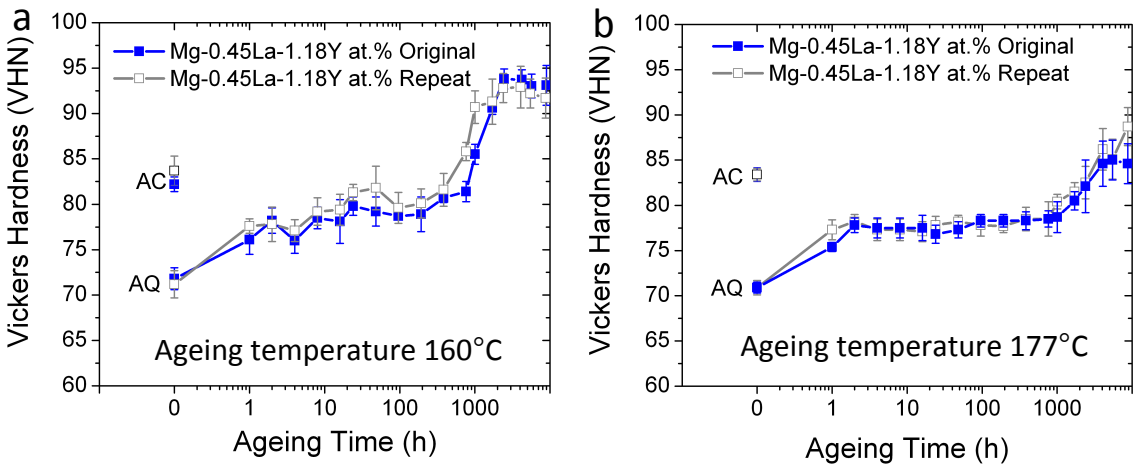

Figure 6.1: Repeated age hardening response of Mg-0.45La-1.18Y solution treated at 520°C for 1 h and aged at a) 160°C or b) 177°C. Note: AC = as-cast and AQ = as-quenched.

The peak hardness at 160°C was reached at 100, 1700 and 1100 h for Mg-0.45La-0.63Nd, Mg-0.45La-1.18Y and Mg-0.45La-0.87Gd alloys, respectively. When the same alloy compositions were aged at 177°C following solution treatment and water quenching, the peak hardness was reached at 16, 4000 and 400 h, respectively (Figure 6.2).

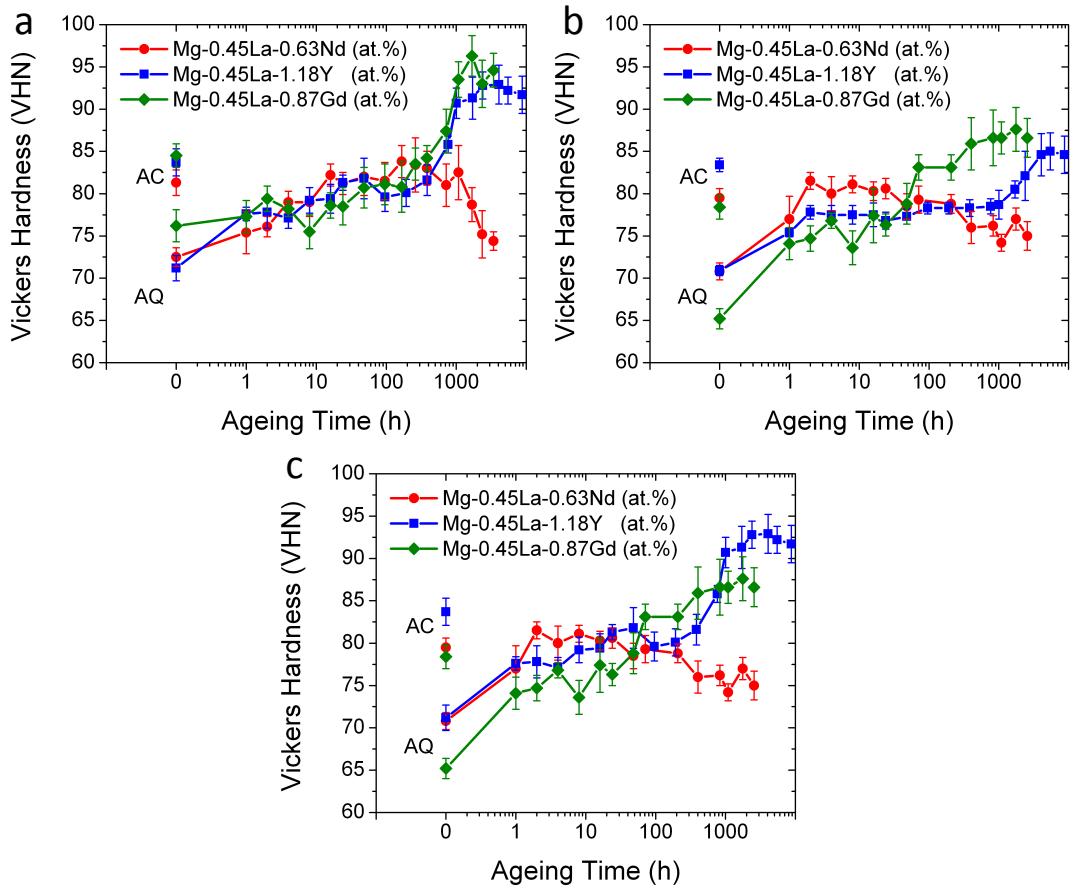

Figure 6.2: Age hardening response for Mg-0.45La-0.63Nd, Mg-0.45La-1.18Y and Mg-0.45La-0.87Gd following solution treatment at 520°C for 1 h and then aged at a) 160°C or b) 177°C. Note c) is a combination of the 177°C ageing curves of the Mg-La-Nd and Mg-La-Gd alloys with the 160°C ageing curve of the Mg-La-Y alloy. Note: AC = as-cast and AQ = as-quenched.

6.3 Tensile Properties of Heat Treated HPDC Mg-La-RE Alloys

The influence of solution treatment (T4) at 520°C for 1 h and also solution treatment at 520°C for 1 h, water quenching and then peak ageing (T6) at 177°C (or 160°C for Y-containing alloys) on tensile strength for each of the alloy systems investigated in this thesis are presented in this section. Alloys with relatively low (approximately 0.1 at.%) ternary RE and intermediate (approximately 0.2 at.%) are also heat treated and tensile tested in addition to alloys with relatively high concentrations of ternary RE. It is important to investigate the properties of the low and intermediate concentrated alloys to determine what influence, if any, would alloys with little to no solid solution

strengthening and/or precipitation hardening have on tensile properties. The low and medium concentrated alloys can thus be used to determine what influence the eutectic or the intermetallic phase at grain boundaries has on tensile properties since there is a minimal influence from other strengthening factors. In addition to this, due to the alloys being solution treated for only a relatively short period of time the average grain size in the alloys does not change (see Section 6.5) which is another variable that can influence strength [200]. Lastly, since all the alloys tensile tested in this chapter were also creep tested following the same heat treatments it is also important to know the yield strength (or in this case the 0.2% PS) to understand the creep properties of these alloys (in particular in the early stages of creep). Tensile property values at room temperature and 177°C including 0.2 % PS, ultimate tensile strength and elongation to fracture are presented in Appendix B for alloys in the T4 and T6 heat treated conditions as well as in the as-cast condition for comparison.

There is little improvement to as-cast 0.2% PS or ultimate tensile strength (UTS) when Mg-La-Nd alloys are subjected to a T4 or T6 heat treatment, in fact they are often lower than in the as-cast condition particularly at lower concentrations (Table 6.1).

Table 6.1: Tensile properties at 177°C of Mg-La-Nd alloys in as-cast, T4 and T6 conditions.

Alloy Composition at.%	Condition	0.2% PS ±SD MPa	UTS ±SD MPa	%Elong. ±SD
Mg-0.47La-0.10Nd	As-Cast	103.4 (± 0.9)	126.5 (± 1.6)	11.9 (± 2.2)
Mg-0.47La-0.10Nd	T4	84.1 (± 2.7)	122.3 (± 1.7)	16.3 (± 1.9)
Mg-0.47La-0.10Nd	T6	92.4 (± 1.3)	125.9 (± 2.0)	13.5 (± 1.6)
Mg-0.43La-0.18Nd	As-Cast	111.2 (± 2.3)	143.4 (± 1.9)	19.1 (± 1.8)
Mg-0.43La-0.18Nd	T4	83.0 (± 1.6)	131.4 (± 5.4)	12.7 (± 4.6)
Mg-0.43La-0.18Nd	T6	96.0 (± 1.5)	135.3 (± 1.1)	9.3 (± 1.1)
Mg-0.45La-0.63Nd	As-Cast	134.4 (± 2.0)	175.8 (± 4.1)	5.6 (± 1.0)
Mg-0.45La-0.63Nd	T4	126.5 (± 3.2)	191.1 (± 3.5)	11.5 (± 1.0)
Mg-0.45La-0.63Nd	T6	144.9 (± 2.3)	201.3 (± 3.4)	6.4 (± 1.4)

It is only at relatively high concentrations of Nd (as in Mg-0.45La-0.63Nd) that some small improvements to 0.2% PS and UTS are achieved with an increase in 0.2% PS from the as-

cast condition, 134.4 (±2.0) MPa, to the T6 condition, 144.9 (±2.3) MPa (Table 6.1). There is an improvement in the elongation to fracture as a result of there being a less continuous brittle intermetallic phase present at the grain boundaries, which will be shown in Section 6.5. There is a yield "plateau" or yield point elongation [184] present in the as-cast Mg-0.43La-0.18Nd, but this is less apparent following either a T4 or T6 treatment immediately following the elastic region of the stress-strain curves (Figure 6.3). However, for Mg-0.45La-0.63Nd sample a T4 solution treatment resulted in an increase in yield point elongation (Figure 6.3c).

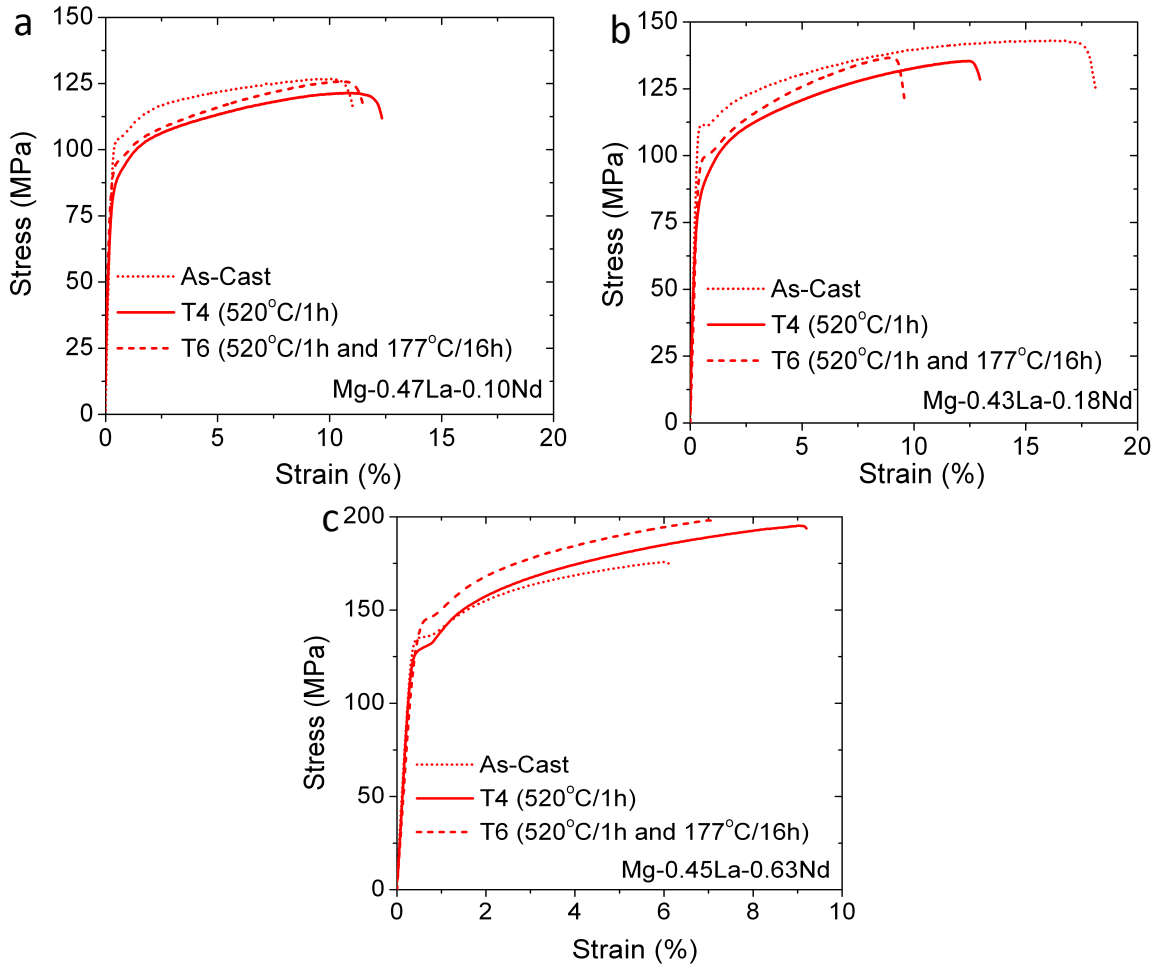

Figure 6.3: Stress-strain curves at 177°C for a) Mg-0.47La-0.10Nd, b) Mg-0.43La-0.18Nd and c) Mg-0.45La-0.63Nd in T4 (520°C/1h) and T6 (520°C/1h and 177°C/16h) conditions. As-cast stress-strain curves are also included for comparison. Note: There is a change in scale size in c) for clarity.

The 0.2% PS for the T4 or T6 treated Mg-La-Y alloys was not improved significantly. In fact, it was generally worse than that of the alloys in the as-cast condition, (Table 6.2). This is similar to the tensile results for the T4 and T6 treated Mg-La-Nd alloys.

Table 6.2: Tensile properties at 177°C of Mg-La-Y alloys in as-cast, T4 and T6 conditions.

Alloy Composition at.%	Condition	0.2% PS ±SD MPa	UTS ±SD MPa	%Elong. ±SD
Mg-0.48La-0.12Y	As-Cast	108.0 (± 1.0)	137.7 (± 2.2)	19.5 (± 3.2)
Mg-0.48La-0.12Y	T4	85.7 (± 1.5)	127.8 (± 1.6)	23.4 (± 2.9)
Mg-0.48La-0.12Y	T6	91.9 (± 2.6)	132.8 (± 2.5)	19.8 (± 2.0)
Mg-0.49La-0.24Y	As-Cast	112.8 (± 1.5)	153.0 (± 2.5)	14.2 (± 2.3)
Mg-0.49La-0.24Y	T4	87.2 (± 0.3)	145.4 (± 1.0)	21.5 (± 1.8)
Mg-0.49La-0.24Y	T6	98.8 (± 1.3)	145.0 (± 1.5)	15.1 (± 1.2)
Mg-0.45La-1.18Y	As-Cast	150.6 (± 1.4)	205.7 (± 3.6)	5.3 (± 0.8)
Mg-0.45La-1.18Y	T4	134.8 (± 2.2)	219.0 (± 12.2)	9.1 (± 3.4)
Mg-0.45La-1.18Y	T6	177.7 (± 6.2)	248.2 (± 7.6)	5.5 (± 1.4)

At relatively low and medium Y additions (Mg-0.48La-0.12Y and Mg-0.49La-0.24Y respectively) neither T4 nor T6 heat treatments improved the as-cast 0.2% PS or UTS of the alloys (Figure 6.4). There was some improvement to the elongation to fracture in these two alloys following a T4 heat treatment. In Mg-0.48La-0.12Y the elongation to fracture increased from 19.5 ± 3.2 % to 23.4 ± 2.9 % and for Mg-0.49La-0.24Y from approximately 14.2 ± 2.3 % to 21.5 ± 1.8 % (Table 6.2).

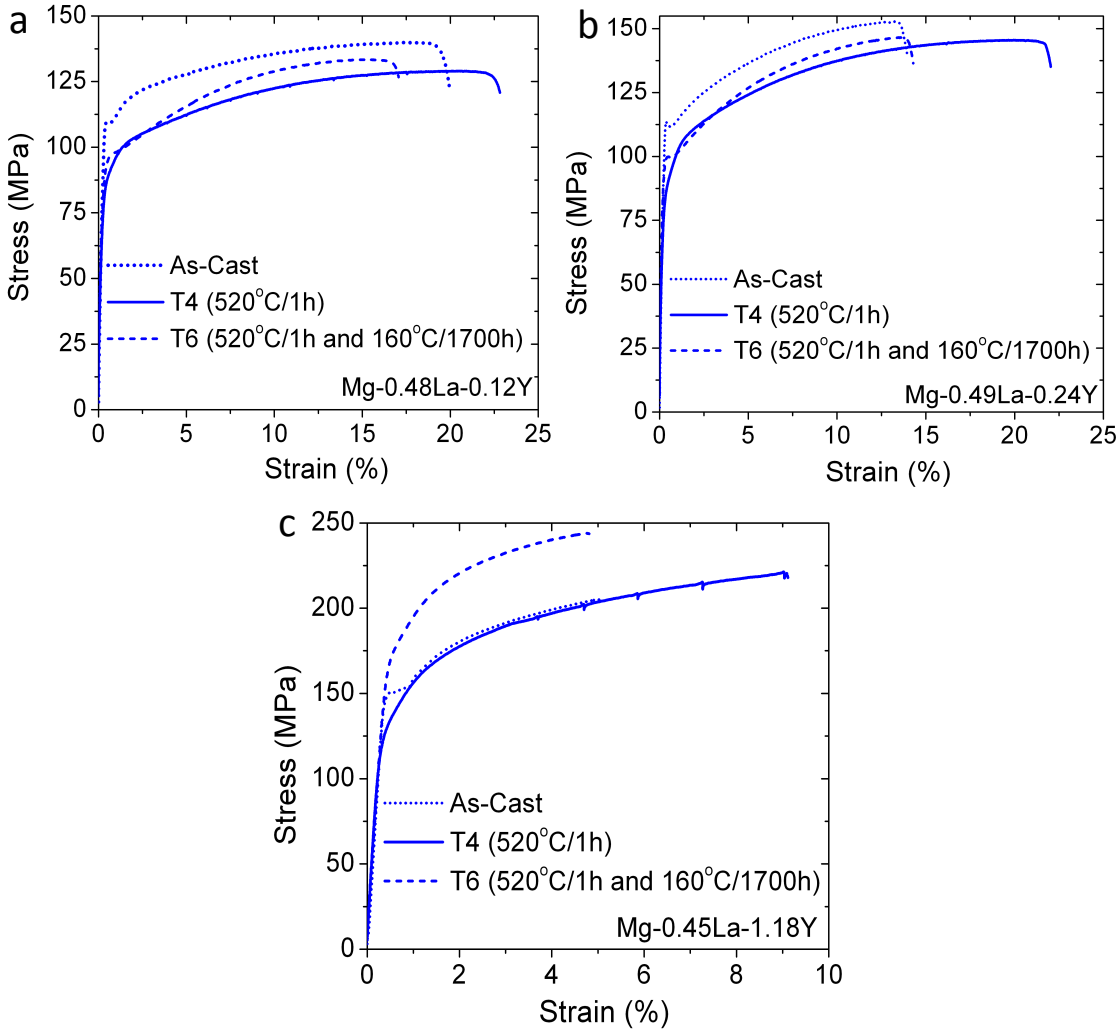

Figure 6.4: Stress-strain curves at 177°C for a) Mg-0.48La-0.12Y, b) Mg-0.49La-0.24Y and c) Mg-0.45La-1.18Y in T4 (520°C/1h) and T6 (520°C/1h and 160°C/1700h) conditions. As-cast stress-strain curves are also included for comparison. Note: There is a change in scale size in c) for clarity.

Once again the exception to this result is the alloy with the highest addition of ternary RE concentration tested, Mg-0.45La-1.18Y, where a significant improvement to the 0.2% PS following a T6 heat-treatment was observed (Figure 6.4c). The average 0.2% PS at 177°C for as-cast Mg-0.45La-1.18Y was 150.6 ± 1.4 MPa and after T6 heat treatment it was 177.7 ± 6.2 MPa. It is also interesting to note that the stress-strain curve for Mg-0.45La-1.18Y, following a T4 heat treatment, has a serrated flow, which is indicative of the Portevin-Le Chatelier effect [201].

For the Mg-La-Gd series, it is again shown that a T4 or T6 heat treatment does little to improve the 0.2% PS or UTS. There is no improvement to 0.2% PS or UTS following heat treatment in the low (Mg-0.45La-0.10Gd) or intermediate (Mg-0.46La-0.21Gd) Gd concentrated alloys (Table 6.3). However, when relatively high concentrations of Gd are added (as in Mg-0.45La-0.87Gd) a T6 heat treatment increased the average 0.2% PS at 177°C from 140.2 ± 4.6 MPa (in the as-cast condition) to 208.3 ± 8.8 MPa (Table 6.3). The Portevin-Le Chatelier effect was also detected in Mg-0.45La-0.87Gd in the T4 condition (Figure 6.5).

Table 6.3: Tensile properties at 177°C of Mg-La-Gd alloys in as-cast, T4 and T6 conditions.

Alloy Composition	Condition	0.2% PS (±SD) MPa	UTS ±SD (MPa)	%Elong. (±SD)
Mg-0.45La-0.10Gd	As-Cast	100.6 (± 1.4)	129.3 (± 3.0)	16.2 (± 4.6)
Mg-0.45La-0.10Gd	T4	87.1 (± 2.6)	127.8 (± 1.6)	20.0 (± 3.9)
Mg-0.45La-0.10Gd	T6	92.3 (± 0.6)	124.6 (± 1.3)	15.4 (± 3.4)
Mg-0.46La-0.21Gd	As-Cast	110.9 (± 1.7)	151.1 (± 2.5)	12.3 (± 0.8)
Mg-0.46La-0.21Gd	T4	82.1 (± 2.2)	145.0 (± 2.1)	15.9 (± 2.1)
Mg-0.46La-0.21Gd	T6	103.5 (± 0.4)	141.7 (± 8.6)	10.0 (± 3.0)
Mg-0.45La-0.87Gd	As-Cast	140.2 (± 4.6)	192.9 (± 2.1)	5.4 (± 0.4)
Mg-0.45La-0.87Gd	T4	127.0 (± 2.8)	205.3 (± 5.9)	10.1 (± 0.6)
Mg-0.45La-0.87Gd	T6	208.3 (± 8.8)	243.3 (± 7.7)	2.4 (± 0.8)

Solution treatment alone does not improve the 0.2% PS of Mg-0.45La-0.87Gd, there was a drop in the 0.2% PS from the as-cast condition, 140.2 ± 4.6 MPa, to the T4 condition, 127.0 ± 2.8 MPa. T6 heat treatment has a significant effect on the 0.2% PS for the Mg-0.45La-0.87Gd, this being 208.3 ± 8.8 MPa. The elongation to fracture results of the T6 treated Mg-0.45La-0.87Gd specimens are worse than those in the as-cast condition, 5.4 ± 0.4 % in the as-cast condition and 2.4 ± 0.8 % in the T6 condition (Table 6.3).

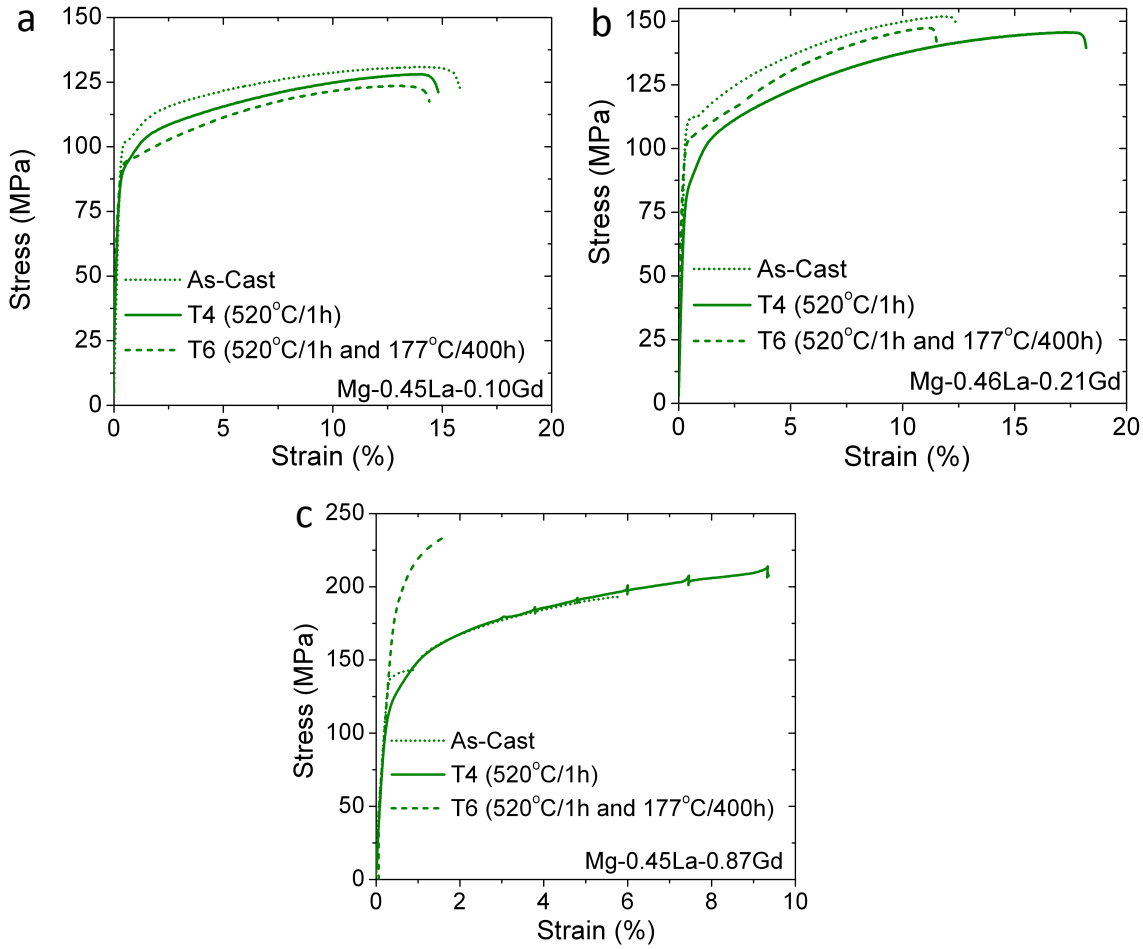

Figure 6.5: Stress-strain curves at 177°C for a) Mg-0.45La-0.10Gd, b) Mg-0.46La-0.21Gd c) Mg-0.45La-0.87Gd in T4 (520°C/1h) and T6 (520°C/1h and 177°C/400h) conditions. As-cast stress-strain curves are also included for comparison. Note: There is a change in scale size in c) for clarity.

Yield point elongations are also less defined or non-existent in the alloys tested following a T4 or T6 heat treatment. This is consistent with the hypothesis that yield point elongation is related to dynamic strain ageing as discussed in Chapter 5.

6.4 Creep Properties of Heat Treated HPDC Mg-La-RE Alloys

The creep strain results for the Mg-La-Nd alloys, show that, in general, the solution treatment (T4) or solution treatment and then peak ageing (T6) of Mg-0.47La-0.10Nd and Mg-0.43La-0.18Nd alloys resulted in poorer creep properties than those in the as-cast condition (Figure 6.6a and b). However, this is not the case for the highest concentrated

Nd-containing alloy Mg-0.45La-0.63Nd (Figure 6.6c). Following a T4 or T6 heat treatment, the Mg-0.47La-0.10Nd alloy failed in less than 40 and 60 h, respectively, which is approximately 67% and 50% faster than in the as-cast condition (Figure 6.6a). Increasing the concentration of Nd to 0.18 at.% improves the creep response of the alloys which were T4 or T6 heat treated but the as-cast Mg-La-Nd alloy still has a significantly better creep response (Figure 6.6b). However, even with an addition of 0.63 at.%Nd, solution treatment alone does not improve the creep strain response of the alloy. Only after a T6 heat treatment was a slight improvement to the creep response at 177°C and 90 MPa observed, compared with the as-cast alloy (Figure 6.6c). Following 600 h of creep testing at 177°C and 90MPa both the as-cast and T6 Mg-0.45La-0.63Nd samples experienced approximately the same creep strain, approximately 3.5 %.

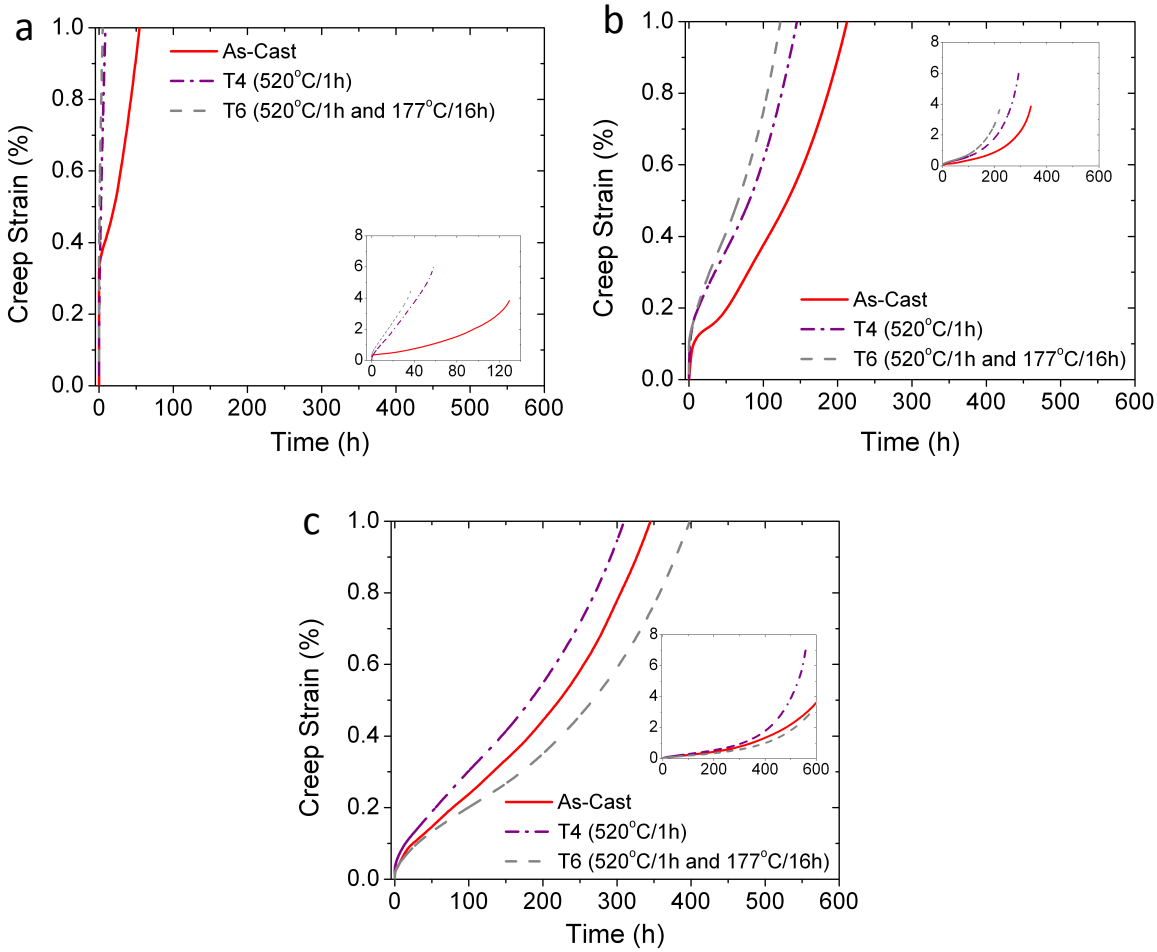

Figure 6.6: Creep strain comparisons of as-cast, T4 (520°C/1h) and T6 (520°C/1h and 177°C/16h a) for Mg-0.47La-0.10Nd, b) Mg-0.43La-0.18Nd and c) Mg-0.45La-0.63Nd alloys creep tested at 177°C and 90MPa.

The most significant difference between as-cast and heat treated Mg-La-Nd alloys is shown in the relatively low ternary concentrated alloys such as Mg-0.45La-0.10Nd (Figure 6.7). At approximately 0.1 at.% Nd the minimum creep rate for the T4 and T6 conditions is approximately 1 order of magnitude higher (worse) than in the as-cast condition, approximately 8 x 10^{-7} for the T4 and T6 conditions and 8 x 10^{-8} for the as-cast condition. At higher concentrations the creep response is very similar.

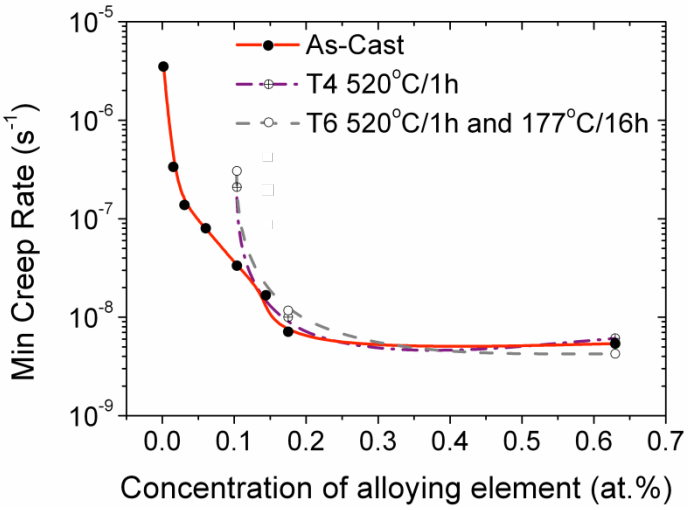

Figure 6.7: Comparison of minimum creep rates as a function of ternary addition concentration in the as-cast, T4 (520°C/1h) and T6 (520°C/1h and 177°C/16h) for the Mg-La-Nd alloy series and creep tested at 177°C and 90MPa.

The relatively low Y concentrated alloy, Mg-0.48La-0.12Y, in a T4 or T6 condition has significantly poorer creep strain response than that in the as-cast condition. In the as-cast condition the Mg-0.48La-0.12Y sample experiences approximately 1 % creep strain following 600 h of creep testing while the T4 equivalent alloy failed after approximately 200 h. A comparison between the as-cast and heat-treated creep strain properties shows that even for Y additions of up to 0.24 at.%, there is also a negative impact on creep strain by a T4 or T6 heat treatment (Figure 6.8b). The negative impact of a T4 heat treatment on Mg-0.49La-0.24Y is mostly noticeable due to the reduction in the 0.2 % PS to 85.7 MPa (in comparison 108.0 MPa in the as-cast condition), which results in the alloy experiencing approximately 1 % strain upon the application of a 90 MPa stress. The remainder of the creep strain curve for the Mg-0.49La-0.24Y T4 sample follows the same trend as its as-

cast counterpart (however, with a higher creep strain). There is no significant difference between the creep properties of the as-cast, T4 or T6 Mg-0.45La-1.18Y samples.

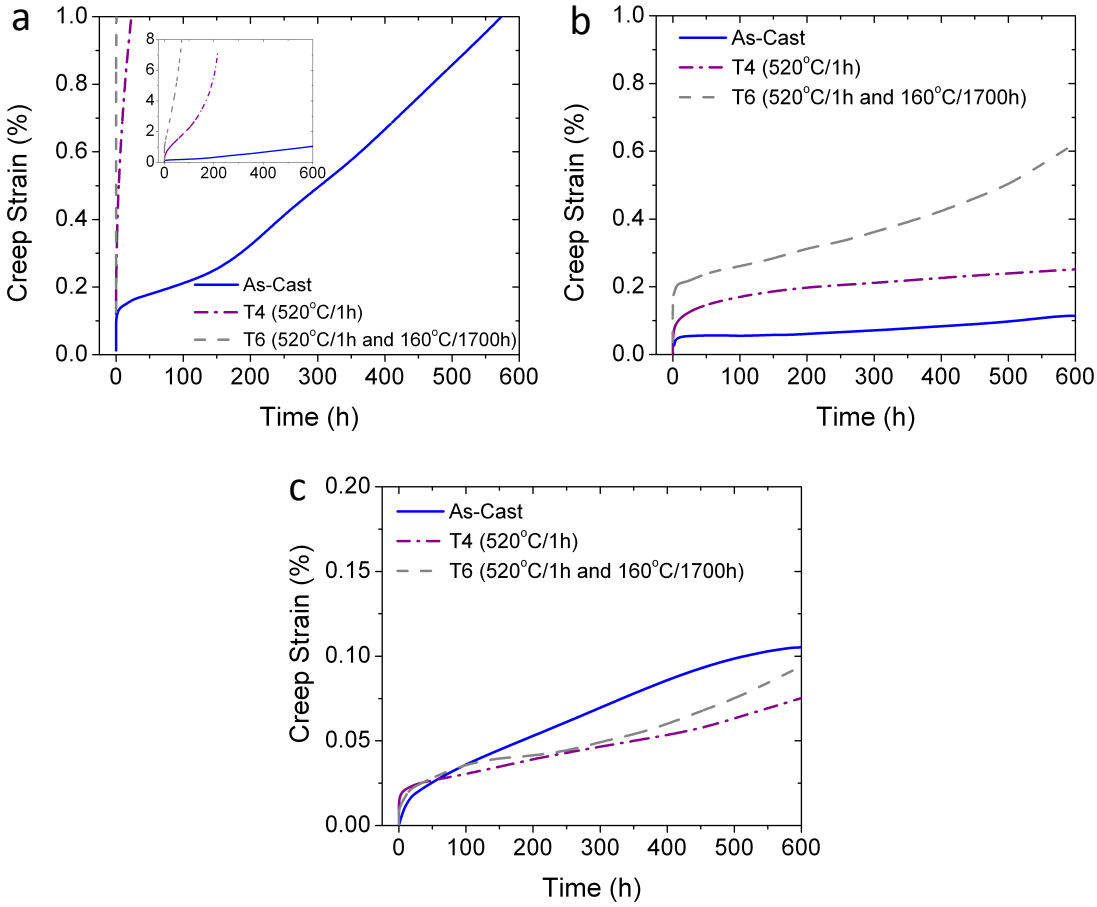

Figure 6.8: Creep strain comparisons of as-cast, T4 (520°C/1h) and T6 (520°C/1h and 160°C/1700h) for a) Mg-0.48La-0.12Y, b) Mg-0.49La-0.24Y and c) Mg-0.45La-1.18Y alloys creep tested at 177°C and 90MPa. Note: There is a change in scale for c) for clarity.

The comparison of the minimum creep rate for Mg-La-Y alloys in as-cast, T4 and T6 conditions (Figure 6.9) shows that the Mg-0.48La-0.12Y as-cast alloy has a minimum creep rate of at least 1 order of magnitude lower than that for the T4 or T6 heat treated alloys (similar to the low concentrated Mg-La-Nd alloy). It is interesting to note for the higher concentrated Mg-La-Y alloys, once the heat-treated alloys reach their respective minimum creep rates, there is no significant difference to the as-cast minimum creep rate.

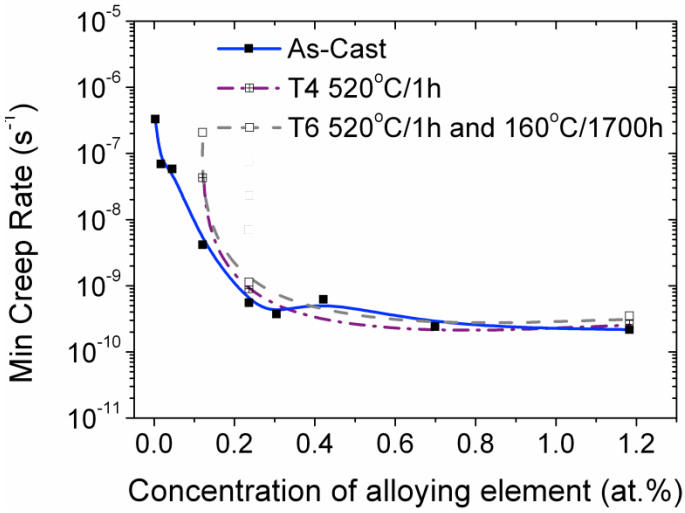

Figure 6.9: Comparison of minimum creep rates as a function of ternary addition concentration in the as-cast, T4 (520°C/1h) and T6 (520°C/1h and 160°C/1700h) for the Mg-La-Y alloy series and creep tested at 177°C and 90MPa.

Increasing the concentration of Gd in Mg-La-Gd reduces the difference between the creep response for the T4 and T6 alloys in relation to the as-cast alloy, as was also observed in the Mg-La-Nd and Mg-La-Y alloys. For relatively low concentrations of Gd in the Mg-La-Gd alloys (Mg-0.45La-0.10Gd) that have been a T4 or T6 heat treatment, the time to fracture reduced from approximately 400 h to less than 100 h (Figure 6.10a). When the concentration of Gd was increased to 0.21 at.% (Mg-0.46La-0.21Gd) the alloy does not fracture even up to 600 h of creep testing at 177°C and 90 MPa in either T4, T6 or as-cast conditions (Figure 6.10b). It is also found that at relatively high concentrations of Gd (such as for Mg-0.45La-0.87Gd) that there is no significant difference between the creep responses of T4, T6 or as-cast alloys, which is similar to the higher concentrated Mg-La-Y alloy.

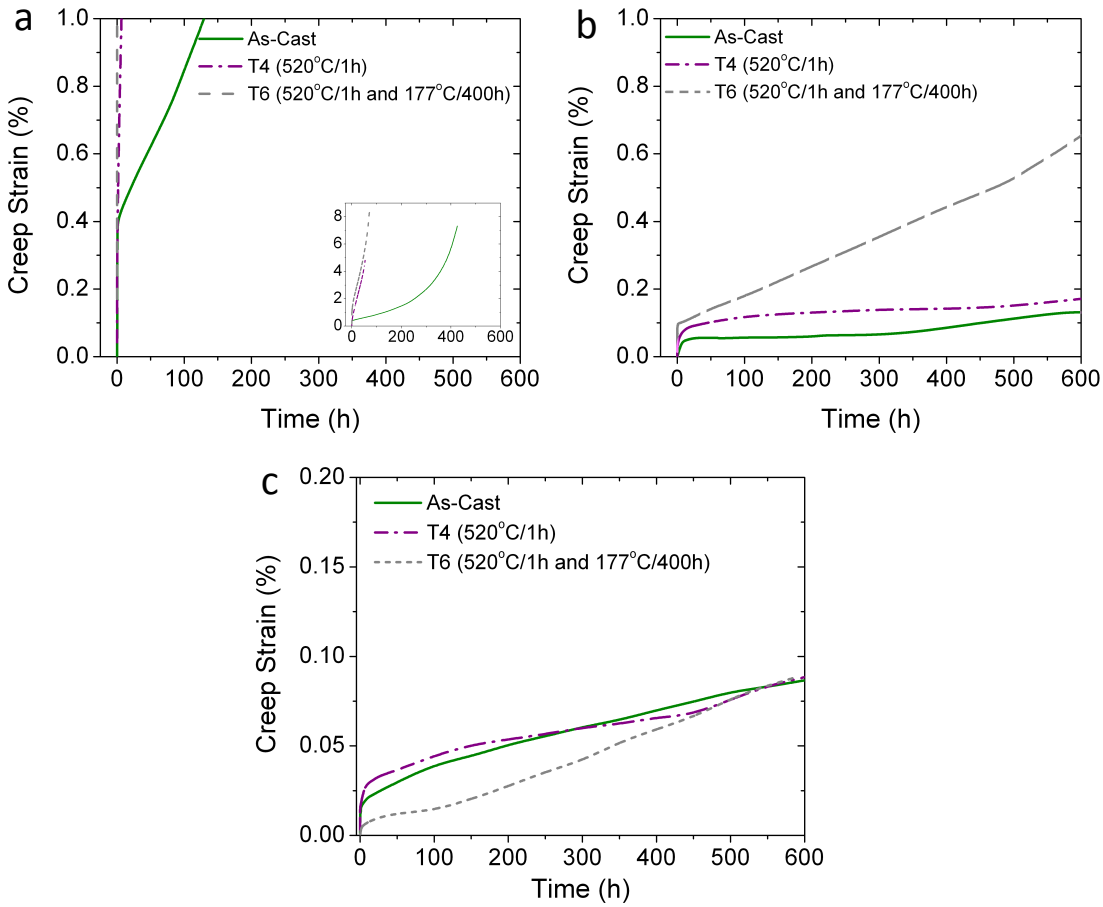

Figure 6.10: Creep strain comparisons of as-cast, T4 (520°C/1h) and T6 (520°C/1h and 177°C/400h) for a) Mg-0.45La-0.10Gd, b) Mg-0.46La-0.21Gd c) Mg-0.45La-0.87Gd alloys creep tested at 177°C and 90MPa. Note: There is a change in scale for c) for clarity.

No significant difference to minimum creep rate was measured between the T4, T6 and as-cast conditions for the alloys with greater than 0.2 at.% ternary RE, which is similar to the previous results shown for the Mg-La-Nd and Mg-La-Y alloys (Figure 6.11). The relatively low concentrated Mg-La-Gd alloys in the T4 and T6 conditions have approximately 1 order of magnitude higher minimum creep rates when compared with that of the as-cast condition, approximately 9 x 10^{-6} s^{-1} for T4 and T6 alloys and 1 x 10^{-8} s^{-1} for the as-cast condition.

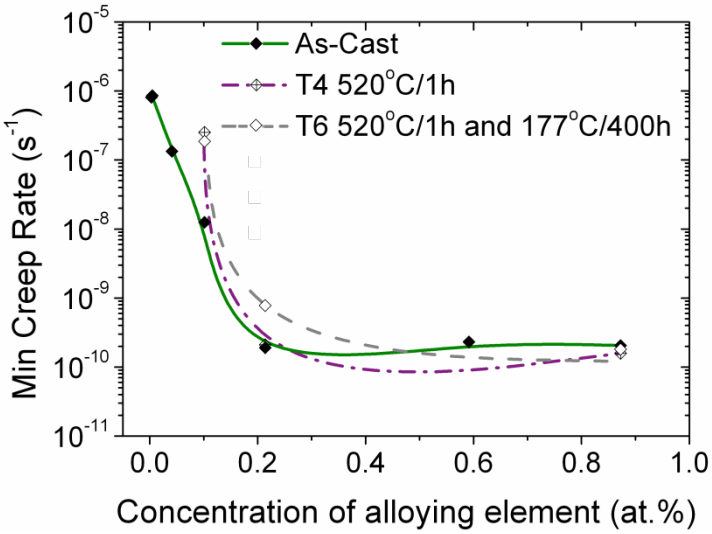

Figure 6.11: Comparison of minimum creep rates as a function of ternary addition concentration in the as-cast, T4 (520°C/1h) and T6 (520°C/1h and 177°C/400h) for the Mg-La-Gd alloy series and creep tested at 177°C and 90MPa.

6.5 Microstructures of Heat Treated HPDC Mg-La-RE Alloys

6.5.1 Surface After Solution Treatment

A relatively short solution treatment duration of 1 h at 520°C was selected following a calculation for the period of time it would take the solute to theoretically be distributed homogeneously throughout the grain and also to ensure that no blistering occurred at the surface region of the samples (Section 6.2).

Figure 6.12 shows that no significant deformation or any observable blisters on the surface of the specimens were present after heat treatment. There was some slight discoloration of the solution treated specimens, however, this is only a superficial blemish.

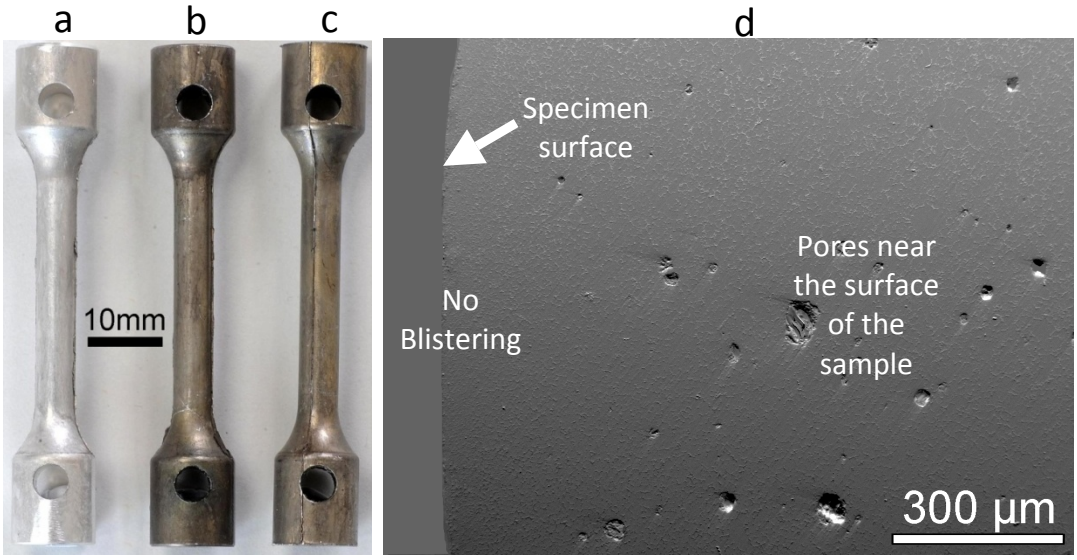

Figure 6.12: Mg-0.49La-0.42Y specimens a) as-cast, b) solution treated at 520°C for 1h, c) solution treated at 520°C for 1h and aged at 160° for 24h, and d) SEM topographical image of 'skin' region in the T6 specimen showing no blistering of pores.

The pockmark-like features in the "skin" region of the sample are gas pores (Figure 6.12d). They do not appear to be connected to the surface of the sample. This is even true for the pores very near to the surface of the sample.

6.5.2 Microstructure After Heat Treatment

Following solution treatment and water quenching (T4) or solution treatment, water quenching and peak ageing (T6) the average grain size for all alloys in the three alloy series investigated remained relatively unchanged compared to that of the as-cast condition, at approximately 9 µm (Table 6.4).

Table 6.4: Average grain size for Mg-0.45La-0.63Nd, Mg-0.45La-1.18Y and Mg-0.45La-0.87Gd in T4 and T6 conditions. As-Cast average grain sizes are included for comparison.

Alloy	Condition	Ave Grain Size (±SD), µm
Mg-0.45La-0.63Nd	As-Cast	9.4 (± 0.8)
	T4 (520°C/1h)	8.9 (± 0.5)
	T6 (520°C/1h and 177°C/16h)	9.1 (± 0.3)
Mg-0.45La-1.18Y	As-Cast	8.5 (± 0.6)
	T4 (520°C/1h)	9.4 (± 0.4)
	T6 (520°C/1h and 160°C/1700h)	8.9 (± 0.6)
Mg-0.45La-0.87Gd	As-Cast	9.0 (± 0.5)
	T4 (520°C/1h)	9.5 (± 0.4)
	T6 (520°C/1h and 177°C/400h)	9.1 (± 0.3)

Following T4 or T6 heat treatment, only a Mg-La-rich $Mg_{12}RE$ intermetallic phase remained at the grain boundary (Figure 6.13). The intermetallic phase is significantly less continuous in comparison to the as-cast condition (Figure 4.1) following heat treatment.

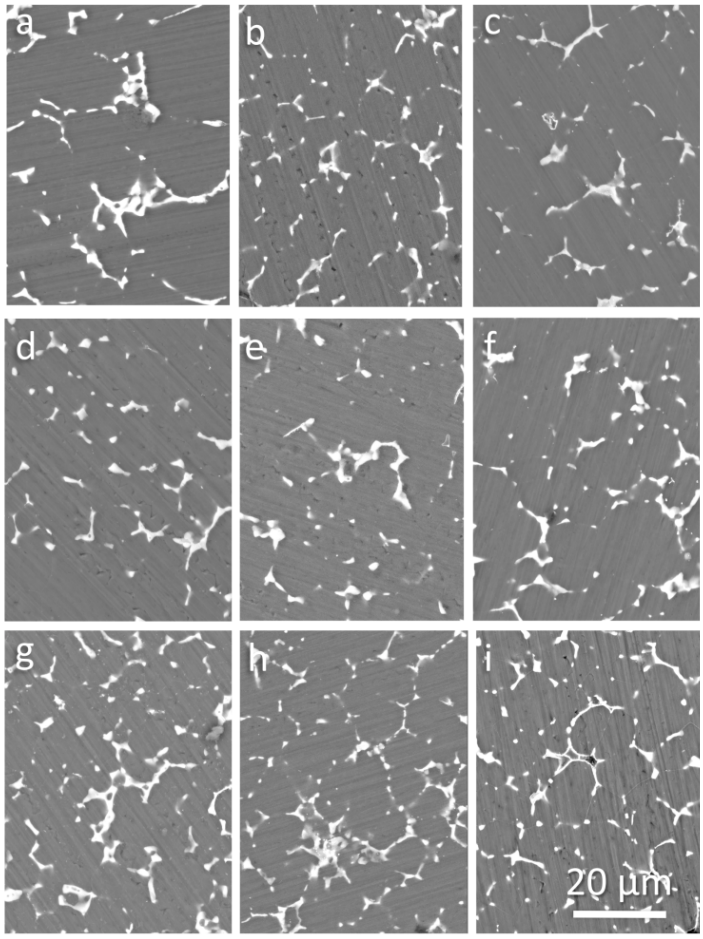

Figure 6.13: SEM BSE micrographs of the "core" region of solution treated (520°C for 1 h) a) Mg-0.47La-0.10Nd, b) Mg-0.48La-0.12Y, c) Mg-0.45La-0.10Gd, d) Mg-0.43La-0.18Nd e) Mg-0.49La-0.24Y, f) Mg-0.46La-0.21Gd, g) Mg-0.45La-0.63Nd, h) Mg-0.45La-1.18Y and i) Mg-0.45La-0.87Gd alloys.

The volume fraction of eutectic in the as-cast alloys is approximately 18 % for alloys with approximately 0.1 or 0.2 at.% ternary RE and 25 % or greater for the alloys with higher concentrations of ternary RE (Figure 6.14a). The volume fraction of the intermetallic phase remaining at the grain boundaries following solution treatment is approximately 10 % in all alloys regardless of the ternary RE concentration. Figure 6.14b demonstrates that the ratio of ternary RE to La decreases significantly following solution treatment. Thus, the volume fraction measured for the alloys in either the T4 or T6 conditions should

actually be considered as a measurement of the volume fraction of the intermetallic phase.

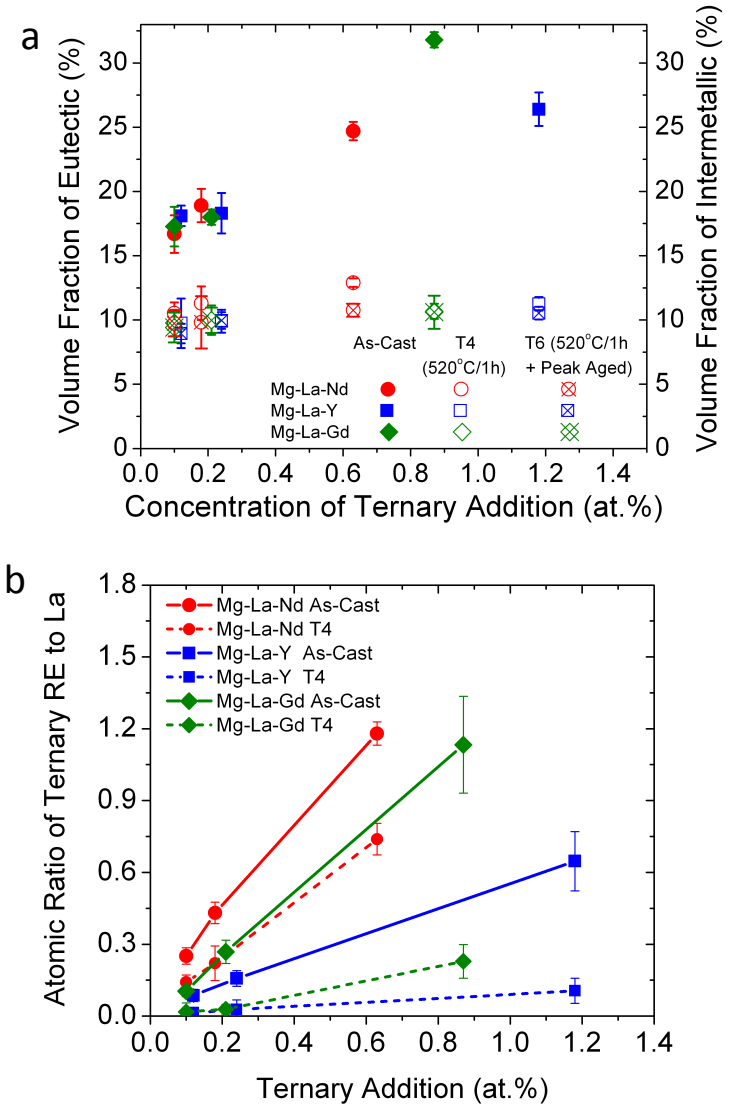

Figure 6.14: a) Measured volume fraction of eutectic in as-cast or intermetallic in T4 (520°C/1h) and T6 (520°C/1h and peak ageing) Mg-La-RE alloys with varying concentrations of ternary alloying additions, and b) Atomic ratio of total ternary alloying addition to La present in the eutectic for alloys in as-cast and in the intermetallic for alloys in the T4 condition determined from EDS.

6.5.3 Microstructure After Heat Treatment and Creep Testing

An investigation into the influence of the T4 and T6 heat treatments on the microstructure of the three alloy series following creep testing is presented in the remainder of this section. Figure 6.15 shows micrographs in Mg-0.47La-0.10Nd, Mg-43La-0.18Nd and Mg-0.45La-0.63Nd alloys following creep testing in the T4 condition.

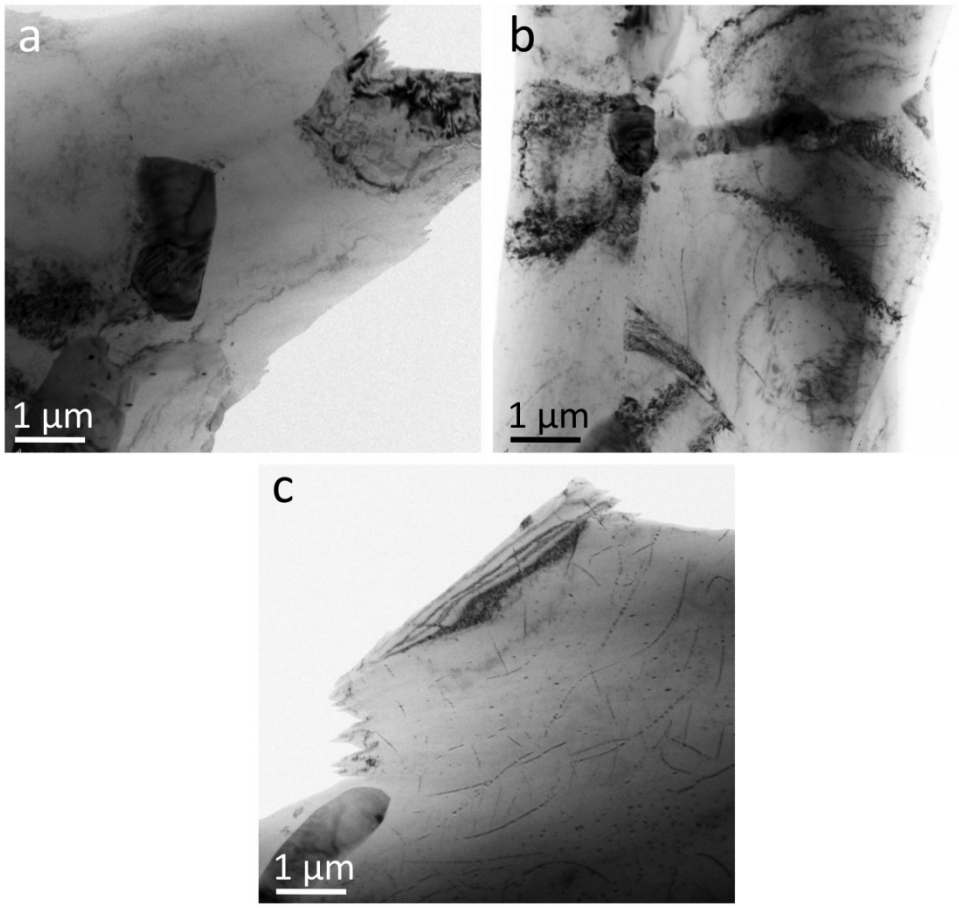

Figure 6.15: Low magnification bright field TEM micrographs along $[0001]_\alpha$ of a) Mg-0.47La-0.10Nd, b) Mg-0.43La-0.18Nd and c) Mg-0.45La-0.63Nd following creep testing at 177°C and 90 MPa T4 (520°C-1h) condition.

Dynamic precipitates are present in Mg-0.47La-0.10Nd, Mg-43La-0.18Nd and Mg-0.45La-0.63Nd alloys following creep testing at 177°C and 90 MPa (Figure 6.16). As the concentration of Nd was increased in the alloys, the number density of the precipitates appeared also to increase (Figure 6.16). In Mg-0.45La-0.63Nd it is clearer that the plate-like β precipitates (as viewed along $[0001]_\alpha$) form on the prismatic planes where the precipitate length ranges from 60 to 150 nm. The irregular shape of the precipitates in Mg-0.47La-0.10Nd and Mg-0.43La-0.18Nd alloys makes it less clear to determine what planes they form on (Figure 6.16). The number density of precipitates appears to increase with increasing concentration of ternary RE.

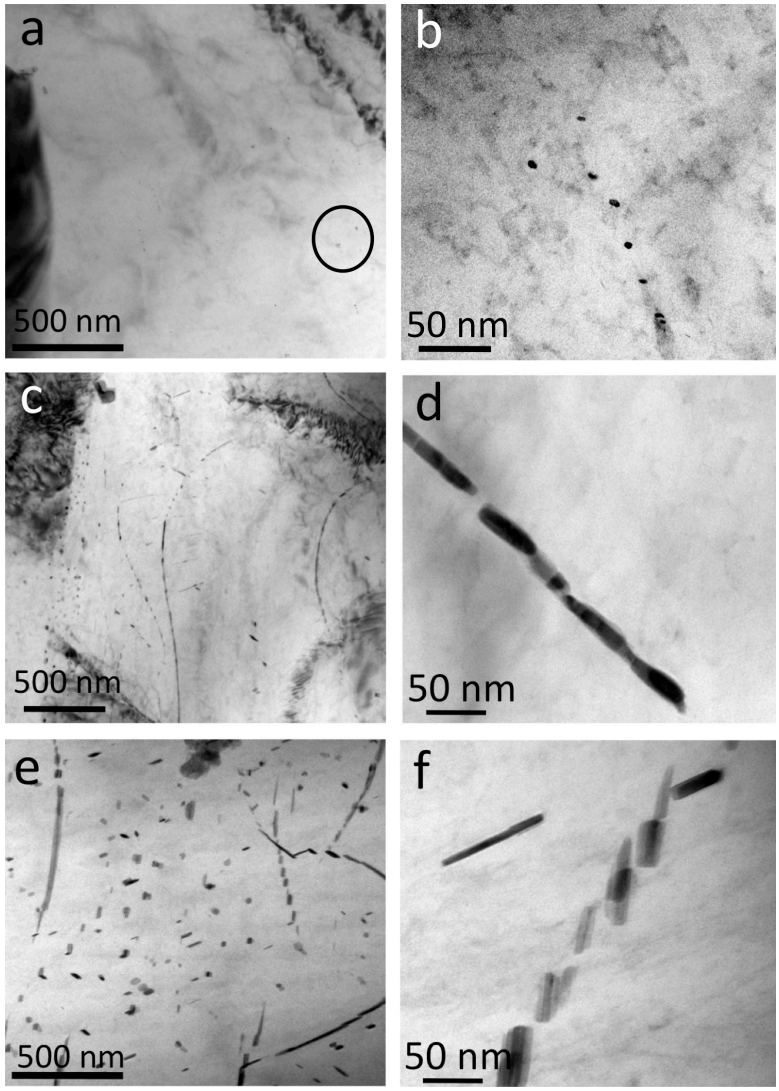

Figure 6.16: Higher magnification bright field TEM micrographs along $[0001]_{\alpha}$ of dynamic precipitates formed during creep testing at 177°C and 90 MPa in T4 a) and b) Mg-0.47La-0.10Nd, c and d) Mg-0.43La-0.18Nd and e) and f) and Mg-0.45La-0.63Nd. Note: precipitates are circled in a) for clarity.

Figure 6.17 shows grains of Mg-0.47La-0.10Nd, Mg-43La-0.18Nd and Mg-0.45La-0.63Nd alloys following creep testing in T6 condition (solution treatment at 520°C and ageing at 177°C for 16h). The post creep microstructure of the Mg-La-Nd series following a T6 heat treatment also revealed that the precipitates nucleate in Mg-0.47La-0.10Nd, Mg-0.43La-0.18Nd and Mg-0.45La-0.63Nd (Figure 6.18).

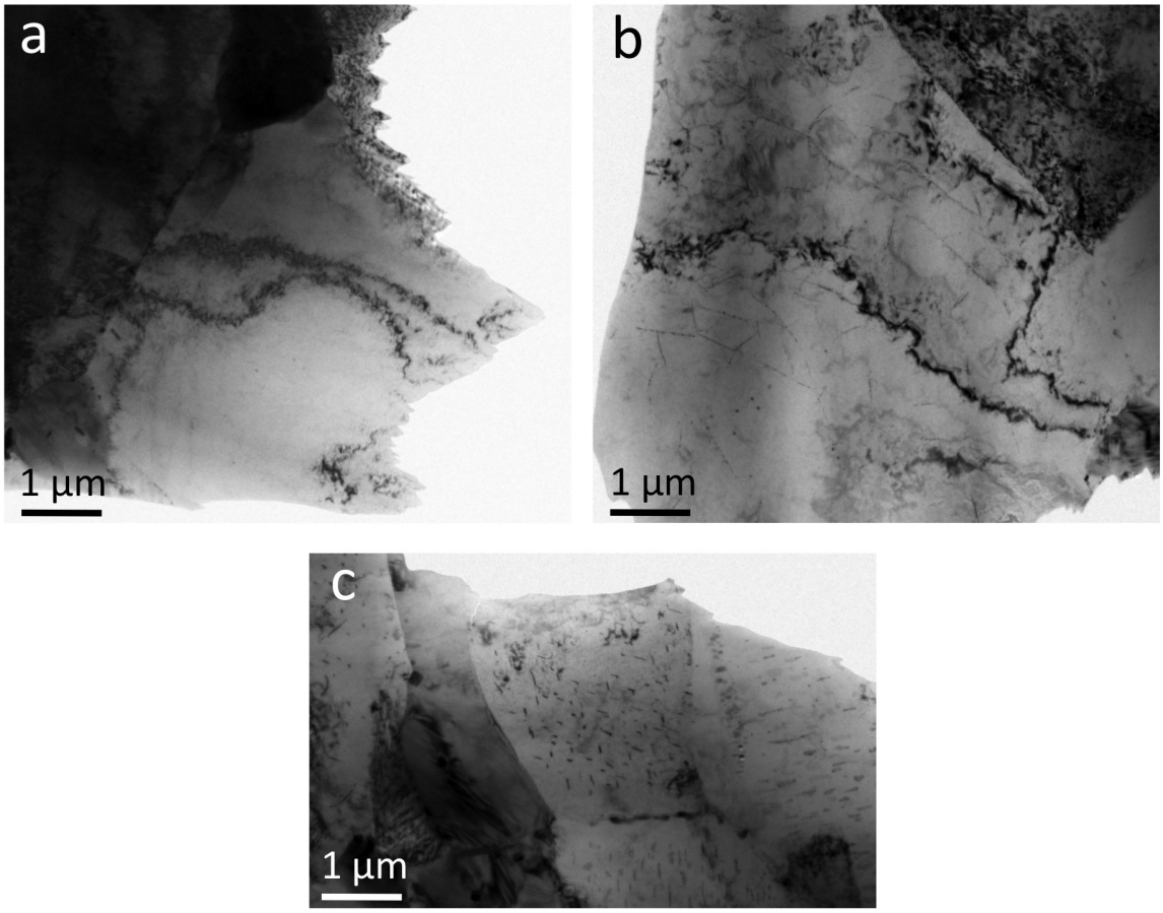

Figure 6.17: Low magnification bright field TEM micrographs along $[0001]_\alpha$ of a) Mg-0.47La-0.10Nd, b) Mg-0.43La-0.18Nd and c) Mg-0.45La-0.63Nd following creep testing at 177°C and 90 MPa in T6 (520°C-1h and then peak aged) condition.

The higher concentration of Nd in Mg-0.45La-0.63Nd resulted in a greater number of precipitates nucleating, in comparison to the other two Mg-La-Nd alloys. In the Mg-0.45La-0.63Nd alloy the precipitate size varies in length between 60 nm and 150 nm, which is comparable to the T4 heat-treated and crept Mg-0.45La-0.63Nd alloy. In the Mg-0.47La-0.10Nd and Mg-0.43La-0.18Nd alloys the precipitates are significantly finer, approximately 5 – 10 nm. The plate-like β precipitates present in Mg-0.45La-0.63Nd tend to be oriented along two directions (Figure 6.18).

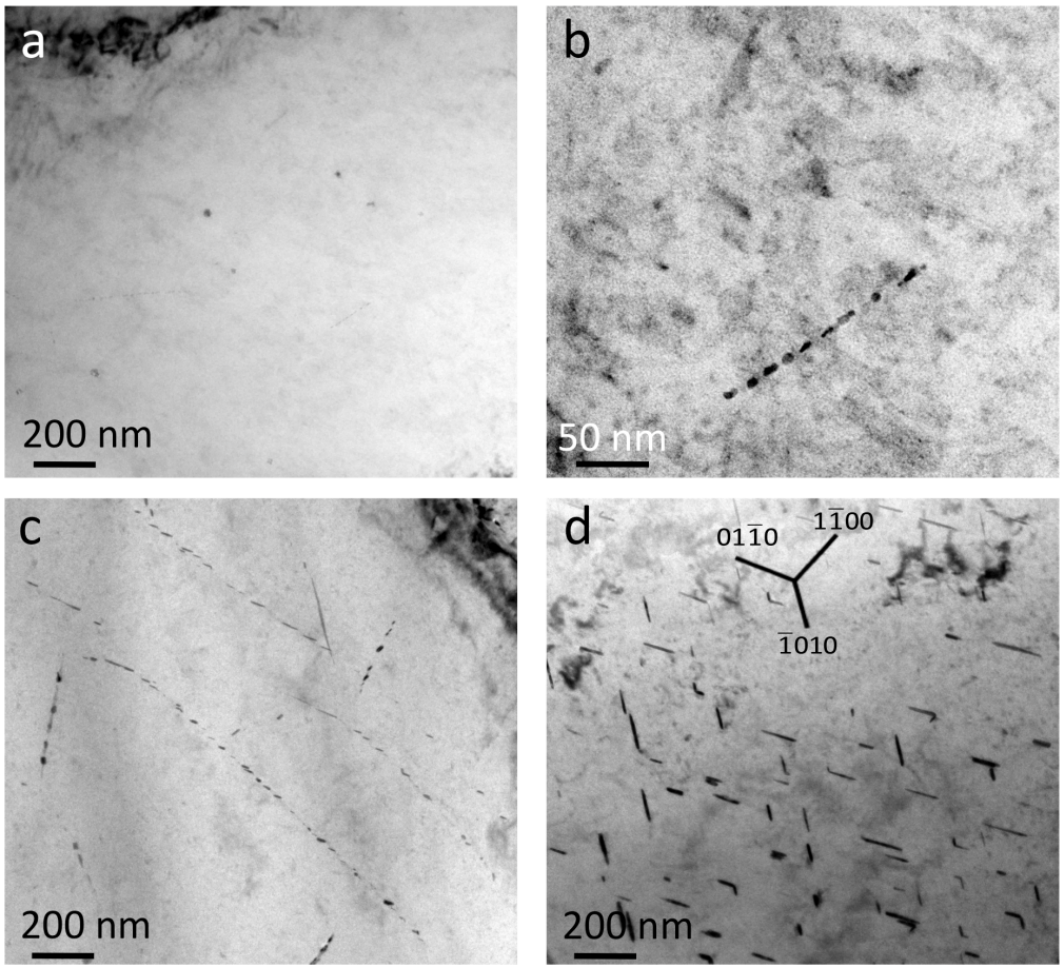

Figure 6.18: Higher magnification bright field TEM micrographs along $[0001]_\alpha$ of precipitates following creep testing at 177°C and 90 MPa in T6 (520°C for 1h and peak aged) a) and b) Mg-0.47La-0.10Nd, c) Mg-0.43La-0.18Nd and d) Mg-0.45La-0.63Nd alloys.

There were no detectable precipitates in any of the Mg-La-Y alloys following just a solution treatment and then creep testing (Figure 6.19). This is different to the results presented in Figure 5.17 of the as-cast Mg-La-Y alloys following creep testing, where a localised region with a dense population of fine β' precipitates was found near grain boundary regions. This is likely related to the slower age hardening response in Mg-0.45La-1.18Y following solution treatment (Figure 6.2) in comparison to the as cast condition (Figure 5.7).

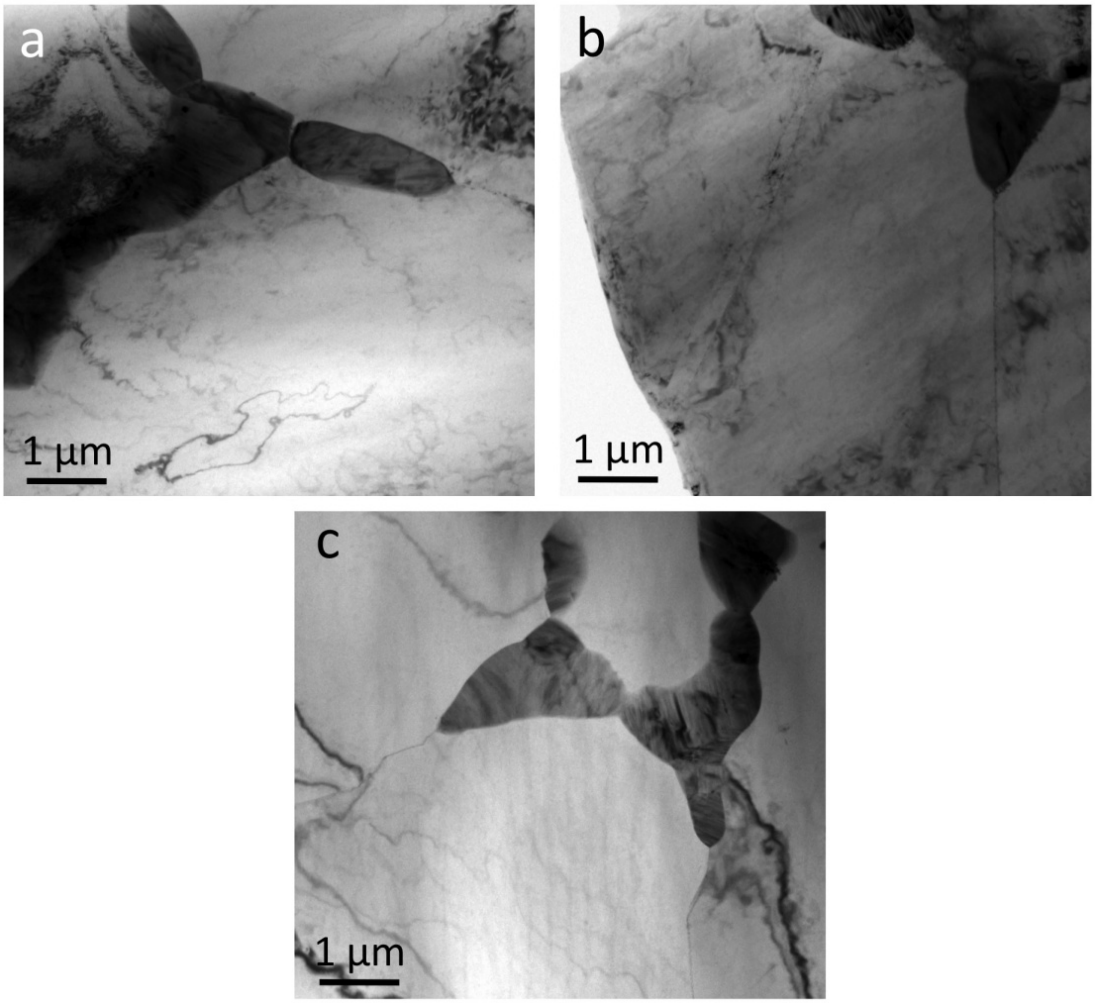

Figure 6.19: Low magnification bright field TEM micrographs along $[0001]_\alpha$ of a) Mg-0.48La-0.12Y, b) Mg-0.49La-0.24Y and c) Mg-0.45La-1.18Y following creep testing at 177°C and 90 MPa T4 (520°C-1h) condition.

Figure 6.20 shows grains of the Mg-0.48La-0.12Y, Mg-0.49La-0.24Y and Mg-0.45La-1.18Y alloys a T6 condition following creep testing. For Mg-0.48La-0.12Y in the T6 and crept condition, no precipitates were observed (Figure 6.20a). However, the Mg-0.49La-0.24Y and Mg-0.45La-1.18Y T6 and crept alloys have resolvable β' precipitates throughout the grains (Figure 6.21).

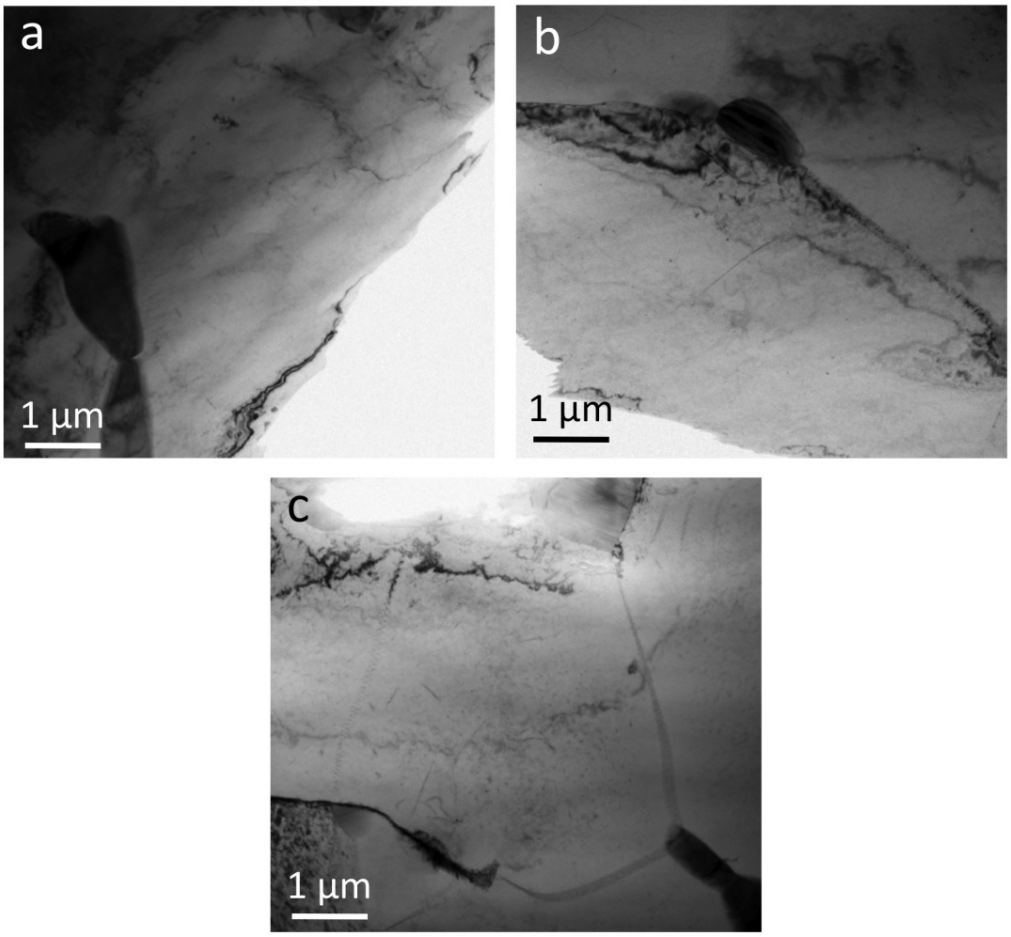

Figure 6.20: Low magnification bright field TEM micrographs along $[0001]_\alpha$ of cast a) Mg-0.48La-0.12Y, b) Mg-0.49La-0.24Y and c) Mg-0.45La-1.18Y following creep testing at 177°C and 90 MPa in T6 (520°C-1h and then peak aged) condition.

Figure 6.21 shows that the precipitates have an irregular shape when viewed along $[0001]_\alpha$ direction and are distributed throughout the grain and also on dislocations.

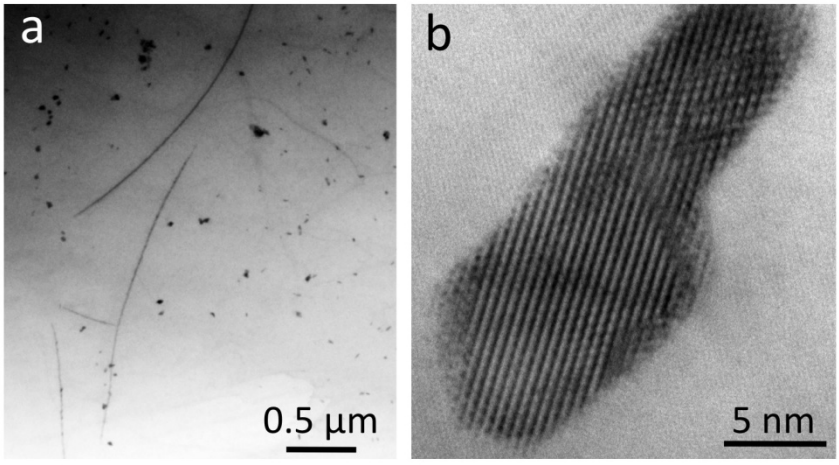

Figure 6.21: Bright field TEM micrographs along $[0001]_\alpha$ of precipitates following creep testing at 177°C and 90 MPa in T6 (520°C for 1h and peak aged) a) and b) Mg-0.49La-0.24Y.

The precipitates in Mg-0.45La-1.18Y have a significantly different morphology than the precipitates in the Mg-0.49La-0.24Y alloy (Figure 6.22). The precipitates in Mg-0.45La-1.18Y appear to have to two different morphologies. One morphology has a cluster of very thin plates (approximately 2 atoms wide) that form on the prismatic plane $\{10\bar{1}0\}$, and the other is globular and these particles are often located in the centre of each cluster of prismatic plates. The globular shape is consistent with the β' phase, as shown in the electron diffraction pattern (Figure 6.22d). The clusters of the prismatic thin plates are not consistent with any precipitate phases reported in the literature, and therefore their identity is unclear.

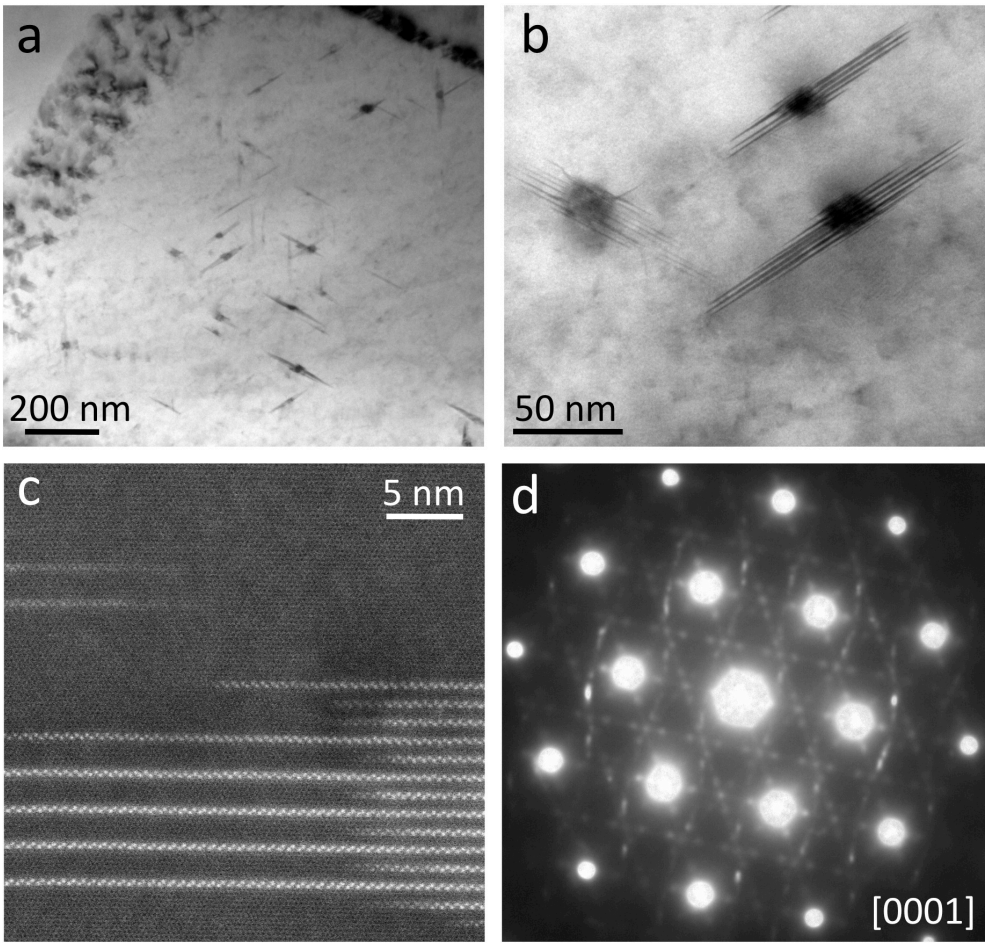

Figure 6.22: TEM micrographs along $[0001]_\alpha$ of precipitates following creep testing at 177°C and 90 MPa in T6 (520°C for 1h and peak aged) a) – c) Mg-0.45La-1.18Y and d) diffraction pattern from the region shown in (a) indicating that the globular phase is β'. Note: image c) was obtained by Ms Wen-Fan Xu on the author's behalf using a FEI F20 TEM in dark field mode.

Figure 6.23 shows grains of Mg-0.45La-0.10Gd, Mg-0.46La-0.21Gd and Mg-0.45La-0.87Gd following T4 solution treatment and creep testing.

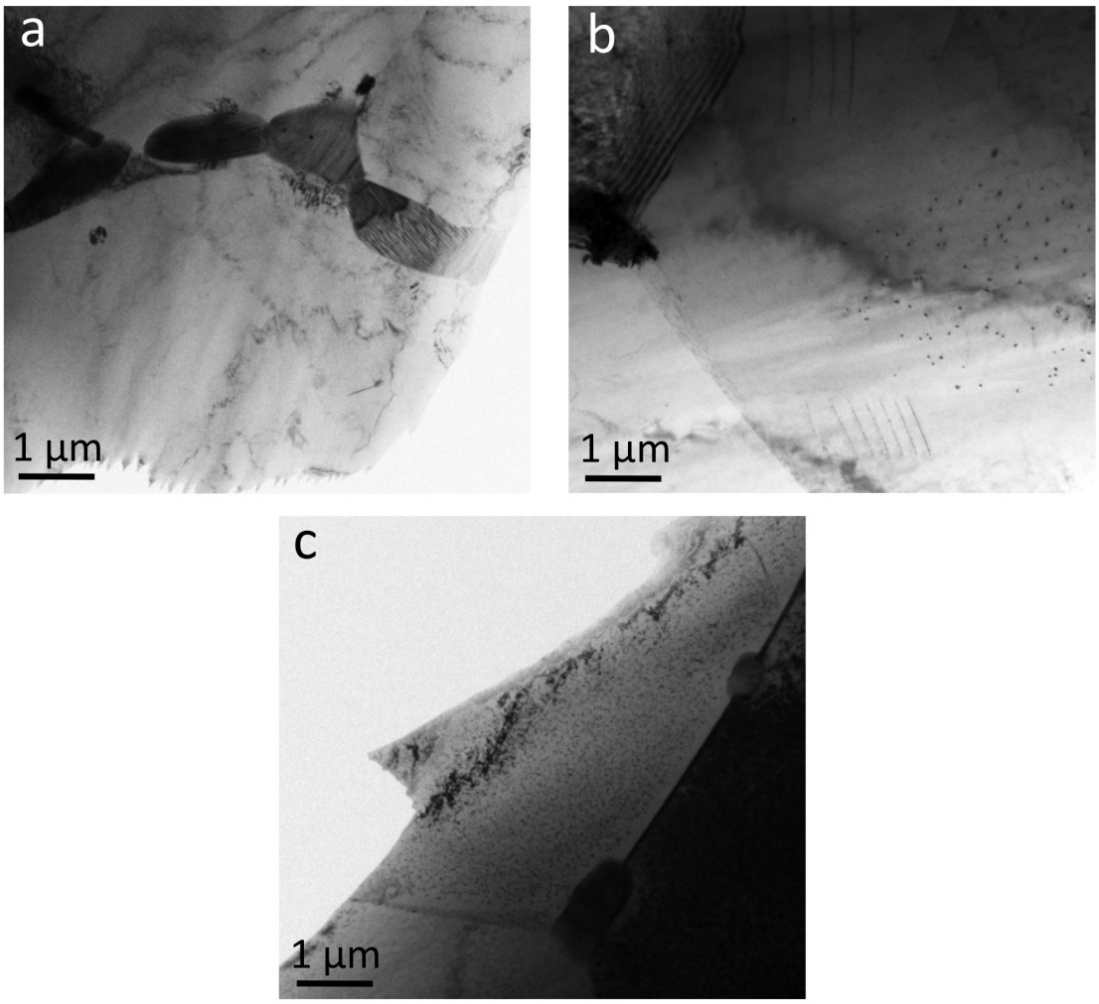

Figure 6.23: Low magnification bright field TEM micrographs along $[0001]_\alpha$ of a) Mg-0.45La-0.10Gd, b) Mg-0.46La-0.21Gd c) Mg-0.45La-0.87Gd following creep testing at 177°C and 90 MPa T4 (520°C-1h) condition.

No precipitates were resolved in Mg-0.45La-0.10Gd following solution treatment (520°C for 1h) and then crept at 177°C and 90 MPa (Figure 6.24a). Precipitates were present in the crept as-cast Mg-0.46La-0.21Gd, decorating dislocations (Figures 6.24b and c).

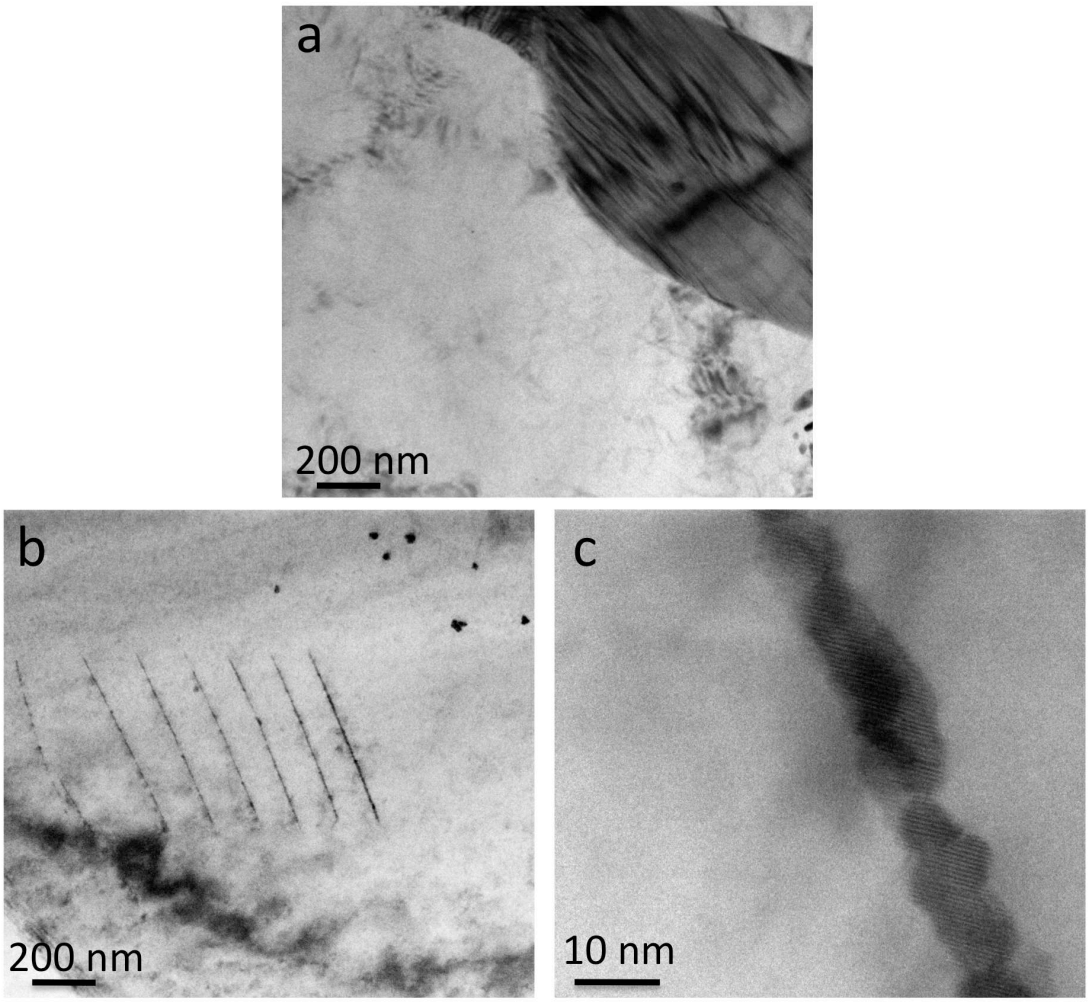

Figure 6.24: Higher magnification bright field TEM micrographs along $[0001]_{\alpha}$ of a) Mg-0.45La-0.10Gd, b) and c) Mg-0.46La-0.21Gd following creep testing at 177°C and 90 MPa T4 (520°C-1h) condition. Note: c) shows a higher resolution micrographs of one of the dislocations decorated with precipitates from b).

The precipitates in the T4 solution treated and then crept Mg-0.45La-0.87Gd alloy are homogeneously distributed throughout the grain (Figure 6.25a). The precipitates are also shown decorating dislocations (Figure 6.25b). The precipitates in Mg-0.45La-0.87Gd have a central spheroidal particle with a number of thinner platelets that are normal to the spheroid (Figure 6.25c). SAED patterns indicate that the precipitates in Mg-0.45La-0.87Gd are β' (Figure 6.25d).

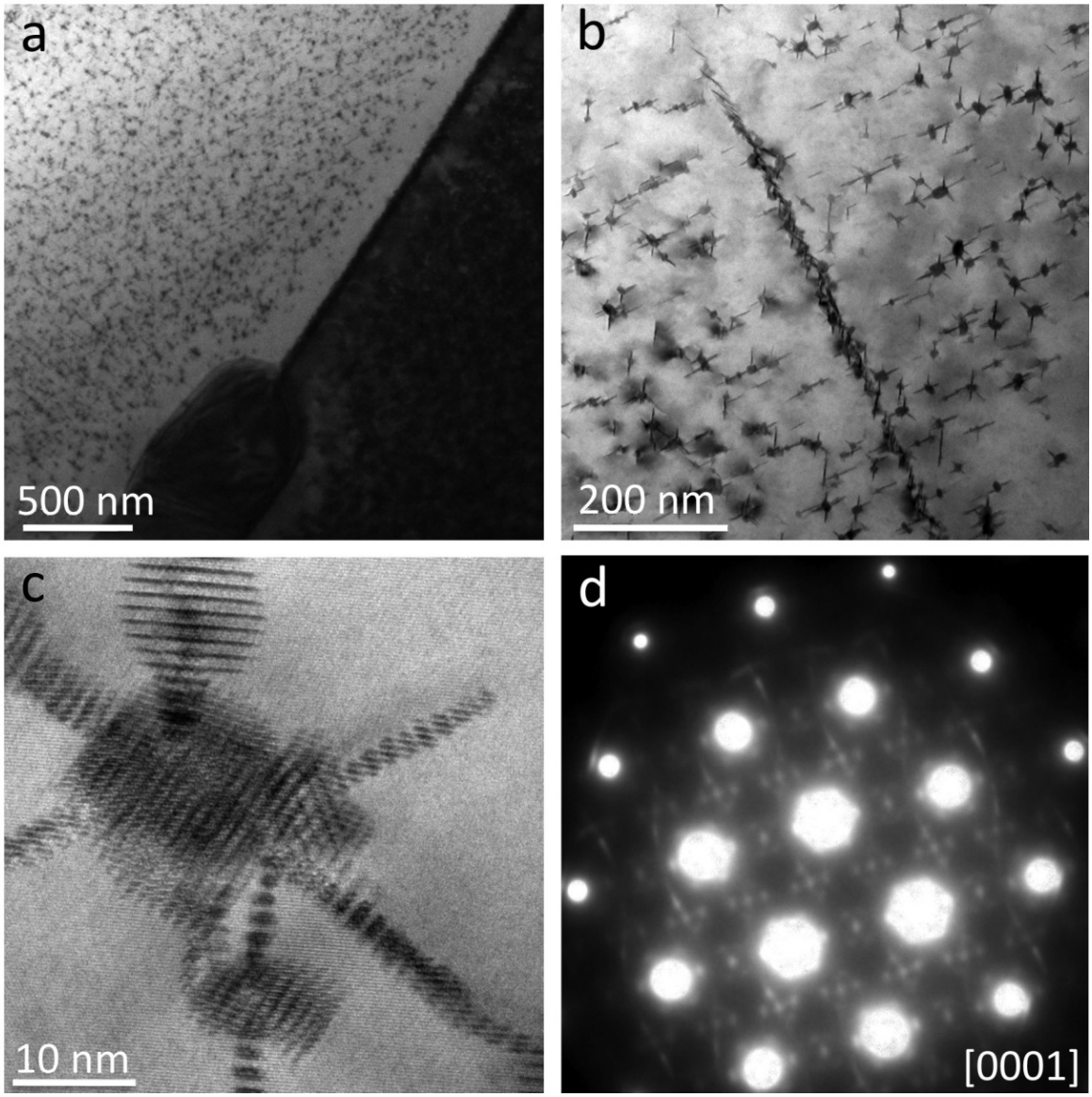

Figure 6.25: a) – c) Bright field TEM micrographs along $[0001]_\alpha$ of dynamic precipitates formed during creep testing at 177°C and 90 MPa in Mg-0.45La-0.87Gd in T4 condition and d) diffraction pattern from the region which identifies the precipitates as β'.

Figure 6.26 shows grains of the Mg-0.45La-0.10Gd, Mg-0.46La-0.21Gd and Mg-0.45La-0.87Gd alloys after a T6 heat treatment and following creep testing. The number density of precipitates increases significantly with increasing concentration of Gd. The grains in the Mg-0.45La-0.87Gd alloy are shown to have a high number of precipitates homogenously distributed throughout the grain (Figure 6.26c).

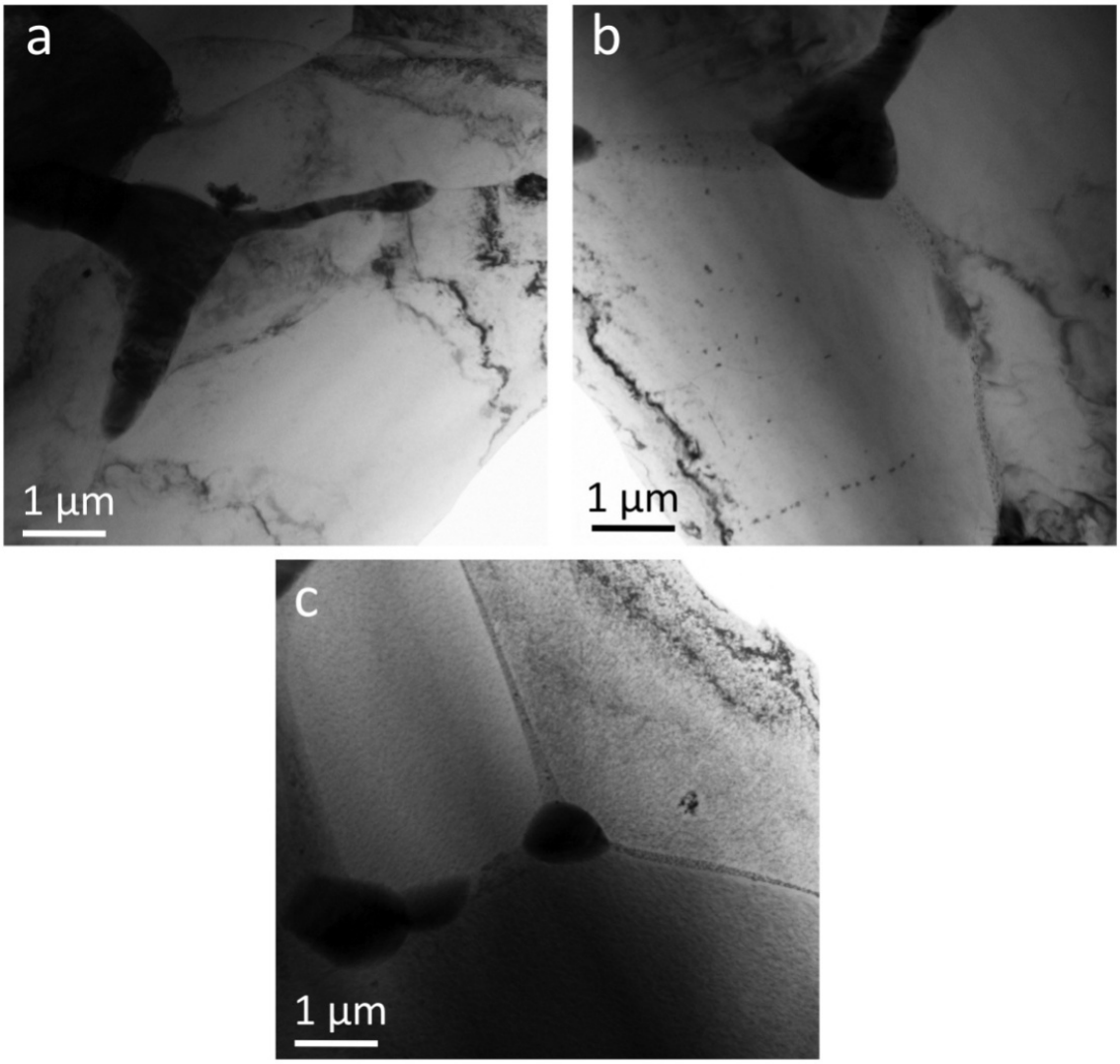

Figure 6.26: Low magnification bright field TEM micrographs along $[0001]_\alpha$ of a) Mg-0.45La-0.10Gd, b) Mg-0.46La-0.21Gd c) Mg-0.45La-0.87Gd following creep testing at 177°C and 90 MPa in T6 (520°C-1h and then peak aged) condition.

No precipitates in Mg-0.45La-0.10Gd could be resolved (Figure 6.27a). Precipitates in Mg-0.46La-0.21Gd are sporadically distributed throughout the grain (Figure 6.27b) and also appear to decorate dislocations. The precipitates in Mg-0.46La-0.21Gd have an irregular morphology when viewed along $[0001]_\alpha$ (Figure 6.27c).

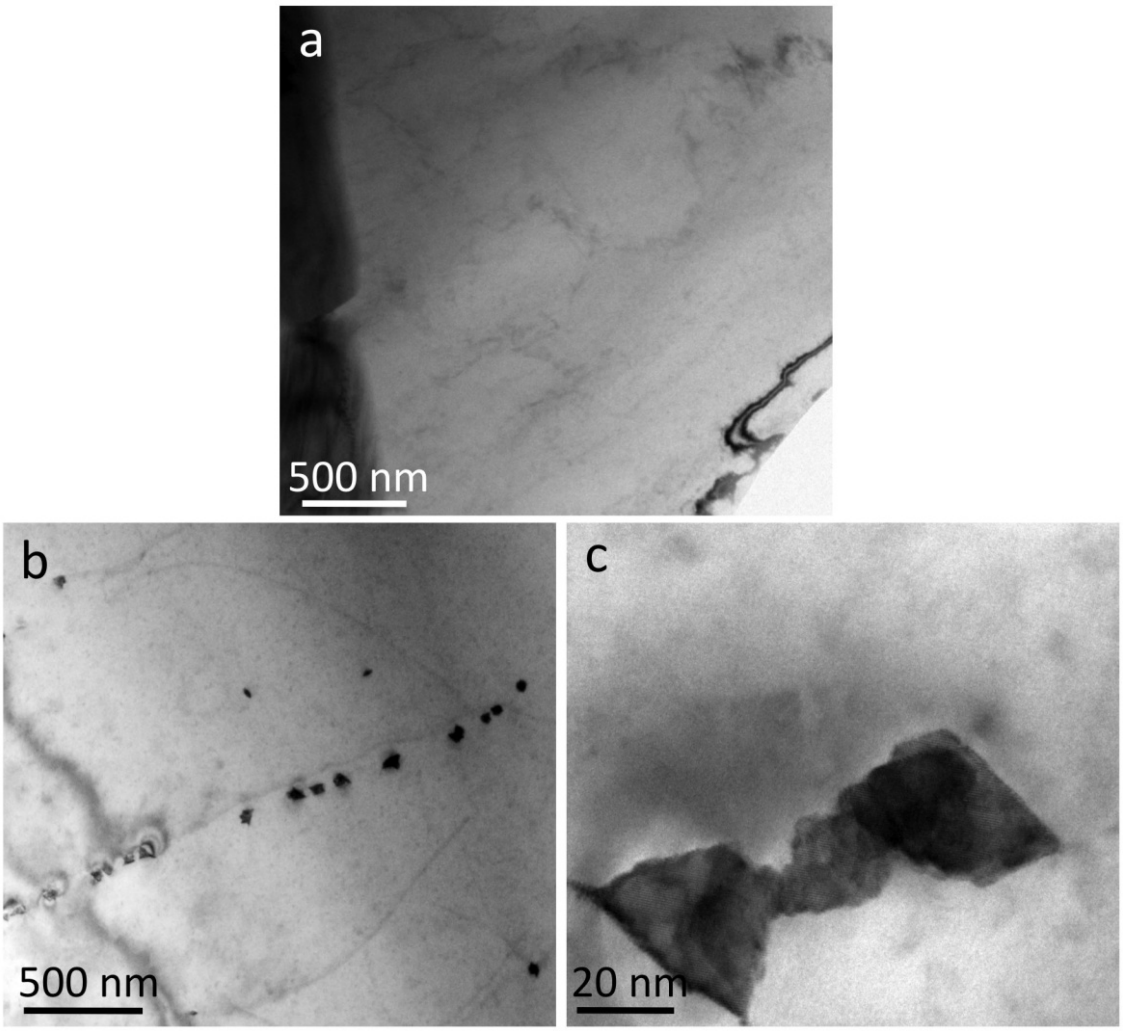

Figure 6.27: Higher magnification bright field TEM micrographs along $[0001]_\alpha$ of precipitates following creep testing at 177°C and 90 MPa in T6 condition (520°C for 1h and peak aged) a) Mg-0.45La-0.10Gd and b) - c) Mg-0.46La-0.21Gd.

However, when significantly higher concentrations of the ternary alloying element is added (as in Mg-0.45La-0.87Gd) the morphology of the precipitates changes remarkably as was also shown in the T4 heat-treated and crept Mg-La-Gd alloys (Figure 6.28). The precipitates of Mg-0.45La-0.87Gd are homogeneously distributed throughout the grain (Figure 6.28a) and also decorate dislocations. The precipitates in the T6 heat-treated and crept Mg-0.45La-0.87Gd alloy (Figure 6.28b) are comprised of the same precipitate phase (β') as the T4 alloy (Figure 6.25c), which is confirmed in Figure 6.28c.

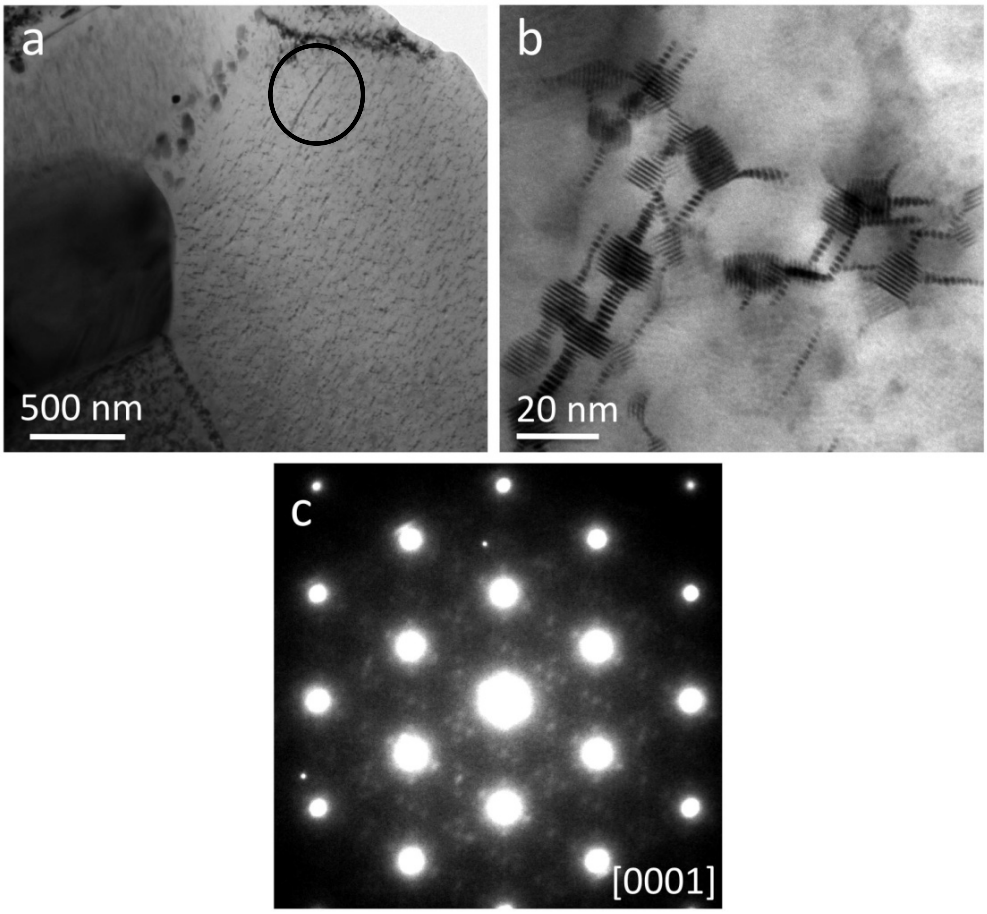

Figure 6.28: Bright field TEM micrographs along $[0001]_{\alpha}$ of precipitates following creep testing at 177°C and 90 MPa in T6 (520°C for 1h and peak aged) a) – b) Mg-0.45La-0.87Gd and c) diffraction pattern from the region which identifies the precipitates as β'. Note: A dislocation decorated by precipitates is circled in a).

6.6 Discussion

6.6.1 Heat Treatment of HPDC Mg-La-RE Alloys

It has previously been found by Gibson (in a personal communication) that short-term heat treatments at moderate temperatures (480°C – 520°C) can successfully be applied to HPDC Mg-RE alloys without causing any damage to the surface of the sample. Due to the relatively short duration of the solution treatment and also due to the use of a moderate solution treatment temperature (520°C), gas pores that were created during the HPDC process did not have the sufficient time or thermal energy to expand. Thus pores near the surface to the casting (in the "skin") region did not cause any blistering to occur. Lumley *et al.* [6] showed that it was possible to achieve a substantive age hardening response in

HPDC Al alloys when heat treated at temperatures of 490°C or less, over durations of 24 h or less without causing damage. This was not true for the HPDC Mg-La-RE alloys investigated in the current work, as will be discussed in this section.

6.6.2 Age Hardening Response

The age hardness curves (Figure 6.2) of solution treated alloys show that longer heat treatments are required in comparison to alloys that were aged from the as-cast condition in order to reach a peak aged condition (Figure 5.6). The length of time taken to reach peak ageing conditions was longer following solution treatment and the peak hardness value lower in comparison to the alloys aged initially from the as-cast condition. This is a result of the removal of the localised region of supersaturated solute in the α-Mg matrix near grain boundaries, which is present in the as-cast alloys. In Chapter 5, it was shown that Mg-0.45La-1.18Y and Mg-0.45La-0.87Gd alloys had densely concentrated precipitates near grain boundaries but with little or no precipitates closer to the grain interior. This, in addition to EDS line scans (Figure 4.8) helped to confirm the cored solute distribution. When HPDC Mg-La-RE alloys are solution treated, the solute becomes homogeneously distributed. As a result of this, it takes significantly longer for the alloys to reach the peak-aged condition due to the lower local supersaturation of solute in solid solution.

The thermal stability of the precipitates in the Y or Gd containing alloys was significantly better than the Nd containing alloys (which was also indicated from the Mg-La-Nd alloys that were aged from as-cast condition in Chapter 5). The precipitates do not appear to coarsen in the Y or Gd-containing alloys as fast as in the Nd-containing alloys. However, there was an unexpected result for Mg-0.45La-1.18Y alloy. Heat-treating Mg-0.45La-1.18Y at the lower temperature of 160°C (in comparison to 177°C) resulted in a shorter duration for the alloy to reach peak hardness. It would be expected that peak hardness would be achieved sooner at higher temperatures, as this would increase the kinetics of the precipitation reaction. In order to verify the results, repeat age hardness tests were performed on another set of Mg-0.45La-1.18Y specimens following a solution treatment of 520°C for 1 h, water quenching and ageing at 160°C and 177°C (Figure 6.1). The results

were consistent with the original set of heat treatment data. Furthermore, this result was only observed in the Mg-La-Y alloy. Both the Mg-La-Nd and Mg-La-Gd alloys reached peak hardness values earlier at the ageing temperature of 177°C. Regardless of this result, it was evident that ageing any of the alloys following solution treatment and water quenching did not improve the ageing response of the alloys in comparison with the aged alloys from the as-cast condition (Figure 5.6).

6.6.3 Influence of Heat-Treatment on Tensile Properties of HPDC Mg-La-RE Alloys

The effects of solid solution strengthening or precipitation hardening on tensile strength were examined in the Mg-La-Nd, Mg-La-Y and Mg-La-Gd alloy series. All three alloy series required concentrations of ternary RE significantly greater than 0.2 at.% before any improvements to the tensile properties were observed (Figure 6.29). Alloys with relatively high concentrations of ternary RE begin to counteract the loss in strength from the grain boundary following heat treatment. For the Mg-0.45La-0.63Nd alloy, either a T4 or a T6 heat treatment resulted in improved tensile properties (Figure 6.3) (T4 causes slight improvement in UTS and ductility even though yield strength reduces while T6 improved 0.2 % PS, UTS and ductility). For the Mg-0.45La-1.18Y and Mg-0.45La-0.87Gd alloys the T6 heat treatment improved the 0.2 % PS significantly. This can be attributed to the higher solid solubility of Y and Gd in Mg in comparison to Nd. The 0.2% PS and UTS appeared not to change significantly following solution treatment in the Mg-0.45La-1.18Y and Mg-0.45La-0.87Gd alloys.

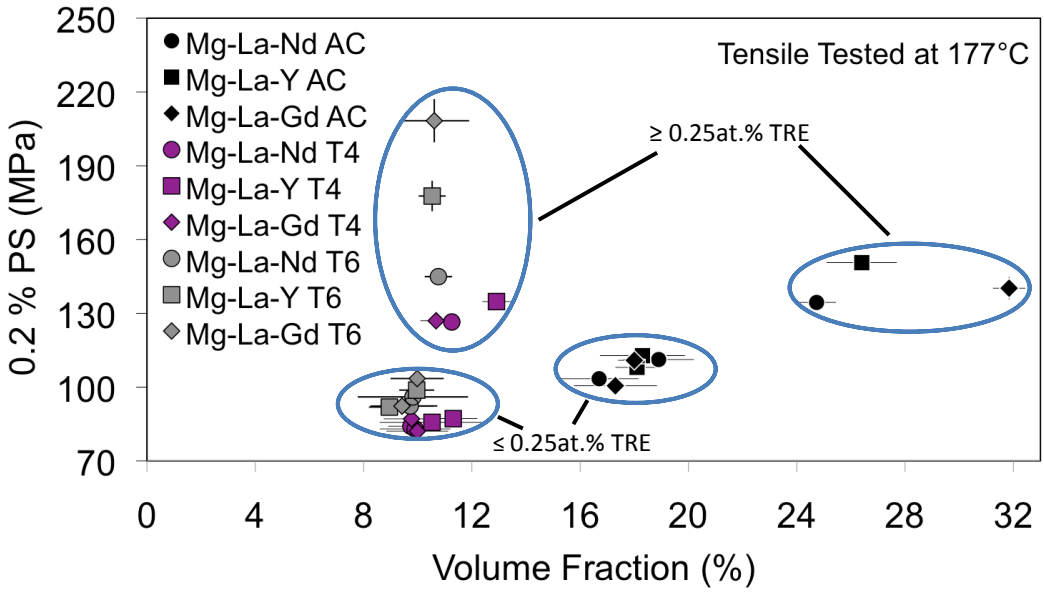

Figure 6.29: Influence of the volume fraction of intermetallic at grain boundaries on 0.2 % PS at 177°C for Mg-La-Nd, Mg-La-Y and Mg-La-Gd in as-cast (AC) T4 and b) T6 conditions. The alloys with the highest concentration of ternary RE and those with approximately 0.25 at.% ternary RE or less that were tested in the present work are indicated.

Following solution treatment the morphology of the intermetallic phase became significantly less continuous (Figure 6.13) compared to the as-cast condition (Figure 4.1). There is also a redistribution of solute in solid solution from the localised region near grain/cell boundaries in the as-cast condition to being distributed homogeneously throughout the grain. These two effects that are caused by the heat treatment process contribute to the lowering of the 0.2% PS of the alloys. Without sufficient strengthening from precipitation hardening or solid solution strengthening, the yield strength of the alloys drops below that of the as-cast condition as seen in all the alloys with approximately 0.2 at% (or less) ternary alloying addition (Tables 6.1-6.3). As shown by Zhang *et al.* [149] a continuous intermetallic phase at the grain boundaries in HPDC Mg-RE alloys can contribute up to 30 MPa of strength to the material.

The stress-strain curves of the highest concentration Y or Gd ternary RE i.e. Mg-0.45La-1.18Y or Mg-0.45La-0.87Gd alloys following solution treatment (T4) demonstrated a serrated flow or Portevin-Le Chatelier (PLC) effect at 177°C. No serrated flow was observed in the alloy in the highest concentration of ternary Nd (Mg-0.45La-0.63Nd)

following solution treatment or in any other alloy investigated in the as-cast or T6 conditions.

The serrated flow is commonly attributed to the dynamic interaction between mobile dislocations and solute atoms diffusing (or dynamic strain ageing) [202]. Solution treatment increases the concentration of solute in solid solution and also helps to homogeneously distribute the solute atoms throughout the grain. The highest ternary RE containing alloys would thus necessarily have the greatest amount of solute in solid solution and a more clearly defined PLC effect. If all of the ternary RE was dissolved in solid solution, the highest concentrated Nd alloy (Mg-0.45La-0.63Nd) would have 0.63 at.% Nd in the α-Mg matrix. The highest concentrated Y or Gd alloys have significantly more solute in solid solution (0.55 or 0.24 at.% ternary RE respectively) than Mg-0.45La-0.63Nd. This may explain why no PLC effect was detected in the T4 processed Mg-0.45La-0.63Nd when tensile tested at 177°C. Zhu and Nie [203] as well as Fang *et al*. [204] have reported on the serrated flow in WE54 and Mg-Gd alloys, respectively, for similar tensile testing temperatures (150°C - 300°C). It was concluded in both [203, 204] that the serrated flow was a result of dynamic strain ageing. Wu *et al.* [205] also recorded the presence of a serrated stress-strain curve in rolled sheets of Mg-2.74Gd-1.06Zn (wt.%) that were annealed and aged at different temperatures. They claimed that the serrated flow was attributed to shearing of precipitates by gliding dislocations.

6.6.4 Precipitates in Mg-La-RE Alloys following Heat Treatment and Creep

It is outside the scope of this thesis to perform a detailed characterisation of the precipitate phases in the Mg-La-RE alloys. However, a brief overview of the different precipitates that form during ageing or creep testing is shown. The morphology of the precipitates was shown to be significantly different between the three alloy series and also within alloy series in some instances. The Nd-rich precipitates are noticeably different in comparison to the Y or Gd precipitates since they are plate-like β_1 or β precipitates that are oriented along the prismatic planes of the α-Mg matrix [139]. The

precipitates in the Mg-0.49La-0.24Y T6 alloy (Figure 6.21) have a significantly different morphology from those of the Mg-0.45La-1.18Y T6 alloy (Figure 6.22). It is unclear precisely what the identity of the precipitates in the Mg-0.49La-0.24Y T6 alloys are after creep testing. However, they have a significantly different morphology to the metastable β' phase that was observed in binary Mg-Y alloys [206]. The precipitates in the T6 Mg-0.45La-1.18Y crept alloys appear to be an unknown phase nucleating from the centre of another metastable β' phase. The β' phase in the Gd containing alloys has a similar morphology to the β' phase in the Y alloys but is much easier to reconcile. The Gd-based β' phase has a spheroidal shaped particle with a number of thinner β'' platelets that are attached to the spheroidal β' particle (Figure 6.25). Liu *et al.* [207] have modelled the formation of the Mg-Y and Mg-Gd β' precipitates and concluded that the difference in morphology is a result of the difference between the interfacial energies and elastic strain energy anisotropy of the two alloys.

6.6.5 Influence of Heat Treatment on Creep Properties and Microstructure

Creep properties of T4 or T6 processed alloys were either worse or at best comparable to the equivalent alloys in the as-cast condition. Following solution treatment or solution treatment and peak ageing, the average grain size of the alloys was not significantly different from that of the as-cast alloys (Table 6.4) due to the relatively short duration time of the solution treatment.

The heat treatments did, however, significantly change the morphology of the microstructure at the grain boundaries. In the as-cast condition there was a eutectic at the grain boundaries, which was comprised of a lamellar morphology (eutectic α-Mg and Mg-La-rich intermetallic phase) that was relatively continuous throughout the material. Following solution treatment or solution treatment and then ageing the continuity of the intermetallic phase at grain boundaries was reduced and became increasingly discontinuous (Figure 6.13) in comparison to the as-cast condition (Figure 4.1). Hence performing a solution treatment assisted in isolating what influence grain boundary

reinforcement had on the creep properties of the alloys particularly since grain size effects could be ignored.

Solution treatment also helped distribute the solute in solid solution homogeneously throughout the grains of the alloys following solution treatment as predicted by the calculation from Eq. (6.1). There is no longer a region of highly concentrated solute near the grain boundaries, which would have been the most likely region for precipitates to form. There were, however, no resolvable precipitates following the T4 heat treatment and subsequent creep testing of the Mg-La-Y alloys. This can be explained by examining the age hardening response for Mg-0.45La-1.18Y (Figure 6.2). It requires at least 1700 h of ageing at 160°C or 4000 h at 177°C before any noticeable change in hardness was observed. The T4 Mg-0.45La-1.18Y crept alloy had been exposed to a temperature of 177°C for only 600 h and as such no precipitates would be expected to have form in the microstructure.

It is important to note that the alloys with approximately 0.1 at.% ternary RE and the alloys with approximately 0.2 at.% following either a T4 or a T6 heat treatment have comparable 0.2 % PS (Table 6.3). The T4 or T6 0.2 at.% alloys experienced less initial strain during creep testing than the 0.1 at.% alloys. The discontinuity of the intermetallic phase at grain boundaries is similar between these two sets of alloys following a T4 or T6 heat treatment (Figure 6.14). In addition, there was no significant change to the average grain size (Table 6.4). The higher concentration of solute in solid solution (following T4 processing) and also the presence of static precipitates (following T6 processing) are likely to counteract the reduced amount grain boundary strengthening as a result of the eutectic dissolving and only a discontinuous $Mg_{12}RE$ intermetallic phase remaining at grain boundaries. However, this is still not effective for improving the creep properties of the as-cast alloys, which have excellent grain boundary reinforcement, and a localised region of supersaturated solute that allows for dynamic precipitation to occur.

It was interesting that precipitates were detected in alloys that should not have precipitates according to their solid solubility in Mg, namely, the Mg-0.49La-0.24Y and Mg-0.46La-0.21Gd alloys in the T6 and crept condition as is shown by the solubility limit of Y or Gd in Mg at 177°C (Table 5.4). The precipitates of these alloys are relatively fine (approximately 10 - 20 nm) and are few in number, Figures 6.21 and 6.27, respectively. Rokhlin *et al.* [208] proposed that when RE elements with low solid solubility in Mg are added with higher soluble RE elements the solubility of the higher solubility RE will be lowered. In this case the La alloying addition (maximum solid solubility of 0.04 at.% in Mg) may lower the solid solubilities for the more soluble Y or Gd alloys (maximum solid solubility of 3.60 and 4.53 at.%, respectively) causing precipitation Mg-0.49La-0.24Y and Mg-0.46La-0.21Gd specimens during a T6 heat treatment.

Precipitation hardening has previously been suggested to be one of the methods to improve creep resistance in Mg alloys [13, 88]. Precipitates are present in all the high concentrated ternary RE alloys following a T6 heat treatment and creep testing. The aspect ratio of the precipitates, precipitate number density and thermal stability of solute can all contribute to alloy strengthening [157]. However the morphology of the precipitates differ significantly between alloy series, in particular of the high concentrated alloys. When the number density of the precipitates varies between alloys it is difficult to isolate the influence of the precipitate aspect ratio on strength because the effective inter-particle spacing also influences the strength of the alloy. These factors may also influence creep resistance with respect to impeding dislocation motion [14].

The precipitate number density of the T6 Mg-0.45La-1.18Y alloy following creep testing (Figure 6.22a) appeared to be less than either T6 Mg-0.45La-0.63Nd (Figure 6.18d) or T6 Mg-0.45La-0.87Gd (Figure 6.28a) heat treated and crept alloys. However, the Mg-0.45La-1.18Y alloy had a substantial increase in 0.2 % PS following T6 heat treatment when compared to the as-cast condition and also the slow age hardening rate. These results may indicate that precipitation strengthening is present but the precipitates are too fine to be resolved with conventional TEM. Yet the Mg-0.45La-1.18Y alloy had a minimum

creep rate, which was approximately 1 order of magnitude lower than Mg-0.45La-0.63Nd (section 6.4). However, the precipitates in Mg-0.45La-0.63Nd were on average larger and coarser than those in either Mg-0.45La-1.18Y or Mg-0.45La-0.87Gd. The precipitates in Mg-0.45La-0.63Nd alloys began to overage earlier than both Mg-0.45La-1.18Y and Mg-0.45La-0.87Gd alloys (Figure 6.2). From this result it can be assumed that the diffusion rate of solute in solid solution was faster in Mg-La-Nd alloys than Mg-La-Y or Mg-La-Gd alloys. This resulted in a reduced number density of precipitates in comparison to the Mg-La-Y or Mg-La-Gd alloys. This is likely to reduce the effectiveness of the precipitates in pinning or otherwise retarding the motion of dislocations within the grain. It is also important to note that the Mg-0.45La-1.18Y alloys following T4 heat treatment and creep testing have no dynamic precipitates (Figure 6.19c) but still have a minimum creep rate (Figure 6.9) that is over 1 order of magnitude lower than T4 heat treated Mg-0.45La-0.63Nd alloy (Figure 6.7). This indicates that excellent creep properties can also be obtained with a solute in solid solution that has a sufficiently low diffusion rate.

It was shown previously, in Chapter 5 for the as-cast alloys following subsequent creep testing, that both Y and Gd containing alloys had better creep properties than Nd containing alloys, even though all alloys (with the appropriate concentration of ternary RE) had precipitation occurring. The thermal stability of the precipitates, which is ultimately related to the diffusivity of the solute in solid solution is also a contributing factor in relation to creep resistance as was also concluded by Nie *et al.* [12].

6.7 Conclusions

- Short-term solution treatments (1h) at 520°C can be applied successfully to HPDC Mg-La-RE alloys without causing any surface blistering. However, subsequent ageing of the alloys does not necessarily result in significantly higher peak age hardness in comparison to the corresponding as-cast alloys that were aged directly. This is likely related to the removal of the localised region of

supersaturated solute in the α-Mg matrix near grain boundaries in the as-cast condition or the intermetallic structure change.

- Yield strength or 0.2% PS is, in general, negatively affected by either T4 or T6 heat treatments. Only Mg-La-RE alloys with relatively high concentrations of ternary RE that were T6 heat treated have higher 0.2 % PS than the as-cast alloys. T4 solution treatments of relatively high concentrations of ternary RE tend to have no influence on the 0.2 % PS. This may indicate a balance between the strength obtained from a continuous eutectic/intermetallic at grain boundaries and increased solid solution strengthening.
- Creep properties of HPDC Mg-La-RE alloys were either negatively affected or showed little or no improvement after a T4 or T6 heat treatment. Due to the reduction in grain boundary strengthening, primary creep strain is increased following T4 and T6 processing for alloys with ternary RE additions of less than 0.2 at.%. However, relatively high concentrations of ternary RE appeared to balance (but not significantly improve) the negative influence of either solid solution strengthening and/or precipitation hardening.
- Further evidence that the thermal stability of the solute in solid solution, which also influences the precipitate number density, is an important factor in the alloy's creep properties.

7 Discussion

7.1 Introduction 177
7.2 Simulating Microstructure 178
7.3 Mechanical Properties 184
7.4 Effect of Microstructure on Creep 187
7.5 Improving Creep Performance by Microstructure Engineering 195
7.6 Summary 197

7.1 Introduction

The creep mechanisms in Mg alloys are still under debate [12, 14, 70, 90, 109]. Conventional thinking suggested that grain boundary reinforcement to prevent grain boundary sliding is the most important approach to improve creep properties [67, 209]. More recently, solid solution strengthening and/or precipitation hardening [13, 14] or the diffusion rate of solute in solid solution have been proposed as alternate factors which affect the creep resistance in Mg alloys [12].

In this chapter, results from Chapters 4 – 6 are discussed and used to develop a deeper understanding of the relationship between the microstructure and properties of HPDC Mg-La-RE alloys. Figure 7.1 summaries the influence of microstructure on creep found in the previous results chapters.

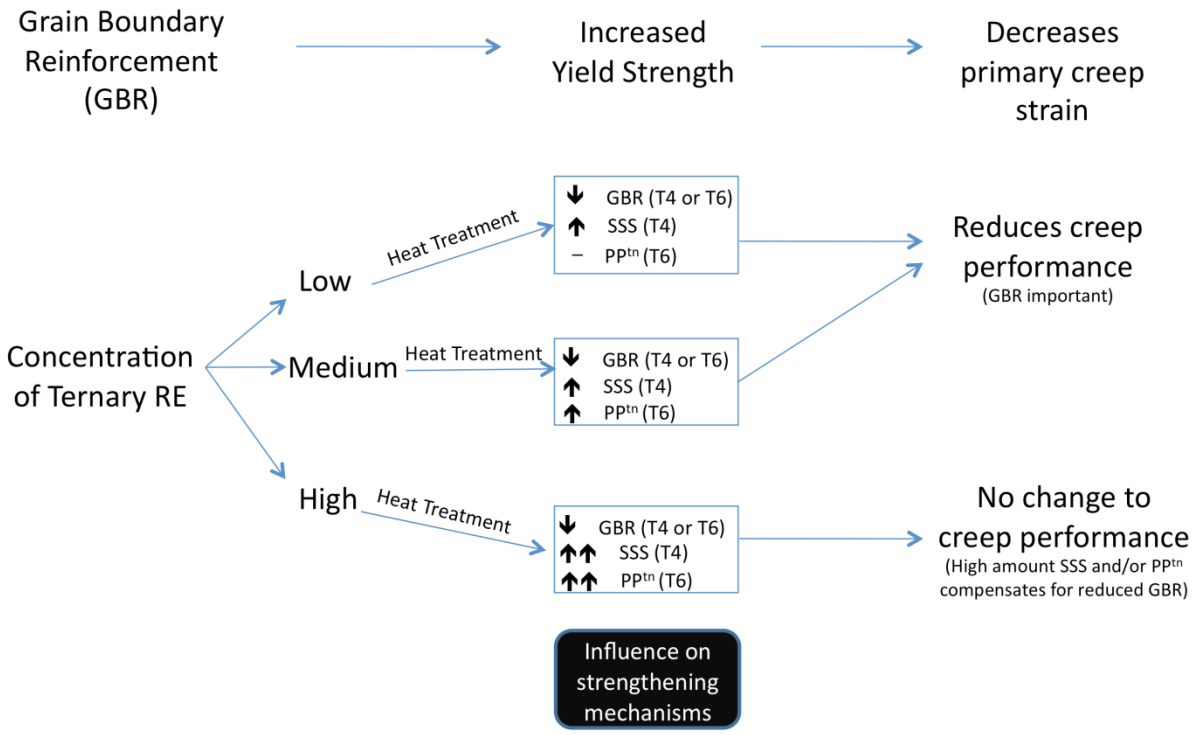

Figure 7.1: Summary diagram of the influence of microstructure including grain boundary reinforcement and varying ternary RE concentrations on the creep properties. Note: GBR is grain boundary reinforcement, SSS is solid solution strengthening and PP^{tn} is precipitation hardening.

The main findings were:

- In the as-cast condition, Mg-La-Nd, Mg-La-Y and Mg-La-Gd had relatively similar microstructural features such as grain size, grain boundary reinforcement and intermetallic phase present in the eutectic. However the creep properties of the Mg-La-Nd alloys were significantly worse than those of Mg-La-Y or Mg-La-Gd alloys.
- Increasing the concentration of ternary RE initially improved creep properties but then no further improvement was found beyond approximately a 0.2 at.% ternary addition of RE.
- The Nd containing alloys reach peak hardness earlier than either Y or Gd containing and also began to overage more rapidly. The thermal stability/diffusivity of solute in solid solution was a key contributing factor in creep resistance.
- Solution treatment did not, in general, improve creep properties. Solution treatment caused the intermetallic phase in the eutectic to become less continuous and thus reduced its effectiveness as grain boundary reinforcement was reduced.
- When there was insufficient grain boundary reinforcement the yield strength decreased, including at elevated temperatures, which reduced creep strength.

7.2 Simulating Microstructure

To assist with the discussion of the influence of different ternary RE elements and concentrations in Mg-La alloys this section attempts to quantify the key microstructural features of Mg-La-RE alloys. This is done using assumptions based on phase diagram predictions and the Scheil-Gulliver equation (S-G) (Eq. (7.1)) for the as-cast microstructure to produce solute distribution curves.

$$C_s = kC_o(1 - f_s)^{k-1} \qquad \textbf{(7.1)}$$

where C_s is the concentration of solute in solid solution, k is the partition coefficient, C_o is the composition of the alloy, and f_s is the fraction solid (or fraction of phase). The Scheil-Gulliver equation assumes a local equilibrium at the liquid-solid interface, no diffusion in

the solid and instantaneous diffusion in the liquid. It is used to estimate the concentration of solute in solid solution in the alloys investigated. The S-G approximation is used due to the non-equilibrium solidification of the alloys analysed in the current work and has been previously used for alloys including binary HPDC Mg-RE [14], thermodynamic modelling of Mg-Zn-Y systems [43, 210] and solute partitioning measurements in Mg-Al-Ca-based cast alloys [22].

Data for the Mg-La-Nd system has been developed recently [132], however, due to the unavailability of ternary thermodynamic data for the Mg-La-Y and Mg-La-Gd systems, binary phase diagrams of Mg-Y and Mg-Gd were used to obtain the partition coefficients and the gradient of the liquidus. Binary Mg-Nd data was used as well as Mg-La-Nd to indicate how La may affect the predictions from the binary system (Figure 7.2). The supersaturation of RE was determined by measuring the area under the solute profile curve down to the solubility limit at 177°C from the Mg-La-Nd solute profiles (as indicated in Figure 7.2a). In the as-cast condition each alloy C_s – fraction of phase profile has three distinct regions as listed below and identified in Figure 7.2e:

i. A region where RE concentration increases with solid fraction that is related to the solute distribution from the centre to the edge of the grain, i.e. coring.
ii. A region of eutectic α-Mg.
iii. A region of the intermetallic phase.

It should be noted that the i and ii regions listed above are relatively small in the C_s – fraction of phase profiles in the low and medium concentrated alloys and thus difficult to see. They are more clearly seen within the alloys with higher concentrations of RE addition. Thus the as-cast C_s – fraction of phase profiles for low and medium concentrations of RE do not have a clearly shown region ii. The C_s – fraction of phase curves for T6 heat-treated alloys following ageing are also represented in the binary C_s – fraction of phase curves. The C_s – fraction of phase profiles for the alloys at equilibrium

conditions following T6 heat treatment is represented by two regions and identified in Figure 7.2f:

x. The concentration of solute in solid solution at equilibrium (this is equal to the solubility of the RE in Mg at the ageing temperature) following ageing (at 160°C for the Y-containing alloys or 177°C for Nd or Gd-containing alloys).
y. If it is possible for precipitates to nucleate there is also a region that is related to the equilibrium concentration of precipitates that form.

It should be noted, since the solute profiles are based on ideal upper bound approximations, precipitates are predicted to form following heat treatment in some alloys such as Mg-0.1Nd following heat treatments where in practise no precipitates were detected. The binary Mg-RE solute profiles were calculated manually using Eq. (7.1) (i.e. not using Pandat^{TM}). The gradient of the liquidus line (assumed to be linear and obtained from [131]) and the partition coefficient used in the Scheil-Gulliver equation to create the solute profile curves are given in Table 7.1.

Table 7.1: Values of the gradient of the liquidus line and partition coefficients for Mg-Nd, Mg-Y and Mg-Gd alloy systems [131].

Alloy system	Gradient of Liquidus Line	Partition Coefficient (k)
Mg-Nd	-13.05	0.0816
Mg-Y	-9.42	0.398
Mg-Gd	-11.39	0.47

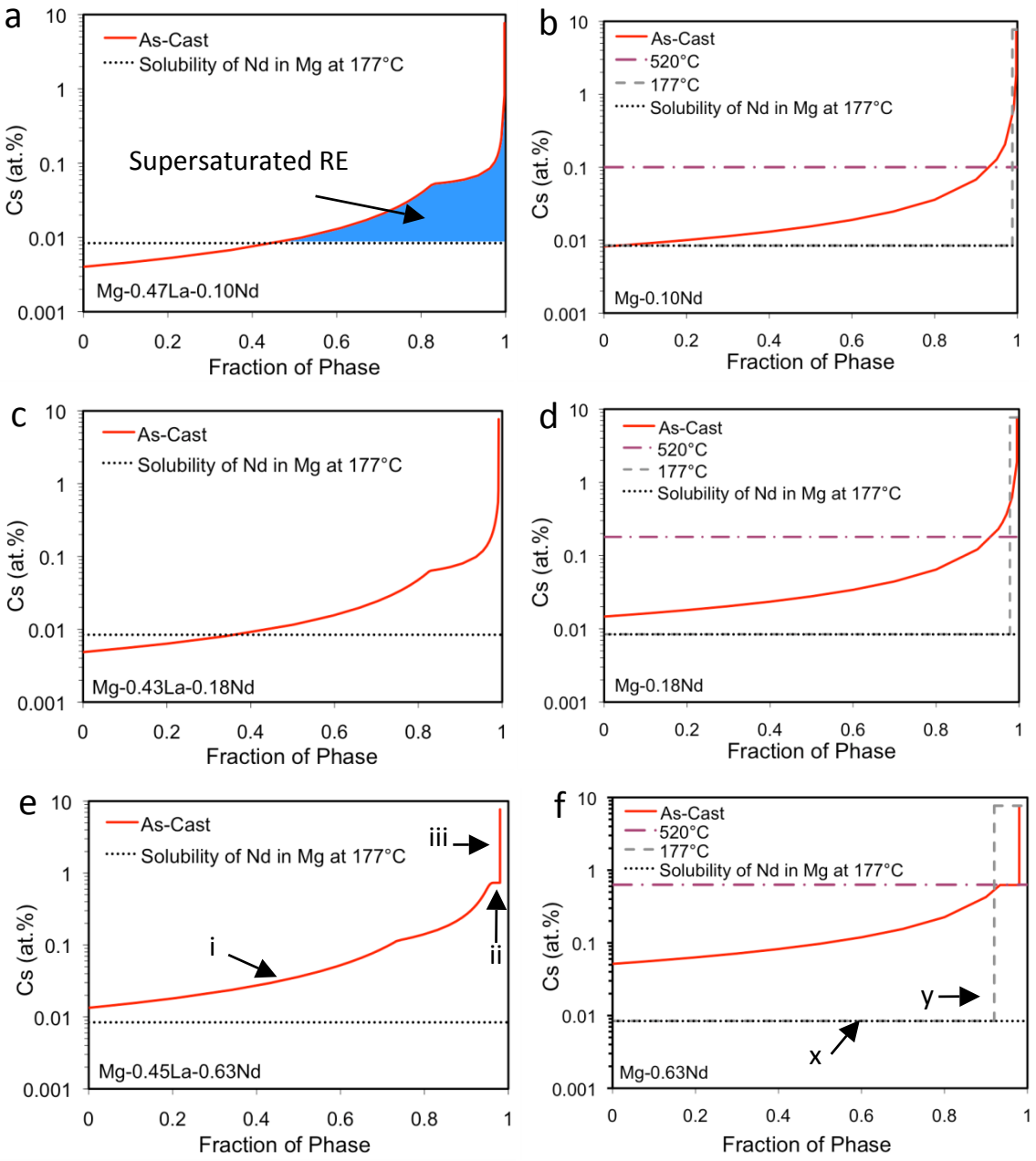

Figure 7.2: Composition profiles of a) Mg-0.47La-0.10Nd, b) Mg-0.10Nd, c) Mg-0.43La-0.18Nd, d) Mg-0.18Nd, e) Mg-0.45La-0.63Nd and f) Mg-0.63Nd in as-cast, equilibrium T4 (520°C) and T6 (177°C) conditions. The solubility of Nd at ageing/testing temperature of 177°C is also included. Note in a) the region of supersaturation is shown, in e) the distinct regions of the composition profile curve are labelled and f) the distinct regions of the curve following solution treatment and then ageing at 177°C are labelled.

Table 7.2 shows that the supersaturation measurements of Nd in Mg for Mg-La-Nd alloys are lower than for Mg-Nd alloys. This is likely related to the low solubility of La in Mg (maximum solid solubility of La in Mg is 0.04 at.%), which may lower the solubility of Nd in

Mg [208]. Thus the C_s – fraction of phase curves should be regarded as ideal upper bound approximations.

Table 7.2: Supersaturation approximations for Mg-La-Nd, Mg-Nd, Mg-Y and Mg-Gd alloys obtained from ternary and binary temperature-fraction of phase curves respectively.

Alloy	Condition	Supersaturation (at.%)
Mg-0.47La-0.10Nd	As-Cast	0.016
Mg-0.43La-0.18Nd	As-Cast	0.024
Mg-0.45La-0.63Nd	As-Cast	0.085
Mg-0.10Nd	As-Cast	0.034
	T4	0.09
Mg-0.12Y	As-Cast	0.011
	T4	0
Mg-0.10Gd	As-Cast	0.018
	T4	0
Mg-0.18Nd	As-Cast	0.059
	T4	0.17
Mg-0.24Y	As-Cast	0.025
	T4	0
Mg-0.21Gd	As-Cast	0.029
	T4	0
Mg-0.63Nd	As-Cast	0.149
	T4	0.62
Mg-1.18Y	As-Cast	0.32
	T4	0.74
Mg-0.87Gd	As-Cast	0.29
	T4	0.31

The binary Mg-RE C_s - fraction of phase curves presented in Figures 7.3 – 7.5 are adequate for a first order approximation to the solute concentrations following casting. It is assumed that following solution treatment all of the ternary RE goes into solid solution and is homogeneously distributed across the grain thus removing the localised region of supersaturation near grain boundaries. The C_s - fraction of phase curves of the alloys following solution treatment (520°C) and water quenching (T4) are also presented in Figures 7.3 - 7.5. The C_s – fraction of phase profiles for the alloys following solution treatment (520°C) are consequently shown as a constant solute concentration in solid

solution. The concentration of solute in solid solution and/or supersaturation of solute (depending on the concentration of RE in the alloy and the temperature of operation) can then be determined.

The Mg-La-RE alloys with relatively low ternary RE (approximately 0.1 at.% ternary RE) all have relatively minor amounts of supersaturated solute in solid solution as indicated in Figure 7.2, i.e. the region of the curve is present above the solubility limit at 160°C or 177°C is relatively small (Table 7.2). In instances where the C_s is below the solubility the alloy has no supersaturated solute in solid solution. Due to the low solubility limit of Nd in Mg at 177°C (0.0084 at.%) the Mg-0.10Nd alloy is the only low concentrated alloy to have some (0.09 at% Nd) supersaturated solute in solid solution (Table 7.2).

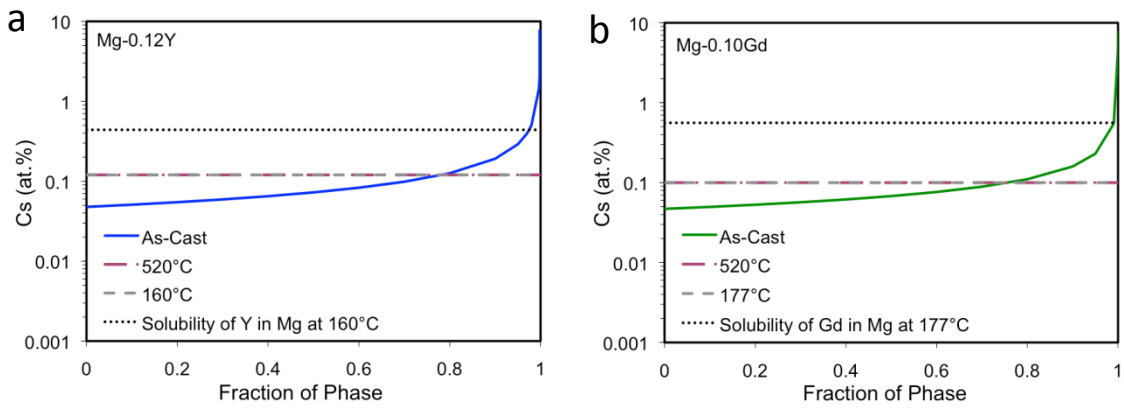

Figure 7.3: Composition profiles of a) Mg-0.12Y and b) Mg-0.10Gd in as-cast condition and at equilibrium following T4 solution treatment (520°C) and T6 ageing (160°C or 177°C) temperatures. The solubility of Y or Gd at their respective ageing temperatures is also included.

When concentrations of RE are increased to approximately 0.2 at.% the amount of solute in solution increases in the as-cast alloys (Figure 7.4). The C_s-fraction of phase curves for Mg-0.49La-0.24Y and Mg-0.46La-0.21Gd following T4 and/or T6 heat treatments indicate that no precipitates should nucleate following creep testing or ageing because the solute content is below the solid solubility limit (Table 7.2). However in certain instances, the experimental evidence presented in Section 6.5.3 shows that precipitates do still nucleate from these alloys following creep testing in both T4 and T6 conditions. This may also be explained by the influence of La on reducing the solubility of the ternary RE in Mg.

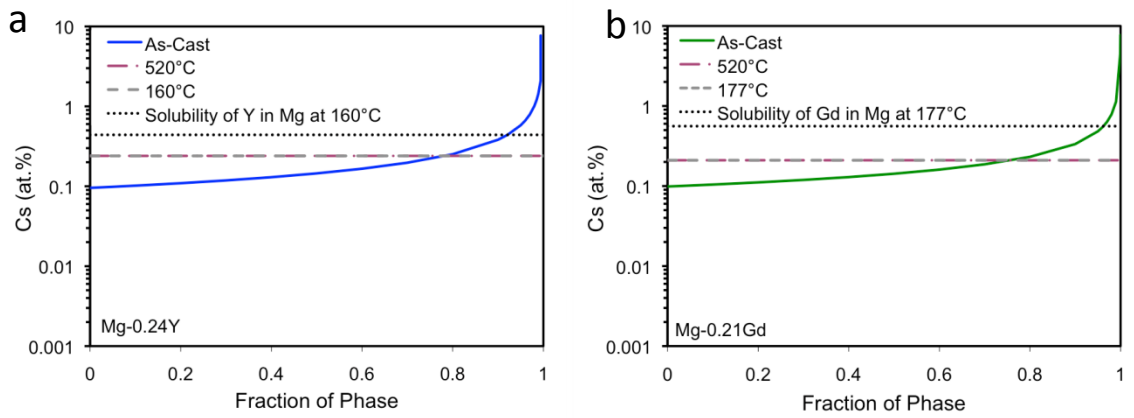

Figure 7.4: Composition profiles of a) Mg-0.24Y and b) Mg-0.21Gd in as-cast condition and at equilibrium following T4 solution treatment (520°C) and T6 ageing (160°C or 177°C) temperatures. The solubility of Y or Gd at their respective ageing temperatures is also included.

The concentrations of RE in the high concentrated alloys used in this thesis were chosen to allow for precipitation to occur at least at an ageing temperature of 200°C (Table 5.4). As a result of this, all highly concentrated alloys are supersaturated in not only the as-cast condition but also following solution treatment (Figure 7.5). Thus T6 heat treatments result in precipitates forming in all of the high RE concentrated alloys (Table 7.2).

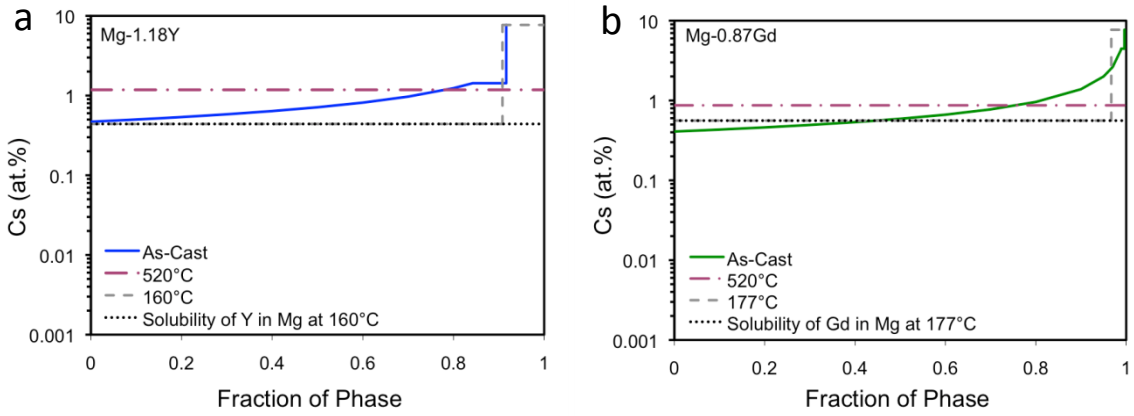

Figure 7.5: Composition profiles of a) Mg-1.18Y and c) Mg-0.87Gd in as-cast condition and at equilibrium following T4 solution treatment (520°C) and T6 ageing (160°C or 177°C) temperatures. The solubility of Y or Gd at their respective ageing temperatures is also included.

7.3 Mechanical Properties

The volume fraction of eutectic or intermetallic phase at grain boundaries can have a significant impact on the subsequent mechanical properties of as-cast alloys [18]. Grain

size has also been shown to influence the yield strength of Mg alloys [200, 211]. In the current work, the average grain size (approximately 9-10µm) does not change significantly between or within alloy series (Table 4.1). In addition, due to the relatively short-term solution treatment duration (1h), referred to as a "flash" annealing by Zhang *et al.* [149], grain size change is also negligible for either T4 or T6 heat treated alloys (Table 6.4). Thus changes to 0.2 % PS in the alloys used in the current work can be more easily correlated with changes to other microstructural features such as grain boundary reinforcement.

When the 0.2 % PS of the as-cast ternary HPDC Mg-La-RE alloys is plotted against the volume fraction of eutectic (for as-cast alloys) or intermetallic (for heat treated alloys) a direct correlation between the eutectic/intermetallic fraction at the grain boundaries and yield strength is observed (Figure 7.6). 0.2 % PS increases with the amount eutectic (or intermetallic phase for the alloys that have undergone T4 or T6 heat treatment). Chia *et al*. [18] have previously shown in binary HPDC Mg-RE that the volume fraction of intermetallic phase at grain boundaries contributes significantly to the yield strength of the alloys. In the present work, the intermetallic phase in the eutectic was confirmed to be $Mg_{12}RE$ in the alloys (Figure 4.7) due to the presence of La in the intermetallic phase. It should be noted that the Mg-La-Nd intermetallic volume fraction simulation over estimates the volume fraction of intermetallic of the final Mg-La-Nd intermetallic point in (Figure 7.6). This may be a result of the difference in eutectic volume fraction measured over a number of different positions from micrographs of an alloy. TerBush *et al.* [22] have previously shown that the S-G equation can approximate the solute profile of HPDC alloys relatively well at lower fraction solid percentages but generally underestimates the solute contribution at high fraction solid percentages. This may also explain why the volume fraction of intermetallic is over estimated.

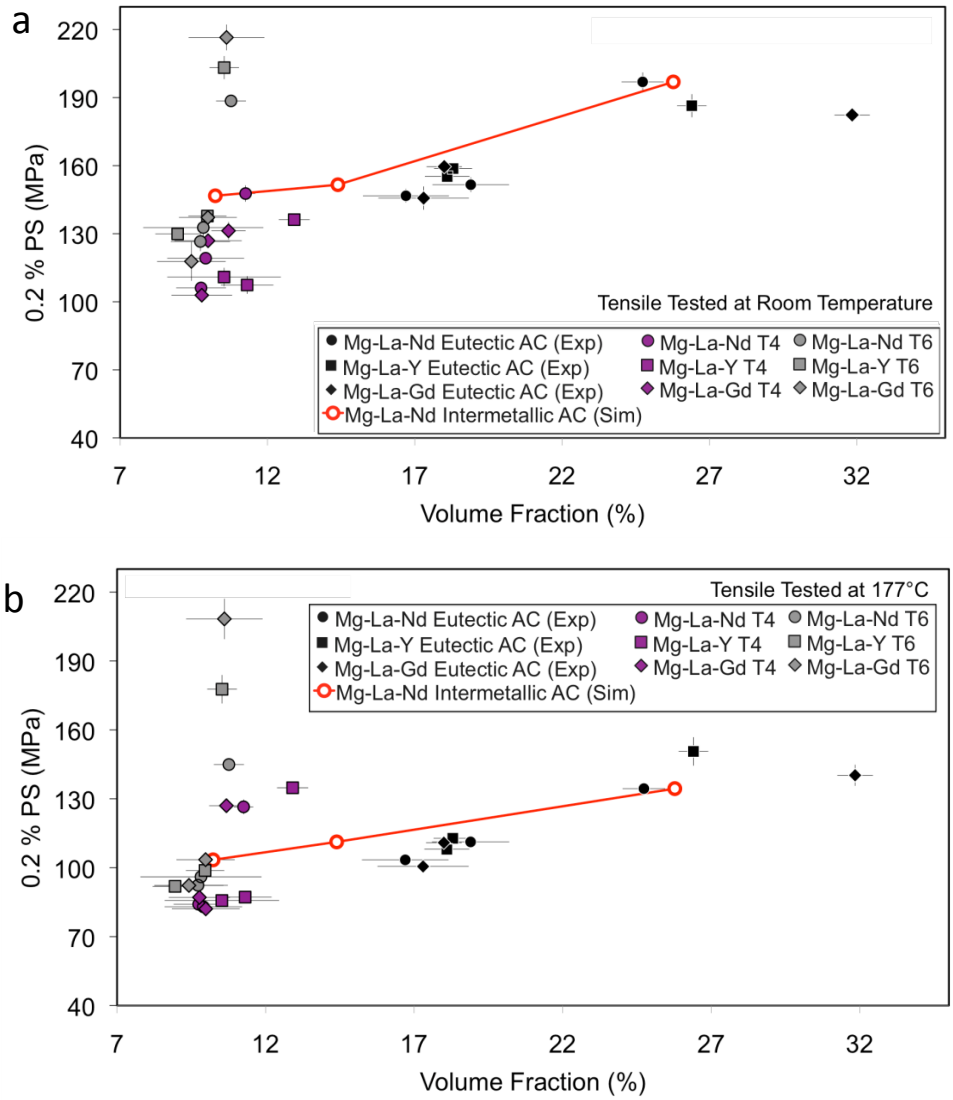

Figure 7.6: 0.2 % PS at a) room temperature and b) 177°C for Mg-La-Nd, Mg-La-Y and Mg-La-Gd alloys as a function of the volume fraction of eutectic in as-cast (AC) alloys or intermetallic in T4 and T6 heat-treated alloys experimentally measured. The volume fraction of intermetallic for Mg-La-Nd alloys determined from temperature-fraction of phase curves (Sim) is included for comparison.

The as-cast Mg-La-Nd intermetallic simulated volume fraction line in Figure 7.6a and b may also be used as an indication of the influence of intermetallic connectivity throughout the alloy on yield strength (or 0.2 % PS). At the beginning of this line (approximately 10 % intermetallic volume fraction) the 0.2 % PS of the alloys with approximately ≥ 0.25 at.% ternary RE is relatively low (approximately 100 MPa or less). The alloys with approximately 10% intermetallic volume fraction also have a significantly more discontinuous intermetallic phase present at grain boundaries (Figure 6.13) in comparison to the alloys with approximately ≥ 17% eutectic in the as-cast alloys (Figure

4.1). The dissolution of the eutectic at the grain boundaries leads to a discontinuous $Mg_{12}RE$ intermetallic phase and the removal of the supersaturated region of solute near grain boundaries (section 7.2). As a result of the weakening of the grain boundary by solution treatment, yield strength (or 0.2% PS) is reduced in HPDC Mg-La-RE alloys when compared to as-cast properties both at room temperature and 177°C (Figure 7.6).

The current work helped to confirm a model created by Zhang *et al.* [149] which attributed a reduction of up to 30 MPa in HPDC Mg-La-RE alloys to the interconnectivity of intermetallic at grain boundaries. The intermetallic phase present at grain boundaries is less continuous following short-term (1 h) solution treatments at 520°C in comparison to the as-cast condition when the intermetallic phase is present in the eutectic. The reduction in grain boundary strengthening can be compensated in alloys with relatively high concentrations of ternary RE addition (i.e. 0.63 at.% Nd, 1.18 at.% Y and 0.87 at.% Gd) (Figure 7.6). Thus solid solution strengthening and/or precipitation hardening can improve the creep properties of an alloy when relatively large concentrations of ternary RE are used. However, from a practical and also an industry viewpoint this is superfluous if properties are at best only marginally better than the as-cast condition.

7.4 Effect of Microstructure on Creep

Microstructures of Mg alloys have been modified in numerous ways in order to improve their creep properties [4, 8, 11, 13-16, 143]. Grain boundaries have been reinforced to prevent grain boundary sliding [4, 11, 84, 99, 143-145]. Alloying additions such as Ca, Sr, Sn and RE have been used to improve precipitation hardening and/or solid solution strengthening [14, 101, 111, 118]. The alloys used in the present work have grain boundary reinforcement due to the presence of a eutectic skeleton that is comprised of eutectic α-Mg and the $Mg_{12}RE$ intermetallic phase at the grain boundaries and also solid solution strengthening and precipitation hardening.

The experimentally determined stress exponents (n) for the Mg-0.45La-0.63Nd and Mg-0.45La-1.18Y alloys at 177°C were 7.3 and 7.4, respectively, which indicated that

diffusion-controlled dislocation climb was the key creep mechanism. However, since this method for determining the creep mechanism is not always accurate [85, 88, 89] the examination of the influence of different ternary RE elements on mechanical and creep properties of HPDC Mg-La-RE is also used to discuss the likely creep mechanism.

The volume fraction of eutectic at the grain boundaries was relatively consistent between alloy series for a given concentration of ternary RE (Figure 6.14). The volume fraction of eutectic at grain boundaries is taken to be an indication of the amount of grain boundary reinforcement. There was still, however, a difference between creep properties (particularly between the Mg-La-Nd alloys and the Mg-La-Y or Mg-La-Gd alloys, Figure 5.8).

In this section both the minimum creep rates and primary creep strain are used in conjunction with microstructural properties to help discuss the influence of microstructure on creep. The minimum creep rate was determined from the region of the creep strain curves where the change in creep strain over time was the lowest. The creep strain following 5 h of creep testing was used to indicate the primary creep strain. This point was chosen as it generally fell within the region of decreasing creep rate and allows for more meaningful and direct comparisons of primary creep strain between alloys (Figure 7.7).

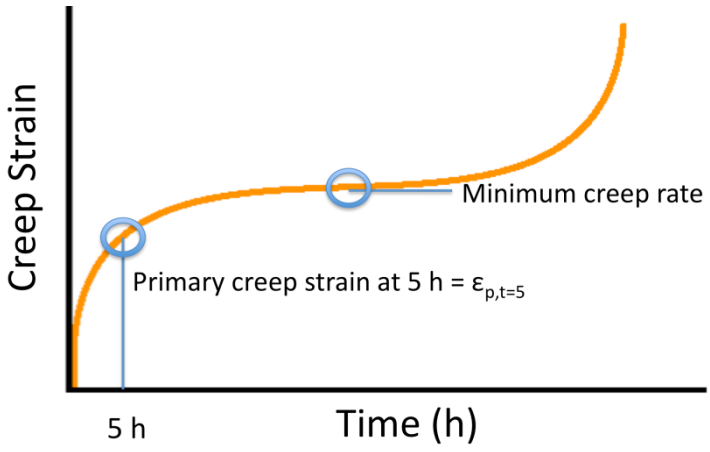

Figure 7.7: Example of a typical creep strain curve of the alloys investigated in the current work. The primary creep strain at 5 h and the region where the minimum creep rate is calculated are indicated.

When a comparison is made between the minimum creep rate and the volume fraction of eutectic (Figure 7.8a), it is clear that increasing the volume fraction of eutectic, by the addition of more ternary RE initially, reduces the minimum creep rate (i.e. from approximately 0.1 to 0.2 at.% ternary RE). However, a further increase in the volume fraction of eutectic did not lead to a significant further improvement in the minimum creep rate. When a comparison is made between the 0.2% PS and minimum creep rate (Figure 7.8b) a similar trend to that shown in Figure 7.8a is found. Initially there is a correlation between 0.2% PS and minimum creep rate but once approximately 0.2 at.% ternary RE is added to the base Mg-La alloy little further improvement in creep is observed even though the 0.2% PS continues to increase.

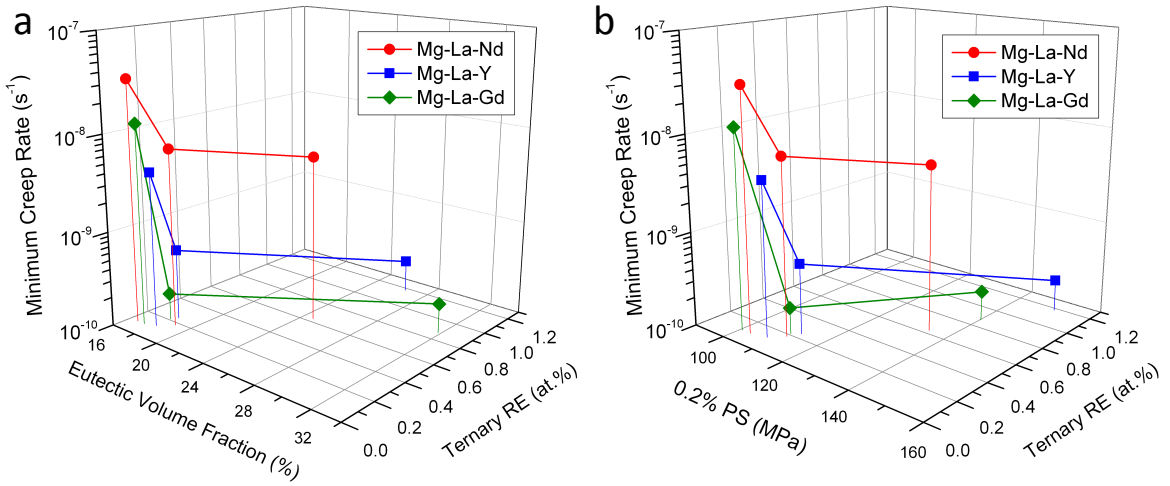

Figure 7.8: Minimum creep rate of as-cast Mg-La-Nd, Mg-La-Y and Mg-La-Gd alloys with change in ternary RE in comparison with a) eutectic volume fraction and b) 0.2 % PS.

If grain boundary reinforcement were the key method to improve creep resistance it would be expected that the creep properties would continue to improve with further grain boundary reinforcement. This indicates that grain boundary reinforcement is not the primary method for the improvement of creep resistance in the alloys investigated. Rather grain boundary reinforcement is useful in improving the 0.2% PS (or yield strength) of the alloys but once this is high enough little further effect is observed. This is particularly important in order to minimise the significant amounts of instantaneous strain (the strain experienced by a sample immediately upon the application of a stress) and appears to also help reduce the extent of primary creep strain.

It was shown in Section 7.2 that the alloys with approximately 0.1 at.% ternary RE have relatively low concentrations of supersaturation in comparison to Mg-0.45La-0.63Nd, Mg-0.45La-1.18Y and Mg-0.45La-0.87Gd and thus have little solid solution strengthening. Furthermore, it was shown in Sections 5.5 and 6.5.3 that alloys with approximately 0.1 at.% ternary RE had no precipitates and therefore no precipitation strengthening. The alloys with ternary RE additions of 0.2 at.% or greater generally had precipitates nucleating either statically (during heat treatment) or dynamically (during creep). It is thus assumed that the 0.1 at.% ternary RE containing alloys only had grain boundary reinforcement as their main strengthening method. When grain boundary reinforcement was the only significant contributing factor to the strengthening of the alloys, the 0.2% PS of the alloys was approximately equal to the creep testing stress of 90 MPa. This was due to the lack of sufficient solid solution strengthening or precipitation hardening. Thus the low concentrated alloys had significantly worse creep properties. Figure 7.9 showed that Mg-0.47La-0.10Nd, Mg-0.48La-0.12Y and Mg-0.45La-0.10Gd had the highest primary creep strain and also had a 0.2 % PS near that of the creep testing strain (90 MPa). This demonstrates that in order to improve creep properties both grain boundary reinforcement and some form of thermally stable solute in solid solution are required.

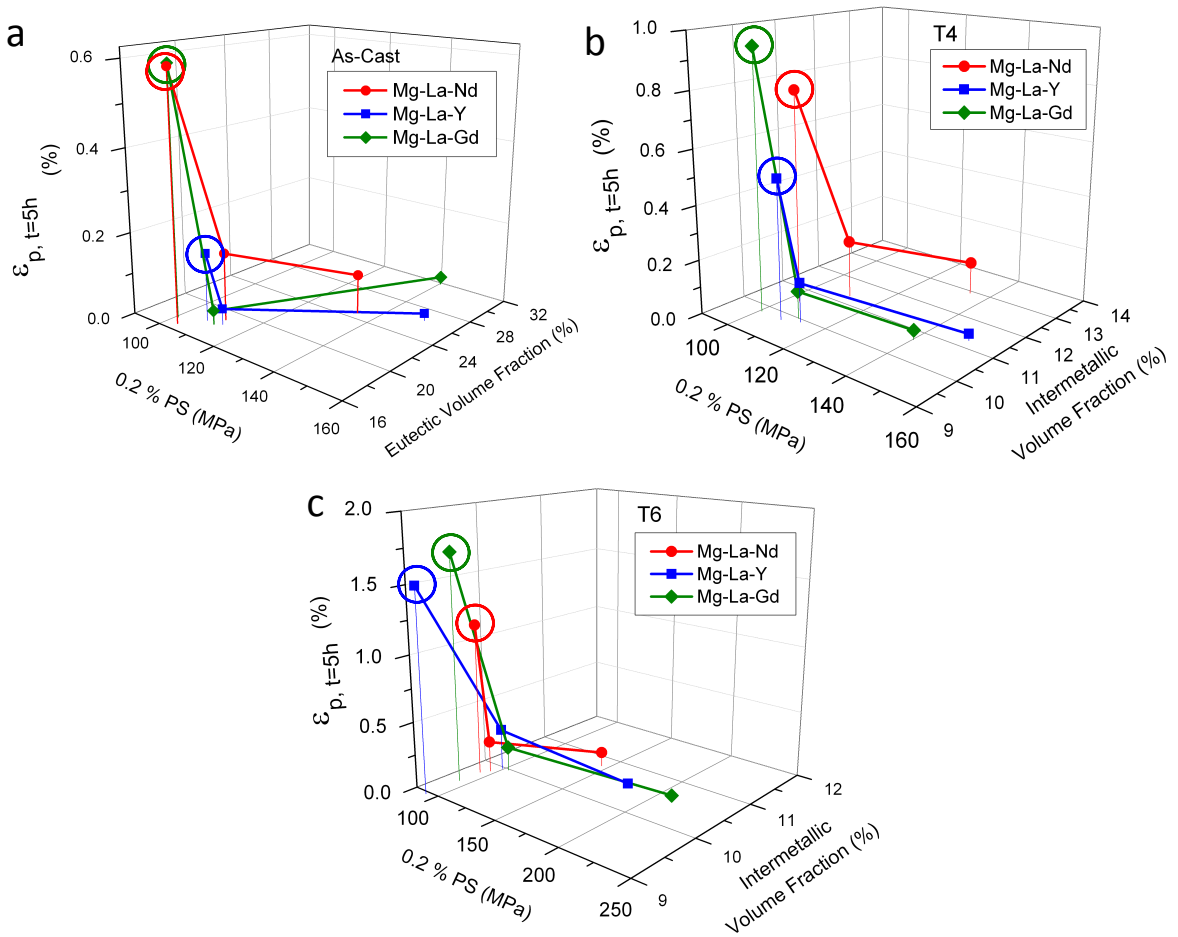

Figure 7.9 Primary creep strain after 5 h of creep strain ($\varepsilon_{p,\ t=5h}$) as a function of 0.2% PS and eutectic or intermetallic fraction for Mg-La-Nd, Mg-La-Y and Mg-La-Gd creep tested at 177°C and 90 MPa and tensile tested at 177°C in a) as-cast, b) T4 and c) T6 conditions. Note: Mg-0.47La-0.10Nd, Mg-0.48La-0.12Y and Mg-0.45La-0.10Gd are circled.

When the alloys are solution treated (T4) (Figure 7.9b) or solution treated and then aged (T6) (Figure 7.9c) the creep rate generally increases. This appears to be due to the intermetallic phase becoming less continuous at the grain boundaries following the solution treatment (Figure 6.13) than that observed in the as-cast condition (Figure 4.1) causing a decrease in yield strength to below or close to the testing stress of 90 MPa. It was similarly shown by Amberger *et al.*[148] that HPDC Mg alloys with a highly interconnected and strong intermetallic phase skeleton, as was shown in MRI 230D, were able to effectively shield the load from the softer α-Mg matrix. However, there is still a difference between the creep properties of the Mg-La-Nd alloys and those of the Mg-La-Y and Mg-La-Gd alloys even though they all have similar grain boundary reinforcement. Zhu *et al.* [14] have shown that different RE elements in HPDC Mg-RE alloys with increasing

amounts of supersaturated solute in Mg can improve creep resistance at 177°C and 90 MPa. In the current work, Mg-0.10Nd had a higher concentration of supersaturated RE (0.034 at.% or 0.016at.% for Mg-0.47La-0.10Nd) than either Mg-0.12Y (0.011 at.%) or Mg-0.10Gd (0.018 at.%). This is also true for Mg-0.18Nd in comparison to Mg-0.24Y or Mg-0.21Gd. A direct comparison of the supersaturation cannot be made with the highest concentrated alloy since the ternary RE concentrations vary. However, the amount of supersaturated solute does not appear to be the only influence on creep resistance since both the Y and Gd-containing alloys have better creep properties (Figure 7.10). This is particularly true for all of the alloys with approximately 0.2 at.% ternary RE.

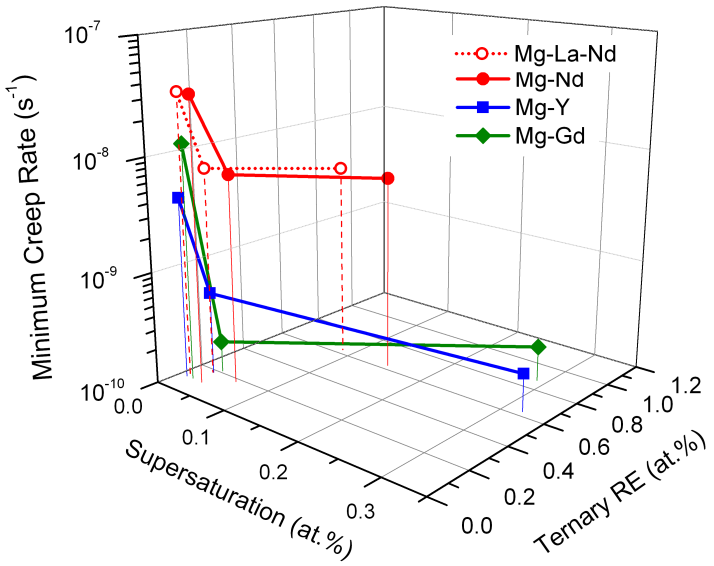

Figure 7.10: Minimum creep rate of Mg-La-Nd, Mg-La-Y and Mg-La-Gd alloys in the as-cast condition in relation to concentration of supersaturation measured from Mg-Nd, Mg-Y and Mg-Gd binary alternative simulations. Note: the supersaturation was calculated from binary Cs – fraction of phase profiles of Mg-Nd, Mg-Y and Mg-Gd.

Both Mg-0.48La-0.12Y and Mg-0.45La-0.10Gd had better creep properties than those of Mg-0.45La-0.63Nd. When the concentration of the ternary RE was increased the creep properties improved in all three alloy series (Section 5.3.1). Mg-0.43La-0.18Nd has more supersaturated solute in solid solution in the as-cast condition but is still the least creep resistant of the three medium concentrated alloys, i.e. in comparison to the Mg-0.49La-0.24Y and Mg-0.46La-0.21Gd alloys (Figure 7.4). Moreover, the Mg-0.43La-0.18Nd alloy is the only alloy of the three that has any concentration of supersaturation following

solution treatment (0.17 at.% Nd) at 520°C (Table 7.2). However, Mg-0.43La-0.18Nd in the T4 or T6 conditions had poorer creep properties than in the as-cast condition (Figure 6.6). Following solution treatment the concentration of supersaturated solute in solid solution is even greater than it is in the as-cast condition but the creep properties of T4 Mg-La-Nd alloys are still not better than in the as-cast condition (Figure 7.11).

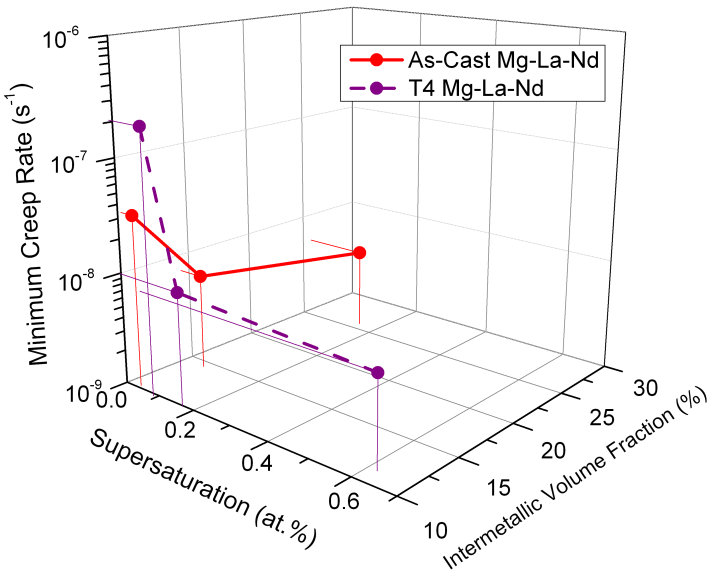

Figure 7.11: Comparison of minimum creep rates in Mg-La-Nd alloys in the as-cast condition and T4 condition as a function of supersaturation of solute and volume fraction of intermetallic. Note the intermetallic volume fraction for the as-cast alloys was determined from the Mg-La-Nd temperature-fraction of phase curves and for T4 from BSE SEM micrograph image analysis.

When the total concentration of solute in solid solution (not just the supersaturated solute) is plotted against minimum creep rate and RE concentration (Figure 7.12) it is shown that for comparable RE additions the Y or Gd-containing alloys have higher concentrations of solute in solid than Nd-containing alloys. This indicates that the Mg-La-Y and Mg-La-Gd alloys have higher amounts of solid solution strengthening than the Mg-La-Nd alloys.

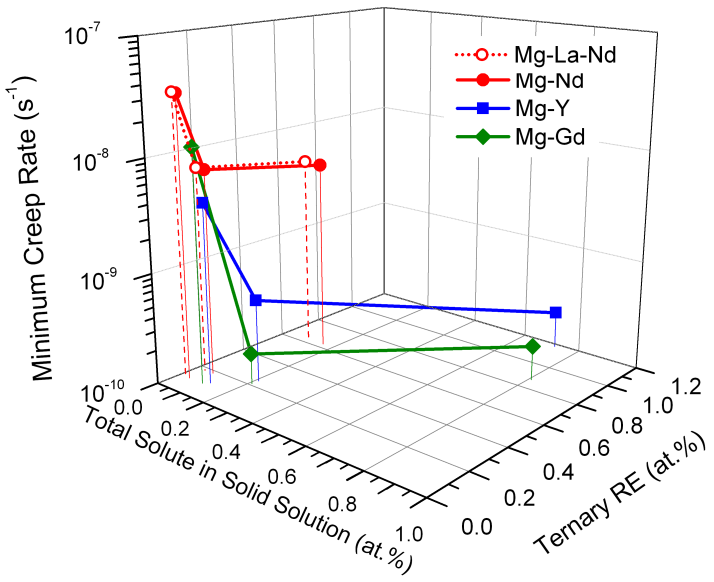

Figure 7.12: Minimum creep rate of Mg-La-Nd, Mg-La-Y and Mg-La-Gd alloys in the as-cast condition in relation to concentration of total solute is solid solution measured from Mg-Nd, Mg-Y and Mg-Gd binary alternative simulations.

Age hardening testing showed that Nd-containing alloys (specifically Mg-0.45La-0.63Nd) reached peak hardness and then overaged before the Y or Gd-containing alloys when aged from the as-cast condition (Figure 5.6) or following solution treatment (Figure 6.2). This indicates Nd is the least thermally stable solute in solid compared with Y or Gd. A comparison is made between minimum creep rate and the time taken to reach peak-aged conditions for the Mg-La-Nd, Mg-La-Y and Mg-La-Gd alloys (Figure 7.13).

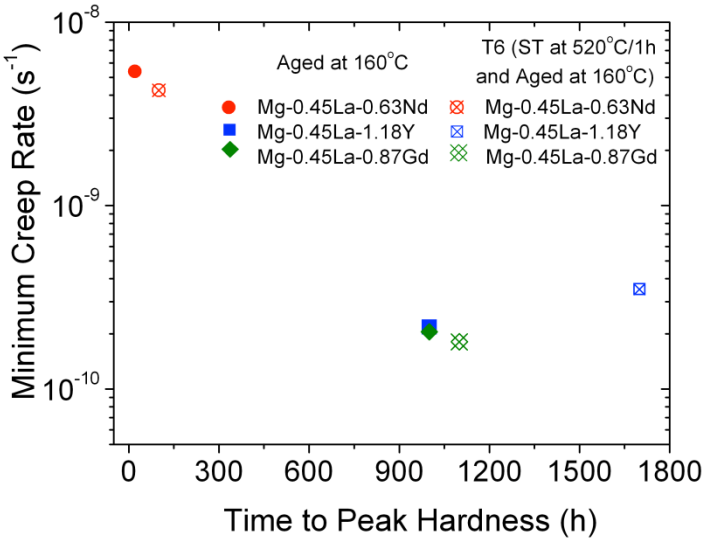

Figure 7.13: Minimum creep rate at 177°C and 90 MPa for Mg-0.45La-0.63Nd, Mg-0.45La-1.18Y and Mg-0.45La-0.87Gd in relation to peak ageing duration at 160°C.

Using the peak hardness duration as an indication of the thermal stability or diffusion rate of the ternary RE in the alloys, Figure 7.13 indicates that the greater thermal stability of Y or Gd solute than Nd in Mg has a significant influence on creep resistance.

7.5 Improving Creep Performance by Microstructure Engineering

By examining the influences of different ternary RE elements on the mechanical and creep properties of HPDC Mg-La-RE a likely creep mechanism can be proposed. The influence of grain boundary reinforcement on creep properties of Mg alloys has long been thought of as the most important way to improve creep strength [4, 11, 84, 99, 143-145]. In this current work, it has been shown that grain boundary reinforcement is directly related to an improvement of yield strength. This is indirectly related to creep strength, particularly primary creep (Figure 7.6). Thus it is firstly important to strengthen the alloy sufficiently via grain boundary reinforcement to achieve sufficient high temperature yield strength in order to minimise any instantaneous strain or primary creep strain experienced by the alloy upon the application of a stress.

Grain boundary reinforcement remained relatively consistent between the alloy series investigated in the current work due to the consistent amount of eutectic or intermetallic phase volume fraction at grain boundaries for a given concentration of ternary RE (Figure 6.14). There is also little difference between the average grain sizes within or between alloys series or after heat treatment. Section 7.2 indicated that the concentration of supersaturation of solute in solid solution may improve creep resistance with increased concentration of supersaturation. However, out of the three alloy systems, the Mg-La-Nd series in general had larger concentrations of supersaturation than either the Mg-La-Y or Mg-La-Gd series.

There was still a significant difference in creep properties, in particular between the Mg-La-Nd alloys and the Mg-La-Y or Mg-La-Gd alloys (Figure 5.8) with the Mg-La-Nd alloys having the poorest creep properties out of the three systems. The Y and Gd-containing

have greater amounts of solid solution strengthening than the Nd-containing alloys due to their higher solid solubility in Mg. However, if higher soluble alloying additions were the reason for improved creep properties, Mg-Al alloys such as AZ91 should also demonstrate good high temperature creep resistance instead of having poor creep resistance [104, 143].

The morphology and number density of the precipitates also varied between alloy series. In general, the Nd-containing alloys had coarse plate-like precipitates oriented along the prismatic planes (as shown in Mg-0.45La-0.63Nd alloys). The precipitates in the Nd-containing alloys also had a lower number density in comparison to alloys in the other two series. The age hardening response of the Mg-La-Nd alloys were significantly faster and lower than the Mg-La-Y or Mg-La-Gd alloys in either the as-cast (Figure 5.6) or heat treated (Figure 6.2) conditions. This is a significant point of difference between the alloy systems. The age hardening response is a good indication that the thermal diffusivity and the kinetics of the solute in solid solution of Mg-La-Nd alloys are faster (less thermally stable) than Mg-La-Y or Mg-La-Gd alloys. Nie *et al.* [12] have also shown previously that the diffusion of solute in solid solution in Mg alloys has a significant effect on creep. A comparison of the diffusion coefficients of the rare earth element Ce and some of the more common elements alloyed with Mg, such as Al and Zn (Table 2.5) showed Ce had the lower diffusion rates at temperatures of 150°C and 175°C. It can be concluded that the relatively slow diffusion rate of rare earth element would help to impeded dislocation motion either by the solute or by the presence of more thermally stable precipitates. The mobility of glide and climb dislocations, which is dependent on effective diffusion coefficient of atoms in the α-Mg lattice, D_{el} may be approximated by the equation (Eq. (7.2)).

$$\dot{\varepsilon}_{dis} = \frac{BD_{el}b}{kT}(\sigma - \sigma_0)^n \qquad \textbf{(7.2)}$$

where B and n are constants, b is the Burgers vector of lattice dislocations of the matrix phase and σ_0 is a threshold stress which is effected by the distribution of second phase particles [12]. D_{el} is given by [212]:

$$D_{el} = \frac{D_s D_{Mg}}{(1 - c_s)D_s + c_s D_{Mg}} \quad \textbf{(7.3)}$$

where D_s is the diffusion coefficient of the solute atoms in α-Mg lattice, D_{Mg} is the self-diffusion coefficient and c_s is the atomic fraction of solute atoms within in the α-Mg phase. This is a good indication that the thermal stability or diffusion of the solute and, in turn, the precipitate size and number density of Mg-La-RE alloys is a contributing factor to creep resistance. It also helps to confirm the creep mechanism, diffusion controlled dislocation creep, which was experimentally determined.

7.6 Summary

In order to produce an optimal high-pressure die-castable and creep resistance Mg-La-RE alloy, the alloy needs to be engineered from the macro to the atomic scales (Figure 7.14).

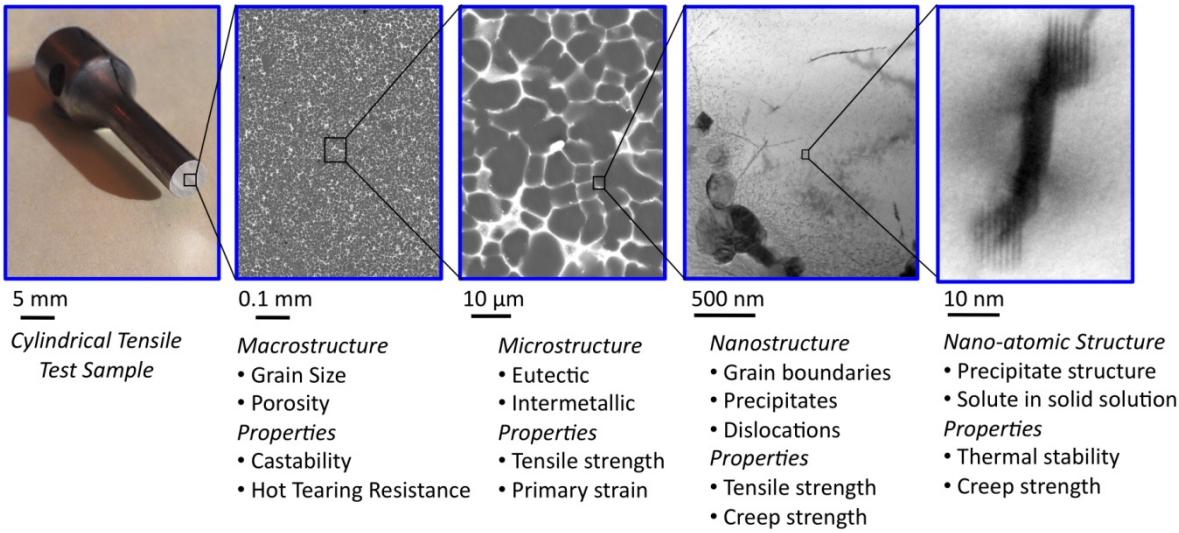

Figure 7.14: Overview of a HPDC Mg-La-RE sample (Mg-0.45La-0.87Gd) that shows the influence of the alloy features on the properties of the sample.

- Grain boundary reinforcement is critical for the improvement of yield strength, which is further related to the influence of instantaneous strain or primary creep strain. However grain boundary reinforcement has little further influence on steady state creep when there is sufficient ternary RE present.

- Precipitate morphology and number density can influence the yield strength of Mg-La-RE. Precipitates may also act as barriers to dislocation movement. However, if the precipitates overage quickly their influence on improving creep properties is diminished.
- The rate of diffusion of solute in solid solution is critically important to the creep resistance. A diagram that summaries the influence of varies RE elements as well as some commonly used Mg alloy elements on creep performance is presented in Figure 7.15.

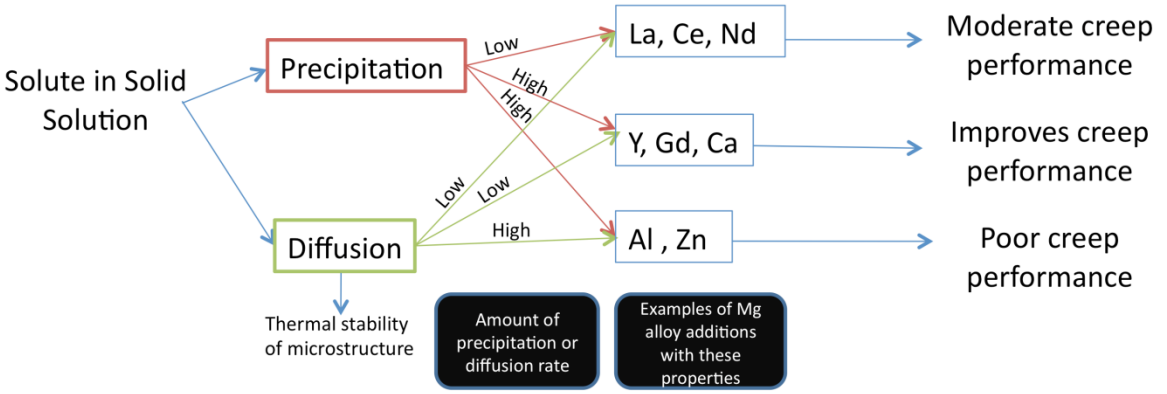

Figure 7.15: Influence of solute in Mg solid solution on creep. Examples of commonly used alloying additions in Mg alloys are included along with RE elements for comparison.

8 Conclusions and Recommendations for Future Work

8.1 Conclusion

The aims of this work were to determine the effects of different ternary rare earth alloying additions (Nd, Y or Gd) and heat treatment on the creep properties and microstructure of high-pressure die-cast Mg-La-RE alloys. It was concluded that improvements to elevated temperature creep resistance of HPDC Mg-RE alloys could be achieved by building on a base Mg-RE alloy (Mg-La) that had sufficiently good castability and grain boundary reinforcement with low diffusivity/thermally stable soluble ternary RE additions in solid solution. This helped to strengthen the alloy from the macro to the atomic scale. The results from this study allow for conclusions on key contributors to elevated temperature creep properties. The following conclusions can be made:

- **To achieve excellent creep properties in HPDC Mg-La-RE alloys the presence of thermally stable precipitates and slow diffusing solute in solid solution in combination with grain boundary reinforcement are required to impede dislocation motion.**

The creep mechanism was determined to be diffusion-controlled dislocation creep. Grain boundary reinforcement via the eutectic or intermetallic phase present at grain boundaries as well as average grain size was approximately equal between the three alloy

series investigated. The creep properties of Mg-La-Nd alloys were, however, significantly worse when compared to Mg-La-Y or Mg-La-Gd alloys with similar ternary RE additions.

The ageing response showed that Mg-La-Nd alloys overage faster than either Mg-La-Y or Mg-La-Gd alloys. The microstructure observations following creep testing of as-cast alloys revealed that all alloys with approximately 0.2 at.% (or greater) ternary RE can form dynamic precipitates. This helped to show that the thermal stability of the solute in solid solution, which also influences the precipitate number density could influence creep properties. The age hardening response showed a significant difference between the Mg-La-Nd and Mg-La-Y and Mg-La-Gd alloys, which indicates differences in thermal diffusivity of solute in solid solution. The diffusion of the solute in solid solution was particularly important since the creep mechanism was related to diffusion-controlled dislocation climb from stress exponent calculations.

- **The as-cast Mg-La-RE alloys investigated had similar grain sizes, intermetallic phase and grain boundary reinforcement. Difference between the alloys arises from the solid solubility of the ternary additions in Mg.**

The morphology of the microstructure of three HPDC Mg-RE alloy series (Mg-La-Y, Mg-La-Gd and Mg-La-Nd) with varying ternary alloying addition concentrations were compared. It was found that all alloys have relatively similar morphologies with respect to grain size, average volume fraction of eutectic present at grain boundaries and the intermetallic phase present in the eutectic. The morphology of the eutectic was found to change from a lamellar eutectic composed of α-Mg and an intermetallic phase of $Mg_{12}RE$ to a fibrous α-Mg phase within a matrix of an intermetallic phase and then a divorced eutectic with increasing ternary RE addition.

It is therefore concluded any difference in creep properties between alloys must be independent of grain size, intermetallic phase and/or grain boundary reinforcement and be related to other alloy attributes such as precipitation hardening and/or solid solution

strengthening which are in turn related to the selection of ternary alloying RE element addition to the alloys.

- **Short-term heat treatments can successfully be applied to HPDC Mg alloys without causing blistering to the surface of a casting. However, there is no significant improvement to creep properties.**

In the as-cast condition the alloys under investigation had a continuous intermetallic phase present in the eutectic at grain boundaries that acted like a skeleton to strengthen the alloys. When the alloys were solution treated at 520°C for 1h the eutectic α-Mg was distributed homogeneously throughout the grain and a discontinuous $Mg_{12}RE$ intermetallic phase remained at the grain boundaries. This caused a reduction in 0.2 % PS but did not significantly increase solid solution strengthening. Furthermore, any subsequent precipitation hardening did little to improve the strength of the alloys. Creep properties were also negatively affected following solution treatment.

Only when significantly high concentrations of ternary RE were added to the alloy do the creep properties become similar to those in the as-cast condition. It was thus concluded that grain boundary reinforcement was a practical method to maintain both good yield strength and to reduce the initial amount of pronounced creep strain. However, without a thermally stable solute present in solid solution and in turn thermally stable precipitates to impede the movement of dislocations, creep properties are still poor.

- **Micro-alloying additions of Nd, Y or Gd to a base HPDC Mg-La alloy significantly increased hot tearing susceptibility. Y or Gd alloying additions of greater than approximately 0.1 or 0.2 at.%, respectively, decreased hot tearing susceptibility. However no significant improvement to hot tearing was detected in Mg-La-Nd alloys for concentrations of Nd up to 0.63 at.%**

The alloys investigated had similar grain morphology and size, solidification range and the amount of eutectic. It was shown that hot tearing susceptibility can be accurately predicted from the integral between the coherency and coalescence points obtained from computational thermodynamic temperature-fraction solid curves.

The ternary alloying content of Mg-La-RE HPDC alloys significantly affected hot tearing susceptibility. Compositions of HPDC Mg-La-RE alloys with low hot tearing susceptibility/good castability either had approximately zero ternary RE or had ≥ 0.6 at.% concentrations of ternary RE. However, an improvement in hot tearing susceptibility was only detected in Mg-La-Y and Mg-La-Gd alloys. Once the concentration of ternary RE of Mg-La-Nd alloys reached approximately 0.2 at.% only a relatively minor improvement in hot tearing susceptibility have measured in the Mg-0.45La-0.63Nd alloy. There was a difference in the morphology of the eutectic between the Y or Gd-containing alloys and the Nd-containing alloys. This was most apparent at ternary concentrations greater than 0.2 at.%. Feeding channels allow for the flow of the molten component of the alloy during final stages of solidification to fill the voids in the castings and prevent hot tearing. The difference in morphology of the eutectic for higher concentrated Y or Gd to Nd containing alloys may influence the feeding channels during solidification.

8.2 Future Work

Whilst this work offers reasonable explanations for creep mechanisms being related to thermally stable solute in solid solution and precipitate so long as there is sufficient grain boundary reinforcement, there are a number of areas where further testing and validation would be useful.

- **Diffusion coefficient measurements for Nd, Y or Gd in Mg:** In this current work the diffusion coefficient (D_o) and the activation energy (Q) of Ce in Mg were used due to the lack of diffusion data on other RE elements such as Nd, Y or Gd. Nie *et al.* [12] similarly had to use diffusion measurements of Ce in Mg for calculations of

a Mg-Y alloy. Since the current work has proposed the importance of thermal diffusivity of the different RE on creep it is important to have diffusion data on these (and ideally all) RE elements in Mg.

A diffusion couple between pure Mg and the various RE elements could be used to measure the diffusion coefficients. This may also help to understand why the Y containing alloys in this current work had significantly slower age hardening response at 177°C than either Nd or Gd.

- **CALPHAD predictions for Mg-La-Y and Mg-La-Gd alloys:** Although there has been work published on ternary phase diagrams for Mg-Ce-RE alloys such as Mg-Ce-La [213], Mg-Ce-Y or Mg-Ce-Nd [180, 214], only a relatively small amount of work has been published on Mg-La-RE alloys such as Mg-La-Nd [132]. In the current work, binary phase diagrams for Mg-Y and Mg-Gd alloys were used in place of ternary Mg-La-Y and Mg-La-Gd phase diagrams. This was sufficient in the present work, however, more accurate analysis could be obtained if ternary Mg-La-RE phase diagrams were available. In relation to hot tearing predications, it was clear that using binary phase diagrams was less accurate than using ternary phase diagrams to help indicate the hot tearing susceptibility of ternary Mg-La-RE alloys. Also, in some instances precipitates were present in alloys that according to their equivalent binary phase diagrams should not be present. Ternary phase diagrams for the Mg-La-Y alloys may also help with the identification of precipitates present in theT6 Mg-0.45La-1.18Y alloy shown in Figure 6.22.

- **Solubility of different metastable phases in Mg:** The composition of solute – fraction of phase curves used to determine the concentration of supersaturation of RE in Mg predicted in some instances that precipitates should form during heat treatment or creep testing. The transmission electron microscopy did not always support the predictions. This is may be the result of using phase diagrams that are based on thermal equilibrium data. The metastable phases may have a different

solubility than that presented in thermal equilibrium phase diagrams. In order to produce more accurate microstructure models or predications it would be useful to determine the solubility of the Mg-RE metastable phase. This can be achieved in a similar way to equilibrium phase determination. However, the selection of appropriate compositions is required in order to determine composition tie lines and other phase data.

- **Model considering the influences of microstructure including grain boundary reinforcement, precipitation strengthening and solid solution strengthening on creep:** The present study has shown that creep properties can be improved through a combination of factors for HPDC Mg-La-RE alloys. These included grain boundary reinforcement, precipitates that were thermally stable at the testing temperature and by solute that had a slow diffusion rate. It would be useful to create a model, which can incorporate properties of alloying additions to Mg such as solid solubility, ageing kinetics and grain boundary reinforcement to help predict creep properties. This would allow for a broader understanding of the influence of alloying additions (not necessarily RE elements) on Mg without having to cast multiple alloys and perform time consuming experiments.

References

[1] J. DeCicco and F. Fung, *Global Warming on the Road. The Climate Impact of America's Automobiles.* 2006, Environmental Defense: New York.

[2] A. Feng and D.J. Santini: SAE Transactions, Vol. 113, (2004), p. 258.

[3] L. Cheah and J. Heywood: Energy Policy, Vol. 39, (2011), p. 454.

[4] P. Humble: Materials Forum, Vol. 21, (1997), p. 45.

[5] B. Andresen, Die Casting Engineering A Hydraulic, Thermal, and Mechanical Process. (CRC Press, 2005).

[6] R.N. Lumley, R.G. O'Donnell, D.R. Gunasegaram, and M. Givord: Metallurgical and Materials Transactions A, Vol. 38A, (2007), p. 2564.

[7] M.A. Gibson, C.J. Bettles, M.T. Murray, and G.L. Dunlop: Magnesium Technology. Ed. A. Luo, N. Neelameggham, and R. Beals, TMS, 2006, p. 327.

[8] L.Y. Wei, G.L. Dunlop, and H. Westengen: Journal of Materials Science, Vol. 31, (1996), p. 387.

[9] I. Polmear, Light Alloys. Materials & Mechanical Science. (Butterworth-Heinemann, 2005).

[10] K. Matucha and R. Cahn, eds. *Materials Science and Technology, Structure and Properties of Nonferrous Alloys*. Vol. 8. 1996, John Wiley & Sons.

[11] R.L. Bell and T.G. Langdon: Journal of Materials Science, Vol. 2, (1967), p. 313.

[12] J.F. Nie, M.A. Easton, T.B. Abbott, S.M. Zhu, and M.A. Gibson: 8th International Conference on Magnesium Alloys and their Applications. Ed. K.U. Kainer, Wiley-VCH, 2009, p. 89.

[13] K. Maruyama, M. Suzuki, and H. Sato: Metallurgical and Materials Transactions A, Vol. 33A, (2002), p. 875.

[14] S.M. Zhu, M.A. Gibson, M.A. Easton, and J.F. Nie: Scripta Materialia, Vol. 63, (2010), p. 698.

[15] W. Blum, P. Zhang, B. Watzinger, B.V. Grossmann, H. Lipowski, and H.G. Haldenwanger: Materials Science Forum, Vol. 350, (2000), p. 141.

[16] S.M. Zhu, M.A. Gibson, J.F. Nie, M.A. Easton, and G.L. Dunlop: Metallurgical and Materials Transactions A, Vol. 40A, (2009), p. 2036.

[17] The Open University, http://core.materials.ac.uk/repository/ou_manufacturing/t173_2_023i.jpg. Pressure-die Casting, 2010.

[18] T.L. Chia, M.A. Easton, S.M. Zhu, M.A. Gibson, N. Birbilis, and J.F. Nie: Intermetallics, Vol. 17, (2009), p. 481.

[19] W. Young-Mok and B.G. Thomas: Metallurgical and Materials Transactions A, Vol. 32A, (2001), p. 1755.

[20] D.A. Porter, K.E. Easterling, and M.Y. Sherif, Phase Transformations in Metals and Alloys. 3rd ed. (CRC Press, 2009).

[21] A. Bowles, 2003, *Moderate Temperature Ageing of HPDC Mg-Al Alloys,* PhD, University of Queensland.

[22] J.R. TerBush, N.D. Saddock, J.W. Jones, and T.M. Pollock: Metallurgical and Materials Transactions A, Vol. (2010), p. 1.

[23] C.M. Gourlay, H.I. Laukli, and A.K. Dahle: Metallurgical and Materials Transactions A, Vol. 38, (2007), p. 1833.

[24] H. Gjestland and H. Westengen: Advanced Engineering Materials, Vol. 9, (2007), p. 769.

[25] K. Yang, A.V. Nagasekhar, C.H. Caceres, and M. Easton: 7th Pacific Rim International Conference on Advanced Materials and Processing. Ed. J.F. Nie, Trans Tech Publications, 2010, p. 691.

[26] M.S. Dargusch, M.A. Easton, S.M. Zhu, and G. Wang: Materials Science and Engineering A, Vol. 523, (2009), p. 282.

[27] D.H. StJohn, A.K. Dahle, T. Abbott, M.D. Nave, and M. Qian: Magnesium Technology. Ed. H.I. Kaplan, TMS, 2003, p. 95.

[28] K. Strobel, M.A. Easton, V. Tyagi, M. Murray, M.A. Gibson, G. Savage, and T.B. Abbott: International Journal of Cast Metals Research, Vol. 23, (2010), p. 81.

[29] A.K. Dahle, S. Sannes, D.H. StJohn, and H. Westengen: Journal of Light Metals, Vol. 1, (2001), p. 99.

[30] W. Xiao, M.A. Easton, S. Zhu, M.S. Dargusch, M.A. Gibson, S. Jia, and J.F. Nie: Advanced Engineering Materials, Vol. 14, (2012), p. 68.
[31] D.G. Eskin, Suyitno, and L. Katgerman: Progress in Materials Science, Vol. 49, (2004), p. 629.
[32] J. Campbell, Complete Casting Handbook: Metal Casting Processes, Metallurgy, Techniques and Design. 1st ed. (Elsevier Butterworth-Heinemann, 2012), 1130.
[33] J. Campbell: Metallurgical and Materials Transactions B, Vol. 37B, (2006), p. 857.
[34] M.A. Easton and D.H. StJohn: International Journal of Cast Metals Research, Vol. 12, (2000), p. 393.
[35] A.L. Bowles, Q. Han, and J.A. Horton: Magnesium Technology. Ed. N.R. Neelameggham, H.I. Kaplan, and B.R. Powell, TMS, 2005, p. 99.
[36] F. Weinberg: Metallurgical Transactions B, Vol. 10 B, (1979), p. 219.
[37] Z. Wang, Y. Huang, A. Srinivasan, Z. Liu, F. Beckmann, K.U. Kainer, and N. Hort: Materials and Design, Vol. 47, (2012), p. 90.
[38] A. Srinivasan, Z. Wang, Y. Huang, F. Beckmann, K.U. Kainer, and N. Hort: Metallurgical and Materials Transactions A, Vol. 44A, (2013), p. 2013.
[39] M. Easton, M. Gibson, S.M. Zhu, and T. Abbott: Metallurgical and Materials Transactions A, (2014), in press.
[40] Z. Wang, Y. Huang, A. Srinivasan, Z. Liu, F. Beckmann, K.U. Kainer, and N. Hort: Journal of Materials Science, Vol. 49, (2014), p. 353.
[41] T. Clyne and G. Davies: British Foundryman, Vol. 74, (1981), p. 65.
[42] M. Rappaz, J.M. Drezet, and M. Gremaud: Metallurgical and Materials Transactions A, Vol. 30A, (1999), p. 449.
[43] P. Gunde, A. Schiffl, and P.J. Uggowitzer: Materials Science and Engineering A, Vol. 527, (2010), p. 7074.
[44] L. Zhou, Y. Huang, P. Mao, K.U. Kainer, Z. Liu, and N. Hort: Magnesium Technology. Ed. W.H. Sillekens, S.R. Agnew, N.R. Neelameggham, and S.N. Mathaudhu, TMS, 2011, p. 125.
[45] M. Easton, T. Abbott, J.F. Nie, and G. Savage: Magnesium Technology. Ed. M. Pekguleryuz, N.R. Neelameggham, R.S. Beals, and E.A. Nyberg, TMS, 2008, p. 323.
[46] L. Sweet, M.A. Easton, J.A. Taylor, J.F. Grandfield, C.J. Davidson, L. Lu, M.J. Couper, and D.H. StJohn: Metallurgical and Materials Transactions A, Vol. 44A, (2013), p. 5396.
[47] M.A. Easton, W. Hao, J. Grandfield, C.J. Davidson, D.H. StJohn, L.D. Sweet, and M.J. Couper: Metallurgical and Materials Transactions A, Vol. 43, (2012), p. 3227.
[48] S. Vernede, J.A. Dantzig, and M. Rappaz: Acta Materialia, Vol. 57, (2009), p. 1554.
[49] Z. Xuezhi, K. Ahmmed, W. Meng, and H. Hu: Advanced Materials Research, Vol. 445, (2012), p. 277.
[50] P.P. Benham, R.J. Crawford, and C.G. Armstrong, Mechanics of Engineering Materials. 2nd ed. (Prentice Hall, 1996).
[51] M.E. Kassner and M.T. Perez-Prado, Fundementals of Creep in Metals and Alloys. (Elsevier Ltd, 2004).
[52] L. Esposito and N. Bonora: Journal of Pressure Vessel Technology, Vol. 134, (2012), p. 061401.
[53] R. Gasca-Neri, C.N. Ahlquist, and W.D. Nix: Acta Metallurgica, Vol. 18, (1970), p. 655.
[54] D. Hull and D.J. Bacon, Introduction to Dislocations. 4th ed. (Butterworth Heinemann, 2001).
[55] W. Blum, P. Eisenlohr, and F. Breutinger: Metallurgical and Materials Transactions A, Vol. 33A, (2002), p. 29.
[56] T.G. Langdon: Materials Transactions, JIM, Vol. 37, (1996), p. 359.
[57] F. von Buch, S. Schumann, H. Friedrich, E. Aghion, B. Bronfin, B.L. Mordike, M. Bamberger, and D. Eliezer: Magnesium Technology. Ed. H.I. Kaplan, TMS, 2002, p. 61.
[58] B.L. Mordike: Materials Science and Engineering A, Vol. 324, (2002), p. 103.
[59] J.H. Gittus: Acta Metallurgica, Vol. 22, (1974), p. 1179.
[60] A.H. Cottrell and M.A. Jaswon: Proceedings of the Royal Society of London, Series A (Mathematical and Physical Sciences), Vol. 199, (1949), p. 104.
[61] M.F. Ashby: Acta Metallurgica, Vol. 20, (1972), p. 887.
[62] G.E. Dieter, Mechanical Metallurgy. 3rd ed. Materials Science and Engineering. (McGraw-Hill, 1986).
[63] M.F. Ashby: Scripta Metallurgica, Vol. 3, (1969), p. 837.
[64] R.L. Coble: Journal of Applied Physics, Vol. 34, (1963), p. 1679.

[65] M.A. Meyers and K.K. Chawla, Mechanical Behavior of Materials. 2nd ed. (Cambridge University Press, 2009).
[66] R. Raj and M.F. Ashby: Metallurgical Transactions, Vol. 2, (1971), p. 1113.
[67] T.G. Langdon: Journal of Materials Science, Vol. 41, (2006), p. 597.
[68] K.U. Kainer, ed. *Magnesium - Alloys and Technology*. Magnesium - Alloys and Technology. 2004, Wiley-VCH Verlag GmbH & Co. KGaA.
[69] H. Oikawa and S. Karashima: Metallurgical Transactions, Vol. 5, (1974), p. 1179.
[70] C.J. Bettles, M.A. Gibson, and S.M. Zhu: Materials Science and Engineering A, Vol. A505, (2009), p. 6.
[71] S. Ansary, R. Mahmudi, and M.J. Esfandyarpour: Materials Science and Engineering A, Vol. 556, (2012), p. 9.
[72] H. Dieringa, N. Hort, and K.U. Kainer: Materials Science and Engineering A, Vol. 510-511, (2009), p. 382.
[73] I.P. Moreno, T.K. Nandy, J.W. Jones, J.E. Allison, and T.M. Pollock: Scripta Materialia, Vol. 48, (2003), p. 1029.
[74] H.J. Frost and M.F. Ashby, Deformation-mechanism maps : the plasticity and creep of metals and ceramics. 1st ed. (Pergamon Press, 1982).
[75] S. Spigarelli: Scripta Materialia, Vol. 42, (2000), p. 397.
[76] S.J. Williams, M.R. Bache, and B. Wilshire: Materials Science and Technology, Vol. 26, (2010), p. 1332.
[77] J. Yan, Y. Sun, F. Xue, J. Bai, S. Xue, and W. Tao: Journal of Materials Science, Vol. 43, (2008), p. 6952.
[78] H. Watanabe, H. Tsutsui, T. Mukai, M. Kohzu, S. Tanabe, and K. Higashi: International Journal of Plasticity, Vol. 17, (2001), p. 387.
[79] S.S. Vagarali and T.G. Langdon: Acta Metallurgica, Vol. 30, (1982), p. 1157.
[80] I.P. Moreno, T.K. Nandy, J.W. Jones, J.E. Allison, and T.M. Pollock: TMS Annual Meeting. Ed. H.I. Kaplan, 2002, p. 111.
[81] J. Yan, Y. Sun, F. Xue, S. Xue, Y. Xiao, and W. Tao: Materials Science and Engineering A, Vol. 524, (2009), p. 102.
[82] F. Kabirian and R. Mahmudi: Metallurgical and Materials Transactions A, Vol. 40, (2009), p. 2190.
[83] O.D. Sherby and E.M. Taleff: Materials Science and Engineering A, Vol. 322, (2002), p. 89.
[84] R.S. Kottada and A.H. Chokshi: Metallurgical and Materials Transactions A, Vol. 38, (2007), p. 1743.
[85] S.M. Zhu, M.A. Easton, M.A. Gibson, M.S. Dargusch, and J.F. Nie: Materials Science and Engineering A, Vol. 578, (2013), p. 377.
[86] Z.Y. Ma and S.C. Tjong: Composites Science and Technology, Vol. 61, (2001), p. 771.
[87] K.T. Park, E.J. Lavernia, and F.A. Mohamed: Acta Metallurgica Et Materialia, Vol. 42, (1994), p. 667.
[88] S.M. Zhu, J.F. Nie, M.A. Gibson, M.A. Easton, and P. Bakke: Metallurgical and Materials Transactions A, Vol. (2012), p. 1.
[89] A. Yawny and G. Eggeler: Materials Science and Engineering A, Vol. 387-389, (2004), p. 905.
[90] T.G. Langdon: Acta Metallurgica Et Materialia, Vol. 42, (1994), p. 2437.
[91] R.W. Evans and B. Wilshire, Creep of Metals and Alloys. (The Institute of Metals, 1985).
[92] J.M. Silcock: Scripta Metallurgica, Vol. 16, (1982), p. 907.
[93] S.S. Vagarali and T.G. Langdon: Acta Metallurgica, Vol. 29, (1981), p. 1969.
[94] J.F. Nie, X. Gao, S.M. Zhu, and B.C. Muddle: Scripta Materialia, Vol. 53, (2005), p. 1321.
[95] S.M. Zhu, B.L. Mordike, and J.F. Nie: Materials Science and Engineering A, Vol. 483-484, (2008), p. 583.
[96] S.M. Zhu, M.A. Gibson, J.F. Nie, M.A. Easton, and P. Bakke: Magnesium Technology. Ed. M. Pekguleryuz, N.R. Neelameggham, R.S. Beals, and E.A. Nyberg, TMS, 2008, p. 437.
[97] S. Spigarelli: Recent developments in the processing and applications of structural metals and alloys. Ed. M. Cabibbo and S. Spigarelli, Trans Tech Publications Ltd, 2009, p. 357.
[98] V. Janik, D.D. Yin, Q.D. Wang, S.M. He, C.J. Chen, Z. Chen, and C.J. Boehlert: Materials Science and Engineering A, Vol. 528, (2011), p. 3105.
[99] E.F. Emley, Principles of Magnesium Technology. 1st ed. (Pergamon Press, 1966).
[100] H. Baker and H. Okamoto, eds. *ASM Handbook Vol. 3 - Alloy Phase Diagrams*. Alloy Phase Diagrams. Vol. 3. 1992, ASM International.

[101] W. Blum, P. Zhang, B. Watzinger, B.V. Grossmann, and H.G. Haldenwanger: Materials Science and Engineering A, Vol. 319-321, (2001), p. 735.
[102] M. Regev, A. Rosen, and M. Bamberger: Metallurgical and Materials Transactions A, Vol. 32, (2001), p. 1335.
[103] D.G.L. Prakash and D. Regener: Journal of Alloys and Compounds, Vol. 467, (2009), p. 271.
[104] A.A. Luo: International Materials Reviews, Vol. 49, (2004), p. 13.
[105] G.V. Raynor, The physical metallurgy of magnesium and its alloys. (Pergamon Press, 1959).
[106] A. Luo and M.O. Pekguleryuz: Journal of Materials Science, Vol. 29, (1994), p. 5259.
[107] M.S. Dargusch, K. Pettersen, K. Nogita, M.D. Nave, and G.L. Dunlop: Materials Transactions, Vol. 47, (2006), p. 977.
[108] B.L. Mordike and T. Ebert: Materials Science and Engineering A, Vol. 302, (2001), p. 37.
[109] M.O. Pekguleryuz and A.A. Kaya: Advanced Engineering Materials, Vol. 5, (2003), p. 866.
[110] S.M. Zhu, M.A. Gibson, J.F. Nie, M.A. Easton, and T.B. Abbott: Scripta Materialia, Vol. 58, (2008), p. 477.
[111] B.R. Powell, V. Rezhets, M.P. Balogh, and R.A. Waldo: JOM, Vol. 54, (2002), p. 34.
[112] M. Pekguleryuz and M. Celikin: International Materials Reviews, Vol. 55, (2010), p. 197.
[113] W. Xiao, M.A. Easton, M.S. Dargusch, S. Zhu, and M.A. Gibson: Materials Science and Engineering A, Vol. 539, (2012), p. 177.
[114] W. Yeshuang, W. Qudong, W. Guohua, Z. Yanping, and D. Wenjiang: Materials Letters, Vol. 57, (2002), p. 929.
[115] A. Nayeb-Hashemi and J.B. Clark, eds. *Phase Diagrams of Binary Magnesium Alloys*. 1988, ASM International.
[116] M. Kunst, A. Fischersworring-Bunk, G. L'Esperance, P. Plamondon, and U. Glatzel: Materials Science and Engineering A, Vol. 510-511, (2009), p. 387.
[117] M.O. Pekguleryuz and A.A. Kaya, *Creep Resistant Magnesium Alloys for Powertrain Applications*, in *Magnesium*, K.U. Kainer, Editor. 2005. p. 74.
[118] J.R. TerBush, 2010, *Creep Deformation in Mg-Al-Ca-Based Alloys,* PhD., University of Michigan.
[119] H. Dieringa, Y. Huang, P. Wittke, M. Klein, F. Walther, M. Dikovits, and C. Poletti: Materials Science and Engineering A, Vol. 585, (2013), p. 430.
[120] A. Suzuki, N.D. Saddock, J.R. TerBush, B.R. Powell, J.W. Jones, and T.M. Pollock: Metallurgical and Materials Transactions A, Vol. 39, (2008), p. 696.
[121] A. Suzuki, N.D. Saddock, J.W. Jones, and T.M. Pollock: Scripta Materialia, Vol. 51, (2004), p. 1005.
[122] http://www.asianmetal.com/. Asian Metal, 2012.
[123] C.J. Bettles, C.T. Forwood, D.H. St. John, M.T. Frost, D.S. Jones, M. Qian, G.L. Song, J.R. Griffiths, and J.F. Nie: Magnesium Technology. Ed. H.I. Kaplan, TMS, 2003, p. 223.
[124] M.A. Gibson, C.J. Bettles, S.M. Zhu, M.A. Easton, and J.F. Nie: Magnesium Technology. Ed. E. Nyberg, 2009, p. 243.
[125] T. Rzychori and A. Kietbus: Magnesium 2010: 8th International Conference on Magnesium Alloys and their Applications. Ed. K.U. Kainer, Wiley-VCH Verlag GmbH, 2010, p. 836.
[126] M.A. Gibson, S. Zhu, M.A. Easton, and J.F. Nie: Magnesium Technology. Ed. S.R. Agnew, N.R. Neelameggham, E.A. Nyberg, and W.H. Sillekens, 2010, p. 233.
[127] N. Jeal: Advanced Materials and Processes, Vol. 163, (2005), p. 65.
[128] I.A. Anyanwu, Y. Gokan, A. Suzuki, S. Kamado, Y. Kojima, S. Takeda, and T. Ishida: Materials Science and Engineering A, Vol. 380, (2004), p. 93.
[129] A.R. Wu and C.Q. Xia: Materials and Design, Vol. 28, (2007), p. 1963.
[130] S. Gavras, S.M. Zhu, M.A. Gibson, M.A. Easton, and J.F. Nie: Magnesium 2012: 9th International Conference on Magnesium Alloys and their Applications. Ed. W.J. Poole and K.U. Kainer, 2012, p. 757.
[131] L.L. Rokhlin, Magnesium Alloys Containing Rare Earth Metals: Structures and Properties. (Taylor & Francis, 2003), 245.
[132] J. Gröbner, M. Hampl, R. Schmid-Fetzer, M.A. Easton, S. Zhu, M.A. Gibson, and J.F. Nie: Intermetallics, Vol. 28, (2012), p. 92.
[133] A. Nayeb-Hashemi and J. Clark: Journal of Phase Equilibria, Vol. 9, (1988), p. 172.
[134] H. Okamoto: Journal of Phase Equilibria, Vol. 12, (1991), p. 249.
[135] H. Okamoto: Journal of Phase Equilibria, Vol. 14, (1993), p. 534.

[136] H. Okamoto: Journal of Phase Equilibria and Diffusion, Vol. 27, (2006), p. 550.
[137] H. Okamoto: Journal of Phase Equilibria and Diffusion, Vol. 27, (2006), p. 431.
[138] T.J. Pike and B. Noble: Journal of the Less-Common Metals, Vol. 30, (1973), p. 63.
[139] J.F. Nie: Metallurgical and Materials Transactions A: Physical Metallurgy and Materials Science, Vol. 43A, (2012), p. 3891.
[140] P. Villars and L.D. Calvert, Pearson's Handbook of Crystallographic Data for Intermetallic Phases. 2nd ed. (ASM International, 1991), 5366.
[141] M. Celikin, A.A. Kaya, R. Gauvin, and M. Pekguleryuz: Scripta Materialia, Vol. 66, (2012), p. 737.
[142] Z. Xiaoqin, Z. Honghui, Z. Chunquan, and D. Wenjiang: Materials Science and Engineering A, Vol. 424, (2006), p. 40.
[143] M.O. Pekguleryuz: Materials Science Forum, Vol. 350, (2000), p. 131.
[144] H. Wei, Q.D. Wang, Y.P. Zhu, H.T. Zhou, and W.J. Ding: Materials Science Engineering A, Vol. A360, (2003), p. 107.
[145] H. Somekawa and T. Mukai: Materials Letters, Vol. 76, (2012), p. 32.
[146] V. Janik, F. Hnilica, P. Zuna, V. Ocenaek, and I. Stulikova: Transactions of Nonferrous Metals Society of China, Vol. 18, (2008), p. 64.
[147] K.J. Hsia, D.M. Parks, and A.S. Argon: Mechanics of Materials, Vol. 11, (1991), p. 43.
[148] D. Amberger, P. Eisenlohr, and M. Goken: Acta Materialia, Vol. 60, (2012), p. 2277.
[149] B. Zhang, S. Gavras, A.V. Nagasekhar, C.H. Caceres, and M.A. Easton: Metallurgical and Materials Transactions A, (2014), in press.
[150] L. Gao, R.S. Chen, and E.H. Han: Journal of Alloys and Compounds, Vol. 481, (2009), p. 379.
[151] L. Gao, R.S. Chen, and E.H. Han: Journal of Alloys and Compounds, Vol. 472, (2009), p. 234.
[152] G. Neumann and C. Tuijn, eds. *Self-diffusion and impurity diffusion in pure metals: handbook of experimental data*. Pergamon Materials Series. Vol. 14. 2008, Elsevier. 349.
[153] J.S. Robinson, R.L. Cudd, and J.T. Evans: Materials Science and Technology, Vol. 19, (2003), p. 143.
[154] J.F. Nie and B.C. Muddle: Scripta Materialia, Vol. 40, (1999), p. 1089.
[155] S. Celotto: Acta Materialia, Vol. 48, (2000), p. 1775.
[156] T. Sato and M.V. Kral: Metallurgical and Materials Transactions A, Vol. 39, (2008), p. 688.
[157] J.F. Nie: Scripta Materialia, Vol. 48, (2003), p. 1009.
[158] S. Spigarelli, M. Regev, E. Evangelista, and A. Rosen: Materials Science and Technology, Vol. 17, (2001), p. 627.
[159] C. Sanchez, G. Nussbaum, P. Azavant, and H. Octor: Materials Science and Engineering A, Vol. A221, (1996), p. 48.
[160] J.F. Nie and R.C. Muddle: Acta Materialia, Vol. 48, (2000), p. 1691.
[161] Y. Gao, H. Liu, R. Shi, N. Zhou, Z. Xu, J.F. Nie, and Y. Wang: Magnesium Technology. Ed. S.N. Mathaudhu, W.H. Sillekens, N.R. Neelameggham, and N. Hort, TMS, 2012, p. 377.
[162] X. Gao, S.M. He, X.Q. Zeng, L.M. Peng, W.J. Ding, and J.F. Nie: Materials Science and Engineering A, Vol. 431, (2006), p. 322.
[163] G. Yan, W. Qudong, G. Jinhai, and Z. Yang: Magnesium Technology. Ed. E. Nyberg, TMS, 2009, p. 279.
[164] C.C. Smith, A.M. Taylor, and P. Greenfield: Journal of Nuclear Materials, Vol. 12, (1964), p. 198.
[165] M.B. Yang, X.F. Liang, H. Li, and F.S. Pan: Transactions of Nonferrous Metals Society of China (English Edition), Vol. 20, (2011), p. 416.
[166] S. Barbagallo: International Journal of Cast Metals Research, Vol. 17, (2004), p. 370.
[167] M.A. Gibson and C.J. Bettles, *HPDC Magnesium Alloy*. 2006. WO 2006/125278 A1
[168] S. Gavras, S. Zhu, M.A. Easton, M.A. Gibson, and J.F. Nie: Materials Science Forum. Ed. H. Dieringa, N. Hort, and K.U. Kainer, 2011, p. 210.
[169] K. Zeng, T. Klassen, W. Oelerich, and R. Bormann: International Journal of Hydrogen Energy, Vol. 24, (1999), p. 989.
[170] A. San-Martin and F.D. Manchester: Journal of Phase Equilibria, Vol. 13, (1992), p. 17.
[171] M. Easton, M. Gibson, S.M. Zhu, and T. Abbott: Metallurgical and Materials Transactions A, Vol. 45, (2014), p. 3586.
[172] O. Anopuo, 2010, *Bolt Load Retention Response and Creep of AS41 Mg-Alloy,* PhD, Technischen Universität Hamburg-Harburg.

[173] A.J. Schwartz, M. Kumar, and B.L. Adams, Electron backscatter diffraction in materials science. (Kluwer Academic, 2000), 339.
[174] A.J. Wilkinson and T.B. Britton: Materials Today, Vol. 15, (2012), p. 366.
[175] A.V. Nagasekhar, M.A. Easton, and C.H. Caceres: Advanced Engineering Materials, Vol. 11, (2009), p. 912.
[176] M.A. Easton, M.A. Gibson, D. Qiu, S.M. Zhu, J. Gröbner, R. Schmid-Fetzer, J.F. Nie, and M.X. Zhang: Acta Materialia, Vol. 60, (2012), p. 4420.
[177] R.A. Rosenberg, M.C. Flemings, and H.F. Taylor: Modern Castings, Vol. 38, (1960), p. 112.
[178] G. Cao and S. Kou: Metallurgical and Materials Transactions A, Vol. 37A, (2006), p. 3647.
[179] W. Kurz and D.J. Fisher, Fundamentals of Solidification. (Trans Tech Publications Ltd., 1986).
[180] J. Gröbner, A. Kozlov, R. Schmid-Fetzer, M.A. Easton, S. Zhu, M.A. Gibson, and J.F. Nie: Acta Materialia, Vol. 59, (2011), p. 613.
[181] L. Zhou, Z. Liu, Y. Huang, and P. Mao: Advanced Materials Research. Ed. S.T. Tu, G.Z. Wang, and J.M. Gong, Trans Tech Publications Ltd., 2012, p. 138.
[182] G. Cao and S. Kou: Materials Science and Engineering A, Vol. 417, (2006), p. 230.
[183] R. Dodd, W. Pollard, and J. Meier: AFS Transactions, Vol. 65, (1957), p. 110.
[184] M.R. Barnett, M.D. Nave, and A. Ghaderi: Acta Materialia, Vol. 60, (2012), p. 1433.
[185] S. Xu, M.A. Gharghouri, and M. Sahoo: Advanced Engineering Materials, Vol. 9, (2007), p. 807.
[186] S.R. Agnew, K.C. Liu, E.A. Kenik, and S. Viswanathan: Magnesium Technology. Ed. H.I. Kaplan, J. Hryns, and B. Clow, TMS, 2000, p. 285.
[187] K.Y. Sohn, J.W. Jones, and J.E. Allison: Magnesium Technology. Ed. H.I. Kaplan, J. Hryns, and B. Clow, TMS, 2000, p. 271.
[188] K. Saito and K. Hiraga: Materials Transactions, Vol. 52, (2011), p. 1860.
[189] C.H. Caceres, W.J. Poole, A.L. Bowles, and C.J. Davidson: Materials Science and Engineering A, Vol. 402, (2005), p. 269.
[190] Q. Han, B.K. Kad, and S. Viswanathan: Philosophical Magazine, Vol. 84, (2004), p. 3843.
[191] M.A. Easton, K. Strobel, S.M. Zhu, M.A. Gibson, and J.F. Nie: Materials Science Forum, Vol. 654-656, (2010), p. 683.
[192] D. Dispinar and J. Campbell: Materials Science and Engineering A, Vol. 528, (2011), p. 3860.
[193] A.M. Gokhale and G.R. Patel: Materials Characterization, Vol. 54, (2005), p. 13.
[194] J.P. Weiler, J.T. Wood, R.J. Klassen, E. Maire, R. Berkmortel, and G. Wang: Materials Science and Engineering A, Vol. 395, (2005), p. 315.
[195] D.J. Lloyd, S.A. Court, and K.M. Gatenby: Materials Science and Technology, Vol. 13, (1997), p. 660.
[196] S. Ohtani and H. Inagaki: Materials Science Forum, Vol. 396-402, (2002), p. 1049.
[197] B.J. Brindley and P.J. Worthington: Acta Metallurgica, Vol. 17, (1969), p. 1357.
[198] K.G. Kent and A. Kelly: Journal of the Institute of Metals, Vol. 93, (1965), p. 536.
[199] D.D. Yin, Q.D. Wang, Y. Gao, C.J. Chen, and J. Zheng: Journal of Alloys and Compounds, Vol. 509, (2011), p. 1696.
[200] A. Jain, O. Duygulu, D.W. Brown, C.N. Tom, and S.R. Agnew: Materials Science and Engineering A, Vol. 486, (2008), p. 545.
[201] M.T. Correia and M.A. Fortes: Material Science and Engineering, Vol. 54, (1982), p. 95.
[202] M. Abbadi, P. Hahner, and A. Zeghloul: Materials Science and Engineering A, Vol. 337, (2002), p. 194.
[203] S.M. Zhu and J.F. Nie: Scripta Materialia, Vol. 50, (2004), p. 51.
[204] X.Y. Fang, D.Q. Yi, and J.F. Nie: Metallurgical and Materials Transactions A, Vol. 40, (2009), p. 2761.
[205] D. Wu, R.S. Chen, and E.H. Han: Materials Science and Engineering A, Vol. 532, (2012), p. 267.
[206] M. Nishijima, K. Yubuta, and K. Hiraga: Materials Transactions, Vol. 48, (2007), p. 84.
[207] H. Liu, Y. Gao, J.Z. Liu, Y.M. Zhu, Y. Wang, and J.F. Nie: Acta Materialia, Vol. 61, (2013), p. 453.
[208] L.L. Rokhlin, T.V. Dobatkina, and N.I. Nikitina: Materials Science Forum. Ed. Y. Kojima, T. Aizawa, K. Higashi, and S. Kamado, 2003, p. 291.
[209] R.C. Gifkins, A. Gittins, R.L. Bell, and T.G. Langdon: Journal of Materials Science, Vol. 3, (1968), p. 306.
[210] G. Shao, V. Varsani, and Z. Fan: Calphad: Computer Coupling of Phase Diagrams and Thermochemistry, Vol. 30, (2006), p. 286.

[211] C. Caceres, G. Mann, and J. Griffiths: Metallurgical and Materials Transactions A, Vol. 42, (2011), p. 1950.
[212] B. Burton and B.D. Bastow: Acta Metallurgica, Vol. 21, (1973), p. 13.
[213] C. Guo, Z. Du, and C. Li: International Journal of Materials Research, Vol. 101, (2010), p. 1424.
[214] C. Guo, Z. Du, and C. Li: International Journal of Materials Research, Vol. 99, (2008), p. 650.

Appendix A

Table A1: Temperatures that correlate to the coherency point (T_0) and the coalescence point (T_{co}) obtained from temperature - fraction solid curves produced using the Gröbner [132] database in Pandat™.

Alloy (at.%)	T_0 (°C)	T_{co} (°C)
Mg-0.46La-0.002Nd	633.9	624.3
Mg-0.46La-0.02Nd	633.6	610.8
Mg-0.45La-0.03Nd	633.3	608.3
Mg-0.46La-0.06Nd	631.8	603.5
Mg-0.47La-0.10Nd	629.7	595.3
Mg-0.47La-0.14Nd	628.3	586.8
Mg-0.43La-0.18Nd	628.6	578.7
Mg-0.45La-0.63Nd	606.5	541.8
Binary Alloys (at.%)		
Mg-0.002Nd	649.8	649.1
Mg-0.02Nd	649.4	643.0
Mg-0.03Nd	649.0	635.1
Mg-0.06Nd	648.2	616.4
Mg-0.10Nd	646.9	582.8
Mg-0.14Nd	645.6	546.7
Mg-0.18Nd	644.7	541.7
Mg-0.63Nd	627.6	541.7
Mg-0.003Y	649.8	649.4
Mg-0.02Y	649.6	647.3
Mg-0.04Y	649.8	642.7
Mg-0.12Y	647.7	630.0
Mg-0.24Y	645.6	611.6
Mg-0.30Y	644.3	601.9
Mg-0.42Y	642.1	587.7
Mg-0.70Y	636.8	574.5
Mg-1.18Y	627.1	574.5
Mg-0.003Gd	649.8	649.2
Mg-0.005Gd	649.8	648.9
Mg-0.04Gd	649.0	640.9
Mg-0.10Gd	647.8	626.7
Mg-0.21Gd	645.4	599.6
Mg-0.59Gd	637.1	576.1
Mg-0.87Gd	630.9	576.1

Appendix B

Table B1: Tensile properties of Mg-La-Nd, Mg-La-Y and Mg-La-Gd alloys in As-Cast, T4 or T6 conditions at room temperature (RT) and 177°C.

Alloy Composition at.%	0.2% PS ±SD (MPa)	UTS ±SD (MPa)	Elong. ±SD (%)	Condition	Testing Temp.
Mg-0.47La-0.10Nd	146.7 (± 3.0)	166.7 (± 2.3)	2.7 (± 0.3)	As-Cast	RT
Mg-0.43La-0.18Nd	151.6 (± 3.2)	167.1 (± 4.5)	2.3 (± 0.7)	As-Cast	RT
Mg-0.45La-0.63Nd	196.9 (± 4.2)	198.6 (± 4.2)	2.1 (± 0.7)	As-Cast	RT
Mg-0.48La-0.12Y	155.2 (± 1.6)	175.8 (± 1.0)	3.9 (± 0.4)	As-Cast	RT
Mg-0.49La-0.24Y	158.7 (± 1.6)	180.4 (± 3.9)	4.4 (± 0.4)	As-Cast	RT
Mg-0.45La-1.18Y	186.4 (± 2.1)	213.6 (± 5.8)	4.0 (± 0.7)	As-Cast	RT
Mg-0.45La-0.10Gd	145.7 (± 5.1)	169.4 (± 8.7)	3.4 (± 0.9)	As-Cast	RT
Mg-0.46La-0.21Gd	159.6 (± 2.4)	180.2 (± 7.9)	4.7 (± 0.8)	As-Cast	RT
Mg-0.45La-0.87Gd	182.3 (± 3.1)	200.2 (± 5.6)	3.8 (± 0.3)	As-Cast	RT
Mg-0.47La-0.10Nd	103.4 (± 0.9)	126.5 (± 1.6)	11.9 (± 2.2)	As-Cast	177°C
Mg-0.43La-0.18Nd	111.2 (± 2.3)	143.4 (± 1.9)	19.1 (± 1.8)	As-Cast	177°C
Mg-0.45La-0.63Nd	134.4 (± 2.0)	175.8 (± 4.1)	5.6 (± 1.0)	As-Cast	177°C
Mg-0.48La-0.12Y	108.0 (± 1.0)	137.7 (± 2.2)	19.8 (± 2.0)	As-Cast	177°C
Mg-0.49La-0.24Y	112.8 (± 1.5)	153.0 (± 2.5)	14.2 (± 2.3)	As-Cast	177°C
Mg-0.45La-1.18Y	150.6 (± 1.4)	205.7 (± 3.6)	5.3 (± 0.8)	As-Cast	177°C
Mg-0.45La-0.10Gd	100.6 (± 1.4)	129.3 (± 3.0)	16.2 (± 4.6)	As-Cast	177°C
Mg-0.46La-0.21Gd	110.9 (± 1.7)	151.1 (± 2.5)	12.3 (± 0.8)	As-Cast	177°C
Mg-0.45La-0.87Gd	140.2 (± 4.6)	192.9 (± 2.1)	5.4 (± 0.4)	As-Cast	177°C
Mg-0.47La-0.10Nd	106.1 (± 2.6)	158.6 (± 3.1)	3.7 (± 0.4)	T4	RT
Mg-0.43La-0.18Nd	119.2 (± 2.4)	163.8 (± 10.6)	4.9 (± 1.2)	T4	RT
Mg-0.45La-0.63Nd	147.7 (± 3.6)	185.3 (± 7.9)	4.0 (± 0.5)	T4	RT
Mg-0.48La-0.12Y	110.9 (± 4.1)	185.9 (± 8.8)	7.2 (± 0.9)	T4	RT
Mg-0.49La-0.24Y	107.4 (± 3.9)	179.1 (± 9.9)	6.5 (± 1.1)	T4	RT
Mg-0.45La-1.18Y	136.2 (± 0.8)	209.2 (± 14.0)	7.6 (± 3.0)	T4	RT
Mg-0.45La-0.10Gd	102.9 (± 2.0)	172.6 (± 6.4)	5.9 (± 0.6)	T4	RT
Mg-0.46La-0.21Gd	126.9 (± 2.6)	174.1 (± 3.4)	5.7 (± 0.5)	T4	RT
Mg-0.45La-0.87Gd	131.3 (± 3.9)	193.8 (± 3.2)	5.8 (± 0.5)	T4	RT
Mg-0.47La-0.10Nd	84.1 (± 2.7)	122.3 (± 1.7)	16.3 (± 1.9)	T4	177°C
Mg-0.43La-0.18Nd	83.0 (± 1.6)	131.4 (± 5.4)	12.7 (± 4.6)	T4	177°C
Mg-0.45La-0.63Nd	126.5 (± 3.2)	191.1 (± 3.5)	11.5 (± 1.0)	T4	177°C
Mg-0.48La-0.12Y	85.7 (± 1.5)	127.8 (± 1.6)	23.4 (± 2.9)	T4	177°C
Mg-0.49La-0.24Y	87.2 (± 0.3)	145.4 (± 1.0)	21.5 (± 1.8)	T4	177°C
Mg-0.45La-1.18Y	134.8 (± 2.2)	219.0 (± 12.2)	9.1 (± 3.4)	T4	177°C

Table B1: cont.

Alloy Composition at.%	0.2% PS ±SD (MPa)	UTS ±SD (MPa)	Elong. ±SD (%)	Condition	Testing Temp.
Mg-0.45La-0.10Gd	87.1 (± 2.6)	127.8 (± 1.6)	20.0 (± 3.9)	T4	177°C
Mg-0.46La-0.21Gd	82.1 (± 2.2)	145.0 (± 2.1)	15.9 (± 2.1)	T4	177°C
Mg-0.45La-0.87Gd	127.0 (± 2.8)	205.3 (± 5.9)	10.1 (± 0.6)	T4	177°C
Mg-0.47La-0.10Nd	126.6 (± 4.3)	164.3 (± 4.8)	4.0 (± 0.6)	T6	RT
Mg-0.43La-0.18Nd	132.7 (± 4.0)	161.0 (± 2.4)	3.6 (± 0.5)	T6	RT
Mg-0.45La-0.63Nd	188.5 (± 0.3)	215.8 (± 2.7)	2.6 (± 0.2)	T6	RT
Mg-0.48La-0.12Y	129.9 (± 2.0)	180.7 (± 6.4)	5.7 (± 0.7)	T6	RT
Mg-0.49La-0.24Y	137.8 (± 2.0)	183.7 (± 7.3)	6.4 (± 1.1)	T6	RT
Mg-0.45La-1.18Y	203.2 (± 5.1)	252.7 (± 8.1)	2.8 (± 0.3)	T6	RT
Mg-0.45La-0.10Gd	117.8 (± 8.6)	179.8 (± 0.9)	5.8 (± 0.0)	T6	RT
Mg-0.46La-0.21Gd	137.2 (± 1.7)	173.6 (± 3.1)	4.9 (± 0.3)	T6	RT
Mg-0.45La-0.87Gd	216.5 (± 5.7)	265.7 (± 7.7)	1.7 (± 0.3)	T6	RT
Mg-0.47La-0.10Nd	92.4 (± 1.3)	125.9 (± 2.0)	13.5 (± 1.6)	T6	177°C
Mg-0.43La-0.18Nd	96.0 (± 1.5)	135.3 (± 1.1)	9.3 (± 1.1)	T6	177°C
Mg-0.45La-0.63Nd	144.9 (± 2.3)	201.3 (± 3.4)	6.4 (± 1.4)	T6	177°C
Mg-0.48La-0.12Y	91.9 (± 2.6)	132.8 (± 2.5)	19.5 (± 3.2)	T6	177°C
Mg-0.49La-0.24Y	98.8 (± 1.3)	145.0 (± 1.5)	15.1 (± 1.2)	T6	177°C
Mg-0.45La-1.18Y	177.7 (± 6.2)	248.2 (± 7.6)	5.5 (± 1.4)	T6	177°C
Mg-0.45La-0.10Gd	92.3 (± 0.6)	124.6 (± 1.3)	15.4 (± 3.4)	T6	177°C
Mg-0.46La-0.21Gd	103.5 (± 0.4)	141.7 (± 8.6)	10.0 (± 3.0)	T6	177°C
Mg-0.45La-0.87Gd	208.3 (± 8.8)	243.3 (± 7.7)	2.4 (± 0.8)	T6	177°C